Imperial College London

Department of Chemistry

Alkali metal solutions in low-polarity solvents

by

René Riedel

Supervisor:

Prof. Anthony G. M. Barrett FRS FMedSci

A thesis submitted in partial fulfilment of the requirements for the degree Doctor of Philosophy

12 October 2018

Declaration of Authorship

The present work was carried out in the period from 13.10.2014 to 12.10.2018 at the Department of Chemistry at Imperial College London and supervised by Prof. Anthony GM Barrett. Results from research visits to the Inorganic Chemistry Laboratories, University of Oxford, Oxford and the ISIS Neutron and Muon Source Facility, Science and Technology Facilities Council, Rutherford Appleton Laboratory, Harwell Oxford are also part of this work.

I declare that I have written this paper on my own and used no other than the named aids. Where results from collaborative experiments have been used it is clearly stated.

Signed: _____

Date: _____

Copyright Declaration

The copyright of this thesis rests with the author and is made available under a Creative Commons Attribution Non-Commercial No Derivatives licence. Researchers are free to copy, distribute or transmit the thesis on the condition that they attribute it, that they do not use it for commercial purposes and that they do not alter, transform or build upon it. For any reuse or redistribution, researchers must make clear to others the licence terms of this work

"If you want to go quickly, go alone.

If you want to go far, go together."

From Africa.

Abstract

Alkali metal solutions in low-polarity solvents

by René Riedel

Alkali metal solutions comprising alkali metal anions, the 'alkalides', and complexed alkali cations side by side provide a large untapped potential with respect to future applications. This is due to their unique properties such as a strongly reducing nature and a high polarisability. The use of organic complexing agents such as crown ethers and cryptands allows for the stabilisation of high concentrations of charge carriers in a weakly polar medium. Nevertheless, the currently available knowledge about those solutions is very limited and their characterisation is mostly centered around alkali metal NMR techniques. A significant upfield shift and exceptionally narrow width of the alkalide NMR signal were ascribed to the high shielding and high symmetry of an effectively unperturbed 'gas-like' anion in solution with little to no interaction with its local environment.

Our investigations extend this traditional picture of the alkalide in solution and unveil the underlying effect of coulomb interactions on the properties of alkalides in low-polarity solvents by a comprehensive combination of spectroscopic methods. Concentration dependent measurement of both conductivity and permittivity of alkalide solutions revealed that ion pairing is a key factor in determining the kinetic properties and the stability of alkali metal solutions. Furthermore, the effect of dissolved metal on the mesoscopic structure of solutions of macrocyclic complexants was probed by small angle neutron scattering. Ultimately, we present a rationale for the rather obscure and unexpected temperature- and concentration-dependence of alkali metal dissolution in organic media and provide a multifacetted understanding of the remarkable preparatory and spectroscopic characteristics of alkalide solutions.

Finally, the synthesis of sterically congested amides and their unique fragmentation under dissolving metal reduction conditions are presented. Synthetic access to amide substrates was achieved by the use of highly electrophilic nitrimine precursors in the formation of imine intermediates.

Acknowledgements

First and foremost, I would like to greatly thank *Prof. Anthony GM Barrett* for taking me on and supervising my PhD studies. He encouraged and supported me throughout and expressed his confidence in my work at all times. In spite of an exceptionally busy schedule, he was always available to give advice and valuable insights in many respects and provided the framework for me to have an invaluable experience throughout my PhD studies.

Further, I am much obliged to *Prof. Peter P Edwards* for warmly welcoming me to his group as a collaborator and for his continuous support and inspiring discussions.

Huge thanks go to *Dr. Andrew Seel*, *Dr. Daniel Malko* and *Michael Sachs* for sharing their expertise with me during numerous intriguing, stimulating and motivating discussions, for their exceptional assistance with experiments both during and beyond standard working hours, and also for being great friends altogether.

Big thanks also go to my collaborators *Prof. Anthony Kucernak* at ICL and *Prof. Adrian Porch*, *Dr. Daniel Slocombe*, and *Dr. Heungjae Choi* at Cardiff University for their readiness to support this project and the access to and assistance with their equipment, as well as *Prof. Eva Zurek*, *Prof. Jochen Autschbach*, and *Daniel Miller* for their valuable support of this project by their expertise in computational chemistry. Furthermore, I would like to thank *Dr. Jochen Brandt* for his kind and special advice and input both on scientific and experimental matters. I would also like to thank *Prof. Philip J Parsons* for his caring support throughout my studies at ICL.

This thesis would not have been possible without the immense support of all involved instrument scientist and technicians. Therefore I thank the *Science and Technology Facilities Council (STFC)* for funding my research proposals, for access to their instruments at the *neutron source ISIS*, and especially *Dr Thomas Headen* for his assistance. I thank *Dr Harold Toms* at Queen Mary's University London for his assistance in acquiring NMR data and I would like to express special thanks to *Pete Haycock* for his constant readiness and kindness in supporting me with numerous NMR experiments at ICL. More special thanks go to all technicians in the chemistry department for always being approachable and helpful and especially to *Pete Sulsh* and *Stefanos Karapanagotidis* for their support

beyond all expectations with keeping all experimental hardware up and running. I would also like to thank *Dr Andrew J.P. White* at ICL for acquiring XRD data.

Gratitude also goes to all members of the *Barrett*, *Fuchter*, *Parsons*, *Edwards*, and *Kucernak* groups that I had the privilege to get to know over the years and that made the lab such a great working environment. I must give huge thanks to the administrative staff at ICL and especially to Virginia for her kind and constant assistance.

I would also like thank my friends and colleagues from my time as a subwarden in Fisher Hall and Woodward Buildings who I had the pleasure to share so much fun and memorable experiences with.

I want to express my gratitude to my parents for having been a constant source of love and aid throughout my entire time abroad which I greatly appreciate.

Finally, I owe my sincere thanks and deep respect to my beloved girlfriend Jenny for her unconditional and permanent emotional support. I am incredibly grateful for her boundless patience with putting up with a scientist and subwarden who cancelled far too many dates for the sake of 'just a few more' scientific results.

Contents

Declaration of Authorship **2**

Copyright Declaration **3**

Abstract **5**

Acknowledgements **6**

List of Figures **10**

List of Schemes **11**

List of Tables **12**

Abbreviations **13**

Physical Constants **17**

Symbols **18**

1 Introduction **21**
1.1 Alkali Metal Dissolution 21
1.2 The Role of Complexants 23
1.3 Alkalide solutions 26
1.4 Motivation and aim of this work 28

2 NMR and UV-Vis spectroscopic investigation of alkalides in THF **30**
2.1 Introduction 30
2.2 Results and Discussion 31
2.2.1 NMR spectroscopy 31
2.2.2 Cryogenic UV-Vis spectroscopy 38
2.3 Conclusion 40
2.4 Experimental Section 41

3 Conductivity measurements **43**

3.1 Introduction . . . 43
3.2 Results and Discussion . . . 46
3.2.1 Metal content analysis . . . 46
3.2.1.1 Evaluation of analytical methods . . . 46
3.2.1.2 Ion Chromatography . . . 49
3.2.2 Optimization of Experimental method for conductivity measurements 50
3.2.3 Viscosity measurements . . . 54
3.2.4 Data collection and processing . . . 56
3.3 Conclusion . . . 62
3.4 Experimental Section . . . 63

4 Dielectric Spectroscopy 65
4.1 Introduction . . . 65
4.2 Results and Discussion . . . 66
4.2.1 Calibration of Coaxial probe . . . 66
4.2.2 Dielectric properties of a sodide solution . . . 68
4.3 Conclusion . . . 72
4.4 Experimental Setup . . . 72

5 Small-Angle Neutron Scattering of alkalide solutions 75
5.1 Introduction . . . 75
5.2 Results and Discussion . . . 76
5.2.1 Conformational analysis . . . 84
5.3 Conclusion . . . 84
5.4 Experimental Aspects . . . 85

6 Synthesis and DMR of sterically demanding amides and lactams 88
6.1 Introduction . . . 88
6.1.1 Dissolving metal reduction of carboxylic acid derivatives . . . 88
6.1.2 Synthesis and Reduction of tertiary amides and *N*-alkylated lactams 93
6.2 Results and Discussion . . . 95
6.2.1 Synthesis of amide and lactam substrates . . . 95
6.2.1.1 Adamantylamines and -amides . . . 95
6.2.1.2 Camphor nitrimine and derived amines . . . 96
6.2.1.3 Formation of stable nitrimines . . . 97
6.2.1.4 Isolongifolanone nitrimine synthesis and characterization 101
6.2.1.5 8-Nitrimino-tricyclodecane and derived amines . . . 102
6.2.1.6 6-Nitrimino-cholestane and derived amines . . . 103
6.2.1.7 Acylation of sterically demanding secondary amines . . . 106
6.2.1.8 NMR characteristics of sterically demanding tertiary amides 107
6.2.1.9 Synthesis of *N*-alkylated lactams . . . 111
6.2.2 Dissolving metal reduction of tertiary amides and lactams . . . 111
6.3 Conclusion . . . 117

7 Concluding Remarks and Future Work 119

8 Experimental Section - Amide Synthesis and Reduction 123
8.1 General Aspects . . . 123

8.1.1 Instrumental procedures 123
8.1.2 General reaction procedures 123
8.2 Preparation of compounds and solutions 124
8.2.1 *N*-alkylated Tricyclodecanyl-8- and Cholestanyl-6-amines 124
8.2.2 Tertiary *N*-8-Tricyclodecanyl- and *N*-6-Cholestanyl-amides 132
8.2.3 Synthesis of Lactams 140
8.2.4 Dissolving metal reduction of tertiary amides and *N*-alkylated lactams 142
8.2.5 Preparation of precursors and other compounds 144
8.3 Crystal data and structures 163
8.3.1 Crystal data and structure refinement for $HMHC(K)^{+}BPh_4^{-}$ . . . 163
8.3.2 Crystal data and structure refinement for *N*-3β-5α-cholestanyl-bornylimine 167
8.3.3 Crystal data and structure refinement for *rac*-isolongifolanone oxime 170
8.3.4 Crystal data and structure refinement for *R*-isolongifolanone oxime 174
8.3.5 Crystal data and structure refinement for 6-nitrimino-5α-cholestane 177
8.4 Supporting information 181

References **182**

List of Figures

1.1 **left** Species present in metal solutions and **right** effect of an added complexant "Cyc()" on the respective equilibria. 23
1.2 Hexamethyl-hexacyclen (HMHC,), the per-methylated aza analogue of 18-crown-6. 25

2.1 ^{39}K **(top)** and ^{23}Na **(bottom)** spectra of HMHC(K^+)K^- and HMHC(K^+)Na^-, resp., in THF at 245 K (chemical shifts referenced to Na^+ and K^+ in an aqueous saturated solution of its chloride, resp.). 31
2.2 ^{23}Na Temperature dependence of NMR spin-lattice (T_1), spin-spin (T_2) relaxation times, and the integral (normalised) of the Na^- (left) and K^- (right) signals of NaK/HMHC/THF and K/HMHC/THF solutions, respectively. 34
2.3 Arrhenius plot of NMR exchange relaxation times of Na^- in solutions of NaK in THF with various complexants. 36
2.4 Schematic representation of the effect of ion pairing on the NMR properties of a sodide solution in THF (values estimated based on discussion is given references). 37
2.5 Magnified sodide line in temperature-dependent ^{23}Na spectra of a solution of 0.3 M NaK in HMHC/THF. 37
2.6 Varied temperature UV-Vis scans of a solution of approx. 10 mM NaK in 15C5/THF over 70 min total, normalised to the absorbance at 400 nm. . . 39
2.7 Temperature dependence of the position of the absorption maximum of a solution of approx. 10 mM NaK in 15C5/THF. 40

3.1 Typical trends of molar conductivity plotted against square root of concentration for different types of electrolytes. 44
3.2 Conductivity cell with electrodes, rubber seal and specially designed glass container for conductivity measurements under cryogenic inert conditions with low sample volume, disassembled (left) and set up during experiment (right). 50
3.3 Monitoring of conductivity during dissolution of NaK in a solution of 0.04 M 15-crown-5 in THF at 243 K and decomposition of the mixture upon an increase in temperature to RT. 52
3.4 Monitoring of metal content over time in solutions of NaK in 0.04 and 0.20 M 15-crown-5 in THF at 243 K, respectively. 52
3.5 Apparatus for the measurement of gas evolution upon quench of an aliquot of an alkalide solution in wet THF. 53
3.6 Typical conductivity experiment with a successive addition of NaK (blue) and 15C5 (red) and the frequent removal of aliquots for metal content analysis (green). 54

3.7 Illustration of color intensity of solutions of NaK in 15C5/THF at various concentrations. 55
3.8 Viscosity measurements (scatter) and exponential extrapolation (lines). . . 55
3.9 Calibration of viscosity *vs.* 15-crown-5 concentration at RT (blue) and 243 K (red). 56
3.10 Original (left) and corrected (right) Walden product of the system NaK/15-crown-5/THF at 243 K obtained from conductivity measurements of five independent sample series. 57
3.11 Original (left) and corrected (right) Walden product of the system NaK/HMHC/THF at 243 K obtained from conductivity measurements of two independent sample series. 61

4.1 **(left)** COMSOL models of coaxial probe (left) and its first resonance mode (right; increase in electric field intensity from red to blue) and **(right)** spectrum of corresponding resonance frequencies. 67
4.2 Depolarisation effect of polypropylene cap at different bottom layer thicknesses. 67
4.3 Calibration of coaxial probe at RT with common solvents. 68
4.4 Increase of dielectric constant / static relative permittivity ϵ_S (measured at 0.35 GHz) during dissolution of NaK in a 0.5 M solution of 15-crown-5 in THF at 243 K. 69
4.5 Dielectric spectra of solutions of different concentrations of NaK in a 0.5 M solution of 15-crown-5 in THF at 243 K. 70
4.6 Conductivity of solutions of 15-crown-5/NaK in THF at 293 K. 72
4.7 PP (polypropylene) and PE (polyethylene) caps for coaxial probe. 73
4.8 Dielectric spectroscopy setup in laboratory. 74

5.1 Count rate for the NIMROD diffractometer (reproduced from reference [123]). 77
5.2 Computational model representation of contrast method to visualise ion pairing in SANS of NaK/HMHC/THF solutions. 78
5.3 SANS spectra of HMHC/THF blank and alkalide solutions. 79
5.4 Schematic representation of contrast method to visualise effect of metal dissolution on SANS of NaK/15C5/THF solutions. 79
5.5 SANS spectra of 15-crown-5/THF blank and alkalide solutions. 80
5.6 Typical Guinier function used for approximate data extraction from SANS spectra. 81
5.7 Determination of Background scattering intensity from baseline of Lorentzian fit (red) as applied to solvent correlation peak at 1.4 Å of each SANS spectrum, respectively. 81
5.8 Crystal structures of **(left)** HMHC(K^+)BPh_4^- (this work) and **(right)** HMHC(K^+)Na^- (reference [31]) with a planar and boat-like conformation of HMHC in its potassium complex, respectively. 85
5.9 **Preparation of SANS samples**, from left to right: Three components of HMHC-sample, sample solution in quartz NMR tube, flame sealing of frozen sample under vacuum, vanadium sheath and mount, sample mounted to sample stick of cryostat. 86
5.10 Temperature-dependent density measurements of blank solutions for SANS correction. 87

6.1 Sterically demanding tertiary amides as substrates for dissolving metal reduction conditions. 93
6.2 ORTEP plot of *N*-3β-5α-cholestanyl-bornylimine as determined by X-ray crystallography. 96
6.3 Stable nitrimines derived from cincholic acid (**(left)** Molecular structure and **(center)** 3-dimensional model) [144] and **(right)** fenchone. [135] . . 100
6.4 **Structure confirmation of isolongifolanone oxime . (left)** Drawing (top) and ORTEP plot (bottom) of isolongifolanone oxime monomer **(right)** ORTEP plots of hydrogen bonded dimer pairs in enantiomerically pure (top) and racemic (bottom) sample of isolongifolanone oxime. 102
6.5 Numbering of atoms in cholestane core. 103
6.6 **(left)** ORTEP plot, **(center)** corresponding three-dimensional representation, and **(right)** side view of key intermediate 6-nitrimino-5α-cholestane 105
6.7 VT-NMR spectra of selected tertiary amides in d_8-toluene. 110
6.8 NMR spectrum of crude mixture after DMR of tertiary di(*N*-8-*endo*-tricyclodecanyl)-amide **e** in $CDCl_3$. 113
6.9 NMR spectrum of crude mixture after DMR of tertiary *N*-8-*endo*-tricyclodecanylamide **b** in $CDCl_3$. 113
6.10 NMR spectrum of crude mixture after DMR of tertiary *N*-8-*endo*-tricyclodecanylamide **a** in $CDCl_3$. 114
6.11 NMR spectrum of crude mixture after DMR of tertiary *N*-6α-cholestanylamide **a** in $CDCl_3$. 115
6.12 NMR spectrum of crude mixture after DMR of tertiary *N*-6α-cholestanylamide **b** in $CDCl_3$. 115
6.13 NMR spectrum of crude mixture after DMR of lactam in $CDCl_3$. 116

List of Schemes

6.1 Aldehyde synthesis via electrolytic reduction of amides by a solution of lithium chloride in methylamine in the presence of ethanol. 89
6.2 Mechanism of the Bouveault-Blanc reduction. 89
6.3 Initial mechanistic steps of acyloin condensation. 90
6.4 Examples of successfully reproduced dissolving metal reductions of sterically congested ester groups. 91
6.5 Possible mechanisms of deoxygenation of esters in alkali metal solutions. Graphic reproduced from reference [29]. 92
6.6 Alkylation of 1-adamantylamine by treatment with alkyl halides under forcing conditions. 95
6.7 Lithium/ethylene diamine reduction of *N*-3β-5α-cholestanyl-bornylimine . 97
6.8 Mechanism of *N*-Nitrimine formation (pathway A, blue) and deoximation (pathway B, red) via *N*-nitrosation of oximes. 98
6.9 Reported mechanism of camphor nitrimine formation from the oxime derivative. [140] 99
6.10 Isolongifolanone oxime formation from crude ketone starting material. . . 101
6.11 Synthesis of tricyclodecane-derived secondary amines. 103
6.12 Synthesis of 6-nitrimino-5α-cholestane . *Reagents and Conditions*: (a) $SOCl_2$, 2 h, RT, 94%; (b) Na, isoamyl alcohol, 4 h, reflux, 92%; (c) HNO_3, 2 h, $-5 \rightarrow 10\,^{\circ}C$, 45%; (d) Zn dust, AcOH, H_2O, 4 h, reflux, 75%; (e) $NH_2OH \cdot HCl$, NaOAc, EtOH, 1 h, reflux, 95%; (f) ether, $NaNO_2/H_2O$, 2 M H_2SO_4, 6 h, RT, 70%. 104
6.13 Synthesis of dicholestanylamine by treatment of ammonia with tosylated 5α-cholestan-3β-ol. 105
6.14 Synthesis of cholestane-derived secondary amines. 106
6.15 Synthesis of selected sterically congested tertiary amides by acylation of *N*-8-tricyclodecanyl and *N*-6-cholestanone amines. 107
6.16 Synthesis of sterically congested tertiary amides from 8-tricyclodecanone without intermediate purification. 108
6.17 Synthesis of lactams by Schmidt reaction of ketone precursors and an alkyl azide. 111
6.18 DMR of tertiary *N*-8-*endo*-tricyclodecanylamide **c** (conversion 49%, unreacted starting material recovered, yield of and 5α-cholestane 48% respectively). 112

List of Tables

2.1 Predicted NMR linewidths for Na^- in anion-cation aggregates in 12-crown-4 solution (CIP: contact ion pair, SSIP: solvent separated ion pair; reproduced from [47]). 35

2.2 Difference between the shielding constants (ppm) of the negatively charged alkali species in the contact ion pair (CIP) and the genuine anion (A) from DFT calculations of alkali metal-ethylenediamine (en) systems (δ(CIP/A) = σ([M(en)$_3$$^{\delta+}$**M**$^{\boldsymbol{\delta-}}$]) - σ(**M**$^-$); reproduced from [57]). 35

2.3 Extraction of activation energy values from Arrhenius plots of NMR exchange relaxation times of Na^- in solutions of NaK in THF shown in Figure 2.3. 38

3.1 ICP-OES analysis results of saturation tests. 48

3.2 Experimentally determined (normal font) and extrapolated (italic) viscosity values of metal-free solutions of macrocycles in THF. 56

4.1 Dielectric paramters of different concentrations of NaK dissolved in a solution of 15C5 in THF and its metal-free control solution at 243 K, estimated by Debye fits of available coaxial probe dielectric spectroscopy data (see Figure 4.5). 70

5.1 Results from fit of HMHC dataset with Guinier function. 82

5.2 Results from fit of 15-crown-5 dataset with Guinier function. 83

5.3 Density of metal-free solutions corresponding to target concentrations of NaK of SANS samples. 87

Abbreviations

15C5	15-crown-5
18C6	18-crown-6
Å	**A**ngstrom (10^{-10} m)
Ac	**ac**etyl
Ac_2O	acetic anhydride
aq.	**aq**ueous
Ar	**ar**yl
bp	**b**oiling **p**oint
br	**br**oad
bs	**b**road **s**inglet
Bu	**bu**tyl
Bz	**b**en**z**yl
°C	degrees **C**elsius
cat.	**cat**alytic
CDI	**c**arbonyl **di**imidazole
CE	**c**ounter **e**lectrode
CES	**c**ounter **e**lectrode **s**ource
CI	**c**hemical **i**onization
conc.	**conc**entrated
CPMG	**C**arr-**P**urcell-**M**eiboom-**G**ill
CTTS	**C**charge **T**ransfer **t**o **S**olvent
δ	chemical shift
d	**d**oublet
DCC	*N,N'*-**dic**yclohexyl**c**arbodiimide
dd	**d**oublet of **d**oublets

DEAD	*N,N'*-**die**thyl **a**zo**d**icarboxylate
DFT	**D**ensity **F**unctional **T**heory
DMAP	4-**dim**ethyl**a**mino**p**yridine
DMF	N,N-**dim**ethyl**f**ormamide
DMSO	**dim**ethyl**s**ulf**o**xide
DS	**D**ielectric **S**pectroscopy
dt	**d**oublet of **t**riplets
dq	**d**oublet of **q**uartets
EDC	1-**e**thyl-3-(-**d**imethylaminopropyl)**c**arbodiimide
EFG	**E**lectric **F**ield **G**radient
en	**e**thylenediami**n**e
eq.	**eq**uivalent(s)
EI	**E**lectron **I**onisation
EPR	**E**lectron **P**aramagnetic **R**esonance
ES(I)	**E**lectro**s**pray (**I**onisation)
Et	**et**hyl
FWHM	**F**ull **W**idth **H**alf **M**aximum
h	**h**our(s)
HOMO	**H**ighest **O**ccupied **M**olecular **O**rbital
HMHC	1,4,7,10,13,16-**H**exa**M**ethyl-1,4,7,10,13,16-**H**exaaza**C**yclooctadecane (**H**exa**M**ethyl-**H**exa**C**yclen)
HRMS	**h**igh-**r**esolution **m**ass **s**pectrometry
Hz	**H**ert**z**
i	**i**so
Ipc	**i**so**p**ino**c**ampheyl
IR	**i**nfrared **s**pectroscopy
J	coupling constant
L	**l**itre
LUMO	**L**owest **U**noccupied **M**olecular **O**rbital
MALDI	**M**atrix-**A**ssisted **L**aser **D**esorption/**I**onisation
μ	micro (10^{-6})
μL	microlitre(s) (10^{-6} L)
μM	micromole(s) (10^{-6} mol)

m	**m**ultiplet
m	meta
M	**m**olar
mCPBA	**3-c**hloro**p**er**b**enzoic **a**cid
Me	**me**thyl
MHz	**M**ega**h**ert**z**
min	**min**ute(s)
mL	millilitre(s)
mmol	millimole(s)
mol	mole(s)
mp	**m**elting **p**oint
MS	**m**ass **s**pectrometry
MW	**m**olecular **w**eight
m/z	mass to charge ratio n normal
NIMROD	**N**ear and **I**nter**m**ediate **R**ange **O**rder **D**iffractometer
NMR	**N**uclear **M**agnetic **R**esonance Spectroscopy
Nu	**nu**cleophile
o	ortho
p	**p**ara
pH	**P**otential **H**ydrogen
Ph	**ph**enyl
ppb	**p**arts **p**er **b**illion
ppm	**p**arts **p**er **m**illion
Pr	**pr**opyl
py	**py**ridine
q	**q**uadruplet
quint	**quin**tuplet
R	general substituent
$\mathbf{R_f}$	**R**etention **F**actor
RT	**R**oom **T**emperature
s	**s**inglet
SANS	**S**mall **A**ngle **N**eutron **S**cattering
sat.	**sat**urated

SLD	**S**cattering **L**ength **D**ensity
SOMO	**S**ingly **O**ccupied **M**olecular **O**rbital
t or **tert**	**tert**iary
t	**t**riplet
td	**t**riplet of **d**oublets
THF	**T**etra**h**ydro**f**uran
TLC	**t**hin **l**ayer **c**hromatography
TOF	**t**ime **o**f **f**light
tt	**t**riplet of **t**riplets
UV	**u**ltra **v**iolet
v/v	volumetric ratio, **v**olume per **v**olume
WE	**w**orking **e**lectrode
WES	**w**orking **e**lectrode **s**ource

Physical Constants

Avogadro constant	N_A	=	$6.022\,140\,857 \times 10^{23}\ \mathrm{mol}^{-1}$
Boltzmann constant	k_B	=	$1.380\,648\,52 \times 10^{-23}\ \mathrm{m}^2\,\mathrm{kg}\,\mathrm{s}^{-2}\,\mathrm{K}^{-1}$
Ideal gas constant	R	=	$8.314\,459\,8\ \mathrm{J}\,\mathrm{K}^{-1}\,\mathrm{mol}^{-1}$

Symbols

A	pre-exponential factor	dimensionless
B	magnetic field strength	G
c	concentration; subscript indicates type	$\mathrm{mol\,L^{-1}}$ *or* ppm
C	cell constant	dimensionless
E_{OCV}	open circuit potential	V
f	frequency	Hz
k	rate constant; subscript indicates type	depending on mechanism
m	mass; subscript indicates type	kg
Q	neutron scattering angle	$\mathrm{Å^{-1}}$
R	resistance; subscript indicates type	Ω
R_M	molar refractivity	$\mathrm{m^3\,mol^{-1}}$
t	time	s
T	temperature	K *or* °C
V	volume	$\mathrm{m^3}$ *or* $\mathrm{dm^3}$
V_M	molar volume	$\mathrm{m^3\,mol^{-1}}$

α	polarizability	$\mathrm{C\,m^2\,V^{-1}}$
$\boldsymbol{\delta}$	chemical shift	ppm
Δ	difference	dimensionless
ϵ	permittivity; subscript indicates type	$\mathrm{A\,s\,V^{-1}\,m^{-1}}$
η	shear viscosity	cP
Λ	conductivity	S/m
Λ_m	molar conductivity	$\mathrm{Scm^2/mol}$
Λ_m^0	limiting molar conductivity	$\mathrm{Scm^2/mol}$
ν	frequency	Hz

ρ	neutron scattering length density	$\mathrm{mol\,cm^{-2}}$
τ	relaxation time	s
ω	angular frequency	$\mathrm{rad\ s^{-1}}$

Dedicated to anyone

Chapter 1

Introduction

1.1 Alkali Metal Dissolution

The discovery of alkali metal solubility in amines and ethers more than two centuries ago built the foundation of an entirely new research field in chemistry. [1, 2] The original metal dissolution experiment is fascinating in its simplicity and its surprising outcome. An alkali metal - when immersed in a transparent liquid phase of cold anhydrous ammonia - immediately loses its integrity, its metallic character and familiar appearance in order for its constituents to dissipate into the liquid phase and develop a characteristic deep blue color. In spite of such dramatic transformation in its appearance as well as a clear drop in conductivity, the capability of the dissolved alkali metal constituents to form a metallic material is not lost: Simply an increase in metal concentration results in the regeneration of the metallic character in the form of a bronze-colored homogeneous liquid. It is this persistent chemical potential well hidden behind its beautiful deep blue facade that has fascinated chemists in alkali metal solutions ever since their discovery.

Based on the investigation of metal solutions in ammonia and low molecular weight amines [3, 4], the range of media, for which alkali metal solubility was known, was extended to ethereal solvents when the dissolution of potassium metal or sodium potassium alloy in ethers, aliphatic, and cyclic polyethers was first demonstrated several decades ago. [5] Whilst the blue appearance of the obtained solutions suggests a great similarity to dilute metal ammonia solutions, it disguises the critical differences and links between the predominant dissolved species in both systems. The insights gained within the following decades [6–8] are illustrated using a representation shown in Figure 1.1.

Exposure of an elemental alkali metal M^0 to a suitable solvent can induce the removal of metal atoms from the bulk by facilitation of its spontaneous dissociation. The energetic penalty of this ionization process (equilibrium 1.1) is offset by the solvation of the formed charge carriers, namely alkali cations M^+ and solvated electrons e^-_{solv}. The intriguing solvated electron species e^-_{solv} is thereby responsible for the characteristic optical absorption spectrum, that was reported for dilute solutions of alkali metals and several other metals such as calcium, strontium, barium, europium, and yterbium in liquid ammonia, as well as for the radiolysis of pure liquid ammonia. [3, 7, 9–12] The metal-independent absorption band is centered at about 1400–1550 nm (0.80–0.88 eV) and gives rise to the characteristic blue color due to a long tail that extends into the visible range up to about 700 nm (1.8 eV). [13]

The first model to rationalize this absorption was introduced by Jortner who described the solvated electron as a particle occupying an explicit spherical solvent cavity within a continuous medium. A cavity radius of 3–3.2 Å led then to a 1s→2p transition of 0.8 eV matching the center of the absorption band, whereby the tail towards lower wavelengths was assumed to be a result of transitions to higher energy levels. [14] However, in spite of further refinements of the original model by Copeland *et al.* with respect to the interaction between the trapped electron and the sorrounding solvent molecules, a mismatch in the lineshapes between the predicted and the experimental absorption bands remained. [15] More recently, a TD-DFT model allowed for the successful calculation of the vertical excitation energies of the excess electron although neglecting the concentration and temperature dependence of the absorption band. [16] The model located the electron more concretely in a diffuse orbital which mainly covers the border of the solvent cavity as constituted by hydrogen and nitrogen atoms of the ammonia molecules, Intruigingly, this orbital has bonding character between the hydrogen atoms of ammonia molecules pointing towards each other. In accordance with Jortner's orgininal model, the probablility to find the electron right in the center of the cavity is actually zero. [16] It is noteworthy that the absorption spectrum of lithium-ammonia solutions is somewhat similar to the experimentally determined electronic spectrum of $Li(NH_3)_4$ in the gas phase. [17] Hence, it cannot be excluded that both the solvated electron as well as $Li(NH_3)_4$ contribute to the blue spectrum of the dynamic lithium-ammonia solution system.

The dissolution process 1.1 is thermodynamically particularly favourable in polar solvents that additionally enable the stabilization of solvated electrons. A lower tendency of a

solvent to stabilise the latter is not only associated with a lower metal solubility but also with the formation of an alternative negative charge carrier in solution, the alkalide M^- (equilibrium 1.2). For media of low polarity, reactions 1.1 and 1.2 can be simplified to the metal dissolution equilibrium 1.3.

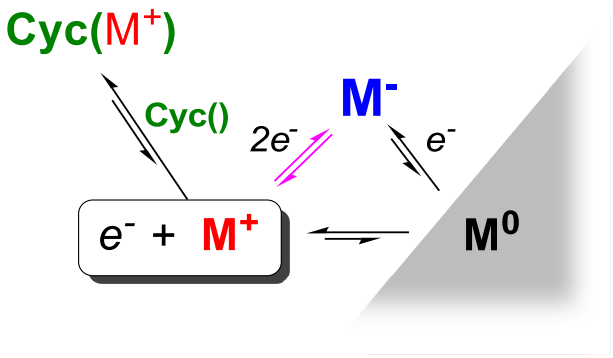


FIGURE 1.1: **left** Species present in metal solutions and **right** effect of an added complexant "Cyc()" on the respective equilibria.

$$\mathbf{M} \rightleftharpoons \mathbf{M}^+ + e^-_{solv} \tag{1.1}$$

$$\mathbf{M} + e^-_{solv} \rightleftharpoons \mathbf{M}^- \tag{1.2}$$

$$\mathbf{2\ M} \rightleftharpoons \mathbf{M}^+ + \mathbf{M}^- \tag{1.3}$$

$$\mathbf{M}^+ + \mathbf{Cyc}(\ ) \rightleftharpoons \mathbf{Cyc}(\mathbf{M}^+) \tag{1.4}$$

$$\mathbf{M}^- \rightleftharpoons \mathbf{M}^+ + 2e^-_{solv} \tag{1.5}$$

1.2 The Role of Complexants

As mentioned above, the metal solubility can be increased even in less polar solvents by the use of co-solvents like crown ethers or cryptands. Those cation complexing agents drive the dissolution 1.1 by removal of the directly solvated cation M^+ from the equilibrium and formation of a complex cation $Cyc(M^+)$ according to process 1.4. [18] The presence of a stoichiometric excess of metal relative to the complexant ensures - according to literature reports [19] - that the increased metal concentration is associated with an increased alkalide concentration (equilibrium 1.2). Without an excess of metal present, equilibrium 1.5 dictates that the complexation of cations leads to a dissociation of anions in favour of

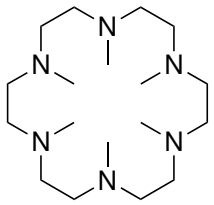
stabilized cations. In other words, the relative concentrations of M^- and e^-_{solv} in the metal solution is reported to be determined by equilibrium 1.1 in the presence of excess metal and by equilibrium 1.5 in its absence. Additional factors that govern the ratio between solvated electrons and alkali anions are the polarity and the binding properties of the involved solvent and complexant. It should be noted that equilibrium 1.5 (highlighted in purple in Figure 1.1) implies that a solution with a certain M^- content always contains a certain concentration of solvated electrons. [19]

The efficiency of cyclic or bicyclic complexants to facilitate metal dissolution is based on the combination of the chelate effect and preorganization. [5, 18] The encapsulation of a metal cation by multiple interlinked and circularly or spherically arranged donor atoms is thermodynamically favourable to an extent that it outcompetes solvation by the surrounding medium and shifts the binding equilibrium 1.4 far towards the complex cation. [6, 20] The binding constant thereby depends on the size match between the cavity formed by the ligand and the bound cation. [21] The dissolution of a metal is enabled if the stabilization of the metal cation and the released electron offset both the ionization potential and the lattice enthalpy of the metal. [22] Their generally low ionization potential renders alkali metals suitable candidates in that regard. [19]
The access to highly concentrated alkali metal solutions by the use of complexing agents allowed for the precipitation and crystallization of the unusual solute. To date, Dye and co-workers accomplished the synthesis and study of a set of alkalide and electride salts in the solid and crystalline state unparalleled in its abundance and variety. [7, 19, 23–25] This class of compounds and especially electrides attracted wide attention of the scientific community not only in synthetic chemistry but most importantly in the field of Theory and Computation which is discussed further below. [24–27]

Whilst cyclic and bicyclic complexants undoubtedly play a key role in the increase of metal solubility and the crystallization of alkalides and electrides from solution [18], they also introduce intrinsic flaws to the system that hamper experimental investigations. From a preparatory point of view, the additional component requires careful purification especially considering that ethers and especially macrocyclic polyethers are highly hygroscopic. Purification by vacuum distillation from alkali metals, indeed, and subsequent storage of the compound under inert conditions is commonly employed to avoid the introduction of fatal impurities. However, the stability of alkalide and electride systems both in the solid and liquid state is endangered even in the absence of common impurities because of

a fundamental incompatability of their components. The release of the valence electron from an alkali atom increases its reactivity. At the same time, the polyether inducing this process is itself prone to decomposition by the reductive cleavage of its carbon-oxygen bonds. As a result, any work with alkalide or electride systems required not only rigorous cleaning procedures but also low temperature at every stage of a synthesis or spectroscopic characterization. [28]

A milestone in the development of more stable alkalide systems was the introduction of polyamine ligands to the field. Barrett *et al.* reported the usage of a fully alkylated aza-crown, namely 1,4,7,10,13,16-Hexamethyl-1,4,7,10,13,16-hexaazacyclooctadecane (Hexamethyl-hexacyclen, HMHC **1**) in the course of a mechanistical study on the dissolving metal reduction of esters. [29] On the one hand, those studies led to remarkable outcomes in their own right and actually provide the basis for the dissolving metal reduction studies presented and discussed in chapter 6 of this work. On the other hand, the report of an increased resistance of the macrocycle to its irreversible decomposition and the demonstration of a prolonged stability of alkali metal solutions in the presence of HMHC even at room temperature stimulated novel approaches to the synthesis of solid alkalides and electrides. The benefits of the polyamine complexant were attributed to the lack of somewhat acidic amino protons which was then considered as a crucial factor for the development of stable alkalide and electride crystals.



1

FIGURE 1.2: Hexamethyl-hexacyclen (HMHC, **1**), the per-methylated aza analogue of 18-crown-6.

The synthesis and crystallization of thermally stable alkalides using HMHC was only the first application of per-alkylated polyamine ligands in solid alkalide salts. [30, 31] The investigation of thermal properties of the potassium sodide salt revealed their extraordinary resistance to reductive decomposition and decomplexation below 74 °C. Decomplexation was found to be generally slow in spite of the close contact between the anion and the

complexed cation in the crystal structure. Additionally, alkali metal NMR and multinuclear ENDOR investigations were carried out on the cesium sodide involving HMHC as the complexant. [32] The introduction of per-alkylated amine ligands also provided the base for the development of other aza-cages and corresponding alkalide salts. [33–35]

1.3 Alkalide solutions

The characterization of alkalides in the liquid state focussed mostly on classic techiques that were established for the investigation of alkali metal solution from research in the field of metal-ammonia solutions. Metal-dependent optical absorption bands - all of which are responsible for the characteristic blue appearance of alkalide solutions - were distinguished from the absorption of solvated electrons and instead assigned to alkali metal anions. [36, 37] Relying on assignments from UV-Vis spectroscopy, sodide solutions in various solvents were employed to study CTTS reactions, recombination dynamics, and the influence of the solvent on electron transfer reactions in solution by ultrafast laser spectroscopy. [38–41] Especially noteworthy is the report of the breakdown of the linear response approximation according to Marcus theory which was claimed based on the solvation dynamics in a photoexcited sodide solution. [42]

Analogously, NMR spectroscopic methods were extended from research on metal ammonia solutions to the characterization of alkalide solutions in polar protic media [43] and subsequently to aprotic and less polar systems. Comparable experiments by different research groups finally resulted in the identification of alkali metal anions in solution and their still prevailing detailed description as diamagnetic "gas-like" species. [44–49] The chosen terminology illustrates that the alkalide stands out as an ionic species in solution due to an exceptionally long spectroscopic lifetime showing minimal interactions with their environment as well as a solvent-independence of the spectroscopic trace. In the context of those reports, the lifetime of genuine alkalide anions in solution as determined by NMR spectroscopy was suggested to be limited due to charge transfer processes, i.e. the potentially reversible loss of an electron by the alkalide ion. Edwards *et al.* demonstrated by NMR spectroscopy that the ionization of alkalides in solution of 12-crown-4 was triggered by the presence of uncomplexed alkali cations that were made available by thermally induced decomplexation. [50] Exchange broadening and coalescence of the NMR signals of the alkalide and its complex countercation in solutions of sodium with 18-crown-6 were observed in the polar solvent methylamine. [51] An exchange of the sodium species between the sites

of a genuine separately solvated anion (Na^-) and that of a complexed cation (Na^+C) was considered as an explanation, potentially *via* intermediary ionisation and complexation equilibria. An increase in linewidth of the sodide signal of solutions of sodium with 2,2,2-cryptand in ethylamine and methylamine as compared to that in the less polar solvent THF was tentatively attributed to the paramagnetic interaction of a higher concentration of solvated electrons in more polar solvents. [51, 52] Other investigations of ion-solvent and ion-ion interactions and exchange processes by NMR and EPR spectroscopy did not yield any conclusive interpretation of the obtained experimental data due to the complexity of relevant ionization processes and equilibria. [53–56]

A stark contrast to the classic picture of unperturbed alkali anions in solution was created by a more recent computational study. Zurek predicted for solutions of alkali metals in ethylenediamine (en) enhanced stability of ion pairs, as compared to all other considered species, consisting of the alkalide M^- and its complexed countercation $[M(en)_3]^+$. [57] This computational finding is in accordance with the only currently available ionic conductivity study of alkalide solutions which provided experimental evidence for the presence of alkalide ion pairs in solutions of ethylenediamine. [58] There are no other reports of the interaction between an alkalide and its countercation in the literature besides those mentioned above as well as the close interionic contact found in solid alkalides by X-ray crystallography. [30, 59] Reports of the liquid structure of alkali metal solutions as determined by neutron diffraction, which might be able to reveal the presence of any ion associates, only focus on metal-ammonia solutions and the investigation of structural effects of the metal-insulator transition in the liquid state. [60–65] In that context, the saturated lithium-ammonia-methylamine system was reported as a novel mixed-amine expanded metal in the liquid state. [66]

Although this class of metallic liquid systems inherently differs from that of ionic alkalide solutions, a comparison between the two reveals critical features and similarities of their molecular components. Solutions of lithium in small amines contain the metal in the form of tetracoordinated lithium-amine species $Li(RNH_2)_4$ with zero net charge. The valence electron of the original metal atom occupies diffuse, Rydberg-like states of the lithium complex which can thus be considered as an "expanded atom". [67] Sufficiently high concentrations allow for an overlap of the electron wave functions. Such interaction of the constituents of the material is paralleled by the emergence of a band structure as well as distinct M–M correlations in the highly structured liquid in spite of a M-M separation

much larger than that of standard metals. Those characteristics classify the system as an "expanded metal" with its intruiging electric ([68–71]) and magnetic ([72–74]) properties. For example, liquid lithium-ammonia undergoes a non-metal to metal transition by a concentration of about 4 MPM (mole-% of metal) in accordance with the Mott criterion for metallization. [75, 76]

While none of the alkalide systems reported to date were found metallic - besides the liquid sodide system LiNa(CH_3NH_2)n with $n < 6$ [77, 78] - this compound class bears a great potential with regards to the adoption of metallic character. Pyper only took metallicity in alkalides into consideration due to their exceptionally large polarizability. [79] According to the underlying Herzfeld theory ([80]), the mutual polarization of one atomic or molecular constituent of a material by the surrounding constituents can lead to a "dielectric catastrophe" and the formation of the metallic state if the ratio as given by equation 1.6 exceeds unity:

$$\frac{R_M}{V_M} = \frac{4\pi\alpha N_A}{3V_M} \tag{1.6}$$

with the molar refractivity R_M, to which the polarizability α is proportional, the molar volume V_M, and Avogadro's number N_A.

Despite the large polarizability of alkalides, the large molar volume prevents metallization due to the size and shape of the complexing agent required to form alkali metal anions in the first place. Hence, accessing metallic alkalides from concentrated electrolytic solutions comes down to the synthetic design of their ionic components and the control over their interaction with each other.

Any notable interaction of the alkalide with its countercation as present in ion associates in solution implicates an effect of any synthetic adaptation of the complex cation on the properties of the alkalide as a spectroscopic target and synthetic reagent. The investigation of ion associates therefore opens the door to the synthetic tailoring and the rational design of bulk properties of solutions and solids containing the alkalide as their key component.

1.4 Motivation and aim of this work

Not least due to intrinsic weaknesses of currently available alkalide solutions systems, past investigations on alkalides were mostly carried out on solid crystalline samples. Alkalides in the liquid state represent electrolyte solutions for which the importance of coulomb

interactions and the role of a respective counter ion are generally understood. [81] An extension of the current knowledge and understanding of the species present in alkalide solutions and the important interaction of the alkalide with their complex countercation and the solvent is required to enable the development of more stable and reliable alkalide solution systems. It will allow for the tailoring of the reactivity of metal solutions in low-polarity media and stimulate the exploration of alkalides in fields like synthesis and catalysis, the generation and characterization of reactive intermediates, electrochemistry and electrochemical devices as well as the development of amorphous electrides and the investigation of their insulator-metal transition.
With the aim to overcome experimental difficulties associated with alkalide solutions, this work provides a comprehensive characterization of alkalide solutions in THF with the focus on the determination of the effects of ion pairing on spectroscopic properties of the liquid system.

Furthermore, the reactivity of organic amides under dissolving metal reduction conditions was investigated. The rationale, the synthetic method and the corresponding results are presented in chapter 6.

Chapter 2

NMR and UV-Vis spectroscopic investigation of alkalides in THF

2.1 Introduction

The characterisation of alkalide solutions profoundly benefitted from the versatility of nuclear magnetic resonance (NMR) spectroscopy in the past and still does. In spite of the rather complex composition of those multi-component systems, the method allows for the spectroscopic isolation and the identification of specific properties of the alkalide species that initially led to the convincing detection of the formerly novel and unusual species in crown ether solutions. [44–46] The application of alkali NMR spectroscopy was possible not least because of the high metal solubility and ease of acquiring data under cryogenic and inert conditions. In contrast, the high absorbance of alkalides in the conventional concentration range presents a challenge to the investigation oftheir optical properties by UV-Vis spectroscopy. Additionally, commercially available UV-Vis spectroscopy setups that allow for measuements under cryogenic and inert conditions are uncommon and frequently impractical to operate. In order to gain a more detailed picture of the nature, solvation and interactions of alkalides in solution, alkali metal NMR spectroscopy was applied to the reportedly more stable aza-crown system HMHC in THF and extended to temperature dependent relaxation time measurements. Furthermore, UV-Vis spectra of a sodide solution were recorded at varied temperatures.

2.2 Results and Discussion

2.2.1 NMR spectroscopy

In analogy to previous literature reports [44–49], alkali metal NMR spectra of the nuclei ^{23}Na and ^{39}K were recorded for solutions of a 1:1 sodium-potassium alloy (referred to as NaK in the context of this work, if not specified otherwise) and pure potassium, respectively, in a 0.3 M mixture of aza-crown HMHC and the co-solvent THF at 243 K (Figure 2.1). It should be noted that NaK was used as a sodium source in place of pure sodium for practical reasons only. While both sources yield identical signals in the negative chemical shift range of the ^{23}Na NMR spectrum of their corresponding alkalide solutions, the liquid state of NaK at room temperature facilitated the handling and purification of the metal using a syringe as well as its dissolution when exposed to a solution of a complexant. The use of NaK with respect to its use in the preparation of alkalide solutions is further justified in chapter 3.2.1 below.

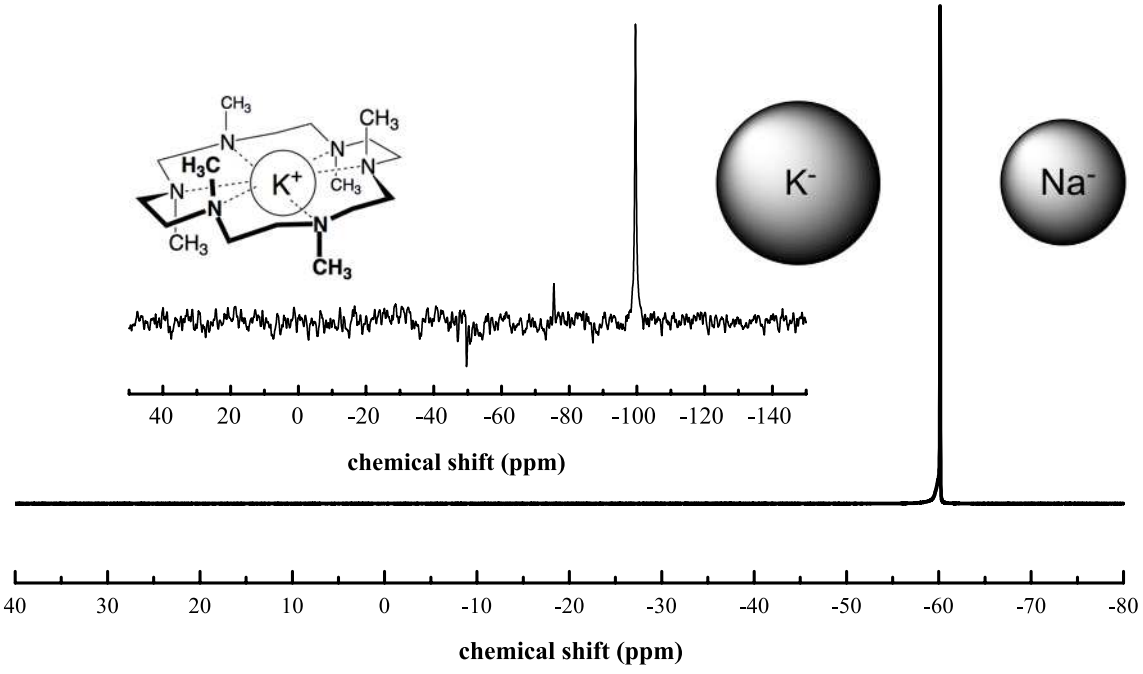


FIGURE 2.1: ^{39}K **(top)** and ^{23}Na **(bottom)** spectra of HMHC(K^+)K^- and HMHC(K^+)Na^-, resp., in THF at 245 K (chemical shifts referenced to Na^+ and K^+ in an aqueous saturated solution of its chloride, resp.).

In accordance with literature reports of various equivalent solution systems, both spectra show the characteristic narrow and upfield shifted signal of alkalide solutions. The signal in the ^{23}Na spectrum is shifted little ($\delta = -62.3$ ppm at room temperature relative to a Na^+-D_2O reference) from the value calculated for gaseous Na^- ($\delta = -63.1$ ppm). [46]

Similarly low chemical shift differences of $\Delta\delta$ = -1.4, -1.6 and -2.3 ppm were reported for sodium-containing solutions of crown ethers in methylamine, ethylamine or tetrahydrofuran, respectively. [51] The extremely low line width (FWHM $\Delta\nu_{1/2} = 10$ Hz at 290 K and 4 Hz at 250 K) provides evidence for a lack of perturbation of the alkalide ion by magnetic fields of surrounding dipoles. It was concluded that the highly symmetric environment of the alkali nucleus is generated by a filled spherical $3s$ valence orbital which effectively screens the alkali metal $2p$ electrons. Hence, the species detected by NMR spectroscopy was referred to as a "gas-like anion in solution" in contrast to a solvated cation with a solvated electron pair in close vicinity. [47] This assessment explains that the NMR signal is effectively independent of the choice of co-solvent. [44] Additionally, it creates a contrast between the nature of alkalides and that of the dissolved species in dilute metal-ammonia solutions, namely the solvated electrons acting as counterions that are not centered at nuclei and that are spatially separated from strongly solvated alkali cations (see chapter 1). The lack of perturbation of the alkalide is additionally rationalised by the strong binding and steric shielding of the metal cation by the used organic complexant. This prevents not only the exchange between the anion and the complex cation but also any proximity between them. The latter is in fact the reason for the great success of the application of macrocyclic complexing agents in organic synthesis, rendering any anionic counterpart "naked" and consequently more reactive.

Questioning the prevalent picture of alkalides in solution

A complete absence of any interaction between the alkalide and its counter cation is surprising in so far as the polarity of the solvent medium THF is too low to enforce complete separation of the dissolved charge carriers. Considering the low efficiency of the solvent to screen the electric field of any charge carriers is particularly important when taking into account the relatively high metal concentration in commonly reported alkalide solutions. On the other hand, any close approach between the alkalide and the complex cation would necessarily imply a large fluctuating electric field gradient (EFG) at the alkalide nucleus, giving rise to very efficient quadrupolar relaxation . [47] The transverse relaxation rate of such perturbed species is expected to be exceedingly high and its NMR line significantly broadened (see Table 2.1). Indeed, the planar complexation of the naturally weakly shielded cation is believed to result in such extensive line broadening that the counterion of the alkalide in some solution systems is difficult to detect if not entirely invisible in its

respective alkali metal NMR spectrum (see for example ^{39}K spectrum in Figure 2.1). [82] The exposure of the sodide nucleus to a similarly large EFG due to close contact with its counter cation seems to be discardable considering the exceptionally narrow line width of the sodide.

This seemingly paradoxical situation was resolved by the study of the effect of temperature changes on the NMR properties of the alkalide solution. Temperature-dependent relaxation time measurements performed by us (see Figure 2.2) and others on alkalide solutions with several different complexants show a common reversible trend for all systems: With increasing temperature, both relaxation times T_1 and T_2 were increasingly suppressed [53–56], in contrast to a steady exponential increase in relaxation times as it would be expected for a chemically unperturbed species. [83] This suppression is particularly noticeable as it resulted in a distinct maximum in the temperature-dependent relaxation time trends at approx. 0 °C for sodide systems and at approx. −50 °C for potasside systems. Clearly, it is the result of a temperature dependent perturbation of the alkalide ion which, in fact, was found to affect the integral of the alkalide signal as well. With increasing temperature, a steady and reversible reduction of the integrated area of both the sodide and potasside signal was observed, respectively (see Rel. Integral in Figure 2.2 normalised to the integral at the lower end of the covered temperature range). The original trend over a temperature range of 80 K was corrected for any loss in signal intensity due to a shift of the Boltzmann distribution of spin states which resulted in the depicted significant reduction in signal intensity with increasing temperature. The only plausible explanation for this observation is an exchange process between the NMR-visible alkalide and a NMR-invisible species involving the probed alkali metal nucleus.

The line width of the alkalide signal showed no significant temperature dependence. An exchange process, however, involves some effect on the line width of the relevant signal unless the system is investigated either at the fast or the slow exchange limit. Those exchange regimes are defined by the relation between the exchange rate k and the difference $\Delta\nu$ between the chemical shifts of the exchanging species [84]:

fast exchange:	$k \gg \Delta\nu$
slow exchange:	$k \ll \Delta\nu$
coalescence:	$k = 2.22\ \Delta\nu$

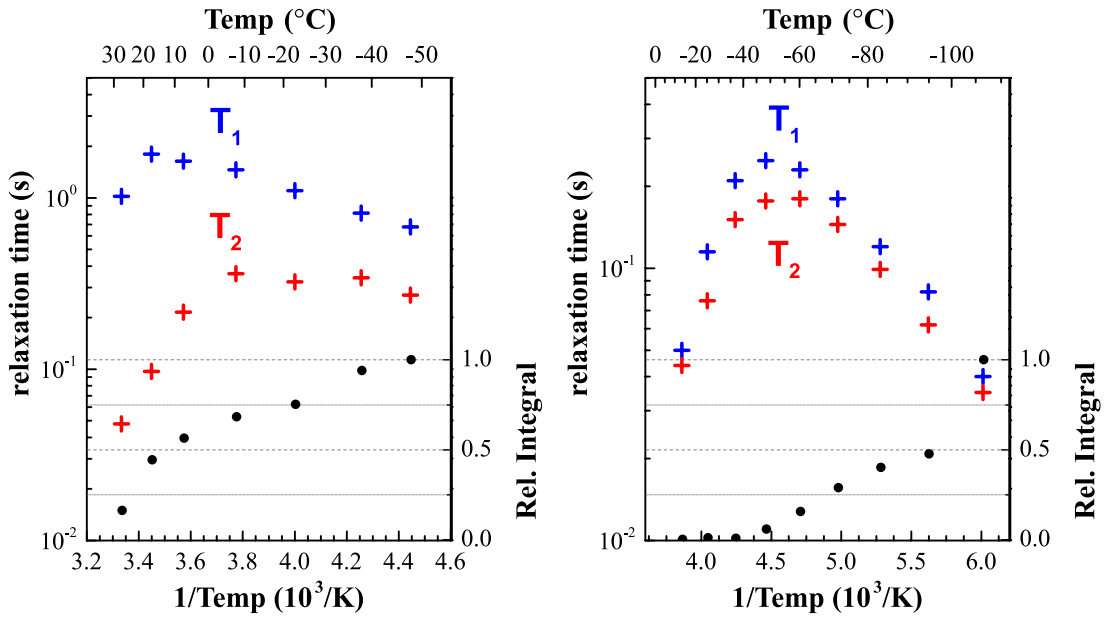


FIGURE 2.2: ^{23}Na Temperature dependence of NMR spin-lattice (T_1), spin-spin (T_2) relaxation times, and the integral (normalised) of the Na^- (left) and K^- (right) signals of NaK/HMHC/THF and K/HMHC/THF solutions, respectively.

At this point, two fundamentally different processes should be considered as potentially operating, namely the ionisation of the alkalide according to equations 2.1 or 2.2 and the ion association equilibrium 2.3.

$$Na^- \underset{k_{recomb}}{\overset{k_{exch}}{\rightleftharpoons}} Na^0_{solv} + e^-_{solv} \tag{2.1}$$

$$Na^- + Cyc(K)^+ \underset{k_{recomb}}{\overset{k_{exch}}{\rightleftharpoons}} Na^0_{solv} + [Cyc(K)^+, e^-_{solv}] \tag{2.2}$$

$$Na^- + Cyc(K)^+ \underset{k_{dissoc}}{\overset{k_{exch}}{\rightleftharpoons}} {}^{\delta-}[NaCyc(K)]^{\delta+} \tag{2.3}$$

Both ionisation processes 2.1 and 2.2 involve a species Na^0 whose NMR signal would be paramagnetically shifted with the result of a very large chemical shift difference $\Delta\nu$ to the upfield shifted alkalide. A contact ion pair formed according to equation 2.3 is characterised by a large FWHM, as mentioned above, and by a relatively small chemical shift difference ($\Delta\nu \approx 6\,\text{ppm} \approx 630\,\text{Hz}$) to the genuine alkalide (see Table 2.2).

TABLE 2.1: Predicted NMR linewidths for Na^- in anion-cation aggregates in 12-crown-4 solution (CIP: contact ion pair, SSIP: solvent separated ion pair; reproduced from [47]).

Ion	$\Delta\nu_{1/2}$ [Hz]
CIP Na^+	2951
CIP $Na^+(12C4)_2$	237
SSIP $Na^+(12C4)_2$	51
passed by $Na^+(12C4)_2$	38

TABLE 2.2: Difference between the shielding constants (ppm) of the negatively charged alkali species in the contact ion pair (CIP) and the genuine anion (A) from DFT calculations of alkali metal-ethylenediamine (en) systems ($\delta(CIP/A) = \sigma([M(en)_3{}^{\delta+}\mathbf{M}^{\boldsymbol{\delta-}}]) - \sigma(\mathbf{M}^-)$; reproduced from [57]).

Metal	$\delta^{(CIP/A)}$
Li	-1.0
Na	-5.9
K	-17.4
Rb	-40.9
Cs	-97.0

Involvement of chemical exchange

The suggested processes can be distinguished by consideration of the effect of chemical exchange processes on the spin-spin relaxation time T_2. Any chemical exchange processes increase the efficiency of spin-spin relaxation due to its great sensitivity to transient magnetic fields. This results in a difference between the otherwise equal values of spin-lattice and spin-spin relaxation rates at any given temperature [50], given as the exchange relaxation rate k_{exch} according to equation 2.4

$$k_{exch} = \frac{1}{T_2} - \frac{1}{T_1} \tag{2.4}$$

whereby the half-time of the investigated species corresponds to the reciprocal exchange relaxation rate ${k_{exch}}^{-1}$. Indeed, the exchange relaxation rate of the unperturbed alkalide ion was found to increase with increasing temperature in the temperature range above the maximum relaxation times (Figure 2.3). This suggests that the predominant relaxation mechanism of the quadrupolar nucleus was strongly related to exchange processes of the observed rate k_{exch} involving the genuine anion. All currently known temperature-dependent exchange rates for sodide systems were shown to be in the range of 0.1 to 50 Hz.

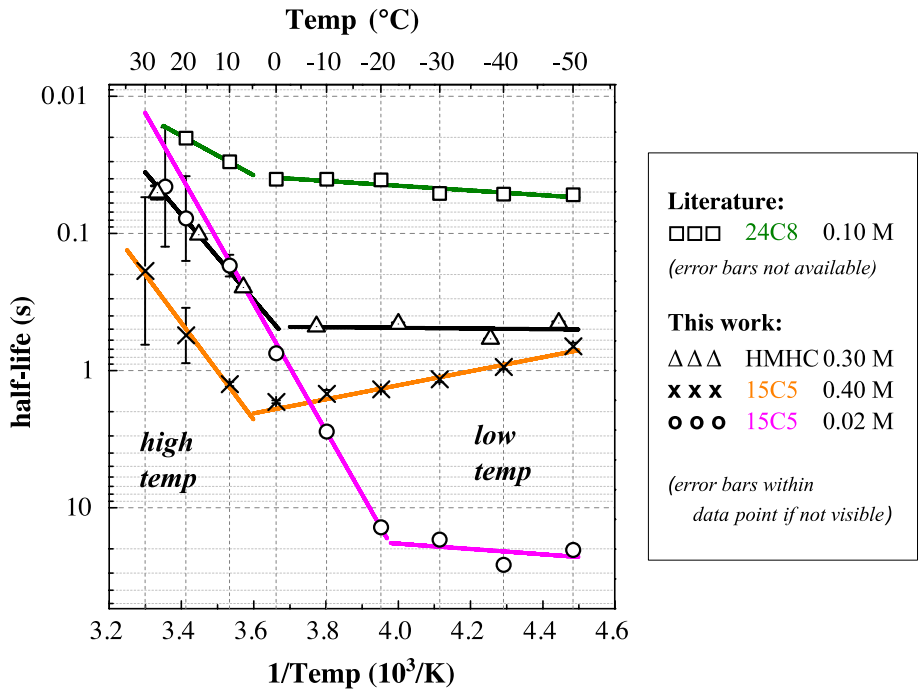
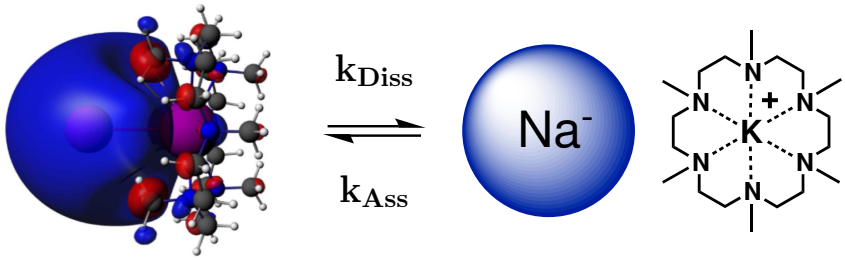


FIGURE 2.3: Arrhenius plot of NMR exchange relaxation times of Na^- in solutions of NaK in THF with various complexants.

By implication, alkalide systems involving exchange processes 2.1 and 2.2 would be investigated far in the slow exchange limit time scale. While this would result in another narrow line for the paramagnetic sodium species, its population in the equilibrium is expected to be very low considering the low lifetime of paramagnetic species in the system as detected by EPR measurements. [85] Any exchange processes would then lead to much stronger line broadening for this species and render it not detectable in the 1D spectrum. It should be noted, however, that the actual alkalide signal would be mostly unperturbed due to the absence of any coalescence effects. In contrast, the difference between the determined exchange relaxation rate and the estimated difference in chemical shift is much lower for the exchange process 2.3. Due to the large line width of the ion pair species, any temperature-dependent shift of the equilibrium towards the ion pair can only be noticed by a decrease in alkalide signal intensity while the change in ion pair signal intensity would be negligible because of the naturally large line width of any ion pair signal. [47] The chemical shift of a relevant ion pair species can be estimated from DFT calculations on related metal-ethylenediamine systems. [57] Despite the lack of macrocyclic complexing agents, those alkalide system are related to alkalide solutions in THF as the alkali cation is complexed by three chelating bidentate ethylenediamine ligands which provides the driving force for the formation and stabilisation of alkalides in solution. The results

indicated that, surprisingly, the signal of the nucleus on the partially negative end of the ion pair - the former alkalide nucleus - is only shifted by few ppm relative to the signal of the genuine anion (see Figure 2.4). While those parameters exacerbate the detection of any ion pair species by NMR spectroscopy, a close inspection of the sodide signal in temperature-dependent ^{23}Na NMR spectra does show a shoulder of the alkalide signal on the lower field side, in accordance with coalescence effects due to the involvement of ion pairs (see Figure 2.5).



Species	**Contact Ion Pair** (Superalkali-Alkali Dimer)	**Gas-like Anion**
FWHM	100–1000 Hz	3–4 Hz [47]
Chemical shift	(−62.5)–(−6) = −56.5 ppm [57]	−62.5 ppm

FIGURE 2.4: Schematic representation of the effect of ion pairing on the NMR properties of a sodide solution in THF (values estimated based on discussion is given references).

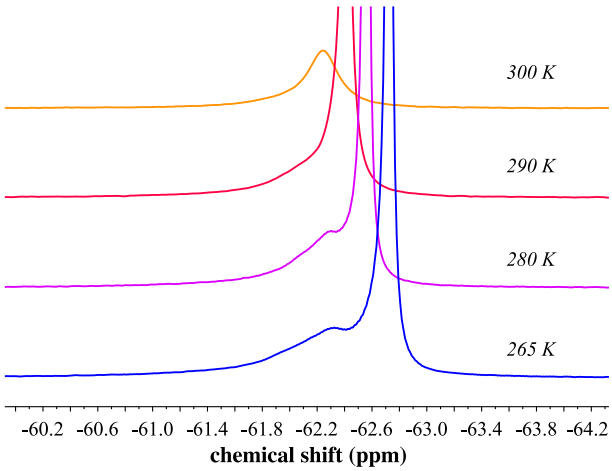


FIGURE 2.5: Magnified sodide line in temperature-dependent ^{23}Na spectra of a solution of 0.3 M NaK in HMHC/THF.

Besides the valuable information on absolute values of exchange rates, Figure 2.3 highlights another intriguing property of alkalide solution systems. In the higher temperature

regime, the exchange rate shows an exponential temperature dependence according to Arrhenius' law 2.5 as expected for processes with an activation energy E_a for all sodide systems shown in Figure 2.3. Corresponding values were extracted for both the high and low temperature regimes from the Arrhenius plot following equation 2.6. At lower temperatures, the exchange rate of the alkalide appears to be independent of or only weakly affected by changes in temperature. Considering the temperature-independence, the type of process that comes to mind is the ionisation of the anion via electron tunneling with potential acceptors being (i) solvent cavities suitable to temporarily stabilize solvated electrons or alternatively (ii) counter cations. However, an electron tunneling process with a defined rate (i.e. linked to a potential barrier of a certain magnitude) as reported for solid systems (i.e. static, with defined distances between donor and acceptor) seems to be an unlikely explanation for the observed temperature-independent exchange rate in the case of this liquid and consequently rather dynamic system. It should be noted that none of the individual chemical systems showed a true temperature-independence of the exchange relaxation rate within the error of the measurement, respectively.

TABLE 2.3: Extraction of activation energy values from Arrhenius plots of NMR exchange relaxation times of Na^- in solutions of NaK in THF shown in Figure 2.3.

$$k_{exch} = k_{0,exch}\, e^{-\frac{\boldsymbol{E_a}}{RT}} \qquad (2.5)$$

$$ln(k_{exch}) = -\frac{\boldsymbol{E_a}}{R}\frac{1}{T} + ln(k_{0,exch}) \qquad (2.6)$$

Complexant, NaK-conc. [M]	**approx. E_a** [kcal/mol] **high temp.**	**low temp.**
HMHC, 0.3	13.1	0.11
15C5, 0.4	16.7	-2.3
15C5, 0.02	17.9	0.89
24C8, 0.1	6.6	0.79

Although the origin of two separate regions with temperature dependent and temperature independent exchange relaxation times, respectively, is not fully understood at this point, the fact of their existence highlights the role of interactions between oppositely charged ions as well as a cascade of ion pairing equilibria in alkalide solutions.

2.2.2 Cryogenic UV-Vis spectroscopy

Alkalide solutions show a characteristic UV-Vis absorption spectrum consisting of a metal dependent absorption band and a high energy shoulder. In contrast to NMR spectroscopic measurements, a low stability of metal solutions in THF using macrocyclic complexing agents render the recording of optical spectra difficult as reflected by the small amount of experimental data reported in the literature. To complement the results obtained from

varied-temperature NMR relaxation time measurements described above, a method was developed to reliably investigate any effects of a change in temperature on the familiar absorption spectrum of a sodide solution.

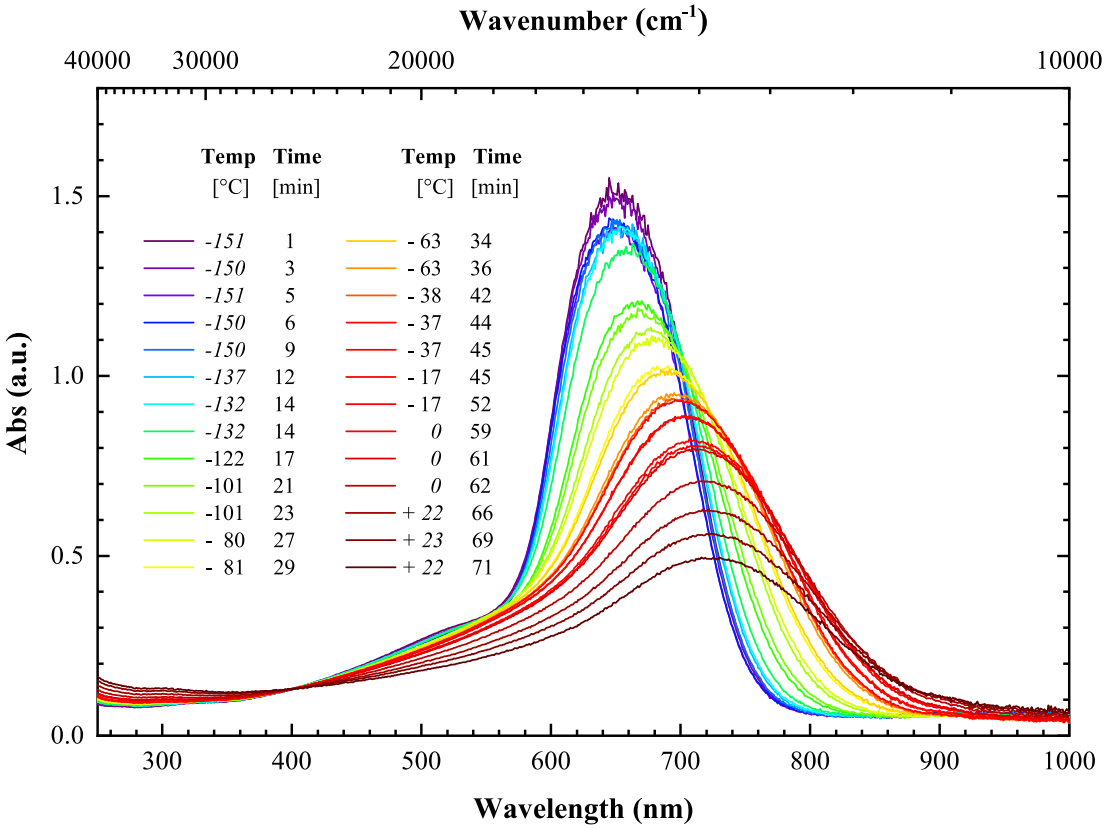


FIGURE 2.6: Varied temperature UV-Vis scans of a solution of approx. 10 mM NaK in 15C5/THF over 70 min total, normalised to the absorbance at 400 nm.

The temperature dependence of the familiar alkalide solution absorption spectrum (Figure 2.6) clearly showed a difference between two features of the spectrum. The absorption band with the global maximum at 722 nm at 0 °C represents the major feature which is traditionally assigned to the alkalide ion. In the intermediate temperature range between −120 to 0 °C, a decrease in temperature resulted in a continuous and reversible narrowing, significant increase in intensity, and a shift of the absorption maximum ν_{max} of this band by 70 nm to lower wavelengths. Such linearly temperature-dependent shift of the absorption maximum was reported for alkalide solutions in various solvents [37] and is in accordance with the absorption band to originate from charge-transfer-to-solvent (CTTS) processes as suggested for solutions of various alkalides [36] as well as halides [86]. A temperature coefficient $\frac{d\nu_{max}}{dT}$ of 9.4 $cm^{-1}\,K^{-1}$ was determined by least-squares analysis as shown in Figure 2.7. The temperature dependence of the absorption maximum and the shape of the spectrum, however, does not give any insight into the nature of the species

initially hosting the transferred charge such as the differentiation between separately solvated or paired alkalide ions. At temperatures below −120 °C (italic labels in Figure 2.6) the spectrum only showed minor changes upon an increase in temperature as the sample was mounted at the instrument in the frozen state. The relatively large drop in intensity after the initial 15 min of the experiment indicated the melting of the mixture.

The shoulder of the absorption band towards lower wavelengths represents the second feature of the sodide spectrum and is traditionally assigned to solvated electrons. In contrast to the major absorption band, the shoulder was not affected by any change in temperature within the intermediate temperature range mentioned above. At temperatures above 0 °C (italic labels in Figure 2.6), an overall loss in intensity showed that decomposition processes led to rapid degradation of the mixture in this temperature range.

2.3 Conclusion

The traditional characterisation of alkali metal anions as diamagnetic species in solution focused on alkali metal NMR techniques. The stability and nature of the genuine anion – resulting in the small width of its NMR signal (see Figure 2.1) – was rationalised by the strong binding and shielding of the metal cation preventing the exchange between the anionic and the complexed cationic species and any proximity between them, respectively.

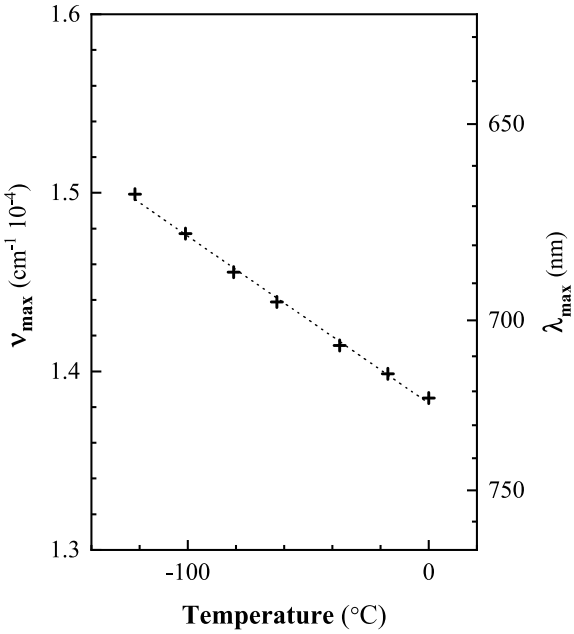


FIGURE 2.7: Temperature dependence of the position of the absorption maximum of a solution of approx. 10 mM NaK in 15C5/THF.

Our NMR relaxation time studies on solutions of NaK and K in mixtures of HMHC/THF showed a steady decrease in effective anion concentration – measured as the integral of the alkalide signal – as well as an increase in exchange relaxation rate with increasing temperature. The latter appears to be a common feature for sodide and potasside solutions in THF and independent of the used complexing agent. From the quantitative evaluation of the obtained exchange

relaxation rates was concluded that the composition of alkalide solutions is dominated by slow exchange equilibria between the genuine alkalide and ion pair species which appear to be NMR invisible for most solution systems.

Furthermore, the nature of processes with temperature-independent exchange rates at low temperatures, the appearance of a positive slope in the Arrhenius plot for a high concentration 15C5 system in same temperature range, and the origin of two distinct temperature ranges with temperature-independent and temperature-dependent exchange relaxation rates is currently unclear and will remain the focus of further investigations.

The associated temperature dependent UV-Vis study suggested the common alkalide absorption band to originate from CTTS processes in accordance with literature reports. Beyond that, it showed that classic optical spectroscopy investigations do not provide any insight into the nature of the species initially hosting the transferred charge such as the differentiation between separately solvated or paired alkalide ions. Hence our focus was shifted to spectroscopic methods that were less established for the investigation of alkalide solutions.

The following chapter describes the developed method and results from classic ionic conductivity measurements to probe ion pairing processes by their concentration dependence.

2.4 Experimental Section

HMHC was prepared following the protocol previously established in our laboratories. [87] Crude HMHC and commercially available 15-crown-5 were purified by Kugelrohr distillation from NaK, kept under an Argon atmosphere and handled inside an argon glovebox.

NMR spectroscopy

^{23}Na NMR spectra and relaxation time measurements were acquired at 106 MHz on a Bruker DRX-400 spectrometer. ^{39}K NMR spectra and relaxation time measurements were acquired at 28 MHz on a Bruker Avance 600 MHz NMR spectrometer. Chemical shifts are reported as δ-values in ppm relative to the cation signal from aqueous solutions of the respective chloride salt. Spin-lattice relaxation time values were obtained using a standard inversion-recovery pulse sequence, spin-spin relaxation time values were obtained using a standard Carr-Purcell-Meiboom-Gill (CPMG) pulse sequence.

All samples were prepared by addition of all components (complexant HMHC (1 eq.) or 15C5 (2 eq.), $_{d8}$-THF, NaK (3 eq.) or K (6 eq.) to an oven- and flame-dried borosilicate NMR tube with J Young valve inside an argon glovebox. The sealed tubes were removed from the glovebox and cooled to 195 K before exposure of the metal droplet to the solution. The samples were stored at 195 K and warmed to 240 K for 10 h in preparation for the respective NMR experiment to ensure complete metal dissolution up to a point of saturation. The equilibration time was scheduled to be immediately followed by the respective NMR experiment. The probe of the NMR spectrometer was cooled to 200 K before the saturated samples with sample holders were quickly loaded into the spectrometer. Care was taken that the sample was kept cool and free from solvent in dry ice before the sample was loaded into the spectrometer.

UV-Vis spectroscopy

Optical spectra were recorded at an Agilent technologies Cary 60 UV-Vis spectrophotometer. The sample temperature was adjusted by means of an Oxford Instruments intelligent temperature controller itc4 in combination with an Oxford Instruments OptistatDN nitrogen bath cryostat which the sample was mounted to.

A sample of suitable absorbance (1.0–1.5) was prepared by dissolution of a minimal amount of NaK in a solution of 40 mM 15-crown-5 in THF. Specifically, a quartz cuvette with 1 mm path length was charged with the metal-free solution (total volume 0.2 mL) under an argon atmosphere, sealed with a rubber septum, and cooled to −30 °C at which temperature a small droplet of NaK (approx. 5 mg) was briefly brought into contact with the solution until the desired absorbance of the blue mixture was reached.

Chapter 3

Conductivity measurements

3.1 Introduction

Alkalide solutions show a characteristic response in the widely applied methods NMR and UV-Vis spectroscopy. The success in their application to alkalide solutions is due to the focus on specific properties of this unusual sample class such as the unique location and shape of the spectroscopic response in the corresponding spectrum and its dependence on the metal used. NMR relaxation time measurements over a wide temperature range did not only reveal the exceptionally long lifetime of the alkali metal anions in solution but also that it is increasingly limited by chemical exchange processes with increasing temperature.

While the high metal solubility facilitated the detection of alkalides by NMR, all related experimental studies were limited to a relatively narrow and high concentration range of 0.1–0.5 M. This is presumably due to the relatively low sensitivity of alkali nuclei in NMR as well as experimental limitations with regards to the reliable access to the lower concentration range considering the sensitivity of the highly reductive mixtures to impurities and temperature.

Ion association effects, however, are commonly identified and characterised by conductivity measurements across a range of varying concentrations and at a higher dilution than previously used in NMR spectroscopic studies. The molar conductivity Λ_m of classic strong electrolytes decreases only slightly with increasing concentration due to the increasing effect of neighbouring ions on their mobility in the medium (see Figure 3.1). The dependence is described by Kohlrausch's law as a consequence of the Debye-Hückel-theory:

$$\Lambda_m \;=\; \Lambda_m^0 \;-\; (A + B\Lambda_m^0)\sqrt{c} \tag{3.1}$$

where c is the electrolyte concentration, Λ_m is the molar conductivity, and Λ_m^0 is the limiting molar conductivity. Constants A and B depend only on known quantities such as temperature, the ionic charges, the overall dielectric constant and the viscosity of the medium.

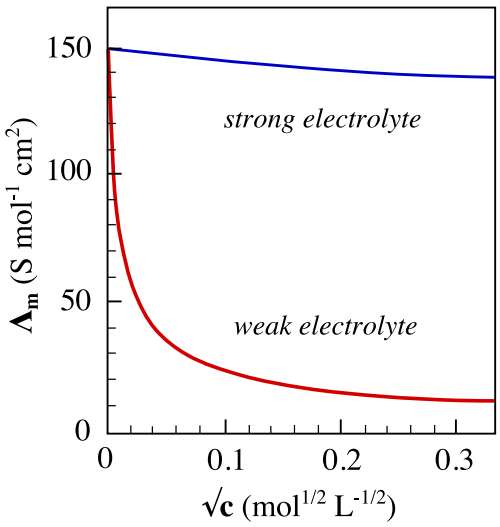


FIGURE 3.1: Typical trends of molar conductivity plotted against square root of concentration for different types of electrolytes.

The description of weak electrolytes, on the other hand, involves an ion association equilibrium between fully dissociated ions and their ion pairs. The corresponding typical trend in the plot of molar conductivity *versus* the square-root of the concentration distinctly differs from the trend of a strong electrolyte following Kohlrausch's law as depicted in Figure 3.1. Particularly in the case of an electrolyte solution in a medium of low dielectric constant, coulombic attraction between oppositely charged ions determines the conductivity of the solution due to insufficient screening of charges by the medium. A concentration-dependent fraction of ion pairs is formed which do not contribute to the overall conductivity of the solution. This results in a characteristic dependence of the molar conductivity on the total concentration of dissolved electrolyte.

Indeed, molar conductivity trends as expected for classic weak electrolytes were reported for solutions of sodium, potassium, rubidium, and cesium in ethylenediamine. [58] The solubility of those metals in ethylene diamine was found to be relatively low with values

of the order of 10^{-3}–10^{-2}M due to the absence of a pre-organised complexing agent capable of driving the metal dissolution. Conveniently, the sufficient stability of solutions in that concentration range enabled conductivity measurements which allowed for the reliable mathematical extraction of limiting equivalent conductance values and ion association constants without any data distortion by secondary effects as expected for higher concentrations. [88]

Given that classic concepts derived from measurements of strong electrolytes do not apply to weak electrolyte systems with entirely different properties, more sophisticated models with corresponding mathematical descriptions were developed by Fuoss and Kraus in order to be able to fit and evaluate data obtained from weak electrolytes. [89] The determination of limiting (equivalent) conductivity values, ion association (i.e. equilibrium) constants and activation energies at different temperatures requires the measurement of data sets for several concentrations over the entire temperature range.

The mathematical description of the classic trend of a weak electrolyte in the corresponding molar conductivity plot was derived from Ostwald's dilution law considering the dissociation constant K_d of a weak electrolyte consisting of cation C^+ and anion A^-

$$K_D \;=\; \frac{[C^+][A^-]}{[CA]} \;=\; \frac{\alpha^2}{1-\alpha} c_0 \tag{3.2}$$

with the degree of dissociation α and the total concentration of electrolyte c_0. The development of this approach by Shedlovsky gave the analytical expression

$$\frac{1}{\Lambda} \;=\; \frac{1}{(K_D \Lambda_0^2)} c\Lambda + \frac{1}{\Lambda_0} \tag{3.3}$$

which allows for the extraction of K_D from the corresponding plot of experimental conductivity data. [90] Fuoss reported that secondary effects, i.e. the formation of higher ion aggregates, cause a deviation from the classic trend of a weak electrolyte at concentrations above approx. $c\,[M] = 3.2 \times 10^{-7}\ D^3$ (with D = dielectric constant; for ethylene diamine ($D = 13.82$): $c = 8.4 \times 10^{-4}$ M). [88] Thus, the access to low concentrations in conjunction with (or indeed due to) the relatively high dielectric constant of the medium allowed for the determination of ion association constants of alkalides in the ethylene diamine solutions.

As mentioned above, literature reports on experimental data of alkalide solutions in low-polarity solvents like THF are limited to a comparatively higher concentration range and difficulties in accessing the low concentration regime were expressed. Therefore, this phenomenon was thoroughly investigated with the aid of ion conductivity measurements using contact electrodes in order to develop a method for the reliable assessment of the effects of ion association in alkalide solutions. Considering that the calculation of molar conductivity values relies on the availability of accurate concentration values of the respective electrolyte, a convenient and robust metal content analysis method was developed and applied to the aforementioned task.

The overarching aim of the electrochemical characterization of alkalide solutions is the assessment whether ion pair formation is a dominant bulk property in alkalide solutions independently of the specific nature of the used organic complexant.

3.2 Results and Discussion

3.2.1 Metal content analysis

3.2.1.1 Evaluation of analytical methods

In order to validate the observed trends, the overall content of dissolved metal – directly related to the concentration of potential charge carriers – of various alkalide solutions was determined by ICP-OES (inductively coupled plasma optical emission spectroscopy) analysis of sodium and potassium concentrations in decanted and quenched alkalide solution samples (see Table 3.1). The analysis was carried out during slots booked with *Analytical Services* at the *Department of Chemical Engineering*. Samples were prepared by the usual method in a glovebox and stored for the given length of time at the given temperature before decanting and quenching.

The results can be summarized as follows:

- Both 15C5 and HMHC samples show a full occupation of available macrocycles in the mixture (i.e. ratio of NaK/HMHC$\approx$ 1 and NaK/15C5$\approx$ 1/2 due to formation of sandwich complex) at every concentration within experimental error (syringe, human, measuring flasks).
- Decomposition is negligible in HMHC samples even after prolonged contact with excess metal.

- Prolonged contact of 15C5 solutions with excess metal at low or room temperature leads to proportional increase of potassium content only, the sodium content is not affected.

- Decomposition processes in HMHC samples occur at room temperature. In contrast to the increase in metal concentration in 15C5 metal solutions, however, decomposition products in HMHC samples seem to precipitate – presumably as the alkoxide-crown(M^+) salt – which leads to a decrease in metal concentration in solution (decanted) but to a large increase in metal concentration if the precipitate is dispersed in the sample and included in the aliquot.

- Ultrasonication during initial dissolution period at RT (<15 min) facilitates decomposition and consequently increase in overall metal content with constant Na:K ratio.

- Use of a molar 1:3 ratio of NaK (sodium content of NaK still in excess to HMHC content of solution) affects the composition of the alkalide solution only slightly (Na:K 3:4 instead of 4:4), the overall metal content was however lower than expected, either due to insufficient metal dissolution (depletion of sodium content from alloy resulting in harder metal droplet) or more facilitated decomposition processes.

Furthermore, ICP-OES analysis of the metal content of alkalide solutions revealed a deviation from the target metal content due to an unexpectedly long time required for complete metal dissolution (i.e. saturation of complexants with metal ions; approx. 5 h). In an attempt to assume saturation during conductivity measurements while avoiding long waiting times for each concentration, the method of conductivity measurements upon continued dilution was introduced. A concentrated mixture was initially prepared (*NB*: rate of dissolution was found to be approximately proportional to concentration of complexant) and is carefully diluted to the next lower target concentration after each conductivity measurement, respectively. However, when applying this method it was observed that a certain time for equilibration was required after each addition of solvent before the resistance values reached a plateau at their lowest end again. This behaviour indicates that each dilution step introduced a perturbation of the metal content, presumably due to dissolved metal crashing out again with the effect of a lower saturation. Since the extent of this effect was found to not be reproducible or predictable, the only option to obtain precise

TABLE 3.1: ICP-OES analysis results of saturation tests.

15C5 Exp.	Total mass crown [mg]	Sample volume [mL]	Target conc. NaK [M] (rounded)	Target conc. NaK [M]	Target √c(NaK)	Temp [K]	Time [days]	Ratio Na/crown	Ratio K/crown	Ratio MM/crown	Ratio Na/K	Comments
1	222	1.2	**0.40**	0.420	0.65	253	1	1.00	1.11	**1.05**	0.90	
1	104	1.05	**0.20**	0.224	0.47	253	1	0.94	1.03	**0.99**	0.91	
1	52	1.0	**0.10**	0.117	0.34	253	1	0.97	1.16	**1.06**	0.84	
1	46	2.0	**0.05**	0.052	0.23	253	1	0.91	1.01	**0.96**	0.89	
2	216	1.3	**0.40**	0.377	0.61	253	4	0.91	1.05	**0.98**	0.86	Seal broken, O_2-exposure
2	110	1.05	**0.20**	0.237	0.49	253	4	2.49	2.39	**2.44**	1.04	
2	50	1.0	**0.10**	0.114	0.34	253	4	1.02	**1.54**	**1.28**	0.67	
2	43	2.0	**0.05**	0.049	0.22	253	4	1.00	**1.14**	**1.07**	0.88	
3	217	1.2	**0.40**	0.410	0.64	293	1	0.97	**1.28**	**1.13**	0.76	
3	41	2.0	**0.05**	0.047	0.22	293	1	0.92	**1.32**	**1.12**	0.69	
3	221	1.2	**0.40**	0.419	0.65	293	3	1.00	**1.72**	**1.36**	0.58	
3	45	2.0	**0.05**	0.051	0.23	293	3	0.94	**1.68**	**1.31**	0.56	
4	42	2.0	**0.05**	0.048	0.22	253	1	1.14	1.33	**1.24**	0.85	*ultrasonication*
HMHC Exp.												
1	87	0.55	**0.50**	0.463	0.68	253	1	0.91	0.96	**0.94**	0.94	
1	49	0.52	**0.30**	0.276	0.52	253	1	0.93	1.04	**0.99**	0.89	
1	34	1.0	**0.10**	0.099	0.32	253	1	0.90	0.96	**0.93**	0.94	
1	39	2.0	**0.06**	0.057	0.24	253	1	0.90	0.92	**0.91**	0.97	
1	15	5.0	**0.01**	0.009	0.09	253	1	0.95	0.90	**0.93**	1.05	*mixture inhomogeneous*
2	87	0.5	**0.50**	0.511	0.71	253	4	0.95	1.00	**0.97**	0.95	
2	38	0.5	**0.20**	0.224	0.47	253	4	0.89	1.09	**0.99**	0.82	
2	33	1.0	**0.10**	0.097	0.31	253	4	0.93	1.01	**0.97**	0.92	
2	33	2.0	**0.05**	0.048	0.22	253	4	0.83	0.90	**0.86**	0.92	
2	15	5.0	**0.01**	0.009	0.09	253	4	1.07	0.75	**0.91**	1.43	Inhomog. or contamin.
3	43	0.5	**0.30**	0.251	0.50	293	1	0.13	0.24	**0.18**	0.54	
3	32	2.0	**0.05**	0.046	0.21	293	1	0.60	0.81	**0.71**	0.74	(precipitate Included)
3	39	0.5	**0.20**	0.230	0.48	293	4	4.18	3.49	**3.84**	1.20	
3	31	2.0	**0.05**	0.045	0.21	293	4	0.15	0.35	**0.25**	0.43	
4	31	2.0	**0.05**	0.045	0.21	253	1	0.61	0.83	**0.72**	0.74	*Excess metal Na:K **1:3***

concentration values is the withdrawing and analysis of solution aliquots and the subsequent correlation of the determined metal content with the determined resistance value, respectively.

Subsequent analyses of the metal content of all alkalide solutions, of which conductivity values were recorded, had to be carried out using an ICP-MS instrument since Analytical Services had replaced their ICP-OES instrument. Whilst the latter is commonly used for the analysis of alkali cations, ICP-MS is more precise and applicable to a wider range of concentrations. However, ICP-MS analysis is far more susceptible to matrix effects (influence of any organic content in the sample). This is the reason why unrealistically low levels of saturation ('recovery rate') were obtained for the tested alkalide solutions and an alternative metal content analysis method was developed.

Experimental procedure (identical for ICP-OES and ICP-MS):
*Aliquots were taken immediately after each conductivity reading and quenched in 50 mL ultrapure water and degassed by purging with nitrogen (removal of excess THF from aqueous solution), acidified with 2% nitric acid [crucial only for ICP-MS], and diluted with ultrapure water to a suitable target concentration of ICP-MS analysis (*0.1 *to* 1.0 ppm*). Calibration standards were prepared by dissolution of NaCl and KCl in ultrapure water and acidification with 2% nitric acid.*

3.2.1.2 Ion Chromatography

Consequently, ion chromatography as an alternative standard technique for the analysis of alkali metal cations was employed (Group of Anthony Kucernak; access through Daniel Malko). After the setup of the instrument for the appropriate conditions (see experimental procedure below), several standard solutions (chloride salt in ultrapure water) were prepared and carefully analysed in order to eliminate any carryover between samples and to ensure a stable recovery rate and calibration (see calibration lines below). Then, samples of all alkalide solutions, of which conductivity values were recorded, were prepared and their Na^+/K^+ content was determined.

Experimental procedure:
*ICP-OES/MS stock solutions in ultrapure water and aliquots of metal solutions quenched in ultrapure water were diluted with eluent to a suitable target concentration (*1 *to* 20 ppm*). Calibration standards were prepared by dissolution of both NaCl and KCl in ultrapure water and further dilution of the mixed-ions stock solutions with eluent to the desired standard concentrations:* 1 ppm*,* 5 ppm*,* 10 ppm*, and* 25 ppm*.*
*Eluent: 1:20 dilution of HNO_3 (*34 mM*) / Dipicolinic acid (*14 mM*) in ultrapure water;*
Column: Metrosep C 2 100 (silica gel with carboxyl groups).

3.2.2 Optimization of Experimental method for conductivity measurements

Prior to conductivity measurements, the stability of platinum electrodes in alkalide solutions in THF was experimentally confirmed. Preliminary measurements with a 0.1 M solution of HMHC and 15-crown-5 demonstrated the stability of the recorded conductivity values at any temperature.

A suitable glass container (see Figure 3.2) was designed to match the size of the conductivity cell and ensure a sufficient seal between the glass rod (accommodating the electrodes) and the container by the use of a rubber ring in conjunction with silicon-based high-performance vacuum grease. The small joint was sealed with a rubber septum to allow for the addition of sample components during sample preparation and the removal of aliquots during conductivity measurements.

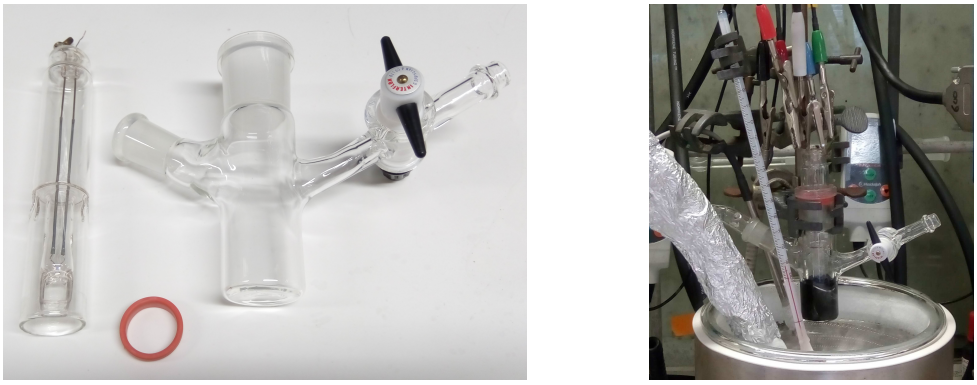


FIGURE 3.2: Conductivity cell with electrodes, rubber seal and specially designed glass container for conductivity measurements under cryogenic inert conditions with low sample volume, disassembled (left) and set up during experiment (right).

Sample solutions were prepared by addition of pure NaK *via* a syringe to a solution of the complexant in THF at −40 °C under an argon atmosphere. Mindful of the successful saturation experiments as described in section 3.2.1, the target alkalide concentration was adjusted by the use of a corresponding concentration of complexant in the presence of an excess of metal. Prior to every measurement, the respective sample was kept at −40 °C for several hours in order to allow for complete metal dissolution, reflected by the stabilization of the conductivity value after a period of steady increase as monitored by occasional conductivity readings.

However, conductivity measurements of several independent samples with intermediate to high metal concentrations (0.1–1.0 M) gave inconsistent molar conductivity values.

This outcome was attributed to an insufficient homogenization of the sample due to the specific layout of the sample container. Diffusion of the electrolyte is hindered in narrow regions within the cooled glass apparatus which leads to the formation of concentration and temperature gradients. Both the speed of metal dissolution in the heterogeneous mixture as well as the removal of aliquots was therefore inconsistent. Thus, all following samples were prepared in a rigorously cleaned standard 50 mL three-necked round-bottom flask. One of the three joints was equipped with a gas adapter using a Glindemann PTFE sealing ring whereas the other two necks were used as described above. The seals were tested by immersion of the entire empty glass apparatus in a water bath and application of a slight argon overpressure which showed no signs of any gas leaks.

Experimental results on alkalide solutions reported in the literature were obtained on solutions in an alkalide concentration range of approx. 0.1–0.4 M as described in chapter 2. This concentration of charge carriers is far higher than appropriate for the detection of molar conductivity values unperturbed by any secondary effects. However, it was found that mixtures of alkali metals with THF in the presence of low concentrations of complexant ($c < 3.2 \times 10^{-7} \times 7.58^3 = 1.4 \times 10^{-4}$ M) do not develop the characteristic deep blue colour but rather remain entirely colourless and transparent. Given that metal dissolution was generally straightforward at high concentrations of macrocycle in THF, samples of low concentration were prepared by successive careful dilution of the deeply coloured high-concentration solution. It was envisaged that this method would allow for an expansion of the accessible sample concentration range of $c > 10$ mM to lower concentrations. Indeed, deeply coloured solutions with lower target concentrations than 0.02 M were accessible by this method. However, conductivity data were found to be unreliable as the alkalide concentration appeared to be strongly affected by temperature fluctuations even in the presence of a metal excess. This is presumably due to unavoidable decomposition processes and a lower metal solubility at higher temperatures, which are naturally introduced by the addition of solvent *via* a syringe that is operated at room temperature. The stability at low temperature (243 K) and the effect of an increase in temperature was demonstrated by monitoring of the conductivity over time.

Figure 3.3 shows a decrease in solution resistance due to the slow dissolution of NaK at 243 K (region I). The resistance increased only slightly when the temperature was kept constant which demonstrated the stability of the mixture. When the mixture was allowed to warm to room temperature (ΔT) the resistance rapidly increased until the present

alkalide content was decomposed (region II). Subsequently, the resistance increased even further, although more slowly, due to the presence of excess metal and intact complexant, which still facilitated the formation of reductive species to a small extent (region III). The high resistance of the decomposed solution confirmed that decomposition products do not significantly contribute to the conductivity of the mixture. In order to specifically confirm this crucial aspect, a control experiment was carried out. The addition of a solution of decomposition products, which was stored under inert atmosphere, to an active alkalide solution did not have any effects on the measured conductivity. Further, monitoring of the content of dissolved metal over time revealed that decomposition processes, that lead to a steady increase in metal concentration, are more pronounced at low concentrations (see Figure 3.4). While decomposition processes operate over the entire concentration range, any resulting alkoxide salts are more likely to precipitate from the solution at higher concentrations and therefore neither contribute to the conductivity nor to the determined content of dissolved metal. Complementarily to the analysis of the overall metal content by

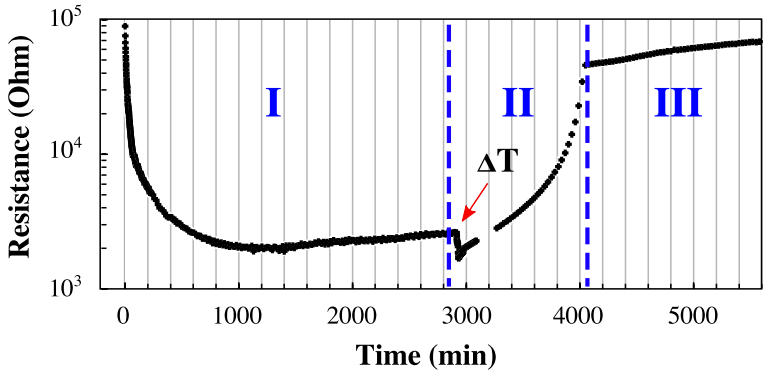


FIGURE 3.3: Monitoring of conductivity during dissolution of NaK in a solution of 0.04 M 15-crown-5 in THF at 243 K and decomposition of the mixture upon an increase in temperature to RT.

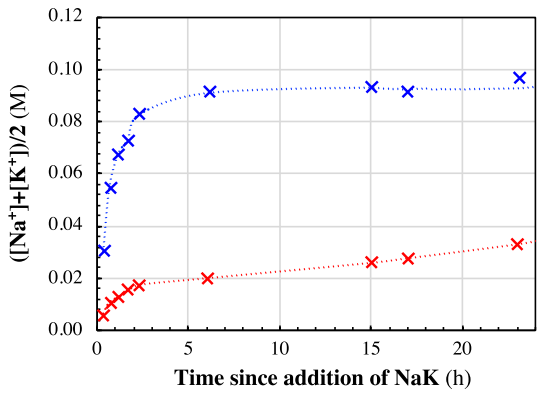


FIGURE 3.4: Monitoring of metal content over time in solutions of NaK in 0.04 and 0.20 M 15-crown-5 in THF at 243 K, respectively.

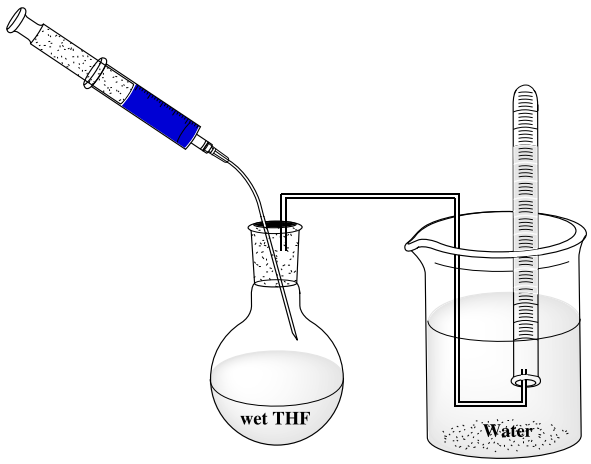


FIGURE 3.5: Apparatus for the measurement of gas evolution upon quench of an aliquot of an alkalide solution in wet THF.

ion chromatography as described in chapter 3.2.1, the concentration of alkalides in highly concentrated solutions was directly probed by the volumetric measurement of evolved hydrogen gas upon quench of an aliquot of a metal solution in wet THF (Figure 3.5). In each instance, the stoichiometric amount of hydrogen matched the expected amount of alkalide species in the respective aliquot within experimental error.

From those studies with solutions of low and equal concentrations of both the complexant and the electrolyte, it was concluded that at a high dilution the binding constant of the complexant is not large enough to facilitate metal dissolution according to the equilibrium

$$\mathrm{M} + \mathrm{Crown} \rightleftharpoons \mathrm{M}^{+} + \mathrm{M}^{-}$$

in spite of the presence of metal excess. In order to access a low alkalide concentration, it was envisaged to shift the dissolution equilibrium to the right by the use of a stoichiometric amount of metal in the presence of an excess of complexant. Neither the conductivity nor the ratio between potassium and sodium species in the mixture differed between solutions with the same metal content but different concentrations of complexant. It was concluded that an excess of complexant does not lead to a dissociation of alkali metal anions to cations and solvated electrons. Clearly, the solvent THF with its relatively low polarity stabilises the alkalide ion to a far greater extent than the solvated electron as the alternative negative counter ion to the complex cation. By implication, the composition of the sample mixture and any conductivity measurements were not affected by decomposition reactions. The low dissociation constant of the sodide in THF is also reflected in the higher stability and

lower reactivity of sodide solutions in low-polarity media in contrast to sodium ammonia solutions.

Figure 3.6 shows a typical conductivity experiment as developed from the considerations mentioned above. A solution of a relatively high concentration of complexant as compared to target alkalide concentrations, in the range of 0.05–0.1 M, in THF and equipped with a magnetic stirrer was cooled to 243 K. Successive addition of liquid NaK in small portions (< 20 mg, blue arrows) and monitoring of the conductivity upon addition of the first metal portion afforded a slow and steady increase of alkalide concentration and conductivity in the mixture, accompanied by precisely controlled and reproducible slow coloration of the solution as illustrated in Figure 3.7. Thereby, homogenization of the solution was achieved by rapid stirring. In order to access higher alkalide concentrations than the maximum value set by the initial concentration of complexant, another portion of complexant was added at an appropriate time during the experiment (red arrow in Figure 3.6). This method allowed for the reliable removal of several aliquots for the analysis of the metal content (green arrows in Figure 3.6) and consequently for the reproducible determination of concentration-conductivity couples for the alkalide solution over a large range of concentrations. As described above, the stability of the alkalide solution under the conditions was thereby confirmed by the long period of time, over which the maximum conductivity value remained constant.

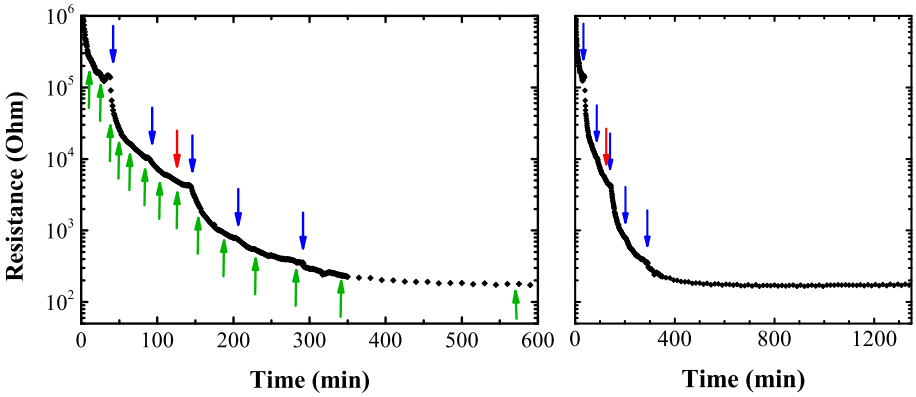


FIGURE 3.6: Typical conductivity experiment with a successive addition of NaK (blue) and 15C5 (red) and the frequent removal of aliquots for metal content analysis (green).

3.2.3 Viscosity measurements

Due to the nature of alkali metal solutions using relatively high concentrations of complexing agents, any experimentally determined conductivity values were to be corrected for viscosity effects on the ion mobility. As a first approximation, the shear viscosity of

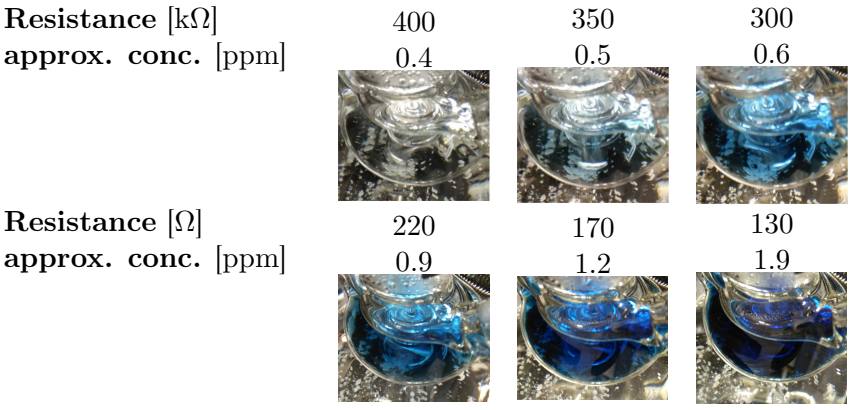


FIGURE 3.7: Illustration of color intensity of solutions of NaK in 15C5/THF at various concentrations.

metal-free solutions of complexant in THF at all relevant concentrations was measured over the temperature range of 15–40 °C. The obtained temperature-dependent viscosity trends for each concentration were fitted by an exponential function (Arrhenius-type) and extrapolated to lower temperatures (see Figure 3.8 and Table 3.2). The viscosity values η for all concentrations - calculated for −30 °C (243 K) (see Figure 3.9) - were then normalized to the viscosity at the lowest solute concentration and the obtained fractions η_{norm} were used to calculate the Walden product $\Lambda_m \eta_{norm}$. It should be noted that a more accurate correction would take into account the expectedly marginally higher viscosity of actual metal-containing solutions. Due to the minor effect on conductivity data in relation to the required far more elaborate experimentation under cryogenic and inert conditions, such measurements were considered redundant at this point. [91]

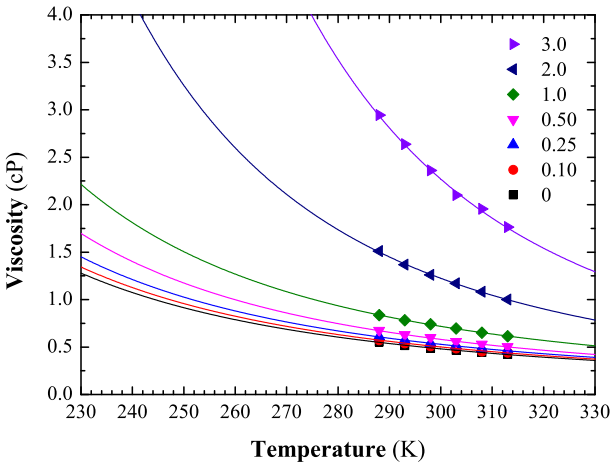


FIGURE 3.8: Viscosity measurements (scatter) and exponential extrapolation (lines).

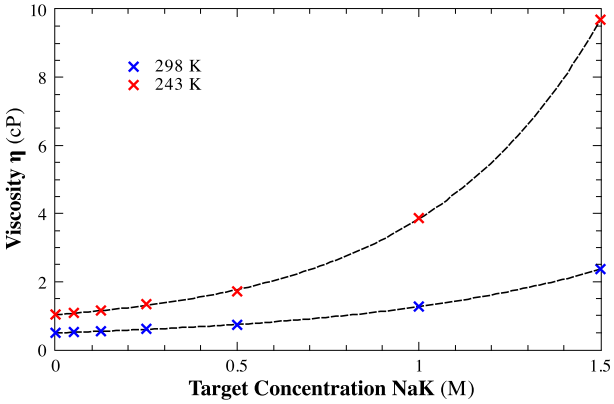


FIGURE 3.9: Calibration of viscosity *vs.* 15-crown-5 concentration at RT (blue) and 243 K (red).

TABLE 3.2: Experimentally determined (normal font) and extrapolated (italic) viscosity values of metal-free solutions of macrocycles in THF.

Temp [K]	**η THF** ([92]) [cP]	**η THF exp.** [cP]	**Viscosity η of 15-crown-5 in THF [M]**						**η 15C5** [cP]
			0.10 [cP]	**0.25** [cP]	**0.50** [cP]	**1.0** [cP]	**2.0** [cP]	**3.0** [cP]	
243	0.903	*1.022*	*1.072*	*1.151*	*1.327*	*1.711*	*3.860*	*9.692*	*462.7*
253	0.779	*0.874*	*0.915*	*0.979*	*1.118*	*1.428*	*3.040*	*7.166*	*242.9*
263	0.679	*0.756*	*0.791*	*0.843*	*0.954*	*1.209*	*2.438*	*5.421*	*133.9*
273	0.598	*0.661*	*0.690*	*0.734*	*0.823*	*1.036*	*1.987*	*4.186*	*77.14*
283	0.532	*0.583*	*0.609*	*0.645*	*0.718*	*0.897*	*1.643*	*3.292*	*46.20*
288	0.503	0.553	0.574	0.608	0.674	0.837	1.510	2.943	36.54
293	0.477	0.516	0.542	0.572	0.629	0.782	1.367	2.637	28.34
298	0.452	0.489	0.511	0.539	0.599	0.735	1.260	2.361	22.53
303	0.430	0.465	0.487	0.513	0.557	0.690	1.170	2.100	18.29
308	0.410	0.443	0.455	0.482	0.529	0.652	1.082	1.955	14.94
313	0.391	0.422	0.442	0.463	0.504	0.613	1.000	1.763	12.42
η_0 [cP]	-	1.92E-2	1.96E-2	1.91E-2	1.71E-2	1.77E-2	9.17E-3	4.66E-3	3.85E-5
E [J/mol]	-	8024	8084	8275	8789	9230	12205	15435	32933
R^2	-	0.997	0.995	0.998	0.997	0.998	0.998	0.998	0.998

3.2.4 Data collection and processing

The results of four independent conductivity measurement series of solutions of NaK in 15-crown-5/THF are shown in Figure 3.10. The plot of the original data (left) illustrates that all data series consistently follow the trend of a decrease of the Walden product with increasing alkalide concentration up to 10^{-3} $\frac{\text{mol}}{\text{L}}$ ($\sqrt{\text{conc}} = 0.1$ mol$^{1/2}$ L$^{-1/2}$) and an increase of the Walden product with further increasing concentrations.

Molar conductivity values and the Walden product were calculated according to

$$\Lambda_m(c) = \frac{\Lambda}{c} = \frac{C}{R}\, c^{-1} \tag{3.4}$$

$$\Lambda_m(c)\eta_{norm} = \Lambda_m(c)\, \frac{\eta_c}{\eta_0} \tag{3.5}$$

with the conductivity Λ, the molar conductivity $\Lambda_m(c)$, the resistance R, the cell constant C, the electrolyte concentration c, the viscosity of THF η_0, and the viscosity of the metal solution η_c at the relevant concentration c as described in chapter 3.2.3. Considering that the conductivity of the solutions was measured at metal concentrations as low as

$$c_{min} = x_{min}^2 = 0.018^2 \ \frac{\text{mol}}{\text{L}} = 3.24 \times 10^{-4} \ \frac{\text{mol}}{\text{L}} = 7.5 \,\text{ppm (Na)} \tag{3.6}$$

$$\begin{aligned} \text{with} \quad 1\,\text{ppm (Na)} &= 1 \ \frac{\text{mg (Na)}}{1000\,\text{g solution}} = 1 \ \frac{\text{mg (Na)}}{\text{L solution}} = \\ &= \frac{1}{10^3\,\text{MW(Na)}} \ \frac{\text{mol}}{\text{L}} = 2.2990 \times 10^{-4} \ \frac{\text{mol}}{\text{L}}, \end{aligned} \tag{3.7}$$

an accurate determination of the metal concentration was crucial to avoid systematic errors in the desired molar conductivity, especially at the lower end of the covered concentration range.

Regardless of all efforts during the experimental procedure, traces of remaining water in the solvent in the range of up to 6 ppm were inevitable. [93] Due to the reactive nature of the electrolyte, any water traces were converted to the corresponding alkali hydroxide. While their contribution to the overall ionic conductivity of the mixture can be neglected due to extensive ion pairing, the chromatographically determined metal concentration c_0 of the mixture was expected to contain a contribution c_{MOH} of alkali hydroxide impurities

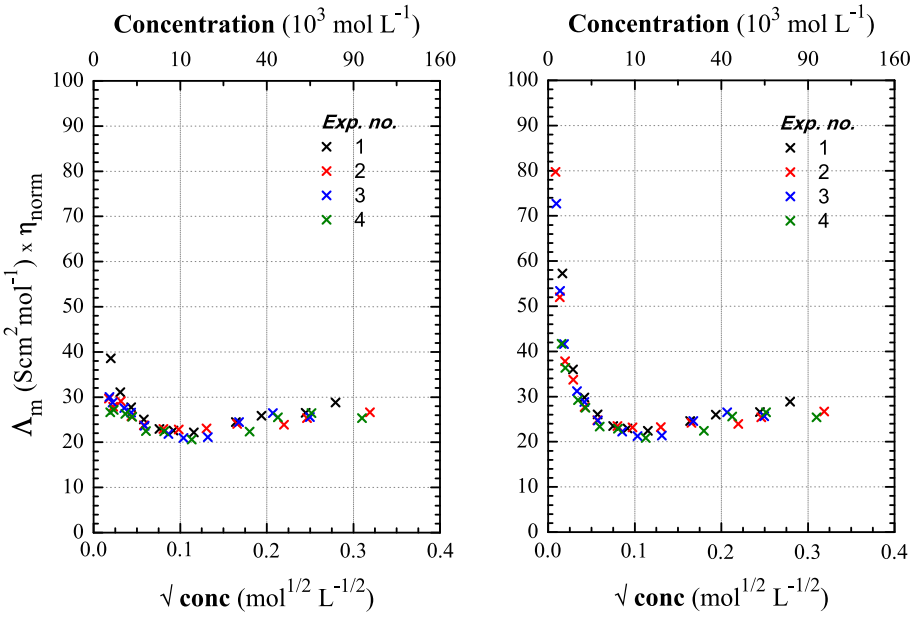


FIGURE 3.10: Original (left) and corrected (right) Walden product of the system NaK/15-crown-5/THF at 243 K obtained from conductivity measurements of five independent sample series.

in addition to the desired alkalide concentration c_A according to equation 3.8.

$$c_0 \;=\; c_A + c_{MOH} \;\Longleftrightarrow\; c_A \;=\; c_0 - c_{MOH} \tag{3.8}$$

A control experiment with the intentional use of wet THF (50 ppm) demonstrated that the presence of any traces of water proportionally delayed the development of the characteristic blue color of the mixture upon addition of the metal.
With the molar conductivity $\Lambda_m(c)$ given by equation 3.4, a deviation $\Delta c = c_{MOH}$ of the metal concentration results in an error $\Delta\Lambda_m$ in molar conductivity of

$$\begin{aligned}
\Delta\Lambda_m &= \Lambda_m(c_0 - \Delta c) - \Lambda_m(c_0) \\
&= \frac{C}{R}\,(c_0 - \Delta c)^{-1} - \Lambda_m(c_0) \\
&= \Lambda_m(c_0)\; c_0\; (c_0 - \Delta c)^{-1} - \Lambda_m(c_0) \\
&= [c_0\; (c_0 - \Delta c)^{-1} - 1]\; \Lambda_m(c_0) \\
&= [(1 - \frac{\Delta c}{c_0})^{-1} - 1]\; \Lambda_m(c_0)
\end{aligned} \tag{3.9}$$

with the corrected molar conductivity value $\Lambda_m(c_A)$ given as

$$\Lambda_m(c_A) \;=\; \Lambda_m(c_0 - \Delta c) \;=\; \Lambda_m(c_0) \;+\; \Delta\Lambda_m \tag{3.10}$$

The significance of the correction becomes apparent when considering an error in metal concentration of, for example, $\Delta c = 6$ ppm for the lower end of the covered concentration range with a determined metal concentration of, for example, $c_0 = 18$ ppm. According to equation 3.9, the ratio of $\frac{\Delta c}{c_0} = \frac{1}{3}$ results in an error in molar conductivity of $\Delta\Lambda_m = \frac{1}{2}\,\Lambda_m(c_0)$.
In order to correct the original molar conductivity data, all points of data series 1–4 were corrected for the background concentrations of up to 5 ppm as determined by Karl-Fischer titration of the used solvent immediately before each conductivity experiment.

The obtained trends of the molar conductivity of NaK solutions in 15-crown-5/THF plotted against the square root of the concentration as shown in Figure 3.10 clearly deviate from that of a strong electrolyte (Kohlrausch's law) as well as the classic trend of a weak electrolyte (equation derived from Ostwald's dilution law considering the dissociation K, further developed to Shedlovsky analysis/plot). Rather than a steady decrease in the

Walden product over the entire concentration range, a conductance minimum at $\sqrt{c} = 0.1$ was observed. As described in the previous chapter 3.2.3, the Walden product was calculated using viscosity values of metal-free solutions rather than those of alkalide solutions. It should be noted, that the use of expectedly marginally higher viscosity values of alkalide solutions would arguably result in an only slightly more pronounced manifestation of the indicated conductance minimum as it was suggested in the literature. [94, 95]

In this higher concentration range, several weak electrolyte systems have been reported since 1917 that show an increase in molar conductivity with increasing concentration between a conductivity minimum at lower concentrations and a conductivity maximum higher concentrations. [94–102] To describe this trend, Fuoss and Kraus developed a model based on the assumption that triple ions are formed from the pairing of an overall neutral (but still dipolar) ion pair and a single ion and stabilised by coulombic forces between the dipole and the separate ion (electrostatic potential energy). [89] The widely applied Fuoss-Krauss equation for triple-ion formation is:

$$\Lambda \; \boldsymbol{g(c)} \; \sqrt{c} \; = \frac{\Lambda_0}{\sqrt{K_P}} \; + \; \frac{\Lambda_0^T \; K_T}{\sqrt{K_P}} \; (1 - \frac{\Lambda}{\Lambda_0}) \; c \tag{3.11}$$

where c is the electrolyte concentration and Λ is the conductance. Λ_0 refers to the sum of the conductance of the simple ions at infinite dilution; Λ_0^T is the equivalent sum for the positive and negative triple ions formed by combination of the ion pair with another positive or negative simple ion, respectively. K_P and K_T are the formation constants of the ion pair and triple ions, respectively. The so-called interionic correction factor $g(c)$ (in every case ≤ 1) includes an estimate of the ionic activity and mobility terms, as well as of factors due to preceding approximations:

$$g(c) \; = \frac{exp(-2.303\boldsymbol{\beta'}\sqrt{c\Lambda} \; {\Lambda_0}^{-\frac{1}{2}})}{(1 - \boldsymbol{S}\sqrt{c\Lambda} \; / \; \sqrt{\Lambda_0}^3)/\sqrt{1 - \frac{\Lambda}{\Lambda_0}}} \tag{3.12}$$

with the dependence on the relative permittivity ϵ and temperature in

$$\beta' = \frac{1.8247 \times 10^6}{\sqrt{\epsilon T}^3} \tag{3.13}$$

as well as the Onsager coefficients α and β and therefore additionally the viscosity of the medium in

$$S = \alpha\,\Lambda_0 + \beta = \frac{0.8204 \times 10^6}{\sqrt{\epsilon T}^3}\,\Lambda_0 + \frac{82.501}{\eta\sqrt{\epsilon T}} \tag{3.14}$$

Upon measurement of the conductance Λ at different stoichiometric concentrations c of alkalide pairs $Cyc(M_1)^+M_2^-$ (assumed equal to concentration of complexant in the first approach), the equilibrium constants K_P (ion pair) and K_T (triple ion) could then be extracted from the slope and the intercept of the plot of $\Lambda g(c)\sqrt{c}$ vs. $(1 - \frac{\Lambda}{\Lambda_0})c$. This approach was recently applied to solutions of 1-butyl-2,3-dimethylimidazolium tetrafluoroborate ([bmmim][BF_4]) [103] or tetraheptylammonium iodide ($Hept_4NI$) [104] in solvents of different dielectric constant.

Most of the assumptions applied during derivation of this set of equations (namely symmetrical / spherical ions, homogeneous dielectric medium, triplet ion defined by maximum distance R between ion pair and free ion from electrostatic potential curve similar to Bjerrum's definition of ion pairs) are applicable to our system, which would justify the use of those equations for the determination of the corresponding equilibrium constants.

Results of more recent work on critical phenomena in ionic liquids, however, suggested that the claimed high stability of triple ions is questionable based on thermodynamic considerations involving the dielectric constant of the residual fluid of dipoles and free ions. [105] It was argued that conductance minima can therefore be rationalised by considering the effect of the previously neglected increase in overall dielectric constant with increasing solute concentration. [99, 106] It was argued that the increasing number of ion pairs leads to an increase of the static dielectric constant which, in turn, facilitates re-dissociation of ion pairs leading to an increase in conductivity. At even higher concentrations, the high viscosity of the mixture prevents any further increase in conductivity. Measurement of the overall dielectric constant of salt solutions and spectroscopic isolation of different contributions supported this theory. Based on a predictive thermodynamic model, it was recently suggested that "[t]he variation of the dielectric constant with solution composition results in a maximum value in the mean activity coefficient of dissociated ions near the concentration of the minimum degree of dissociation. With increasing solvent concentrations, free

ions can be better stabilized by the solvent. With the decrease of solvent concentration, the free ions are stabilized by the solvation of polar [undissociated] ion-pairs". [107]

Results of corresponding measurements of the system NaK/HMHC/THF are shown in Figure 3.11.

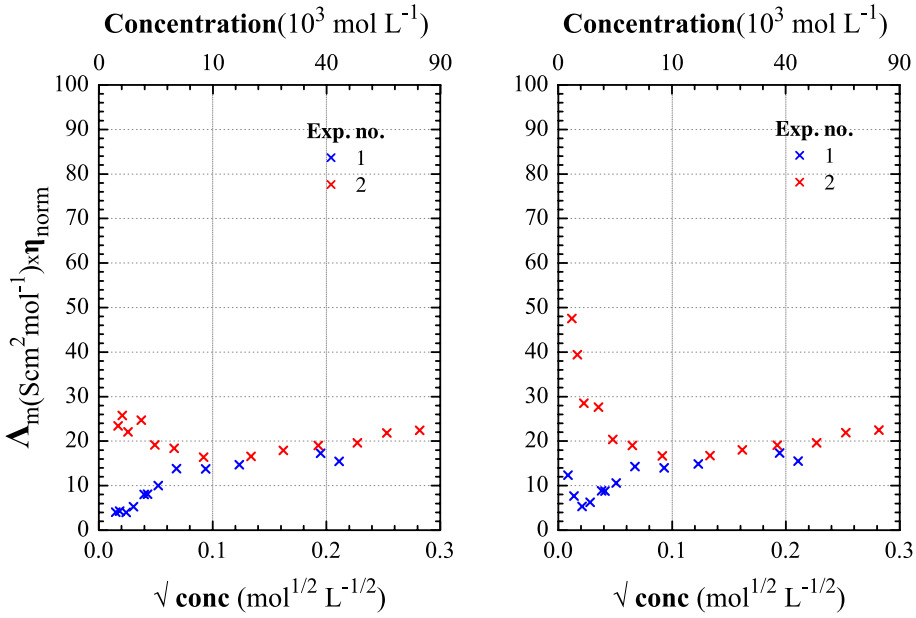


FIGURE 3.11: Original (left) and corrected (right) Walden product of the system NaK/HMHC/THF at 243 K obtained from conductivity measurements of two independent sample series.

Experiment 1 (blue) was carried out in analogy to previously conducted experiments with the 15C5 system in every respect (presence of excess of complexant from the start, frequency and amounts of added NaK, removal of aliquots, etc.). Despite that, the decrease in resistance over time (referring to Figure 3.6) and the development of the characteristic blue color of the solution (referring to Figure 3.7) were significantly delayed in comparison to experiments involving 15C5. Previous observations on 15C5 solutions indicated that a highly dilute metal solution in THF is significantly more prone to decomposition relative to higher concentrations even in the absence of traces of water and at low temperatures. It was speculated that the ionic products of equation 3.15

$$\mathbf{2\ M^0} + \mathbf{Cyc(\,)} \rightleftharpoons \mathbf{Cyc(M^+)} + \mathbf{M^-} \tag{3.15}$$

may be unstable and, as such, may collapse by charge transfer to yield highly reactive paramagnetic species according to equation 3.16

$$\mathbf{Cyc(M^+)} + \mathbf{M^-} \rightleftharpoons [\mathbf{Cyc(M^0)}]^* + [\mathbf{M^0}]^* \tag{3.16}$$

This would lead to a seemingly paradoxical situation with respect to metal solutions involving HMHC: While highly concentrated metal solutions were evidently significantly more stable than their crown ether equivalents, this relation would be inverted for highly dilute solution due to the naturally lower binding constant of the aza-crown. The generation of reactive species would thereby be facilitated by the weaker stabilization of charge carriers which would render highly dilute metal solutions with HMHC even more prone to decomposition. The consequent formation of *O*- and *N*-nucleophilic decomposition products, in turn, could explain the unexpectedly high metal concentrations in relation to the measured conductivity at the time of aliquot removal. In other words, the added alkali metal would simply be converted to non-conducting alkali alkoxides and result in unrealistically low molar conductivity values as shown in Figure 3.11.

In order to overcome this obstruction and to probe the described hypothesis, another experiment was conducted (red data set in Figure 3.11) whereby a larger portion of NaK (55 mg instead of 15 mg) was added at the start of the experiment. This led to a generally more rapid increase in conductivity and metal concentration that was comparable with that of experiments with 15C5 and gave - to our satisfaction - a very similar trend in molar conductivity. The aforementioned application of a correction with a background metal concentration of 3.4 ppm was required in this case as well. The great improvement of the quality of experimental results that was obtained by a slight change in experimental conditions demonstrated the validity of the described hypothesis as well as the great similarity of both alkalide systems in their conductivity footage.

3.3 Conclusion

Following indications from NMR and UV-Vis spectrosopy, the effects of ion pairing were investigated by conductivity measurements based on the theory of weak electrolytes. Considering the high sensitivity of alkalide solutions towards decomposition, a robust experimental method for the reliable recording of molar conductivity plots was developed. It was found that the presence of an excess of complexant did not lead to a higher conductivity of the solution by dissociation of alkali anions but rather to a higher stability of the electrolyte solution. In the presence of only minimal amounts of NaK, however, the

system was rendered much more prone to decomposition. Since the low concentration range is highly relevant to the characterization of weak electrolytes, the developed conductivity measurements involved an initially rapid increase in concentration and frequent removals of aliquots in order to correlate conductivity values with metal concentration values determined by ion chromatography.

Finally, a number of accurate measurements yielded reliable molar conductivity trends over a range of concentrations for alkalide solutions with HMHC and 15C5 as the complexing agent. The obtained trends showed a molar conductivity minium at a concentration of approx. 10 mM for both systems which is a characteristic phenomenon of weak electrolytes in low-polarity media that has attracted wide attention from the scientific community. Nevertheless, it is a clear evidence that ion association is operative in alkalide solutions in THF. Whether higher order effects due to the formation of larger aggregates are predominant in those systems was determined by further spectroscopic investigations as described in the following chapters.

3.4 Experimental Section

15-crown-5 was purified by Kugelrohr distillation from NaK, kept under an Argon atmosphere and handled inside an inert gas box.

The glass apparatus (including electrodes) was assembled inside an inert gas box, sealed, removed from the box, immediately connected to an Argon inert gas line, and kept under a slight overpressure of Argon throughout the entire experiment.

In a typical experiment, NaK was added in small portions (< 20 mg) to a solution of 0.06 M 15-crown-5 in dry THF at 243 K while the conductivity of the mixture was monitored in set intervals of 0.5 min (see also Figure 3.6).

The experimental setup for the contact measurement of the electrolyte conductivity included:

- Potentiostat *Gamry Reference 600* with connections for working electrode and source (WE, WES), counter electrode and source (CE, CES), and reference electrode (R)
- Computer for data processing
- Immersion cooler with temperature sensor
- Isopropanol cooling bath

- Magnetic stirrer
- External thermometer

Conductivity values were calculated from the cell constant and the specific resistance. The latter was determined by impedance measurement in the high frequency range (10-100 kHz). The cell constant of the conductivity cell with platinum electrodes was determined by multiplication of the measured resistance and the specific conductivity of aqueous KCl standard solutions with three different concentrations 0.01 M, 0.1 M, and 1.0 M. Specific conductivity values were taken from the literature. Determination of the cell constant before and after alkalide experiments gave identical values. Preliminary tests showed that none of the transition metals gold, nickel or titanium dissolved or even showed any noticable signs of degredation upon prolonged exposure to alkalide solutions in THF.

Viscosity measurements were carried out using a RheoSense m-VROC Viscometer.

Chapter 4

Dielectric Spectroscopy

4.1 Introduction

The dissolution of alkali metals is driven by the use of macrocyclic ligands in co-solvents with a low permittivity, resulting in the formation of an electrolyte consisting of complex cations and alkalides. Carefully assessed conductivity measurements described in chapter 3 suggested that ion association is a dominant factor in determining the bulk properties of those solution systems. The molar conductivity of solutions in THF – determined for a wide range of concentrations of dissolved NaK – followed the trend of a weak electrolyte, i.e. a rapid decrease in molar conductivity with increasing concentration in the range of concentrations up to 10 mM. In the higher concentration range between 10 to 100 mM, an intruiging deviation from the trend of steadily decreasing molar conductivity was observed. Such opposing trend was previously explained by the formation of triple ions, i.e. the pairing of non-conducting ion pairs with single ions which would result in an increase in molar conductivity with increasing concentration. An alternative more recent explanation considers the crucial role of the overall dielectric constant in a given electrolyte solution. An increase in the absolute concentration of ion pairs would thereby result in an increased dielectric constant of the medium due to the higher polarity of ion pairs in comparison to the low-polarity solvent. This, in turn, would lead to the re-dissociation of ion pairs, i.e. an increased dissociation constant and consequently an increase of molar conductivity with increasing concentration in the intermediate range.

In order to probe whether this hypothesis applies to the investigated alkalide system, to confirm the presence of ion pairs, and as an approach to the detailed characterisation of

their dielectric properties, it was envisaged to utilise a dielectric spectroscopy method. This technique was widely applied in the characterisation of ion pairing both in aqueous and non-aqueous media [108–114].

This chapter provides details on the experimental considerations and procedure of dielectric spectroscopy measurements using a coaxial probe under inert and cryogenic conditions. Furthermore, the application of this method to the characterisation of stable alkali metal solutions was demonstrated.

4.2 Results and Discussion

4.2.1 Calibration of Coaxial probe

The coaxial probe technique for dielectric spectroscopy allowed for the measurement of dielectric properties of a bulk sample under inert gas and cryogenic conditions. As the name suggests, the method employs a straight coaxial cable as a wave guide which can accommodate resonance microwave frequencies according to its length. *COMSOL Multiphysics* models[1] of the used 30 cm coaxial probe with and without the illustration of the electric field intensity of the first resonance mode are shown in Figure 4.1 together with the corresponding spectrum of resonance modes. From literature reports of the characterisation of ion pairing in organic solutions it was expected that the coverage of the frequency range between 0.35 to 6.0 GHz would allow for the detection and preliminary characterisation of any alkalide ion pairs by their impact on the dielectric properties of the solution [109, 114]. Further, the insertion of the probe into a three-necked reaction vessel allowed for the creation of a tight seal by the use of a common thermometer compression fitting adapter.

Sensing of dielectric properties of a sample occurs due to their effect on the resonance frequency by interaction with the evanescent field at the open end of the probe. In order to avoid any degradation of the probe upon exposure to alkalide solutions and to improve the air-tightness of the probe, a protective cap made from polypropylene was used in which the probe was inserted with a tight fit. The bottom cover layer of the cap was designed to have a thickness of less than 0.5 mm to allow for the interaction of the sample with the evanescent field whose spactial extent is minimal. Consequently, the presence of even just

[1] All *COMSOL* modelling referred to in this chapter was carried out by Heungjae Choi, Cardiff University, *unpublished results*.

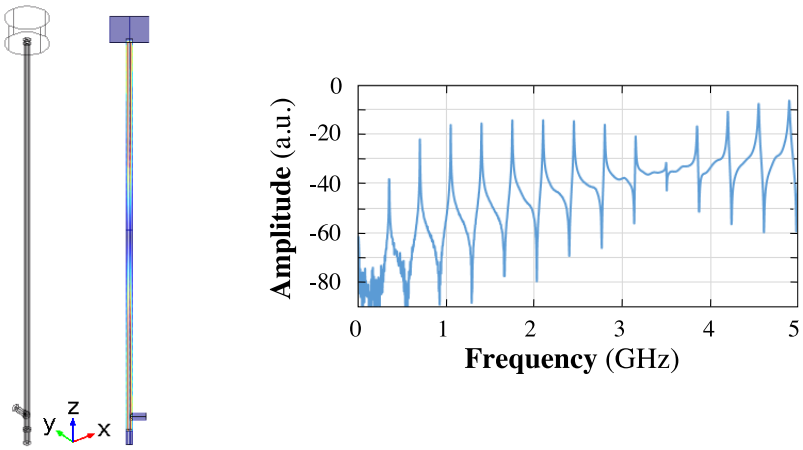


FIGURE 4.1: **(left)** COMSOL models of coaxial probe (left) and its first resonance mode (right; increase in electric field intensity from red to blue) and **(right)** spectrum of corresponding resonance frequencies.

a thin protective layer of polypropylene with a permittivity of 2.2 [115] would result in a depolarisation effect. This effect on the sensitivity of the coaxial probe was modelled using the aforementioned *COMSOL* model (Figure 4.2) which shows that the fractional shift of resonance frequencies (RFS) $\frac{\Delta f}{f_0}$ becomes insensitive to a change in sample permittivity in the higher permittivity range at a cap layer thickness above 1.0 mm. Considering that a protective cap with a bottom layer thickness of approx. 0.3 mm was used in subsequent measurements, it was concluded from the obtained trends shown in Figure 4.2 that a logarithmic function according to equation was appropriate to fit calibration data of the RFS.

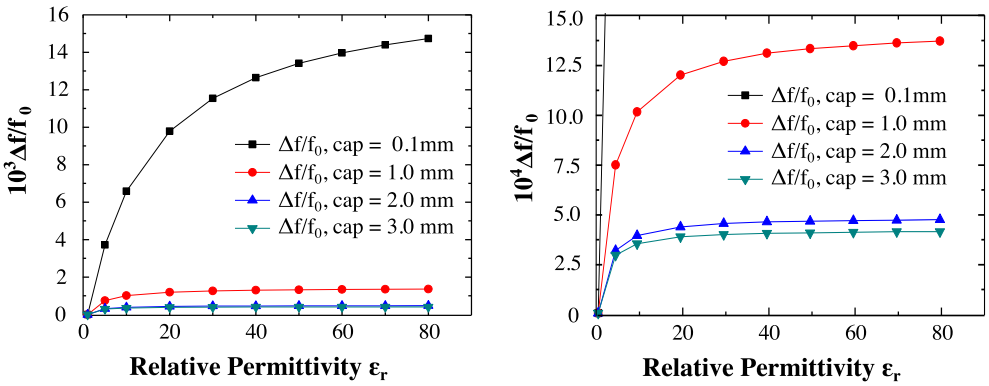


FIGURE 4.2: Depolarisation effect of polypropylene cap at different bottom layer thicknesses.

In order to calibrate the coaxial probe with a protective cap, the RFS of a number of pure solvents were determined. To achieve that, the frequencies of all resonance modes were recorded upon immersion of the protected tip of the probe in a given solvent at

243 K under inert gas once a stable temperature gradient within the coaxial probe was reached (typically within less than 30 min). The obtained values were then subtracted from the values of the corresponding modes recorded with the sample container kept under vacuum. Plots of the obtained RFS for the fundamental mode (0.35 GHz) against literature permittivity values of respective solvents on a linear and a logarithmic scale are shown in Figure 4.3.

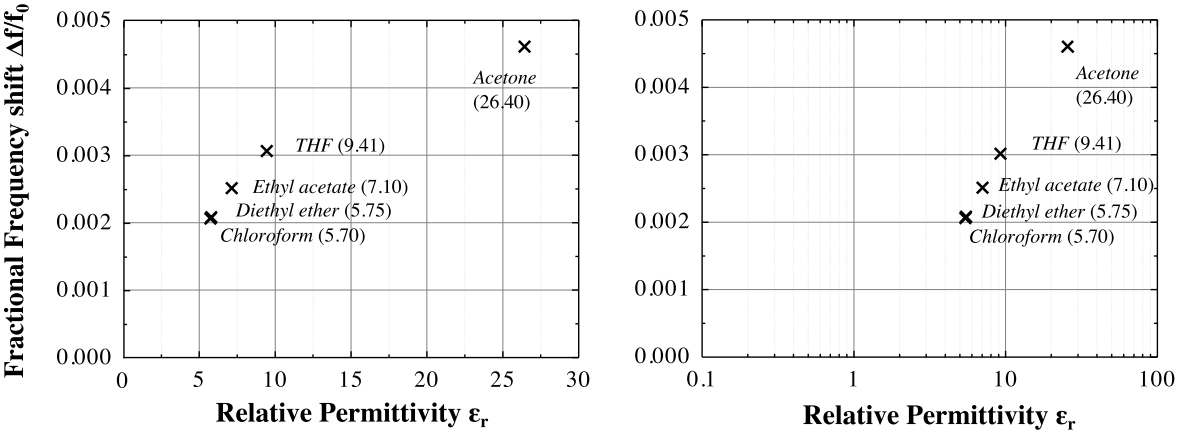


FIGURE 4.3: Calibration of coaxial probe at RT with common solvents.

As predicted, the obtained RFS data show a linear trend in the covered range of sample permittivity on log scale of the static permittivity ϵ'. The corresponding calibration function of the form

$$\left(\frac{\Delta f}{f_0}\right) = A\ ln(\epsilon')\ +\ B \tag{4.1}$$

with the fitting parameters A and B was used to fit the obtained calibration data. The entire calibration process was to be carried out directly before the measurement of an unknown sample because of the high sensitivity of the calibration to the prevalent daily conditions such as the temperature inside the laboratory and smallest movements of any parts of the coaxial wave guides including the coaxial probe itself.

4.2.2 Dielectric properties of a sodide solution

With a robust calibration method for the coaxial probe under cryogenic conditions in hand, the RFS at all available resonance modes were recorded for a solution of 15-crown-5 in THF at 243 K during the partial dissolution of a threefold excess of NaK that was initially added in one portion. The obtained RFS values were subsequently converted to

static relative permittivity values and the change over time is shown in Figure 4.4 for the fundamental mode. Within the first 3 h upon metal addition to the cold solution, a significant increase in permittivity by more than 100% of the original value was observed before the trend appeared to reach the plateau of a maximum permittivity value. It was concluded that a metal content close to saturation was reached after 5 h which is the same order of magnitude as reported in chapter 3 for our conductivity measurements.

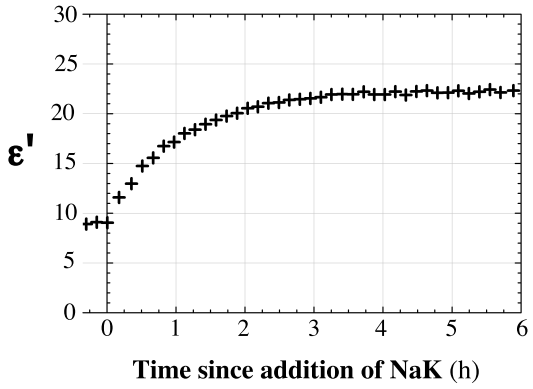


FIGURE 4.4: Increase of dielectric constant / static relative permittivity ϵ_S (measured at 0.35 GHz) during dissolution of NaK in a 0.5 M solution of 15-crown-5 in THF at 243 K.

In an attempt to identify the species that caused this increase in permittivity during metal dissolution, the frequency dependence of the permittivity $\epsilon'(f = \frac{\omega}{2\pi})$ of both the saturated metal solution as well as the metal-free starting solution as a control were plotted from the RFS values measured at all resonance modes (Figure 4.5).

Rearrangement of the Debye equation 4.2

$$\epsilon(\omega) \;=\; \epsilon_\infty + \frac{\epsilon_S - \epsilon_\infty}{1 + i\omega\tau} \tag{4.2}$$

gives the real and imaginary parts according to 4.3 and 4.4, respectively.

$$\epsilon'(\omega) \;=\; \epsilon_\infty + \frac{\epsilon_S - \epsilon_\infty}{1 + (\omega\tau)^2} \tag{4.3}$$

$$\epsilon''(\omega) \;=\; \frac{(\epsilon_S - \epsilon_\infty)\omega\tau}{1 + (\omega\tau)^2} \tag{4.4}$$

The mathematical description of the real part $\epsilon'(\omega)$ of the complex permittivity was used to fit the obtained data and extract corresponding dielectric parameters of the solution systems. The fit functions are shown in grey in Figure 4.5 and the extracted values are given in Table 4.1. As expected, the frequency range covered by the resonances of the used coaxial probe was far from being wide enough to reproduce the plateau of $\epsilon'(\omega)$ towards

lower frequencies. The depicted fit functions, as a consequence, demonstrated that the real static permittivity ϵ_S of any characterised alkalide solution lies even higher than the value obtained at the fundamental resonance frequency. While the obtained values of the fit variables ϵ_S, ϵ_∞, and τ do not raise the claim of high accuracy, the monitored frequency range did cover any increase in frequency dependent relative permittivity relevant to ion associates and the characteristic trace outlined by the recorded data points did allow for a rough estimate of the corresponding Debye function and its variables. Furthermore, It should be noted that the large deviation of data points from the corresponding fit function at frequencies around 3.5 GHz is a consequence of the low sensitivity of the coaxial probe in this frequency range due to low amplitudes of the respective resonances (see Figure 4.1 right). Those intrinsic detriments were considered as an acceptable compromise in favour of the reliability of the sample with respect to its composition when this dielectric spectroscopy method was chosen.

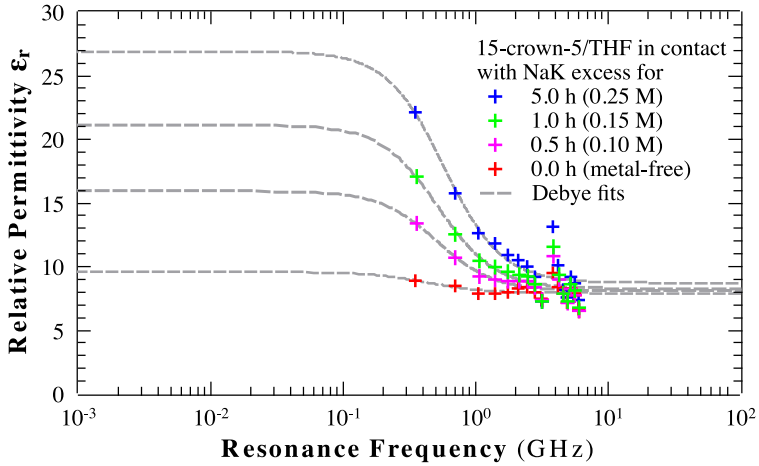


FIGURE 4.5: Dielectric spectra of solutions of different concentrations of NaK in a 0.5 M solution of 15-crown-5 in THF at 243 K.

TABLE 4.1: Dielectric paramters of different concentrations of NaK dissolved in a solution of 15C5 in THF and its metal-free control solution at 243 K, estimated by Debye fits of available coaxial probe dielectric spectroscopy data (see Figure 4.5).

	Blank solution	0.10 M	0.15 M	0.25 M
ϵ_S	9.6 ± 3.2	16 ± 3.4	21 ± 3.8	27 ± 3.8
ϵ_∞	7.9 ± 0.22	8.2 ± 0.34	8.3 ± 0.40	8.7 ± 0.51
$10^9\ \tau[s]$	0.37 ± 0.75	0.32 ± 0.16	0.31 ± 0.11	0.28 ± 0.072

The effect of the electrolyte on the dielectric constant of the mixture became clear from the comparison of the static permittivity values ϵ_S during metal dissolution.

THF is classified as a radio frequency transparent material with minimal dielectric loss in a frequency range up to 10 GHz at room temperature [116]. The dielectric relaxation frequency $1/\tau$ of organic solvents typically decreases with a decrease in temperature which could shift the maximum in dielectric loss ϵ'' of THF into the frequency range that overlaps with the spectroscopic signature of the alkalide solution. However, control measurements confirmed that dielectric loss effects originating from the solvent are comparably low and can be neglected in the assessment of alkalide solutions in a first approximation.

The relaxation time values τ as estimated from Debye fits of the experimentally determined relative permittivity values were found to be essentially concentration independent within the covered concentration range, in accordance with results reported for electrolyte solutions in organic solvents [109]. Given that the concentration range lay above the conductance minimum as reported in chapter 3, no significant changes in charge separation and therefore no variation of τ were expected. More importantly though, τ was found to be significantly larger than that of neat THF (2.53×10^{12} s at 298 K [117]) which provides evidence for the increase in dielectric constant being caused by an entirely different and larger species. Although the lower sensitivity of the coaxial probe technique applied in this study as compared to, for example, time domain spectroscopy rendered the characterisation of highly dilute solutions impossible, the studies clearly showed that the overall dielectric constant of alkalide solutions increases with increasing concentration of an electrolyte that is characterised by a certain relaxation time.

Furthermore, a significant ionic contribution to the dielectric loss ϵ" was expected due to the conductivity of the sample (separately solvated ions). However, only the lower end of the frequency spectrum far outside the frequency range covered in this work would be concerned by such contribution. The static relative permittivity ϵ' and its determination at the lowest accessible resonance frequency would therefore not be negatively affected. For completion, Figure 4.6 shows the conductivity of alkalide solutions over the entire concentration range covered by our investigations. Note that the x-scale is given as the square-root of the concentration of charge carriers in accordance with the traditional plot of molar conductivities for electrolyte solutions. The conductivity of alkalide solutions in low-permittivity solvents is generally low and comparable with aqueous alkali chloride solutions up to a concentration of 0.1 M.

Given that the dielectric relaxation time τ for the alkalide solution was in the same order

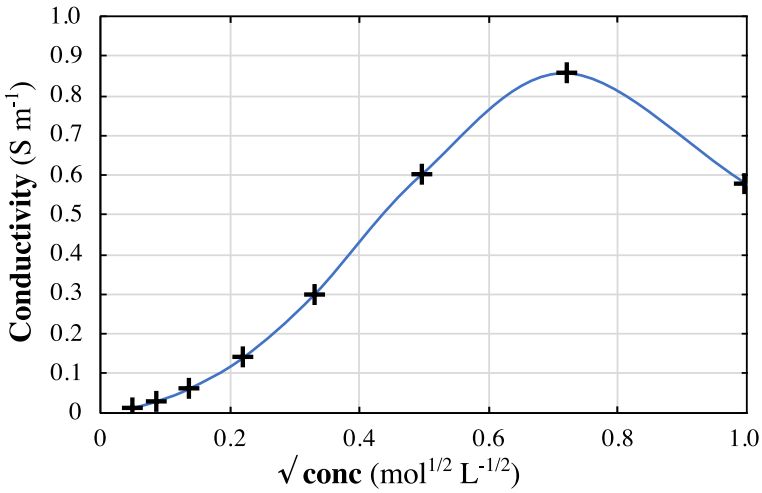


FIGURE 4.6: Conductivity of solutions of 15-crown-5/NaK in THF at 293 K.

of magnitude as that of weak electrolytes in the same solution medium [114], the increase in permittivity in alkalide solutions may indeed originate from ion pairs.

4.3 Conclusion

In order to probe the potential contribution of ion pairs to the overall dielectric constant in alkalide solution systems, a resonance-based dielectric spectroscopy method was developed for the application under cryogenic, inert and highly reactive conditions up to a point that it produced robust and insightful results. The use of a coaxial probe in conjunction with a protective plastic cap allowed for measurement of the bulk permittivity of alkalide solutions. In spite of a large depolarisation effect due to the required plastic cap, calibration of fractional resonance frequency shifts for the coaxial probe was straightforward. Based on those developments, a large increase of the static permittivity of an alkalide solution was detected and attributed to alkalide ion pairs by extraction of the dielectric relaxation time from the frequency dependence of the static permittivity. The precise description of the experimental methodology will allow for its application to more alkalide solution systems (concentrations, complexants, etc.) whose investigation was beyond the scope of this thesis.

4.4 Experimental Setup

- FieldFox Handheld RF and Microwave Analyzer: analysis of microwave frequencies within coaxial probe, controlled by software developed by members of the research

group of Prof. Adrian Porch[2];

- Coaxial Probe: 30 cm length, connected to FieldFox with flexible coaxial wave guides;
- Flexible coaxial cables: connecting coaxial probe to FieldFox, to be immobilised during dielectric measurements to avoid artefacts in FFS;
- Polyethylene (PE) and polypropylene (PP) protection caps: manufactured from pure plastic rods using a CNC lathe, respectively (see items and length scale in Figure 4.8). The resistance of both types of caps towards common solvents and alkali metal solutions in THF was confirmed by exposure tests with prototypes, no noticeable decomposition processes were observed by visual inspection after exposure to metal solutions at RT for several days.



FIGURE 4.7: PP (polypropylene) and PE (polyethylene) caps for coaxial probe.

[2]Cardiff University

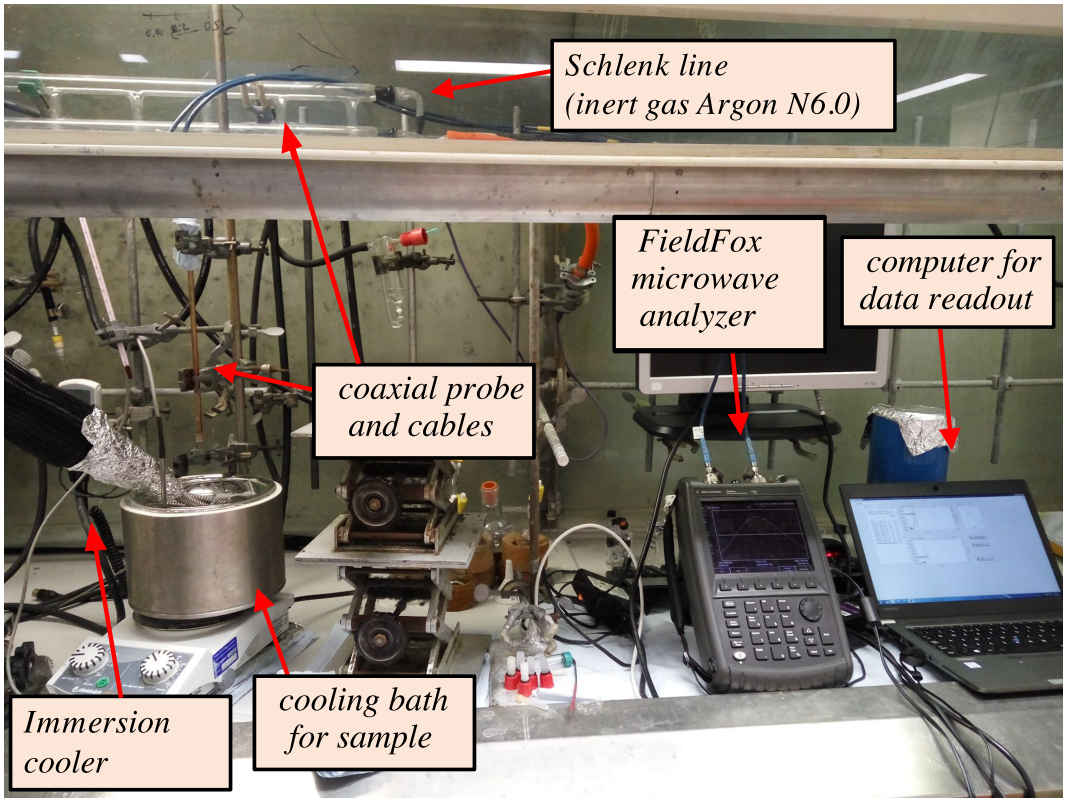


FIGURE 4.8: Dielectric spectroscopy setup in laboratory.

Chapter 5

Small-Angle Neutron Scattering of alkalide solutions

5.1 Introduction

Both conductivity and dielectric spectroscopy measurements revealed that ion pairing is a predominant factor in alkalide solutions in a low-polarity medium. Results from spectroscopic measurements and molecular dynamics simulations of ionic liquids and their dilutions in molecular solvents suggested that the consideration of higher aggregates in binary mixtures can in some cases be crucial for the understanding and tailoring of those mixtures. [118, 119] For several systems, ionic liquids were found to form networked structures, bicontinuous systems consisting of separated phases of the molecular solvent and the ionic liquid on the mesoscopic scale [120, 121]. The latter of which was suggested to consist of a bimodal distribution of fully dissociated mobile ions and large rather stationary aggregates [102]. An increase in temperature or dilution might affect the stability of such aggregates which could be linked to the behaviour of alkalide solutions observed in the course of NMR relaxation time measurements. Breaking of mesoscopic aggregates might lower the interionic/dipolar coulombic stabilisation of the species and particularly the stability of the complex cation, resulting in decomplexation, electron transfer from the alkalide to the free cation and consequently collapse of the originally charge-separated system.

This type of large dynamic aggregation is difficult to precisely characterise. Nevertheless, their qualitative existence as well as certain parameters such as the coherence length (i.e. the average spatial dimensions of the phases) can be determined by scattering techniques and corresponding conductivity data can be evaluated based on percolation theory [122].

The better understanding of stabilising and destabilising factors in alkalide solutions allowed for the extension of our studies to techniques requiring longer time scales and higher resolution data collection. It was the purpose of neutron diffraction experiments to clarify whether the formation of larger aggregates in solution determines the properties of alkalide solutions in addition to pure ion pair formation. It was also demonstrated that neutron scattering is a particularly suitable technique for the investigation of alkalide multi-component systems.

5.2 Results and Discussion

The investigation of alkalide solution benefited from the characteristics of the neutron diffractometer NIMROD (**N**ear and **I**nter**m**ediate **R**ange **O**rder **D**iffractometer at Neutron Source *ISIS*, *Rutherford Appleton Laboratories*). Due to its particular angular neutron flux distribution (see Figure 5.1), NIMROD provides a high resolution in the low and intermediate Q-range of 0.05–10 $Å^{-1}$. We envisaged that this would not only give access to a length scale of up to 600 Å, the usual application range for the investigation of large structures like micelles, biomolecules, nanoparticles, polymers, and bicontinuous systems in ionic liquids and their solutions (Edler, Hammond). The particularly high resolution in the range of 0.1–1 $Å^{-1}$ can also provide insights on a length scale of 5–20 Å which is applicable to the investigation of scattering particles with dimensions of alkali cation complexes with organic macrocycles and corresponding alkalide ion pairs.

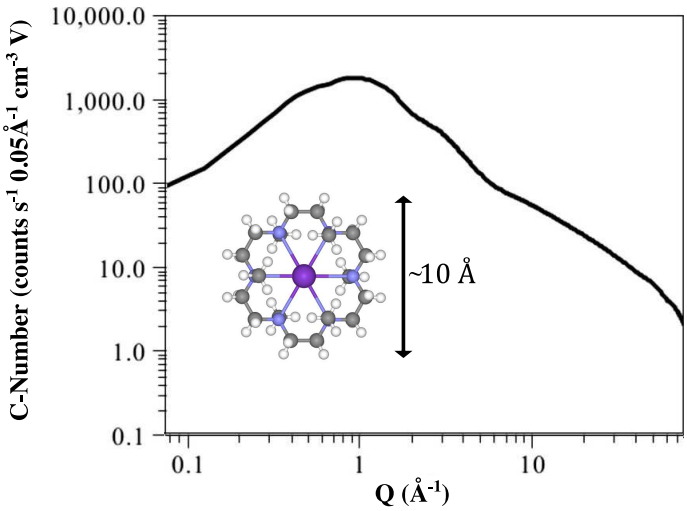


FIGURE 5.1: Count rate for the NIMROD diffractometer (reproduced from reference [123]).

A suitable contrast is achieved by combining fully protiated macrocyles with a fully deuterated solvent:

- Coherent scattering length of ^1H (-3.74 Å) leads to an approximate scattering length density of $0.4 - 0.5\,10^{-6}$Å^{-2} for the macrocycles used;
- Coherent scattering length of ^2H (6.67 Å) leads to an approximate scattering length density of $7.0\,10^{-6}$Å^{-2} for d_8-THF.

This large difference in scattering length densities (SLD) between the scattering particles and the solvent ensures the visibility of the electroyte in the scattering experiment.

Figure 5.2 illustrates that the presence of paired species was expected to affect both the shape and the size of the scattering particles (white voids) dissolved in the fully deuterated medium (red). A separately solvated complex-cation was expected to appear with a similarly sized if not slightly contracted solvation shell as the unoccupied macrocycle in the blank sample. A separately solvated alkalide ion with its atomic form factor would not contribute to the small angle scattering intensity due to its small size. Ion pairing, however, is expected to noticably expand the solvation shell of the macrocyclic species due to the large HOMO of the contact ion pair.[1] It is noteworthy that the particle size appears larger only due to the additional void space surrounding the complex-cation as the coherent scattering length of alkali metals (ca. 3.6 Å for ^{23}Na or ^{39}K) do not create a sufficient contrast to the solvating medium.

[1]Isosurface plot of HOMO of the alkalide contact ion pair with HMHC was obtained from DFT calculations by D. Miller and E. Zurek, *unpublished results*.

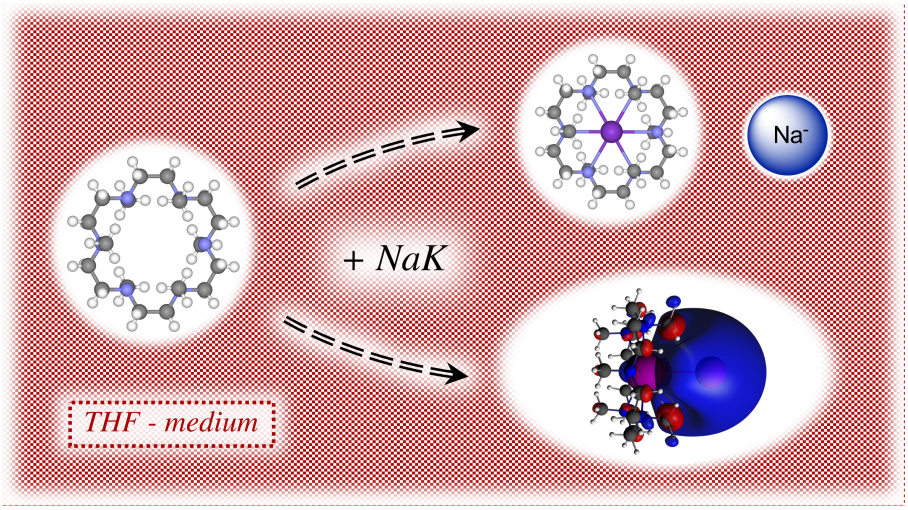


FIGURE 5.2: Computational model representation of contrast method to visualise ion pairing in SANS of NaK/HMHC/THF solutions.

The small angle scattering intensity corresponding to the differential cross section $\frac{d\Sigma}{d\Omega}$ extrapolated to $Q = 0$ according to equation 5.1 [124]

$$\frac{d\Sigma}{d\Omega}(Q=0) \sim \boldsymbol{N}\, V_P^2\, (\Delta\rho)^2 \tag{5.1}$$

was significantly increased upon dissolution of NaK in a solution of 0.05 M HMHC in THF (see Figure 5.3). This is directly related to an increase in particle volume V_P given that both the number of particles N as well as the difference in SLD $\Delta\rho$ are identical in the metal-free control and the corresponding alkalide solution. Hence, the contrast between both SANS spectra provides evidence for the presence of ion pairs in alkalide solutions in THF.

The effect was found to be greater for samples with lower concentration due to two contribution factors (see equation 5.1): Firstly, the SLD contrast $\Delta\rho$ between the scattering particle and its surrounding is smaller at higher concentration of the electrolyte due to its contribution to the SLD of the bulk solution. Secondly and more importantly, following our hypothesis, the increased dielectric constant of the medium at higher alkalide concentrations results in an increase in ion pair dissociation and consequently to a reduced average particle volume V_P. Samples with lower metal concentrations, i.e. a lower number N of scattering particles, were not considered as the investigated samples generally yielded a low small angle scattering intensity.

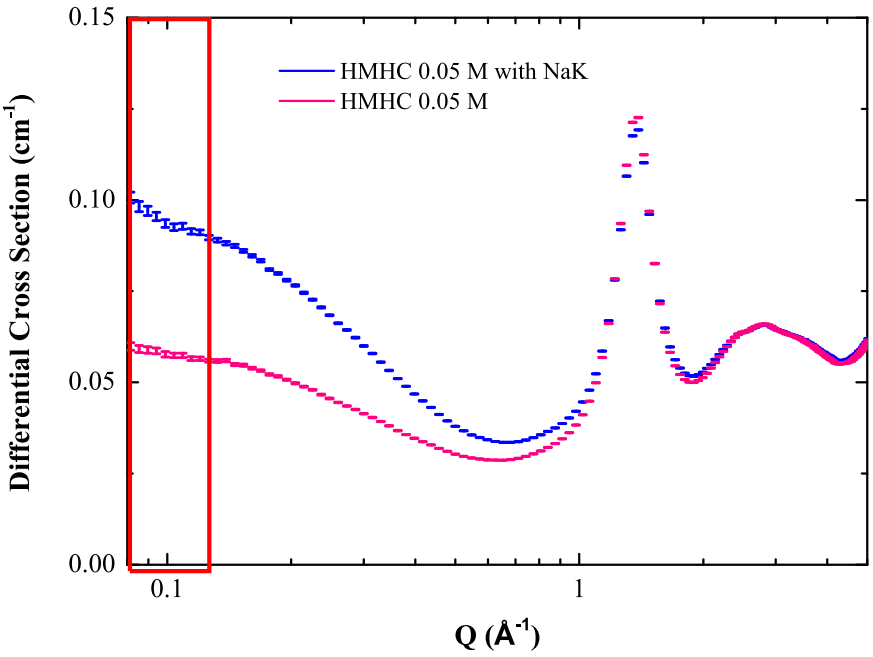


FIGURE 5.3: SANS spectra of HMHC/THF blank and alkalide solutions.

The same arguments apply to the analysis of scattering data from metal solutions involving 15C5. However, as illustrated in Figure 5.4, the formation of a sandwich complex upon metal dissolution naturally leads to an increase in SANS intensity. Consequently, an increase in scattering intensity was observed for all investigated samples using 15C5 (see Figure 5.5). A detailed analysis of structural changes upon metal dissolution must take into account this particularity of the 15C5 solution system.

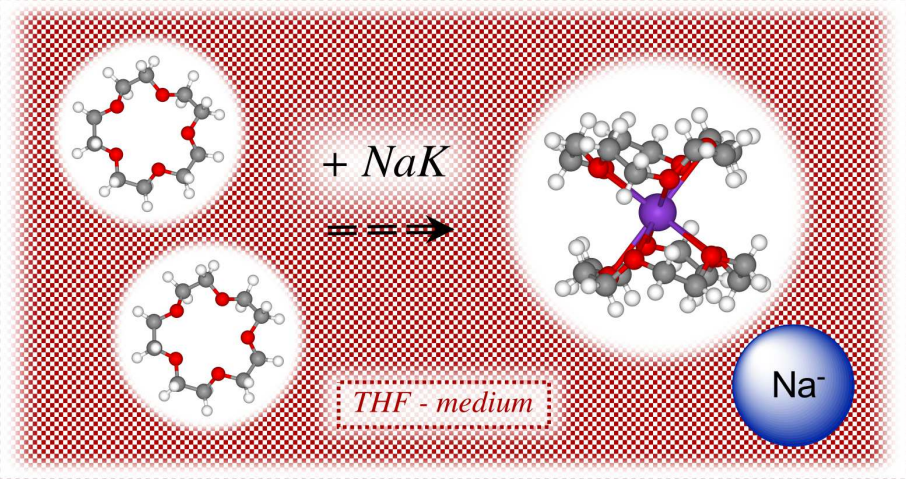


FIGURE 5.4: Schematic representation of contrast method to visualise effect of metal dissolution on SANS of NaK/15C5/THF solutions.

Generally, no significant effects were observed for changes in temperature bar a change in density revealed by a slight shift of the principal peak at 1.5 Å^{-1} due to thermal expansion.

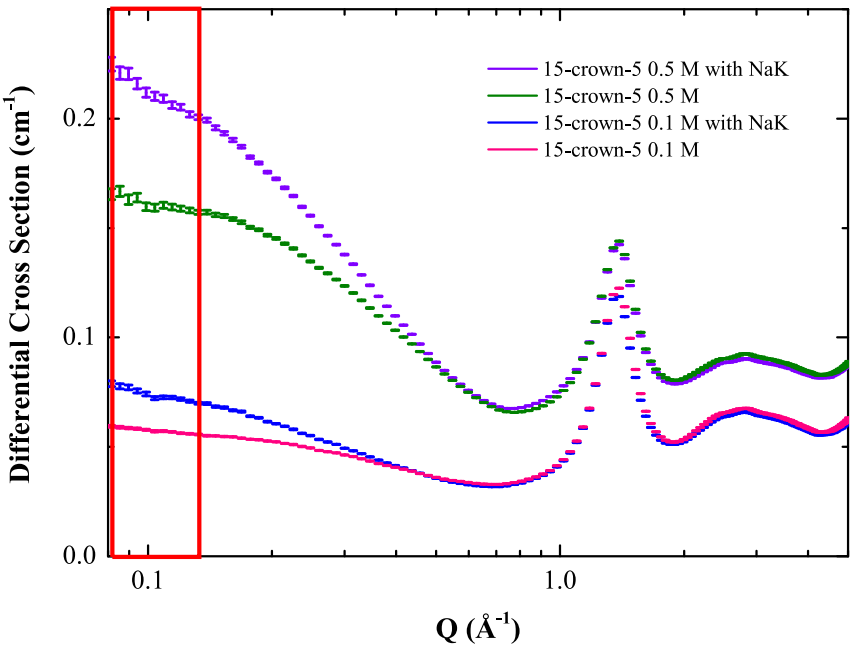


FIGURE 5.5: SANS spectra of 15-crown-5/THF blank and alkalide solutions.

In an attempt to quantitatively assess the aforementioned observations, certain parameters describing the species in solution were extracted from the experimental data by the application of Guinier's approximation [125]:

$$I(Q) = scale \cdot exp[\frac{-Q^2 R_G^2}{3}] + background \tag{5.2}$$

Thereby, '*scale*' corresponds to the product of all terms in equation (5.1) and R_G corresponds to the so-called *Radius of Gyration*. This term is somewhat misleading as it represents an equivalent scattering radius rather than an equivalent radius related to the particle mass. A representation of a typical corresponding fit function covering the entire Q-range is depicted in Figure 5.6. In order to determine a reasonable approximation of the background scattering level at the high end of the Q-range, Lorentzian fits were applied to the solvent correlation peak as shown in Figure 5.7.

Due to the limitation of the Guinier approximation to the range with $Q \leq R_G^{-1}$ [124] (see range framed in red in Figures 5.3 and 5.5) and the relatively small particle size of the macrocycles used (as compared to micelles or proteins), any resulting fits are of low quality. Nevertheless, the obtained results do reveal prevalent trends (see Tables 5.1 and 5.2).

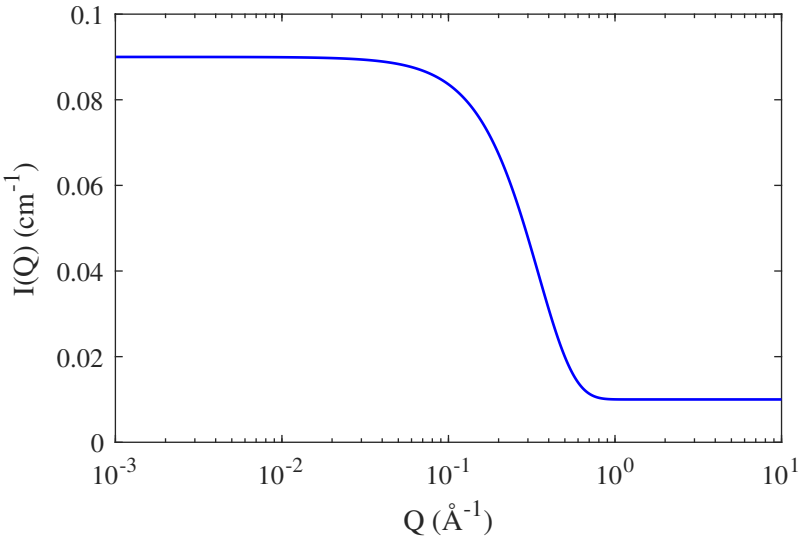


FIGURE 5.6: Typical Guinier function used for approximate data extraction from SANS spectra.

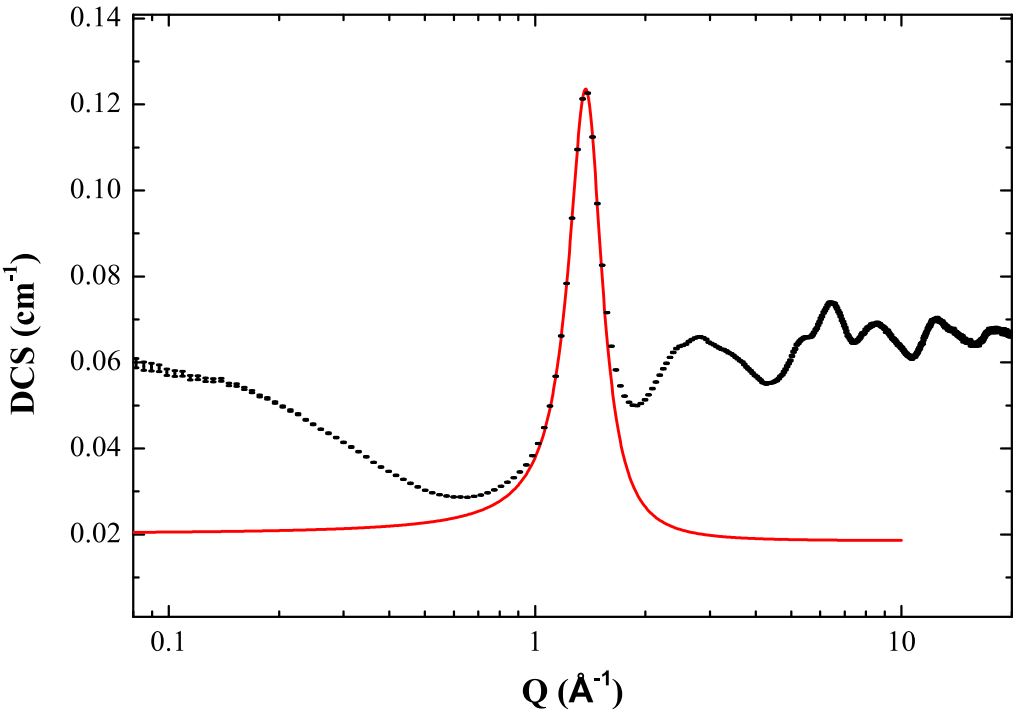


FIGURE 5.7: Determination of Background scattering intensity from baseline of Lorentzian fit (red) as applied to solvent correlation peak at 1.4 Å of each SANS spectrum, respectively.

TABLE 5.1: Results from fit of HMHC dataset with Guinier function.

Conc. [M]	**0.05**	**0.05**	**0.10**	**0.10**	**0.25**	**0.25**
Sample	**blank**	**NaK**	**blank**	**NaK**	**blank**	**NaK**
Run #	54089	54076	54036	53974	54044	54053
	Lorentzian fit of 'solvent peak' – Determination of Background level					
min Q [Å^{-1}]	1.20	1.20	1.20	1.20	1.20	1.20
max Q [Å^{-1}]	1.45	1.45	1.45	1.45	1.45	1.45
red. Chi^2	1.13E-10	1.03E-09	4.20E-10	2.37E-09	1.16E-09	3.07E-09
background [cm^{-1}]	0.0186	0.0242	0.0323	0.0295	0.0567	0.0575
center [Å^{-1}]	1.37	1.38	1.37	1.37	1.37	1.37
width [Å^{-1}]	0.355	0.354	0.358	0.355	0.365	0.357
area [Å^{-1} cm^{-1}]	0.0586	0.0532	0.0550	0.0611	0.0530	0.0537
height [cm^{-1}]	0.105	0.0958	0.0977	0.110	0.0925	0.0956
	Guinier fit 1 – narrow Q-window					
min Q [Å^{-1}]	0.07	0.07	0.07	0.07	0.07	0.07
max Q [Å^{-1}]	0.10	0.10	0.10	0.10	0.10	0.10
Chi^2/#points	0.21	1.2	0.99	0.76	0.64	0.58
scale	0.0430	0.0811	0.106	0.126	0.197	0.206
error scale	0.00170	0.00254	0.00357	0.00360	0.00661	0.00628
R_G [Å]	5.07	6.60	4.97	6.57	4.84	5.67
error R_G [Å]	1.79	0.945	1.47	0.834	1.61	1.10
	Guinier fit 2 – wider Q-window					
min Q [Å^{-1}]	0.07	0.07	0.07	0.07	0.07	0.07
max Q [Å^{-1}]	0.15	0.15	0.15	0.15	0.15	0.15
Chi^2/#points	0.50	1.2	0.57	1.1	0.57	0.85
scale	0.0422	0.0776	0.105	0.122	0.194	0.200
error scale	5.24E-04	7.79E-04	9.71E-04	0.00102	0.00169	0.00168
R_G [Å]	4.58	5.50	4.61	5.95	4.46	4.79
error R_G [Å]	0.259	0.176	0.195	0.133	0.179	0.166
#THF / crown	247	300	97	112	44	44
vol. fract.	0.017	0.014	0.043	0.037	0.091	0.089
sqrt(conc) [mol$^{1/2}$ L$^{-1/2}$]	0.22	0.22	0.32	0.32	0.50	0.50
vol. (particle) [Å^3]	566	757	626	675	544	552
radius (sphere) [Å]	5.13	5.65	5.31	5.44	5.06	5.09

TABLE 5.2: Results from fit of 15-crown-5 dataset with Guinier function.

Conc. [M]	**0.05**	**0.05**	**0.10**	**0.10**	**0.25**	**0.25**	**0.50**	**0.50**
Sample	**blank**	**NaK**	**blank**	**NaK**	**blank**	**NaK**	**blank**	**NaK**
Run #	54967	54100	53928	53964	54012	53988	54066	54021
	Lorentzian fit of 'solvent peak' – Determination of Background level							
min Q [Å^{-1}]	1.20	1.20	1.00	1.00	0.900	0.900	0.850	0.850
max Q [Å^{-1}]	1.45	1.45	1.45	1.45	1.55	1.55	1.55	1.55
red. Chi²	4.08E-09	1.72E-09	3.05E-09	3.41E-09	4.85E-08	9.57E-08	5.47E-07	6.09E-07
background [cm^{-1}]	0.0250	0.0239	0.0499	0.0338	0.0568	0.0608	0.101	0.101
center [Å^{-1}]	1.38	1.37	1.37	1.38	1.38	1.38	1.38	1.38
width [Å^{-1}]	0.354	0.354	0.356	0.347	0.382	0.368	0.430	0.411
area [Å^{-1} cm^{-1}]	0.0545	0.0532	0.0446	0.0500	0.0523	0.0471	0.0481	0.0424
height [cm^{-1}]	0.0979	0.0956	0.0796	0.0918	0.0871	0.0815	0.0712	0.0657
	Guinier fit 1 – narrow Q-window							
min Q [Å^{-1}]	0.070	0.070	0.080	0.070	0.070	0.070	0.070	0.070
max Q [Å^{-1}]	0.10	0.10	0.10	0.10	0.10	0.10	0.10	0.10
Chi²/#points	0.72	0.74	0.13	0.52	0.75	0.83	0.94	0.94
scale	0.0360	0.0596	0.0465	0.126	0.114	0.176	0.178	0.224
error scale	8.40E-04	0.00208	0.00234	0.00395	0.00483	0.00526	0.00518	0.00819
R_G [Å]	5.20	6.93	5.29	8.49	4.97	6.61	3.51	5.32
error R_G [Å]	0.963	0.993	2.06	0.713	2.08	0.888	1.93	1.50
	Guinier fit 2 – wider Q-window							
min Q [Å^{-1}]	0.070	0.070	0.070	0.070	0.070	0.070	0.070	0.070
max Q [Å^{-1}]	0.15	0.15	0.15	0.15	0.15	0.15	0.20	0.15
Chi²/#points	0.95	1.2	0.51	1.4	0.57	1.0	1.1	0.71
scale	0.0357	0.0570	0.0449	0.119	0.110	0.171	0.181	0.219
error scale	2.60E-04	6.30E-04	3.90E-04	0.00106	0.00123	0.00168	0.00109	0.00234
R_G [Å]	5.08	5.96	4.36	7.31	3.89	5.80	3.91	4.78
error R_G [Å]	0.140	0.177	0.189	0.110	0.274	0.157	0.0844	0.212
#THF / crown	135	135	61	60	22	23	9	9
vol. fract.	0.020	0.020	0.045	0.045	0.12	0.11	0.23	0.23
sqrt(conc) [mol$^{1/2}$ L$^{-1/2}$]	0.22	0.22	0.32	0.32	0.50	0.50	0.71	0.71
vol. (particle) [Å^3]	378	653	306	667	304	512	381	416
radius (sphere) [Å]	4.49	5.38	4.18	5.42	4.17	4.96	4.50	4.63

5.2.1 Conformational analysis

A much more detailed picture of structural properties of the dissolved species can be obtained by the extraction of structural parameters from the analysis of the line shape. A difference in slope and line shape in the Q-range of 0.1–0.5 $Å^{-1}$ is related to a change in size and shape of the solvation shell, represented by the form factor $P(Q)$, as well as any changes in aggregation of scattering particles, represented by the structure factor $S(Q)$, according to equation 5.3 [125]. considering that the full scattering intensity (differential scattering cross section DSC) is given by equation (5.3):

$$\frac{d\Sigma}{d\Omega}(Q) \approx \boldsymbol{N}\, V_P^2\, (\Delta\rho)^2\, P(Q)\, S(Q) \tag{5.3}$$

However, such analysis requires an accurate simulation of the form factor $P(Q)$ from a 3-dimensional molecular model which is currently not available.

This approach is particularly important in order to determine whether ion pairing may lead to changes in the conformation of macrocyclic ligand in a complex cation. Crystallisation of the potassium salt of the large non-coordinating tetraphenylborate anion in the presence of HMHC gave a crystal of the complex cation in a planar conformation in accordance with a recent literature report [126] (see Figure 5.8 left). In contrast, crystallisation of the corresponding sodide salt showed the macrocyclic ligand in a boat conformation allowing for a close contact between the alkali cation and anion [30, 31] (see Figure 5.8 right). It is currently not known whether contact ion pair formation in solution can trigger a conformational change and whether such effects are concentration dependent in the light of the concentration dependence of ion pairing in those solutions as elaborated in chapter 3.

5.3 Conclusion

The purpose of neutron scattering experiments was the unprecedented characterisation of any changes in the microscopic structure of the bulk solution upon dissolution of alkali metals in solutions of HMHC or 15C5 in THF. The large Q-range of NIMROD and the possibility to provide various contrasts in our multi-component system allowed for the recording of highly resolved and unprecedented neutron scattering data of alkalide solutions involving macrocyclic complexant. The generally low small scattering intensity of all

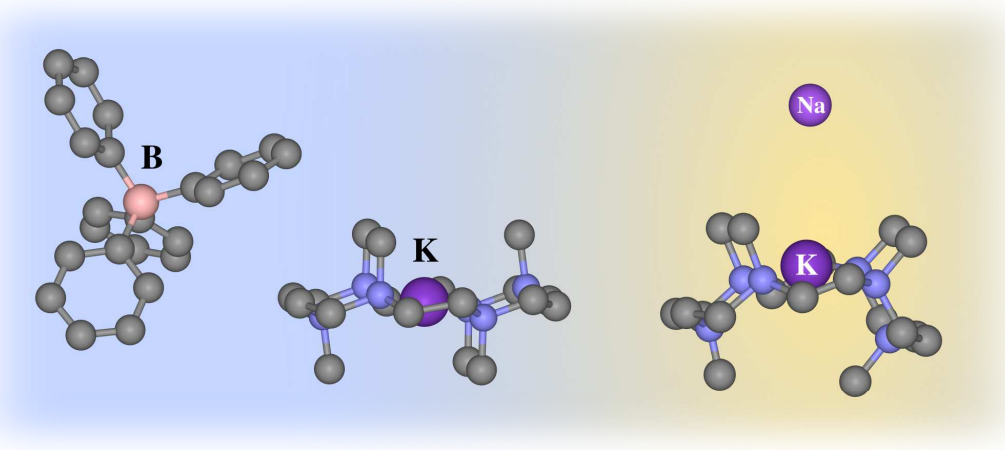


FIGURE 5.8: Crystal structures of **(left)** HMHC(K^+)BPh_4^- (this work) and **(right)** HMHC(K^+)Na^- (reference [31]) with a planar and boat-like conformation of HMHC in its potassium complex, respectively.

samples confirmed the absence of any microscopic phase separation in the metal concentration range of 0.05–0.25 M. An increase in small angle scattering intensity upon metal dissolution in HMHC/THF and its rough quantification by application of the Guinier approximation provided distinct evidence for an increase in particle volume that can be attributed to the formation of ion pairs as a major component in alkalide solutions as opposed to separately solvated ions. The same conclusion was less straightforward to be drawn for the 15C5 system given that an increase in particle size upon sandwich complex formation would result in an increase in scattering intensity in the same order of magnitude. Metal dissolution appeared to generally have a relatively larger effect on the small angle scattering intensity at lower concentrations. Whilst this agreed with the idea of a decreasing association constant at higher electrolyte concentrations, the quantitative evaluation of the acquired data by application of the Guinier approximation alone could not be adduced to support the theory at this point. The simulation of the obtained data using a detailed molecular model in subsequent work might provide a precise characterisation of the structure and dimensions of the alkalide electrolyte, any aggregates, and potentially the nature of interactions between solute and solvent.

5.4 Experimental Aspects

Small angle neutron scattering spectra were collected at the neutron diffractometer NIMROD at the ISIS Neutron and Muon Source Facility, Science and Technology Facilities

Council, Rutherford Appleton Laboratory, Harwell Oxford, U.K.. All samples were prepared by mixing of all components (complexant HMHC (1 eq) or 15C5 (2 eq), $_{d8}$-THF, NaK (3 eq)) in a quartz NMR tube inside an argon glovebox. The samples were immediately sealed using a gas line adapter with valve, removed from the glovebox and frozen at liquid nitrogen temperature after little to no exposure of the metal droplet to the solution for metal-containing samples. The frozen samples were flame-sealed under high vacuum and stored at liquid nitrogen temperature. In preparation for the respective neutron scattering experiment, a sample was warmed to 240 K and it was ensured that the chunk of NaK alloy was fully immersed in the liquid. Further storage at 240 K for 10 h ensured complete metal dissolution up to a point of saturation. This equilibration time was scheduled to be immediately followed by the respective scattering experiment. The saturated samples were placed into a vanadium sheath with a threaded mount in order to allow for the attachment of the sample to the sample stick (see illustrations in Figure 5.9). All mounting steps were carried out while the sample was kept cool and free from solvent in dry ice before the sample stick was inserted into the cryostat of the scattering instrument.

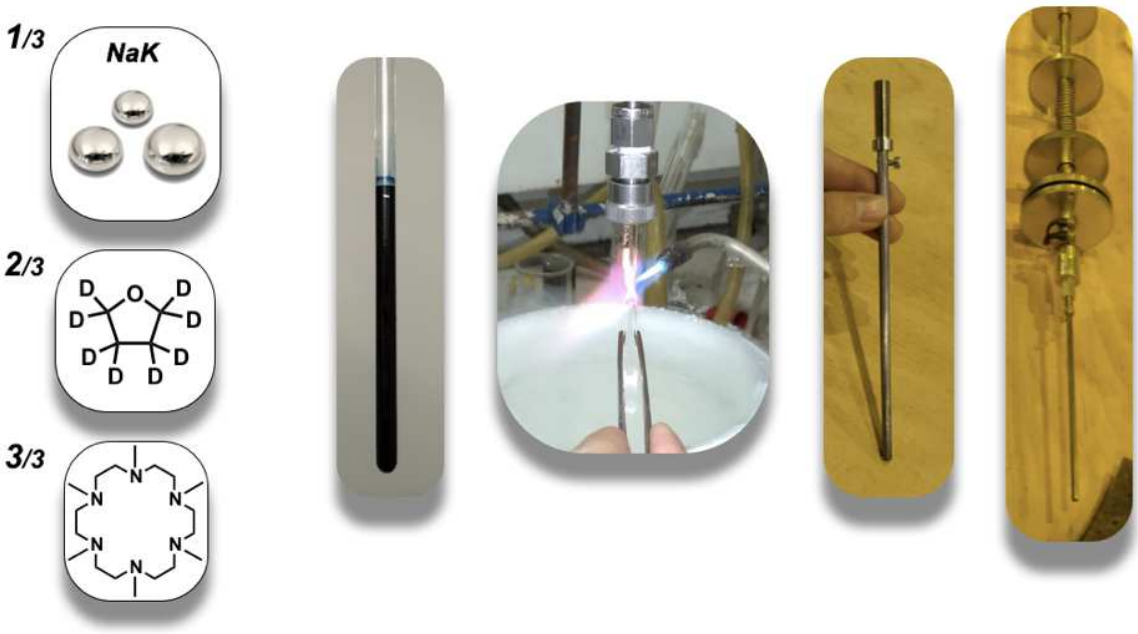


FIGURE 5.9: **Preparation of SANS samples**, from left to right: Three components of HMHC-sample, sample solution in quartz NMR tube, flame sealing of frozen sample under vacuum, vanadium sheath and mount, sample mounted to sample stick of cryostat.

Scattering intensity plots shown in Figure 5.3 and 5.5 were obtained by data processing using GudrunN (software provided by neutron source *ISIS*). Stoichiometric atom ratios were applied as calculated from sample weights/volumes and the scattering intensity was

calculated after the application of direct or iterative corrections for CCR, sample container, and inelastic scattering background, respectively. Density values were precisely determined for all relevant blank solutions (no metal content!) in protiated THF using a 4 place digital *LiquiPhysics*^{TM} *Excellence density meter DM40* over the temperature range of $273 - 303\,\mathrm{K}$. Density values at lower temperatures ($243\,\mathrm{K}, 213\,\mathrm{K}$) were determined by linear extrapolation (see Figure 5.10) and an overview of all values is given in Table 5.3.

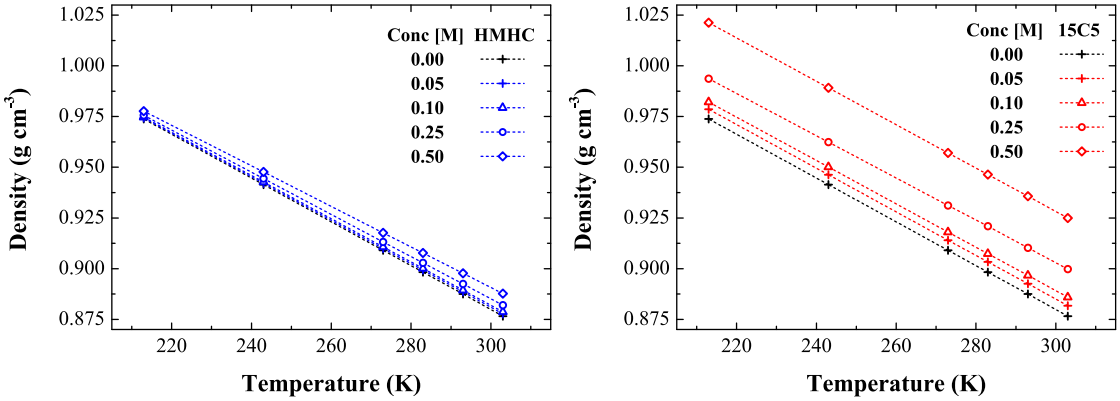


FIGURE 5.10: Temperature-dependent density measurements of blank solutions for SANS correction.

TABLE 5.3: Density of metal-free solutions corresponding to target concentrations of NaK of SANS samples.

Temp	**ρ THF**	**Density ρ [g cm^{-3}] THF/*15C5***			
[K]	[g cm^{-3}]	**0.05 M**	**0.10 M**	**0.25 M**	**0.50 M**
213	0.9738	0.9786	0.9822	0.9937	1.0213
243	0.9414	0.9463	0.9501	0.9624	0.9892
273	0.9090	0.9140	0.9180	0.9311	0.9571
283	0.8983	0.9033	0.9074	0.9209	0.9464
293	0.8875	0.8926	0.8967	0.9103	0.9357
303	0.8766	0.8817	0.8859	0.8998	0.9250

Temp	**ρ THF**	**Density ρ [g cm^{-3}] THF/*HMHC***			
[K]	[g cm^{-3}]	**0.05 M**	**0.10 M**	**0.25 M**	**0.50 M**
213	0.9738	0.9743	0.9747	0.9756	0.9777
243	0.9414	0.9421	0.9427	0.9444	0.9477
273	0.9090	0.9099	0.9107	0.9132	0.9177
283	0.8983	0.8993	0.9001	0.9029	0.9077
293	0.8875	0.8885	0.8894	0.8925	0.8977
303	0.8766	0.8777	0.8787	0.8820	0.8877

Chapter 6

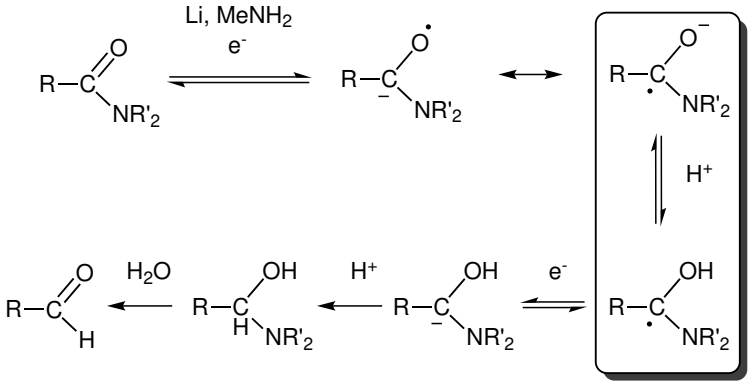
Synthesis and DMR of sterically demanding amides and lactams

6.1 Introduction

6.1.1 Dissolving metal reduction of carboxylic acid derivatives

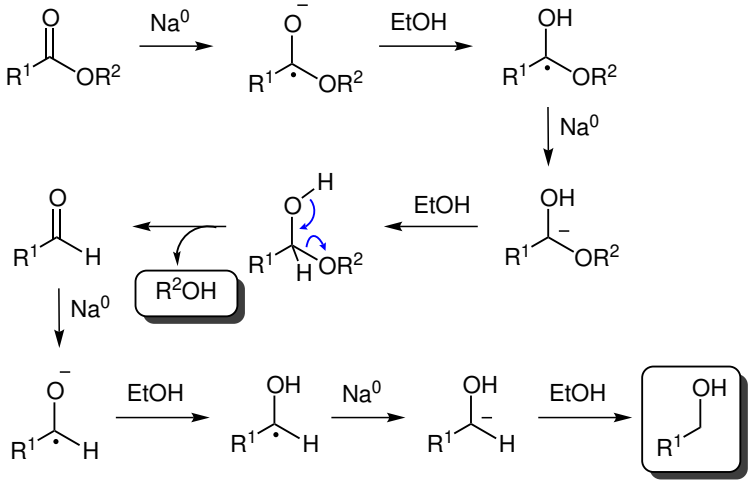
Although metal hydrides have nowadays, to a large extent, replaced dissolving metal systems as reducing agents, the latter were commonly applied to the stereospecific partial reduction of alkynes or the reduction of carbonyl compounds and their derivatives. The simplest dissolving metal reduction media are those formed by dissolution of the metal in small ether or amine solvents, lithium in methylamine having been one of the most frequently employed systems in synthetic chemistry. The mechanism of the reduction of amides was reported to result in the formation of the corresponding aldehydes via a mechanism that takes into account the presence of ethanol as proton source: after an initial electron transfer reaction, the radical anion of the amide carbonyl group is formed. In the presence of a proton donor, the resulting charge is immediately compensated by protonation of the carbonyl oxygen, whereupon the addition of another electron/proton couple leads to the formation of an hemiaminal as depicted in Scheme 6.1. [127, 128]

Similar results are obtained in the case of the reduction of esters in the presence of proton donors. Under *Bouveault–Blanc* reduction conditions, the mechanistic pathway leading to the aldehyde intermediate is analogous to above-mentioned amide reduction: With the charge of the initially formed radical anion being compensated by protonation, the species



SCHEME 6.1: Aldehyde synthesis via electrolytic reduction of amides by a solution of lithium chloride in methylamine in the presence of ethanol.

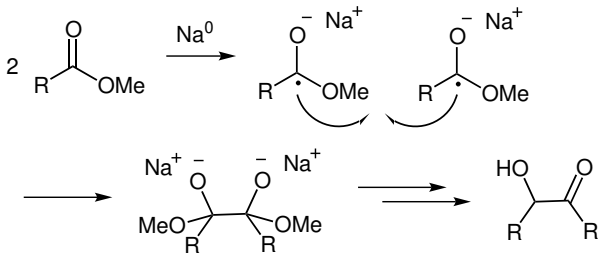
is set up for accepting another electron (its charge is again compensated by protonation) before the resulting hemiacetal undergoes acyl oxygen fragmentation and formation of the aldehyde (see Scheme 6.2). [129–131]



SCHEME 6.2: Mechanism of the Bouveault-Blanc reduction.

In contrast to those more familiar reduction protocols, the introduction of preorganised complexing agents such as crown ethers or cryptands allowed for the dissolution of alkali metals in far less polar and aprotic media. The absence of a proton source during the reduction process enables a longer lifetime of the initially formed radical anion which provides access to entirely different and unusual reaction pathway.

Aprotic conditions are employed in acyloin condensations to achieve the coupling of two radical anions (with their charge compensated by alkali metal cations) and the bond formation between the respective carbon centers (see Scheme 6.3).



SCHEME 6.3: Initial mechanistic steps of acyloin condensation.

This large contrast in reactivity when comparing protic and aprotic reaction conditions provides a high potential for the discovery of novel synthetic transformations and reaction pathways of intermediate species. The development of dissolving metal reductions using aprotic conditions to date is rather modest, however, presumably due to seemingly tedious protocols, comparably high costs of required complexing agents, and a low reliability of synthetic results due to the interference of nucleophilic decomposition products derived from crown ethers.

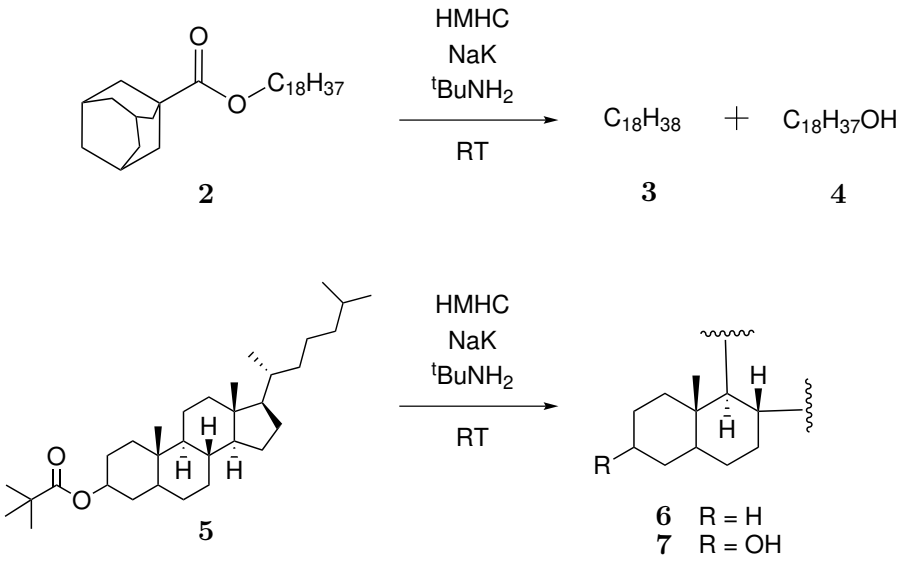
A solution of NaK in 18-crown-6/THF was found to reduce the aromatic system anthracene to the dianion which was inert under the reaction conditions and gave dihydroanthracene by protonation during the workup. In contrast, the reduction in the presence of *tert*-butanol as a proton source gave a complex mixture products due to the possibility of multiple single electron/proton transfer steps. [132]

In contrast to those results, the reduction of benzene by treatment with a solution of NaK and HMHC **1** in benzene in the presence of hydrogen (10 atm) was reported to selectively yield cyclohexene rather than cyclohexane as the final product at a 45% conversion of benzene. Whilst the lower electron affinity of cyclohexene as compared to benzene and a cyclic diene intermediate was used to rationalise the observed high selectivity of this transformation, it does not explain the low conversion of benzene to cyclohexane as the only observed product under the same reaction conditions but in the absence of hydrogen.[133] The latter observation as well as the production of a substantial amount sodium hydride in the presence of hydrogen rather points towards entirely different reaction mechanisms in the presence and absence of the proton source. Further, pure sodium did not show any reactivity under these conditions. This is in accordance with our observation that sodium without addition of a larger alkali metal does not dissolve in solutions of HMHC and THF.

Chemoselectivity between fluoro and vinyl groups in the reduction by toluene radical

anions generated in a system of K/dicyclohexano-18-crown-6/toluene was reported to yield 1-hexene as the major product. When the protic system K/crown ether/diglyme/iPrOH was used, however, the terminal vinyl group was easily saturated, again suggesting a significant difference in the reaction mechanism, namely altering single electron reduction and protonation of the monoanion. [134]

Barrett et al.[29] have demonstrated the formation of an alkalide solution at ambient temperature and its first successful application in revealing novel transformation - in fact, the principal reaction pathway of ester radical anions. Stabilization of the latter in solution of lithium in ethylamine or - even more distinctly - in the entirely aprotic alkalide solution led to a bond scission between the bridging ester-oxygen and the adjacent alkyl-carbon, an unprecedented principal fragmentation of the ester radical anion. A selection of ester substrates reported in the literature were recently prepared and reduced in our laboratories following the respective reported procedures (Scheme 6.4). [87]

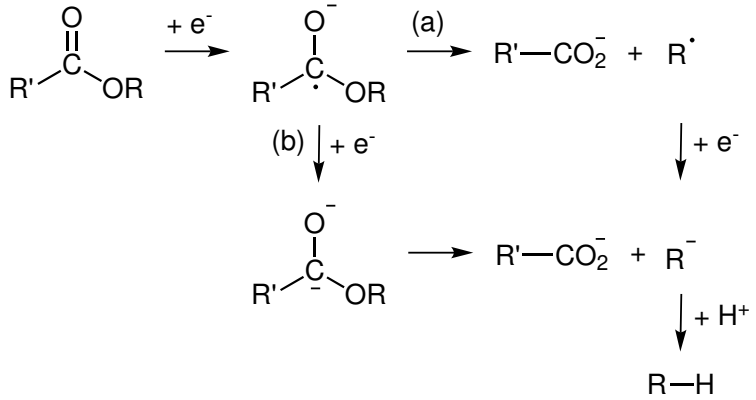


SCHEME 6.4: Examples of successfully reproduced dissolving metal reductions of sterically congested ester groups.

In accordance to literature reports, reduction of adamantyl ester **2** reproducibly gave products **3** and **4** with modest selectivity of 7:3 in favour of the deoxygenated product **3**. The reduction of sterically more demanding pivalic acid ester **5** resulted in a higher selectivity of 4:1 in favour of the deoxygenated product **6** as compared to **7**. This experimental result was rationalised by the effective prevention of competitive deacylation by nucleophilic species such as solvent molecules or charged decomposition products of the complexing

agent. These results were in accordance with the yields reported in the literature and generally corroborated the reliability of the reported novel transformations.

Possible mechanisms were ascribed to the unusual deoxygenation (Scheme 6.5), by which a radical anion is formed in the first step as it is already known from Birch and Bouvault-Blanc reduction mechanisms. In the second step, the radical anion either fragments to give an alkyl radical, which is rapidly reduced to an carbanion, or it is reduced a second time immediately to give a dianion, which then collapses to yield a carbanion and carboxylate anion. Thereby it was confirmed by means of the known rearrangement of the 3α,5α-cyclocholestan-6-yl to the more stable cholest-5-en-3-yl radical, that the deoxygenation occurs predominantly *via* fragmentation of the radical anion (pathway **a** in Scheme 6.5).



Scheme 6.5: Possible mechanisms of deoxygenation of esters in alkali metal solutions. Graphic reproduced from reference [29].

However, the yield of this deoxygenation was found to be limited by the competing deacylation by solvent- or crown ether-derived nucleophiles. The peralkylated aza-crown HMHC **1** was reported to be more resistant to irreversible decomposition than their oxygen analogues because of their lack of somewhat acidic amino protons which are readily attacked by alkali-metal anions or solvated electrons. It was shown that it is feasible to form dark blue solutions from mixtures of potassium, sodium and HMHC, which are stable even at room temperature. The utility of potassium-sodium eutectic solubilised by HMHC in *tert*-butylamine for selective deoxygenation of rather bulky esters was therefore demonstrated.

Even though selectivity in deoxygenation could be significantly improved using HMHC instead of 18-crown-6, the highest selectivity was achieved using sterically hindered esters due to the suppression of the competitive deacylation as mentioned above. Based on the described findings from the reduction of esters under aprotic DMR conditions, we studied the preparation of sterically congested tertiary amides (Figure 6.1) and the reactivity of

this biologically and synthetically highly relevant compound class under aprotic DMR conditions.

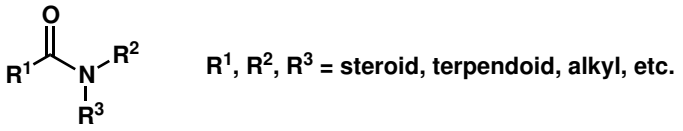


FIGURE 6.1: Sterically demanding tertiary amides as substrates for dissolving metal reduction conditions.

6.1.2 Synthesis and Reduction of tertiary amides and *N*-alkylated lactams

The synthesis of amides is a common task in organic chemistry and received considerable attention of synthetic chemists due to its fundamental importance in the synthesis of biologically active natural products, pharmaceuticals and peptides. The classical synthesis from basic precursors involves reductive amination protocols to access secondary amines that are subsequently converted to amides by so-called amide coupling protocols. Each of those steps summarizing a large variety of synthetic protocols currently available in the literature in order to address the specific properties and reactivity of any substrate, respectively. Popular and widely effective protocols involve 1,1'-carbonyldiimidazole (CDI), 1-Ethyl-3-(3-dimethylaminopropyl)carbodiimide (EDCI), benzothiazole additives, or phosphonium reagents amongst many others.

In spite of the large variety of available reagents that facilitate the formation of the amide bond, the synthesis of targets suitable for dissolving metal reduction studies is not trivial due to unusual mandatory requirements. Firstly, the chosen synthetic route is required to permit a tailored amide construction from different, versatile, and simple precursors. The determination of any selective fragmentation requires a set of tertiary amide substrates with discriminable substituents, especially at the nitrogen center (R_2 and R_3 in Figure 6.1). Those substituents are required to be characteristic entities with respect to stereoelectronics as well as their spectroscopic traces. Hence, combinations of such are not commercially available and therefore to be accessed from simple precursors. Secondly, in analogy to reported ester reduction studies, a sufficient degree of steric shielding of the targetted functionial group by the periphery of the substrate molecules was expected to be crucial in order to prevent interference of side reactions. At the same time however, the desired high steric demand would compound the synthesis itself due to the inhibition

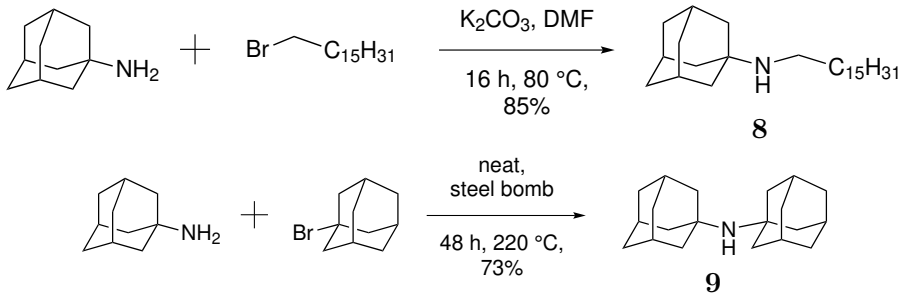
of C-N bond formations *via* common reductive amination and amide coupling protocols. Hence, a thorough assessment of the synthetic accessibility of potential amides substrates was required.

6.2 Results and Discussion

6.2.1 Synthesis of amide and lactam substrates

6.2.1.1 Adamantylamines and -amides

In the first approach to the synthesis of desired sterically demanding mono-functional amides, different synthetic routes to precursor secondary amines from a variety of bulky starting materials were considered. It was envisaged that the highest degree of steric hindrance at the amine/amide nitrogen provides a directly bound tertiary carbon center - a relevant and readily available precursor being 1-amino-adamantane. Various synthetic approaches to *N*-alkylated adamantylamines *via* reductive amination of aliphatic ketones or aldehydes with 1-adamantylamine failed due to a lack of imine formation. Finally, an effective method for the alkylation of 1-adamantylamine turned out to be the reaction of a saturated alkyl halide with 1-adamantylamine under forcing conditions, either neat or using a polar solvent dimethylformamide (DMF) at elevated temperature. This resulted in the formation of desired secondary amines **8** and **9** comprising combinations of tertiary-tertiary and tertiary-primary carbon centers adjacent to the amine/amide nitrogen in good yields as shown in Scheme 6.6.



Scheme 6.6: Alkylation of 1-adamantylamine by treatment with alkyl halides under forcing conditions.

However, this class of substrates suffers from several drawbacks with respect to the desired DMR investigations. Firstly, similar conditions applied to other relevant starting materials such as steroidal or terpinoidal amines and halides resulted in the formation of numerous side products which renders this approach unsuitable for the efficient preparation of a range of compounds with varied substitution patterns. Secondly and more importantly, alkylated adamantylamines were increasingly resistant to acylation under standard conditions with increasing degree of steric hindrance at the amine nitrogen. Diadamantylamine as the most extreme case was entirely resistant to an excess acetyl chloride at elevated temperature

as well as phosgene (Cl – C(O) – Cl) in toluene below room temperature. Lastly, molecular adamantane easily sublimes at room temperature under reduced pressure which exacerbates its quantitative isolation and characterization and consequently renders adamantane as a less suitable substituent of substrates for DMR studies.

6.2.1.2 Camphor nitrimine and derived amines

N-alkylated bornyl-amines comprise a lower degree in steric hindrance at the amine/amide nitrogen. In this potential terpenoidal starting material, the amino group is situated at a secondary carbon center with an adjacent tertiary carbon center and both being included in a rigid bicyclic saturated carbon structure. Although camphor presented similar difficulties as adamantylamine with respect to its transformation *via* reductive amination, imine derivatives are readily accessible from the treatment of camphor nitrimine **10** with primary amines. [135] Camphor nitrimine **10** can be prepared on a large scale by addition of an aqueous solution of sodium nitrate to a solution of camphor oxime in glacial acetic acid. The nitrimine is highly stable and resistant to hydrolysis especially under acidic conditions so that it can be isolated by precipitation from the reaction mixture by the addition of water. Recrystallization from ethanol yields the pure nitrimine. Nucleophilic attack by primary amines in methanol at elevated temperature gives desired imine intermediates. Due to the efficient steric shielding in this case, most imine derivatives can be isolated, dried under vacuum, stored under standard conditions and in some cases recrystallised to obtain crystalline samples. As an example, the crystal structure of *N*-3β-5α-cholestanyl-bornylimine **11** confirms its molecular identity and the structure assignment by spectroscopic footprints (see Figure 6.2).

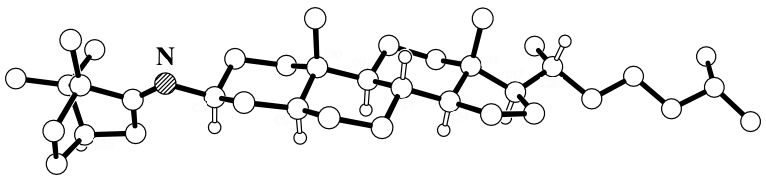
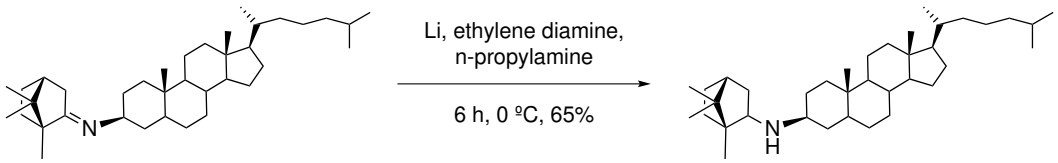


FIGURE 6.2: ORTEP plot of *N*-3β-5α-cholestanyl-bornylimine **11** as determined by X-ray crystallography.

The stability of camphor imines is paralleled by their extraordinary resistance to common reduction methods such as hydride reagents or catalytic hydrogenation protocols. An effective protocol for the subsequent reduction of camphor derivatives to the respective secondary amines was established. The amine **12** was only formed in an acceptable yield

(65%) by treatment with lithium/ethylenediamine in *n*-propylamine followed by aqueous workup (Scheme 6.7). [136] This power of single-electron-reductions with respect to sterically congested substrates will also be employed in the course of our desired dissolving metal reduction of amides as part of this project.



11 **12**

SCHEME 6.7: Lithium/ethylene diamine reduction of *N*-3β-5α-cholestanyl-bornylimine **11**.

Nevertheless, *N*-alkylated bornyl-amines are generally resistant to standard acylations to a certain extent. Formation of the carbamoyl chloride derivative by treatment of the hindered secondary amine with phosgene was envisaged to be a potential alternative. Subsequent exposure to reported [137] alkylation conditions with cyano-Gilman reagents however resulted in elimination reactions and the formation of other byproducts.

6.2.1.3 Formation of stable nitrimines

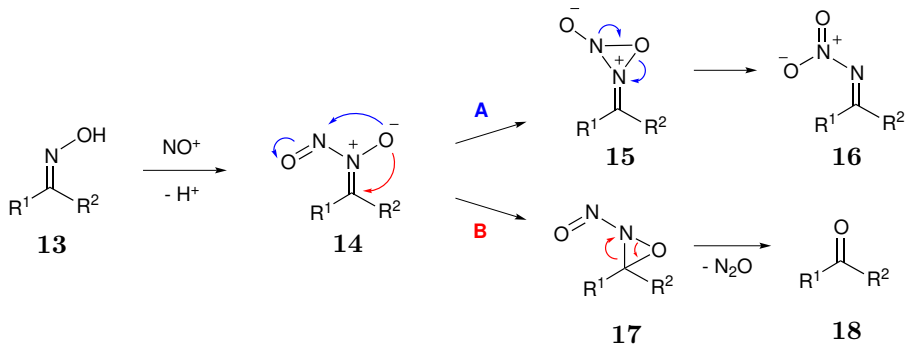
As a result of all findings described above, the most promising method to access a broad range of bulky secondary amines is the amination of nitrimines derived from readily available ketones. The example of camphor nitrimine demonstrated the practicability of this approach. It allows for a large substrate scope whereby the clean reaction conditions render the reaction monitoring and product characterization straightforward. The easy purification of products that are stable to moisture is another advantage since the high molecular weight and low polarity of typical products results in a precipitation directly out of the rather polar reaction medium. However, attempts of subsequent imine reduction and amine acylation with this class of substrates demonstrated that a lower degree of steric hindrance is required to enable the reduction and acylation of all derived imines and amines, respectively. The steric demand of both amine substituent is to be carefully balanced in order to still reach a maximum degree of steric shielding of the functional group to allow for an efficient and reproducible study of its reduction under dissolving metal reduction conditions.

There are only few nitrimine derivatives reported [138] in the literature. That is not surprising considering that this highly electrophilic and therefore easily hydrolysed species

is only stable in the case of sufficient steric shielding of the electrophilic center. A high degree of substitution at the carbon centers adjacent to the electrophilic center was reported to be essential. Of course, this is the case for 2-adamantyl derivatives as well as nitrimines with an adjacent tert-butyl group. Synthetically relevant for our studies are the reported nitrimines derived from camphor and related terpenoidal structures as well as those derived from steroids.

Likewise, only a limited number of conditions for the preparation of nitrimines from ketone precursors are reported in the literature with the nitrosation of the respective oxime – frequently in a biphasic system - being the most widely applied method. Exact protocols reported for different substrates together with their respective stability are discussed in the following and presented in conjunction with synthetic routes to secondary amines and corresponding precursors as well as practical considerations.

Treatment of oximes with nitrous acid can result in *O*-, *N*- or *C*-nitrosation. O- and *N*-nitrosation of oximes - frequently observed for steroidal and terpenoidal substrates and leading to synthetically useful nitrimine derivatives – occurs by the electrophilic attack of the oxime by the nitrosyl cation (NO^+). According to an initial mechanistic proposal as depicted in Scheme 6.8, *N*-nitrosation of oxime **13** would form nitrosonitrone **14** which was considered to be responsible for the usually observed coloration of the reaction mixture. Intramolecular cyclization of **14** following reaction pathway A would then give the three-membered ring intermediate **15** which would rearrange to the desired nitrimine **16**.



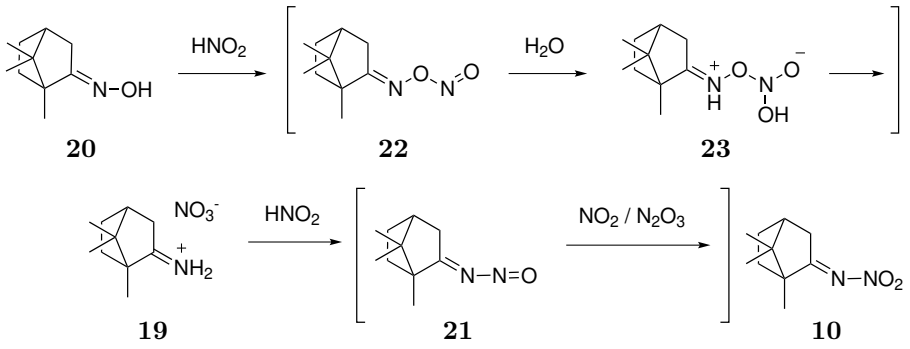
SCHEME 6.8: Mechanism of *N*-Nitrimine formation (pathway A, blue) and deoximation (pathway B, red) via *N*-nitrosation of oximes.

Following this mechanistic proposal, a possible decomposition pathway is accessible from intermediate **14** by *C*-cyclisation *via* the three-membered ring intermediate **17**[139] leading to the respective ketone derivative **18** which we indeed observed as a major byproduct. The intensity of this side reaction is dependent on the substrate – more precisely on the

steric hindrance of the electrophilic carbon - and can significantly lower the yield of the desired nitrimine.

However, the mechanism of the nitrimine formation was reviewed later which resulted in the report of a different mechanistic proposal - outlined in Scheme 6.9 - supported by convincing evidence. [140] The authors noted that *Ferdinand Tiemann*[1] reported in 1895 the isolation of the camphor imine nitrate salt **19** upon treatment of camphor oxime **20** with only a single equivalent of nitrous acid. [142] Similar protocols for such preparation were also reported later. [143] Subjecting camphor imine to the same nitrosating conditions, *Adamopoulos et al.* [140] found that the color is produced more rapidly, and in greater intensity compared to the preparation of the nitrimine from the oxime, the products being identical in both cases. It was therefore argued that nitrimines are formed via the key intermediates as outlined in Scheme 6.9 with the involvement of the colored nitrosoimine **21**.

Indeed, the proposed mechanism matches our own observation that upon dropwise addition of acid to the biphasic mixture, coloration only occurs after exposure of the oxime to a significantly larger amount of nitrous acid (generated *in situ*) than one equivalent. Formation of the ketone derivative as the major byproduct can thereby be envisioned from cyclization reactions and the hydrolysis of several depicted intermediates especially considering the transformation is carried out in a biphasic reaction mixture.



SCHEME 6.9: Reported mechanism of camphor nitrimine formation from the oxime derivative. [140]

As mentioned above, the stability of nitrimines appears to correlate with the steric shielding of the electrophilic carbon center in the first approximation. Contributing factors are the surrounding intramolecular structure as well as the degree of substitution at directly

[1] Johann Karl Wilhelm Ferdinand Tiemann, 1848-99, German chemist, development of Reimer-Tiemann-reaction (see commendaces to Ferdinand Tiemann in reference [141])

adjacent carbon centers with the latter being put most emphasis on in the literature. *Barton et al.* reported one of the most stable nitrimines **24** known to date showing resistance to hydrolysis in refluxing aqueous sulfuric acid/dioxane solution. [144] Its exceptional stability can be assigned to the efficient shielding of the electrophilic center by the surrounding framework (see Figure 6.3), the incorporation in a large crescent-shaped structure with the only neighboring carbons constituting a tertiary center at the fusion of two cyclohexane rings. Similar arguments regarding the degree of substitution at adjacent carbon centers hold true for the terpenoidal derivatives fenchone nitrimine **25** and the above-mentioned camphor nitrimine **10** both of which are stable and isolatable representatives of this class of electrophiles.

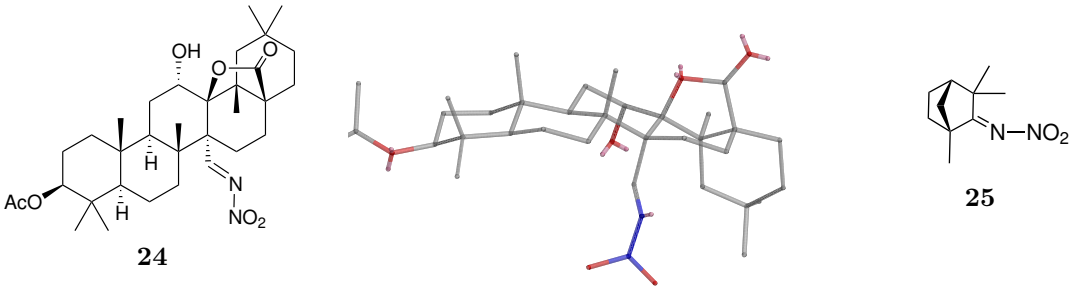


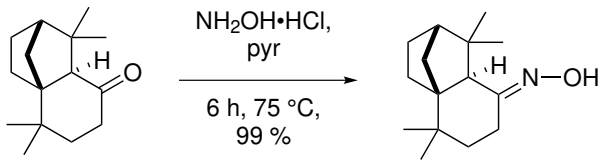
FIGURE 6.3: Stable nitrimines derived from cincholic acid (**(left)** Molecular structure and **(center)** 3-dimensional model) [144] and **(right)** fenchone. [135]

Both the electrophilic nitrimine derivative and a primary amine as the nucleophile represent the final *N*-substituents at any amide substrate to DMR studies. A suitable choice of substituents of the secondary amine as precursor of the target amides is crucial since it is those substituents which are expected to be deaminated upon fragmentation of the amide radical anion. As mentioned above, a bulky environment surrounding the amide bond is essential in order to prevent deacylation of the amide by competing nucleophilic attacks and the resulting decreased predominance of the desired radical fragmentation. Hence, desired amine precursors would possess at least one secondary or tertiary carbon center directly attached to the amine nitrogen. The selectivity of the radical fragmentation can be studied if this center is combined with another primary, secondary or tertiary carbon center as the second amine substituent. Hence, we aimed to access a suitable range of secondary amine precursors by reacting synthetically accessible and sufficiently stable nitrimines with a range of primary amines which are considered suitable according to above-mentioned criteria. Specifically, the large molecular weight and characteristic spectroscopic footage of steroids and terpenoids render their quantification and identification

as fragments cleaved during DMR reactions straightforward.

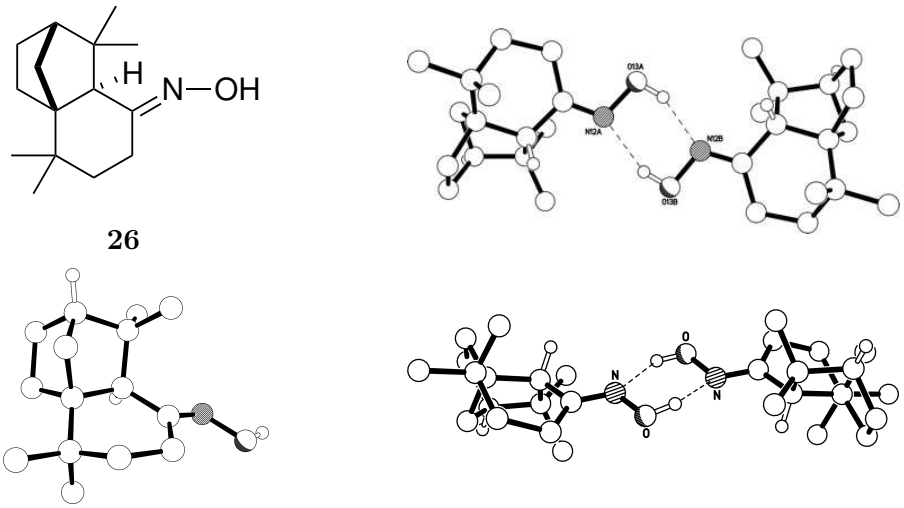
6.2.1.4 Isolongifolanone nitrimine synthesis and characterization

The isolongifolanyl fragment was considered as a suitable amide substituent due to both its appropriate steric demand and its unique spectroscopic footage. The oxime derivative **26** was prepared quantitatively by treatment of the commercially available crude ketone **27** (unknown mixture of isomers) with hydroxylamine hydrochloride in hot pyridine (Scheme 6.10). In the light of a complicated NMR spectroscopic signature, structural confirmation was achieved by X-ray crystallography of a crystalline sample obtained by careful recrystallization from hexane (see Figure 6.4). The assessment of the sample indicated a significant enantiomeric excess in the crude ketone starting material. Different types of crystals were identified representing racemic (Figure 6.4, bottom right) and enantiomerically pure (Figure 6.4, top right) samples, respectively. Both structures showed strong hydrogen bonding within oxime dimers as the predominant structure determining factor. Unfortunately, exposure of the obtained material to various nitrosation conditions only resulted in the recovery of the ketone which suggests that any nitrosoimine or nitrimine intermediates are too sensitive to hydrolysis so as to allow for isolation or any controlled treatment with amine nucleophiles *in situ*. Hence, the effects of the enantiomeric excess on the yield of subsequent synthetic steps was not further explored.



27 **26**

SCHEME 6.10: Isolongifolanone oxime **26** formation from crude ketone starting material.



26

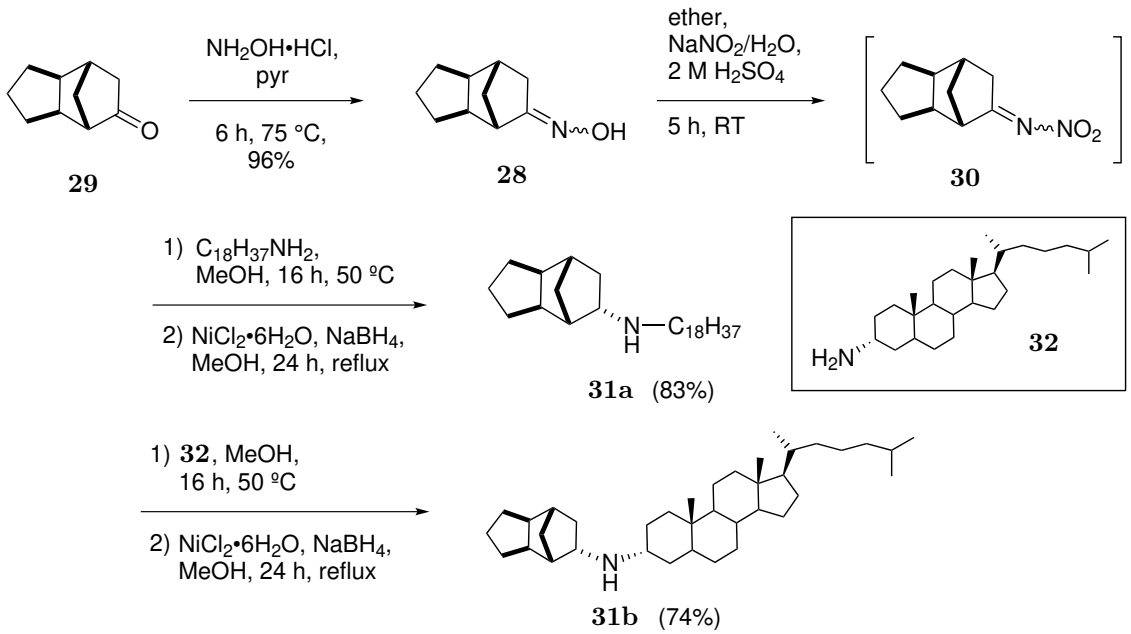
FIGURE 6.4: **Structure confirmation of isolongifolanone oxime 26.**
(left) Drawing (top) and ORTEP plot (bottom) of isolongifolanone oxime monomer **(right)** ORTEP plots of hydrogen bonded dimer pairs in enantiomerically pure (top) and racemic (bottom) sample of isolongifolanone oxime.

6.2.1.5 8-Nitrimino-tricyclodecane and derived amines

An expectedly less stable terpenoidal nitrimine derivative as compared to camphor nitrimine **10** was envisaged to be accessible by nitrosation of 8-tricyclodecanone oxime **28**. Possessing no tertiary carbon center adjacent to the carbonyl carbon, its imine and amine derivative is sterically more accessible for subsequent transformations. For the same reasons, however, the corresponding nitrimine was expected to be less stable and the collapse to the original ketone **29** favourable.

The oxime derivative **28** was prepared almost quantitatively by treatment of the racemic ketone **29** as obtained from the supplier with hydroxylamine hydrochloride in hot pyridine (see Scheme 6.11) and triturated with hexane to obtain the pure racemic mixture as a beige solid. The nitrimine derivative **30** was prepared *in situ* by nitrosation of **28** in a biphasic ether/water system [145] with subsequent neutralization and washing of the organic solution. The identity of the nitrimine could be confirmed by infrared and ^{13}C NMR spectroscopy due to the characteristic signature of those species (^{13}C NMR ($CDCl_3$) δ 186 ppm; IR (ATR) 1650 (C=N), 1561, 1312 (NO_2) cm^{-1}). Due to its high sensitivity to nucleophiles, nitrimine **30** was used *in situ* and converted in subsequent synthetic steps either in ethereal solution as obtained from the synthesis or after a change of solvent to dry methanol. Analogously, careful removal of the solvent under inert gas and re-dissolution in deuterated chloroform allowed for its spectroscopic characterization.

With the solution of nitrimine **30** in hand, two desired secondary amines **31a** and **31b** were readily prepared by addition of respective primary amines and subsequent *in situ* reduction of the corresponding imine intermediates using a catalytic hydrogenation protocol with nickel boride at elevated temperatures (Scheme 6.11). [146, 147] The primary amine 3(a)-amino-5(a)-cholestane **32** as required for the synthesis of **31b** was prepared from 5(a)-cholestan-3(b)-ol by conversion to the respective alkyl azide **33** via Mitsunobu reaction involving diphenylphosphoryl azide [148] and subsequent reduction using $LiAlH_4$. [149] The conversion of nitrimines was found to generally yield simple crude mixtures for a large scope of primary amine nucleophiles. Hence, the obtained secondary amines were typically used as the crude mixtures in the next step which allowed for a more efficient synthetic throughput including a straightforward purification of the desired targets as will be described further below.



SCHEME 6.11: Synthesis of tricyclodecane-derived secondary amines.

6.2.1.6 6-Nitrimino-cholestane and derived amines

A number of cholestane-derived nitrimines are reported in the literature, including 5α-cholest-2-one nitrimine, 5α-cholest-4-one nitrimine and 5α-cholest-6-one nitrimine **34** (see Figure 6.5). [150] The latter is synthetically accessible on a reasonably large scale from the

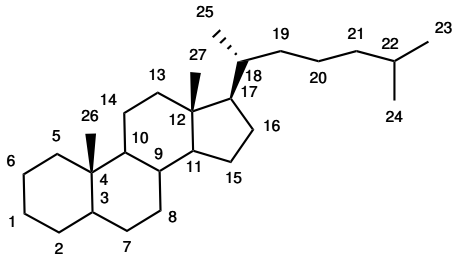
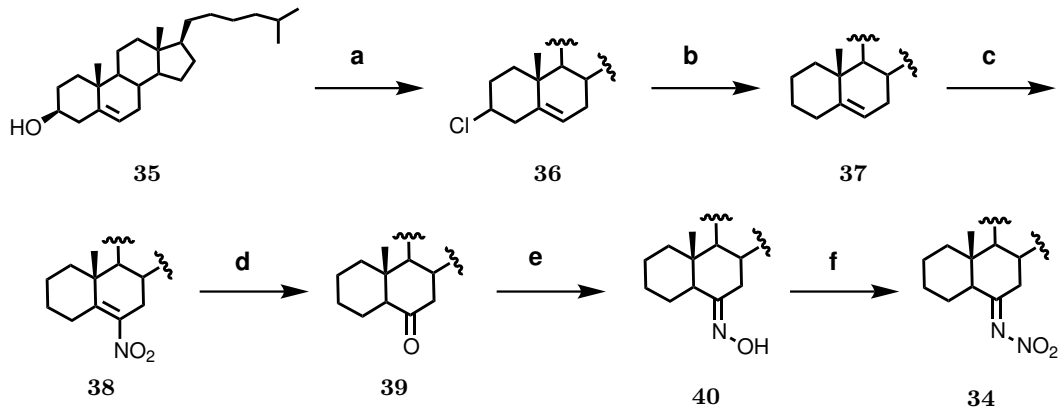


FIGURE 6.5: Numbering of atoms in cholestane core.

cheap commercially available starting material
cholesterol *via* seven steps (Scheme 6.12). [151,
152] Treatment of cholesterol **35** with thionyl chloride and subsequent reductive dehalogenation of cholesteryl chloride **36** by exposure to sodium in boiling isoamyl alcohol readily furnished 5-cholestene **37**. [153] The latter was nitrated with freshly distilled fuming nitric acid in a moderate yield. [152] 5-Nitro-cholest-5-ene **38** was then reduced and hydrolysed by treatment with zinc dust in dilute boiling acetic acid to give 5α-cholest-6-one **39** in 75% yield. [154] The oxime derivative **40** was readily available by treatment with hydroxylamine hydrochloride and sodium acetate in boiling ethanol. [152] All intermediates **36-39** were purified by recrystallization which renders the established synthetic pathway very convenient. Finally, the desired steroidal nitrimine derivative **34** was prepared by nitrosation of the oxime **40** and purified by column chromatography and recrystallization. [145] This ensures a clean conversion to desired imines and amines in subsequent synthetic steps



SCHEME 6.12: Synthesis of 6-nitrimino-5α-cholestane **34**. *Reagents and Conditions*: (a) $SOCl_2$, 2 h, RT, 94%; (b) Na, isoamyl alcohol, 4 h, reflux, 92%; (c) HNO_3, 2 h, $-5 \rightarrow 10\,^{\circ}C$, 45%; (d) Zn dust, AcOH, H_2O, 4 h, reflux, 75%; (e) $NH_2OH \cdot HCl$, NaOAc, EtOH, 1 h, reflux, 95%; (f) ether, $NaNO_2/H_2O$, 2 M H_2SO_4, 6 h, RT, 70%.

The stability of nitrimine derivative **34** is comparable to that of camphor nitrimine **10**. Recrystallization of **34** from methanol yielded a sample suitable for X-ray crystallography which confirmed the molecular identity that was predicted based on the infrared spectroscopic trace of the material. The obtained structure is shown in Figure 6.6. The identity of the nitrimine containing the $N{=}NO_2$ group is clear whereby the close proximity of the steroidal A-ring leads to the shown major stereoisomer. The chair-like conformation of the steroidal six-membered rings causes the nitrimine group to point out of the plane corresponding to the steroidal core. Together with the shielding effect of the methyl group in close proximity, this renders the two faces of the nitrimine group being distinguished in

their approachability with respect to nucleophiles employed in subsequent synthetic steps. This, in turn, results in the preferential formation of certain imine isomers as well as preferential formation of certain amine configurations upon reduction of the imine precursors, finally allowing for the accumulation of specific amide isomers.

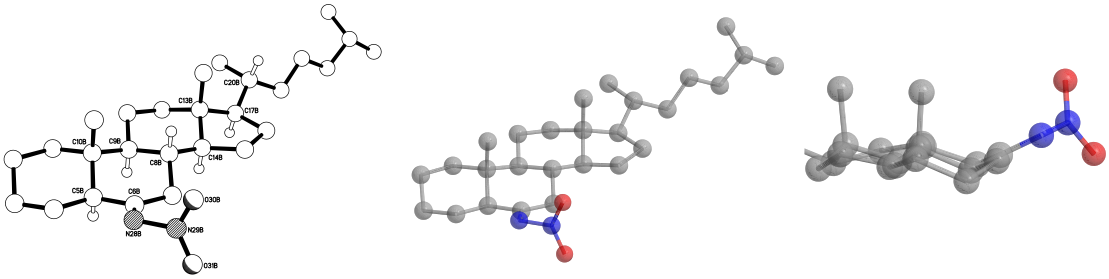
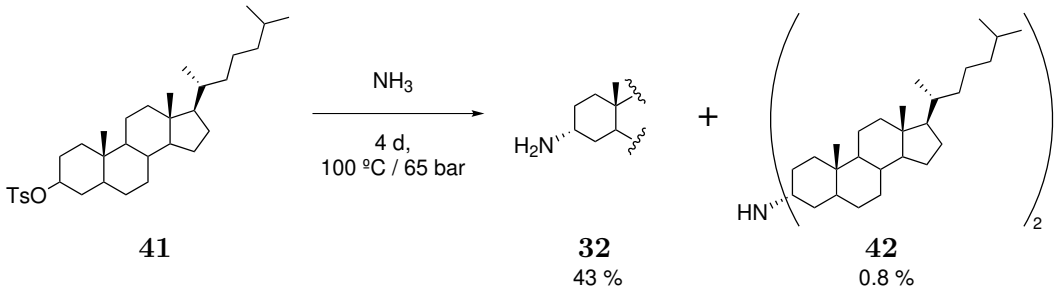


FIGURE 6.6: **(left)** ORTEP plot, **(center)** corresponding three-dimensional representation, and **(right)** side view of key intermediate 6-nitrimino-5α-cholestane **34**.

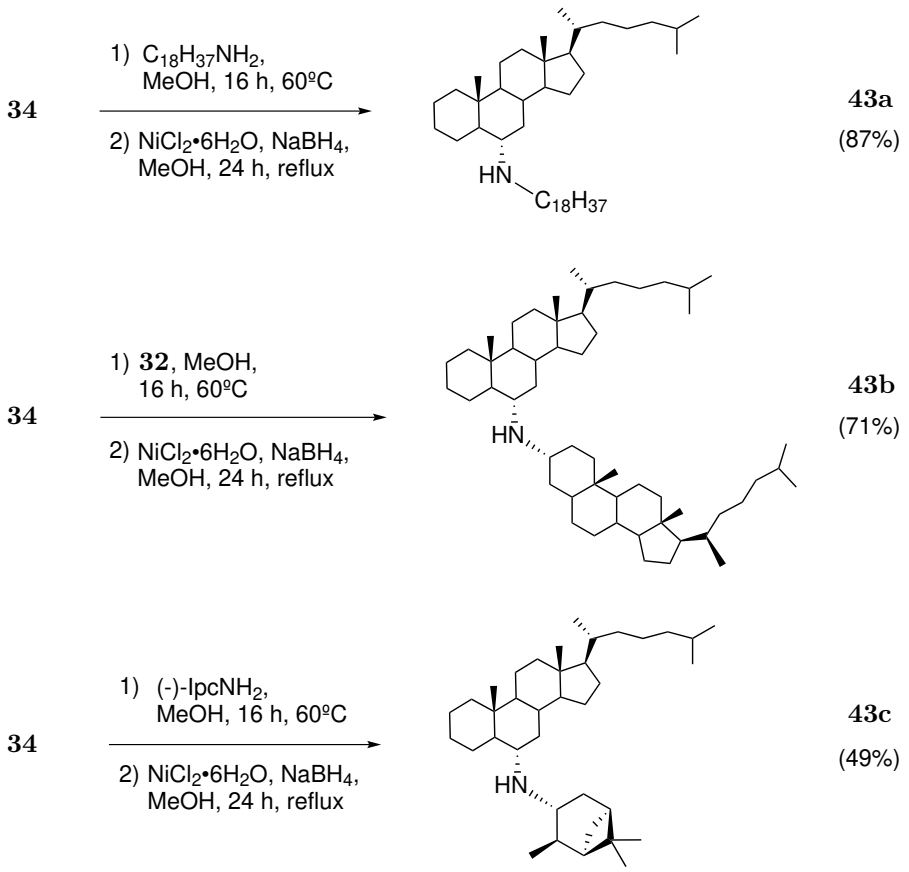
Bulky secondary amines derived from the steroidal nitrimine **34** include the sterically very demanding class of disteroidal amines. The link of two steroidal secondary carbon centers by one nitrogen atom was expected to be particularly challenging due to the exceptional steric bulk surrounding the reactive center. To the best of our knowledge, the only reported synthesis of a disteroidal amine involves dialkylation of ammonia by treatment of tosylated 5α-cholestan-3β-ol **41** under harsh conditions (high temperature and pressure) to yield di(5α-cholestan-3α-yl)amine **42**. [155] Although the reported results were reproducible on a general basis as outlined in Scheme 6.13, the synthetic approach was found to be impractical due to the requirement of an extensive workup (see reference [155]) and the low yield of this transformation (< 5 %) which necessitates resubmission of the major product **32** to the reaction conditions to achieve acceptable yields.



SCHEME 6.13: Synthesis of dicholestanylamine by treatment of ammonia with tosylated 5α-cholestan-3β-ol.

All target secondary amines **43a-43c** were prepared following the above-mentioned protocol for the formation and immediate reduction of imines derived from 8-tricyclodecanone

29. Due to the lower solubility of steroidal derivatives as well as the higher stability of the steroidal nitrimine **34**, steroidal imine derivatives and the related amine targets **43a**-**43c** were prepared at higher temperatures and longer reaction times, respectively, as shown in Scheme 6.14.

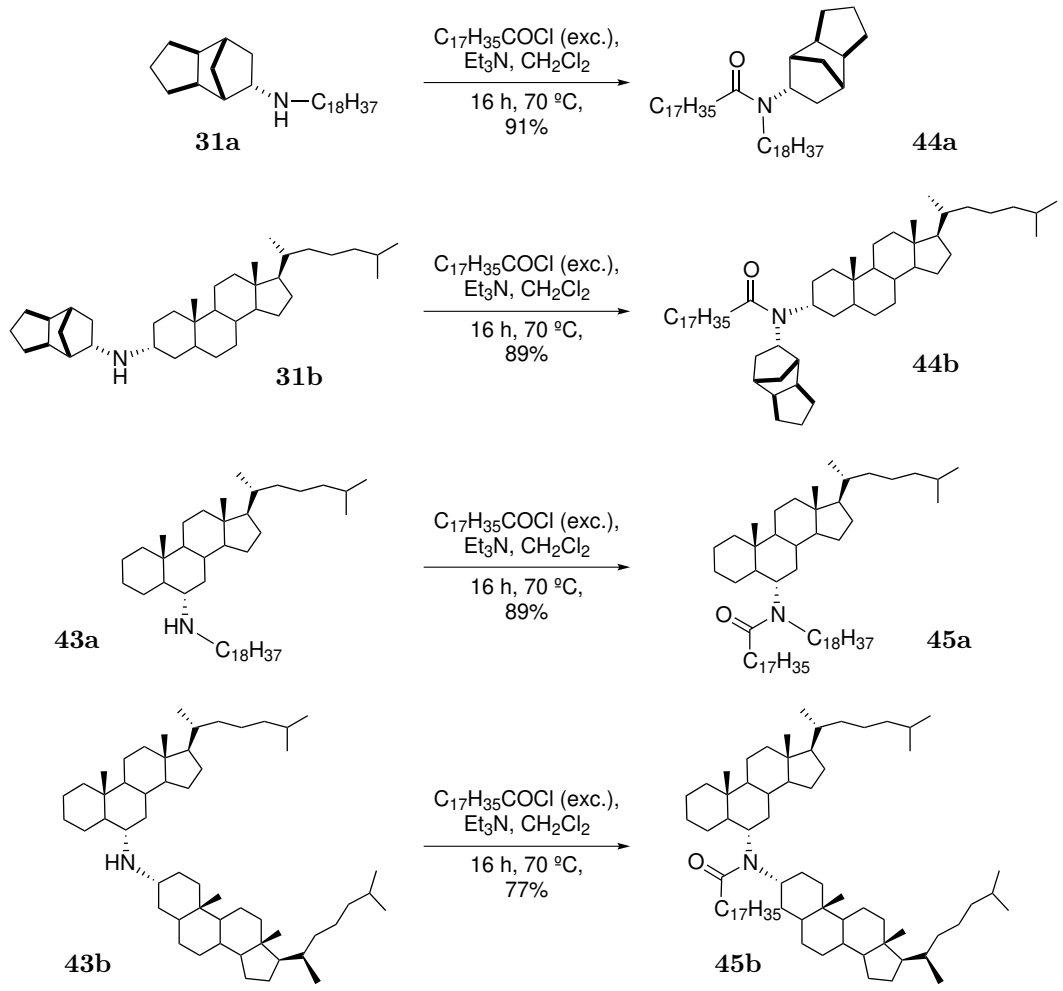


SCHEME 6.14: Synthesis of cholestane-derived secondary amines.

6.2.1.7 Acylation of sterically demanding secondary amines

As discussed above, the steric demand of secondary amines and was balanced in order to allow for the desired *N*-acylation whilst reaching a maximum degree of shielding of the amide bond in the target DMR substrates. To our satisfaction, acylation tests using an excess of acetyl chloride under basic conditions at elevated temperatures did result in amide formation with yields higher than 70%. The obtained mixture of stereoisomers and rotamers for a given amide derivative was readily isolated from any byproducts by column chromatography. Accordingly, purified amines **31a** and **31b** as well as **43a** and **43b** were converted to the respective amides **44a** and **44b** and **45a** and **45b** by treatment with stearoyl chloride under the previously established forcing conditions (Scheme 6.15). Additional targets **44c**-**44e** were prepared from **28** without intermediate purification as shown

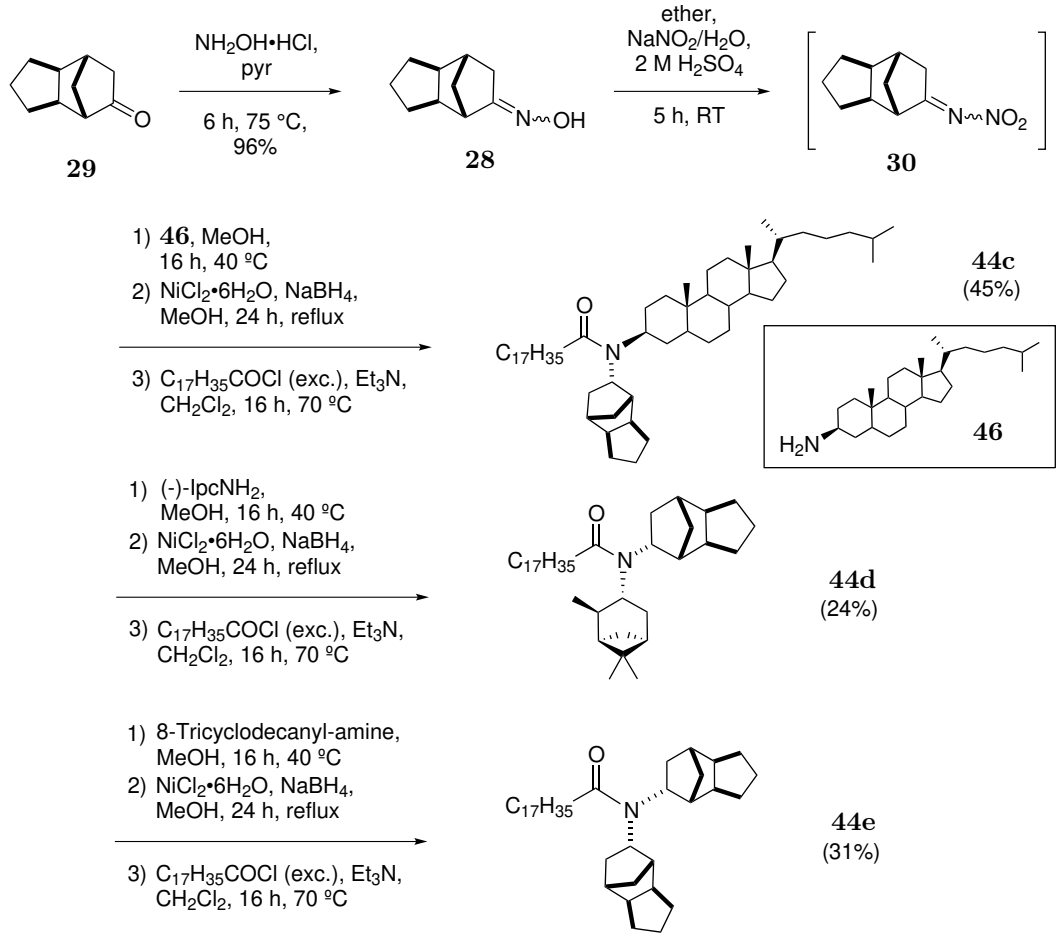
in Scheme 6.16 below. The primary amine 3β-amino-5α-cholestane **46** as required for the synthesis of **44c** was prepared from 5α-cholestan-3β-ol by conversion to the corresponding epimeric alkyl bromide **47** via Appel reaction using carbon tetrabromide, transformation to the alkyl azide **48** with the desired 3β-configuration by treatment with sodium azide [156] and subsequent reduction using $LiAlH_4$. [149] Purification by column chromatography gave highly pure amide substrates the identity of which was confirmed by complete spectroscopic characterization including mass spectrometry, NMR, and IR spectroscopy. Needless to say, a high purity of target amide materials was crucial to ensure reliability and reproducibility of any results during subsequent DMR studies.



SCHEME 6.15: Synthesis of selected sterically congested tertiary amides by acylation of *N*-8-tricyclodecanyl and *N*-6-cholestanone amines.

6.2.1.8 NMR characteristics of sterically demanding tertiary amides

NMR spectroscopy undoubtedly represents an essential tool for synthetic chemists to visualize relationships between constituents of a molecular structure and ultimately reveal the



SCHEME 6.16: Synthesis of sterically congested tertiary amides from 8-tricyclodecanone without intermediate purification.

latter in its entirety including any stereochemical peculiarities. Thereby, classic organic chemistry especially benefits from the probing of the very fundamental building blocks of its molecular entities by ^{1}H and ^{13}C NMR spectroscopy. The syntheses of this work relied on those powerful methods as they allowed for the spectroscopic isolation of the relevant constituting atoms from the bulk and spectroscopically irrelevant periphery of the prepared targets. First and foremost, however, the applicability of this method to validate any synthetic outcome is directly linked to the visibility of the nuclei of interest. As for alkali metal NMR spectroscopy discussed above, chemical exchange processes can hamper the detection of involved nuclei if the respective exchange rate happens to be on the order of magnitude of the difference in chemical shift of the exchanging species. The consequence is coalescence line broadening and blurring of any signal multiplicity as well as a change in chemical shift. Additional line broadening occurs for nuclei of large molecules as the relatively slow molecular motion leads to an efficient spontaneous spin relaxation

due to the long correlation time of transient magnetic fields. All of those combined factor can render obtained NMR signals less informative, both in ^{1}H and ^{13}C NMR spectra. The presented monofunctional amides show extraordinary NMR spectroscopic characteristics for a number of reasons. The intentionally large steric demand efficiently hinders the rotation of rigid substituents at the nitrogen center around the C–N bond. The chiral nature of the majority of used substituents automatically renders rotamers diastereoisomers with potentially large differences in the chemical shift values of their constituting nuclei and exchange broadening effects as described above. Furthermore, it is the very nature of the resonance between the nitrogen lone pair and the carbonyl π bond of the amide group to generate a energetic barrier of rotation around the C(O)–N bond due to its double bond character C(O)=N. In the present case, this rotational barrier is further increased by steric hindrance. To provide evidence for the intended steric hindrance of the prepared amides and to gain a better understanding of their NMR characteristics, the effect of the described phenomena on the ^{1}H NMR spectra was demonstrated by varied temperature studies in the high-boiling solvent d_8-toluene. Figure 6.7 compares the ^{1}H NMR spectra of selected amides at elevated temperatures with their cryptic room temperature spectrum, respectively, in the chemical shift range relevant to amide-related signals. In all cases, the resolution of relevant signals was significantly improved at 100 °C as the temperature range with coalescence line broadening effects was exceeded. Amide **44c** gives two characteristic multiplets at δ 3.88 and 3.10 ppm of its two different 2° carbon center substituents, respectively, without any indication of exchange between different amide bond rotamers. In contrast, amide **44a** shows different sets of multiplets for exchanging amide bond rotamers with significantly different population in the equilibrium at elevated temperature. This can be rationalised by lower rotational barriers due to the presence of the aliphatic C_{18} chain as a smaller 1° carbon center substituent. The difference in degrees of freedom between 1° and 2° carbon center substituents is demonstrated by amide **45a**. The diagnostic signal of the steroidal substituent at δ 5.32 ppm only experienced a change in chemical shift with increasing temperature while a complex and unresolved splitting was resolved to a single diagnostic multiplet at δ 3.38 ppm for the alkyl substituent at elevated temperature. It should be noted that all target amides were distinctly identified by mass spectrometry and IR spectroscopy.

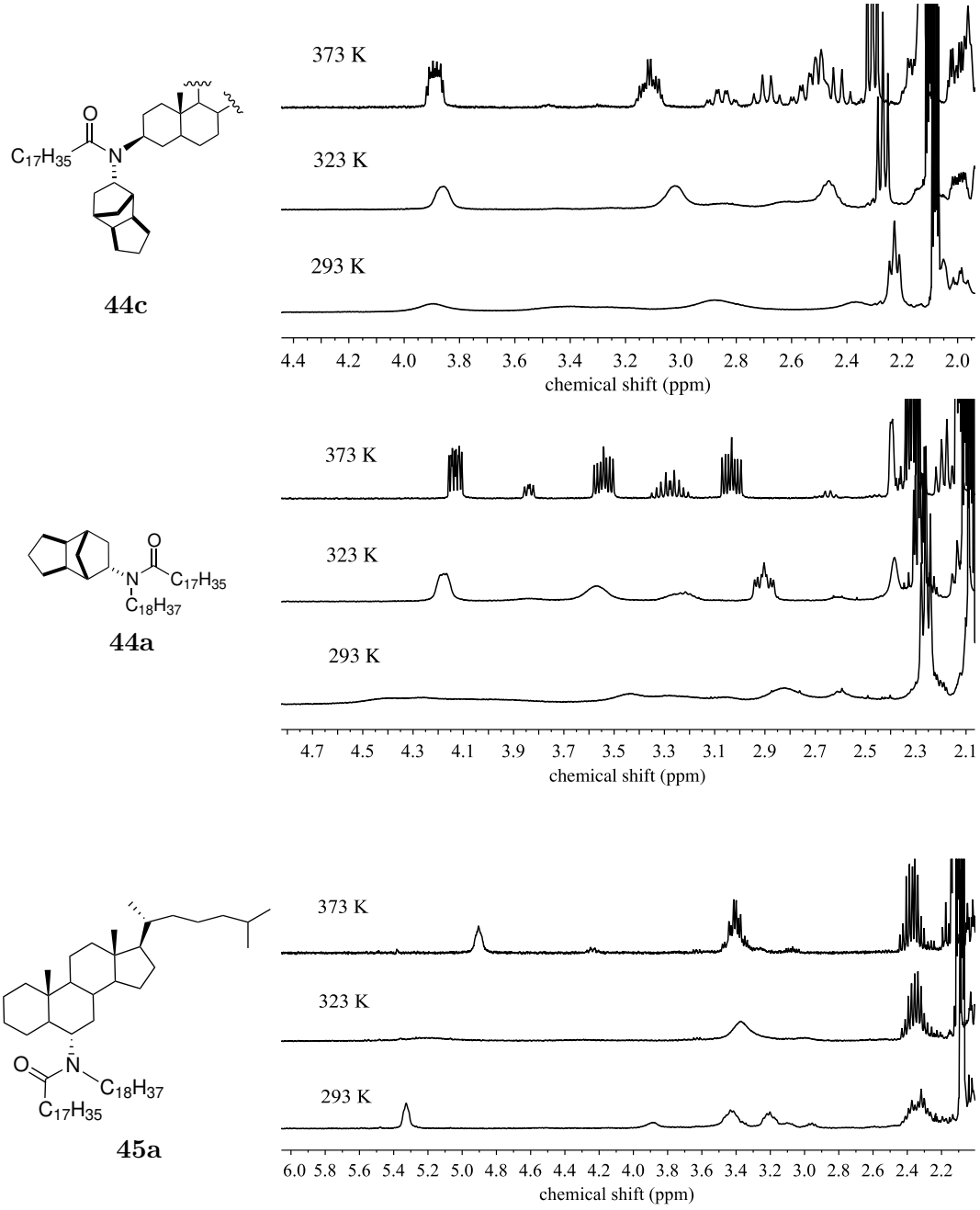
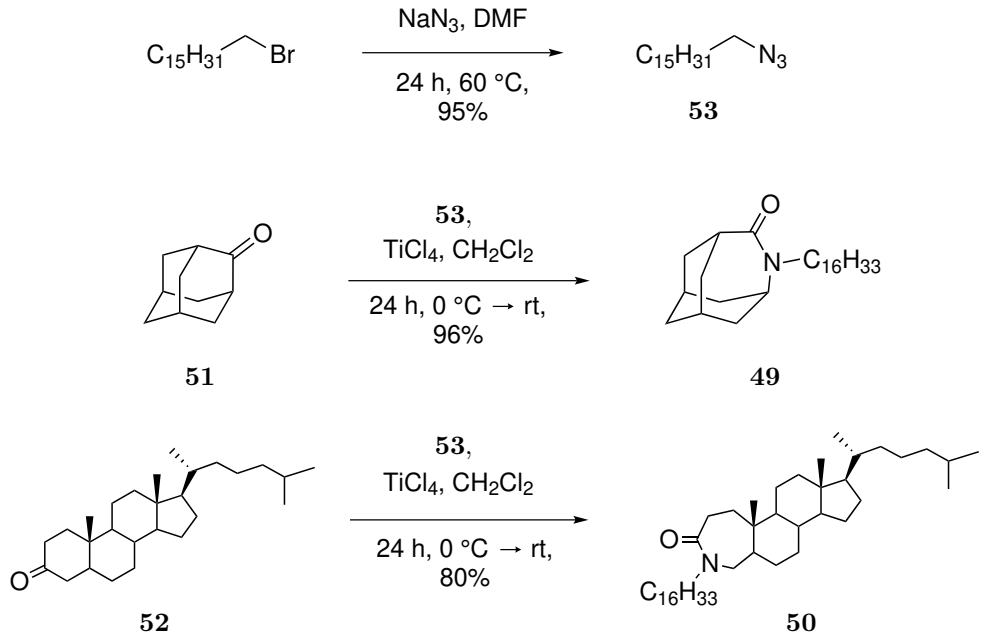


FIGURE 6.7: VT-NMR spectra of selected tertiary amides in d_8-toluene.

6.2.1.9 Synthesis of *N*-alkylated lactams

Lactams represent a related class of interesting substrates as the functional group is integrated in a rigid ring system which still provides a reasonable degree of steric shielding. Suitable DMR substrates **49** and **50** were readily prepared by treatment of the ketone precursors 2-adamantanone **51** and 5α-cholestan-3-one **52** with 1-azidohexadecane **53** under Schmidt reaction conditions (Scheme 6.17).



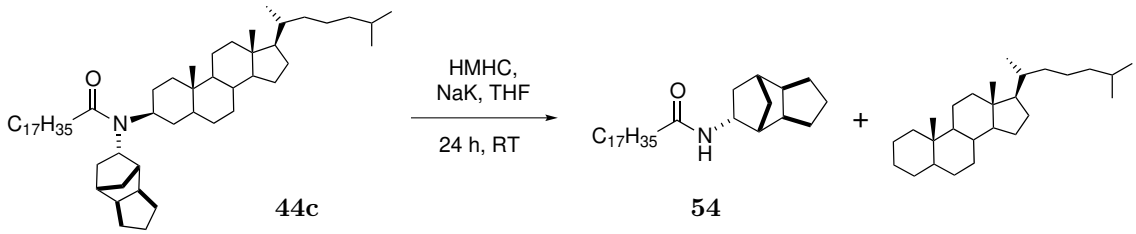
SCHEME 6.17: Synthesis of lactams by Schmidt reaction of ketone precursors and an alkyl azide.

6.2.2 Dissolving metal reduction of tertiary amides and lactams

All amides and lactams were subjected to identical DMR conditions (details described in the experimental section). An alkalide solution using a large excess of HMHC **1** and NaK as compared to the amount of DMR substrate was prepared in THF at 0 °C. To this mixture, a 50 mM solution of the respective substrate in dry THF was added dropwise *via* a syringe at such a rate as to maintain a blue solution. It is noteworthy that initial DMR attempts were performed using alkalide solutions in *tert*-butylamine following the literature procedure of ester reductions. [29] However, the alkalide mixture adopted the characteristic blue color only very slowly and every addition of two drops of substrate solution completely decolored the metal solution. This indicated that the alkalide concentration in the equilibrated metal solution in *tert*-butylamine is not high enough to allow for a reliable conduction of the experiment. The conversion of the target amides during

initial tests at temperatures below 0 °C is impractically slow. Therefore, the mixtures were allowed to warm to room temperature while stirred for 20 hours. After separation of the crude mixture from excess NaK, it was quenched by addition to wet ether and inorganic salts were removed by sequential washing with water, sat. aq. sodium bicarbonate solution, water and brine.

The chromatographic and NMR spectroscopic analysis of crude mixtures obtained at this stage showed that the applied DMR conditions resulted in incomplete but clean conversions of the tertiary amides. This assessment was confirmed by a detailed analysis of the mixture obtained from the treatment of amide **44c** under the described reaction conditions (Scheme 6.18). The isolation of all components by column chromatography (SiO_2, pentane/EtOAc 49:1 → 4:1) demonstrated that the DMR exclusively yielded secondary amide **54** and the unfunctionalized fragment 5α-cholestane in equimolar amounts at a yield of 48% while unreacted starting material was recovered (51%). It should be noted that no acidic components were identified upon analysis of all acidified aqueous layers of the workup.



44c **54**

SCHEME 6.18: DMR of tertiary *N*-8-*endo*-tricyclodecanylamide **44c** (conversion 49%, unreacted starting material recovered, yield of **54** and 5α-cholestane 48% respectively).

In spite of the presence of two 2° substituents, cleavage occurred selectively at the C–N bond to the β-configured carbon center incorporated in a more flexible chair-like cyclohexane ring of the steroidal substituent as compared to the rigid tricyclodecane substituent. The inertia of the tricyclodecanyl C–N bond under DMR conditions was overcome in the presence of two identical substituents in amide **44e** as shown in Figure 6.8. Direct analysis of the crude mixture (black spectrum) showed that the clean reaction yielded the same secondary amide product **54** (blue spectrum) as the fragmentation of amide **44c** besides unreacted starting material **44e** (red spectrum) at a higher conversion of 61%.

The same result as for the reduction of amide **44c** was obtained for the reduction of amide **44b** (Figure 6.9, 70% conversion). The substrates only differed in the configuration of the

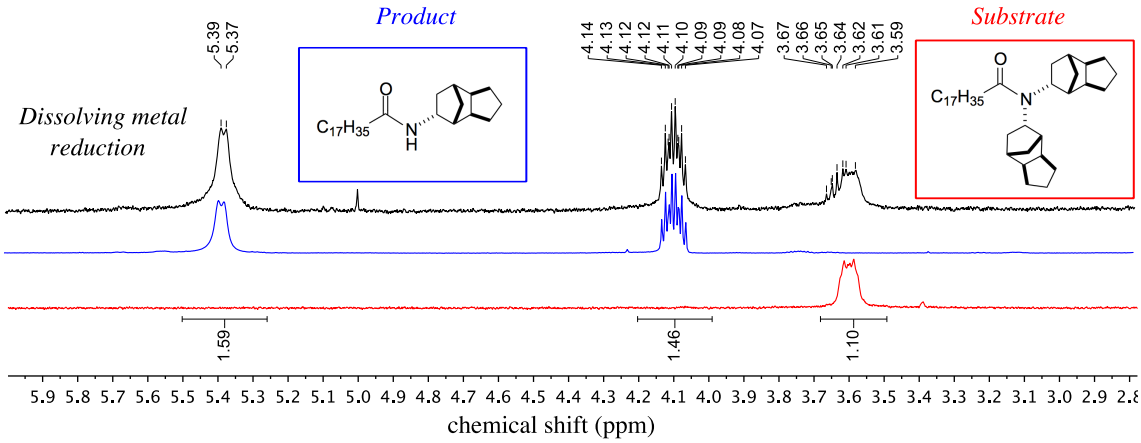


FIGURE 6.8: NMR spectrum of crude mixture after DMR of tertiary di(*N*-8-*endo*-tricyclodecanyl)-amide **44e** in $CDCl_3$.

N-bound carbon center of the steroidal substituent which - considering the outcome of the reductions - appeared to not solely determine the selectivity of the fragmentation.

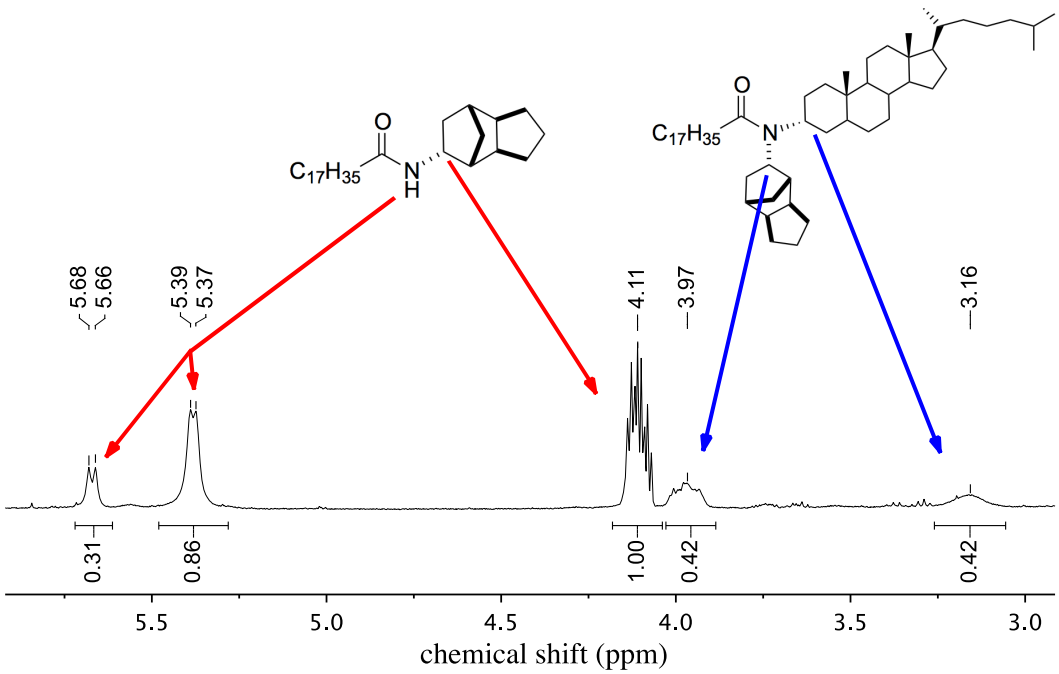


FIGURE 6.9: NMR spectrum of crude mixture after DMR of tertiary *N*-8-*endo*-tricyclodecanylamide **44b** in $CDCl_3$.

Another way to challenge the inertia of the 2° tricyclodecane substituent was discovered by combining it with an aliphatic 1° substituent within one substrate. Submission of amide **44a** to DMR conditions resulted in the cleavage of both substituents 1°:2° in a ratio of 1:1 as shown in Figure 6.10. The lack of selectivity is presumably due to a high resistance of both substituents to cleavage under DMR conditions considering the low conversion of only 21%. It should be noted that the *N*-octadecanyl secondary amide was obtained as

a mixture of equally populated amide bond isomers the equilibrium of which was driven to the thermodynamically more favourable isomer by heating of the mixture in d_8-toluene (see bottom spectrum).

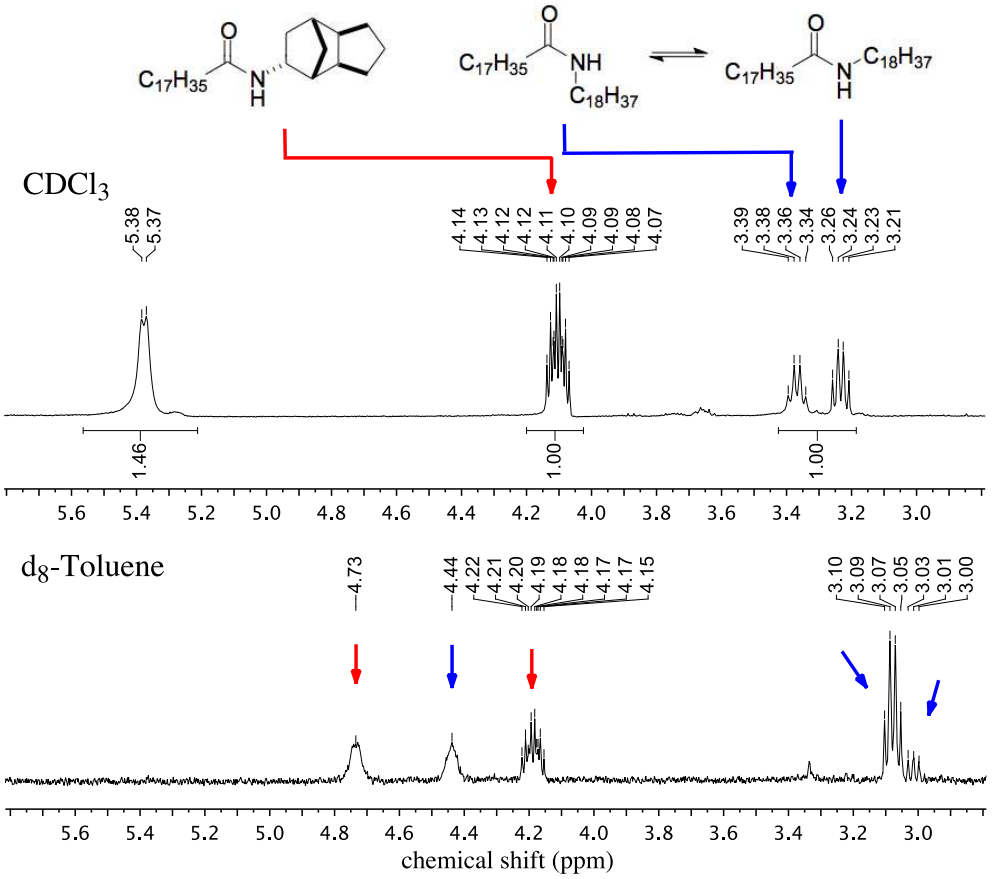


FIGURE 6.10: NMR spectrum of crude mixture after DMR of tertiary *N*-8-*endo*-tricyclodecanylamide **44a** in $CDCl_3$.

The resistance of primary carbon center substituents to cleavage under DMR conditions was additionally tested using *N*-6α-cholestanylamide **45a** (Figure 6.11). Its exposure to the usual reaction conditions resulted in complete conversion of the substrate and exclusive cleavage of the steroidal substituent. Whilst the spectroscopic footage of the secondary amide product with multiplets at δ 3.23, 2.14, and 1.22 ppm may be questionable, the signature of the unfunctionalised fragment in the spectrum of the crude mixture is conspicuous.

A direct comparison of the 3α-cholestanyl and 6α-cholestanyl amide substituents in their tendency to be cleaved under DMR conditions was achieved by submission of amide **45b**

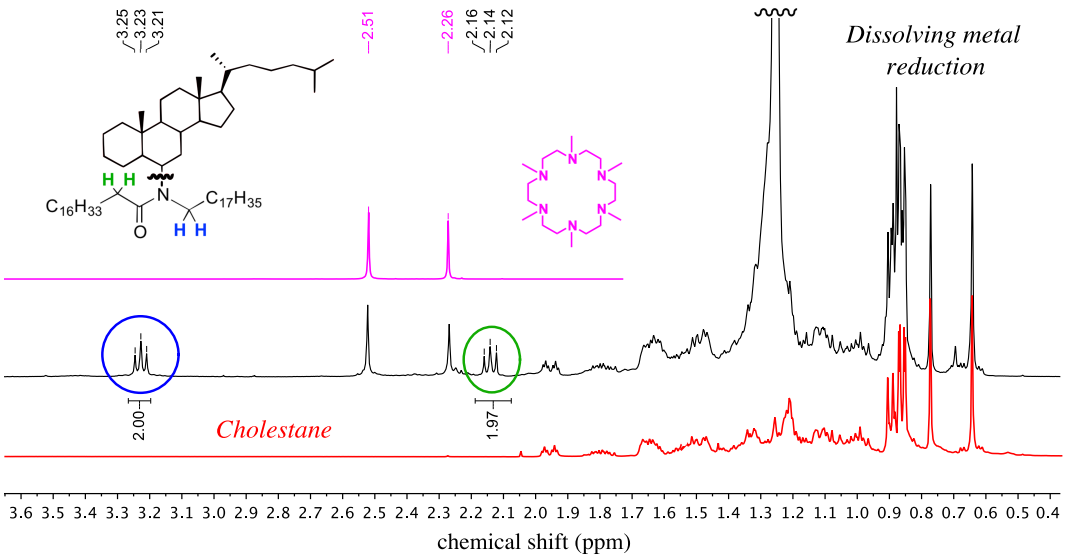


FIGURE 6.11: NMR spectrum of crude mixture after DMR of tertiary *N*-6α-cholestanylamide **45a** in $CDCl_3$.

to the reaction conditions (Figure 6.12). Both possible secondary amide products *N*-3α-cholestanyl amide and *N*-6α-cholestanyl amide were obtained in a ratio of 3.5:1, respectively. Again, the lower selectivity appeared to be linked to the comparably lower conversion of 42%.

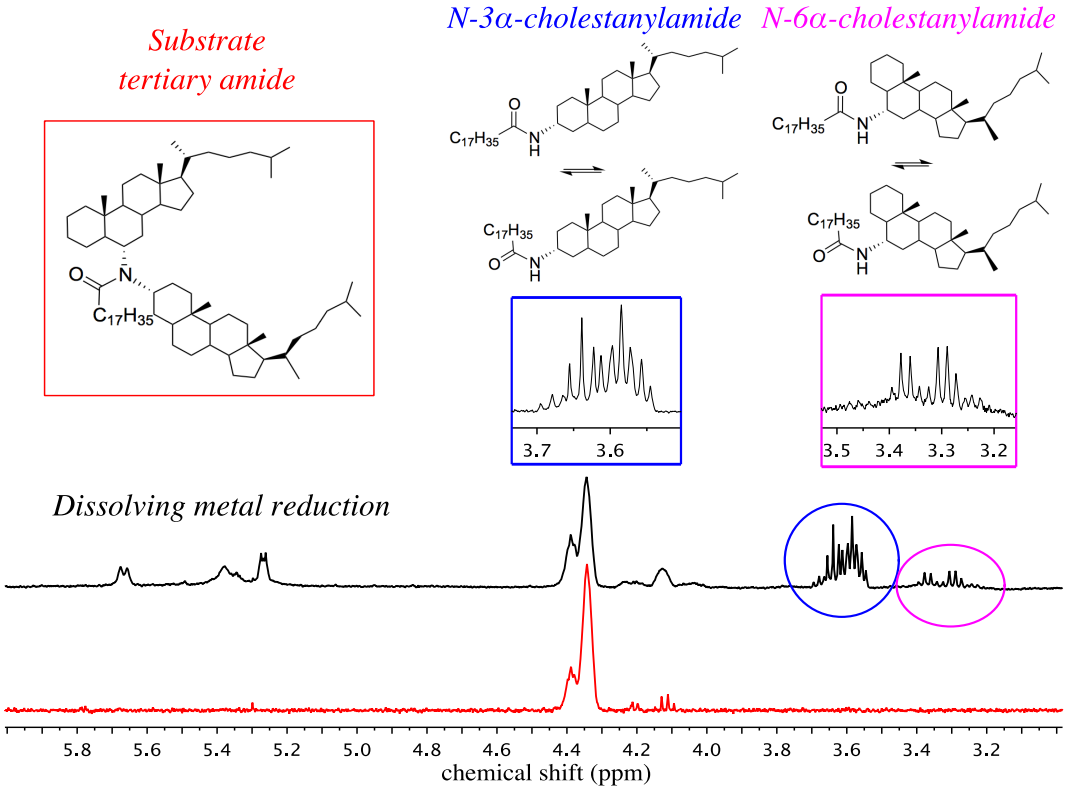


FIGURE 6.12: NMR spectrum of crude mixture after DMR of tertiary *N*-6α-cholestanylamide **45b** in $CDCl_3$.

Furthermore, the behavior of two different lactams were tested under identical DMR conditions in order to identify any preference in fragmentation pathways. Interestingly, 5α-cholestan-3-one derived lactam **50** with two primary carbon centers adjacent to the amide nitrogen was found to be entirely inert under the reaction conditions with only traces of decomposition products detected after 72 h of exposure. This result confirmed the inertia of 1° *N*-substituents to cleavage in doubly alkylated amides described above. Also in accordance with above-mentioned findings, lactam **49** showed exclusive cleavage of the 2° substituent in preference over the 1° substituent with an overall conversion of 35% (Figure 6.13).

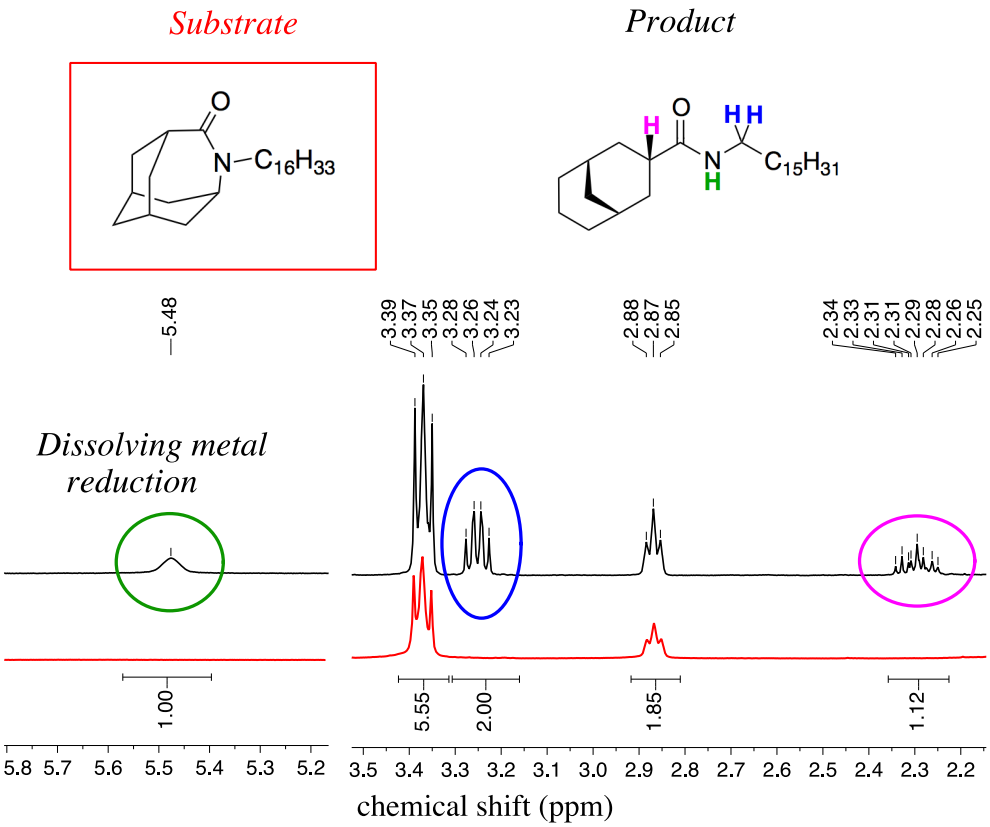


FIGURE 6.13: NMR spectrum of crude mixture after DMR of lactam **49** in $CDCl_3$.

6.3 Conclusion

The synthesis of bulky sterically encumbered amides was accomplished via the catalytic reduction of corresponding imine precursors and subsequent acylation. Given that standard reductive amination protocols failed to yield the imine intermediates, they were only accessible by the reaction of nitrimine derivatives of suitable ketones with a variety of primary amines. This synthetic route allowed for the preparation of tertiary amides with a range of different combinations of *N*-substituents, including terpenoidal, steroidal and aliphatic building blocks, suitable for the investigation of the cleavage of non-carbonyl C-N ς bonds under DMR conditions. Additionally, lactams were readily prepared by Schmidt reaction of ketone precursors with an aliphatic primary azide.

Reductive fragmentation under aprotic conditions was induced using an alkalide solution from sodium-potassium alloy and the per-alkylated aza-crown HMHC. Generally, the stability of the non-carbonyl C-N ς bonds of tertiary amides under the employed reducing conditions was found to be the lower the higher the degree of substitution at the connected carbon center. Aliphatic substituents comprising a primary carbon center connected to the amide nitrogen showed the highest resistance to cleavage. Treatment of a tertiary amide combining an aliphatic and an steroidal *N*-substituent resulted in exclusive cleavage of the latter.

Amide substrates combining two substituents with secondary carbon centers attached to the amide nitrogen readily fragmented under the conditions, whereas the selectivity was governed by the respective combination of substituents. Reduction of a substrate with a combination of steroidal 3α- and 6α-cholestanyl substituents showed a moderate selectivity for the cleavage of the latter. In contrast, the C-N bond attaching the rigid 8-tricyclodecanyl substituent was found to be significantly more resistant to cleavage under the conditions than the C-N bond to any other substituent comprising a secondary carbon center connected to the amide nitrogen. Specifically, combination of the 8-tricyclodecanyl substituent with the steroidal 3α-cholestanyl substituents within an amide substrate resulted in exclusive cleavage of the latter. Notably, submission of a substrate with a combination of the 8-tricyclodecanyl substituent and an aliphatic substituent comprising a primary carbon center connected to the amide nitrogen showed low conversion and no selectivity in the cleavage of the two different C-N bonds.

Lactams with primary carbon centers in both non-carbonyl C-N bonds were stable under the DMR reaction conditions, while a C-N bond comprising a secondary carbon center

was selectively cleaved leaving a C-N bond with primary carbon center within the same substrate intact.
All produced secondary amides were stable under the DMR reaction conditions.

The observed correlation of the susceptibility of a non-carbonyl C-N ς bond to cleavage with the degree in substitution of that carbon center is in accordance with a radical fragmentation pathway similar to that proposed for the reductive deoxygenation of ester substrates.
Strikingly, most reduction reactions did not go to completion in spite of a large excess of reducing agent and prolonged reaction times. The complete recovery of remaining starting material demonstrates, however, that the large degree of steric hindrance at the amide bond effectively prevented nucleophilic attacks, which enabled a clear investigation of the reductively induced unusual cleavage of non-carbonyl C-N ς bonds.

Chapter 7

Concluding Remarks and Future Work

The nature of alkali metal solutions in low-polarity media is every bit as fascinating as complex and has therefore remained a challenging subject of scientific curiosity for several decades. As described in chapter 1, experimental progress in the field has always been hampered by the ineluctable instability of alkalide solutions. The most obvious of their common weak spots was improved to a large extent by replacing reducible polyether complexing agents by the peralkylated aza-crown HMHC. This allowed us to advance to the investigation of characteristics of alkalide solutions, which received less attention in the past, and to highlight further critical aspects with respect to the solution stability in the course of this project as follows.

The picture of highly reducing alkali metal anions in solution as separately solvated species - fully unperturbed by the surrounding medium - was established decades ago based on NMR spectroscopic characteristics and has not significantly changed since. The temperature dependence of NMR relaxation times, the alkalide signal intensity, as well as its asymmetrical line shape upon careful inspection indicated the involvement of Na^- and K^- in chemical exchange processes which limit the lifetime of the genuine alkalide species in solution. Extracted exchange relaxation rates in the range of 0.1–50 Hz were rationalised by considering a slow exchange process between the NMR-visible separately solvated alkalide and NMR-invisible ion associates due to significant quadrupolar line broadening.

In accordance with this suggestion, a close inspection of spectra of a sodide solution involving the aza-crown Hexamethyl-hexacyclen (HMHC) at various temperatures revealed unprecedented additional signals with a larger FWHM but only a minimal chemical shift difference to the common alkalide signal. Whilst it is reasonable to assume the presence of both contact ion pairs and solvent separated ion pairs as parts of exchange processes operating in solution, the precise nature of such ion associates can not be deduced from the described NMR data.
However, the effect of ion pairing equilibria on the NMR properties of alkalides in solution can be demonstrated by a subsequent study using NMR relaxation dispersion experiments. This NMR method allows for the detection of exchange intermediates that cannot be observed directly in spectra, for example due to a low population or their relaxation properties, as long as they exchange with an observable state of the entity of interest on the millisecond time scale. The methodology makes use of the fact, that the rate of magnetization decay during the CPMG (Carr-Purcell-Meiboom-Gill) sequence is dependent on the frequency of application of 180°_{x} pulses in the CPMG sequence whenever the species of interest is involved in exchange processes.

The significance of the suggested interaction of alkalides with their complex cations was probed by ionic conductivity measurements. A robust method for the accurate determination of the alkali metal content in alkalide solution in THF by ion chromatography was developed which is viable using standard synthetic laboratory equipment. The method was applied in the course of the determination of molar conductivity values for alkalide solutions in the presence of 15C5 and HMHC, respectively.
The obtained molar conductivity data showed characteristic trends of weak electrolytes in a medium with low dielectric constant. The awareness of the conclusively detected molar conductivity minima at 0.01 M and a steady increase of molar conductivity with increasing metal concentration independent of the complexing agent is of particular importance for the understanding of alkalide solutions at higher concentrations. The stability of alkalide solutions in THF was found to be significantly enhanced at concentrations beyond the conductance minimum while lower concentrations facilitated self-decomposition. A correlation between solution stability and ion association constant was suggested and the increase of molar conductivity with increasing concentration was rationalised by ion pairs contributing to the overall dielectric constant of the medium.

Moreover, the suggested increased reactivity of alkalides in a high dilution and the kinetics of corresponding decomposition processes can be investigated in more detail by gas chromatographic analysis of any decomposition products and their concentration. This would additionally validate the application of corrections to concentration values in the low concentration range of molar conductivity data.

In order to gain insight into the potential influence of the dielectric properties of the weak electrolyte on its concentration dependent conductivity, coaxial probe dielectric spectroscopy was applied to the alkalide system for the first time. A robust calibration of the coaxial probe under cryogenic and inert gas conditions was developed. This allowed for the detection of a large contribution of the alkali metal content to the dielectric constant of the mixture. From the analysis of the frequency dependent permittivity was concluded that the increase in dielectric constant upon metal dissolution was indeed due to the presence of ion pairs in the mixture.

An analogous conclusion was drawn from the results of small angle neutron scattering experiments. An increase in scattering intensity upon metal dissolution in a solution of HMHC in THF was qualitatively and quantitatively attributed to the formation of alkalide ion pairs in the mixture. The accurate extraction of the dimension and shape of the scattering particles from the high-resolution SANS data in the Q-range of 0.1–0.6 $Å^{-1}$ in both the 15C5 and the HMHC systems requires a three-dimensional molecular model for the simulation of the respective form factor.

The comprehensive studies of this work demonstrated that ion associates play a major role in the characteristics of alkalide solutions. The importance of ion pairing and its consequences have been widely neglected in the past in spite of the large untapped potential it provides with respect to future applications of the highly reducing and polarisable alkalide species. The presented findings in their entirety prove that the spacial separation between the alkalide ion and its bulky counterion is variable and depends on the properties of the mixture and the applied conditions. Mindful of the higher stability of the peralkylated aza-crown and its synthetic adaptability, this enables the controlled tailoring of the reactivity of the alkalide and its kinetic properties.
Further insight into various properties of contact ion pairs of alkalides involving HMHC or 15C5 can be obtained by DFT calculations that were previously employed in the computational characterisation of alkalide ion pairs [57]. Obtained results can be related to

experimentally determined properties to support the hypothesis of the increased stability of alkalide ion pairs (alkali-superalkali-dimers) in low-polarity media.

In parallel to the thorough understanding of the reductive medium itself, clear and reliable results on the reductive fragmentation of the synthetically and biologically highly relevant amide group were accomplished under otherwise complicated dissolving metal reduction conditions. A good correlation of the selective cleavage of an amide substituent with its degree in substitution pointed towards a radical fragmentation pathway similar to that proposed for the reductive deoxygenation of ester substrates. However, the outstanding stability of non-carbonyl C-N bond to the 8-tricyclodecanyl substituent as well as the fact that most reduction reactions did not go to completion despite a large excess of reducing agent and prolonged reaction times leave room for further investigations.

We believe that the potential of alkalide solution systems with respect to future applications is currently underestimated in the scientific community due to the limited prevalent knowledge about their properties, reliable practical handling and tailoring options. This project represents a crucial milestone in the development of the field. Our investigations render alkalide solutions more approachable, stimulate more detailed studies of the property-determining aspects, and finally allow for the conversion of the large untapped potential of this extraordinary system into applications in various research fields, novel synthetic transformations and technologies in the future.

Chapter 8

Experimental Section - Amide Synthesis and Reduction

8.1 General Aspects

8.1.1 Instrumental procedures

Melting points were determined using a Reichert-Thermovar hot-stage apparatus and are uncorrected. IR spectra were recorded as thin films with the absorption bands reported in wave number (cm^{-1}) using a Mattson 5000 FTIR apparatus with automatic background subtraction. ^{1}H NMR spectra were recorded at 400 MHz and ^{13}C NMR spectra at 100 MHz on Bruker DRX-400 spectrometers, respectively. Chemical shifts are reported as δ-values in ppm relative to the $CDCl_3$ residual peaks (δH 7.26, δC 77.0). Coupling constants (J) were recorded in Hertz (Hz) and quoted to the nearest 0.5 Hz. Low and high resolution mass spectra (ES, ESI) were recorded by Imperial College Mass Spectrometry service using a Micromass Platform II and a Micromass AutoSpec-Q spectrometer. X-ray diffraction data were recorded by the Imperial College Department of Chemistry X-ray diffraction service.

8.1.2 General reaction procedures

All reactions were carried out with a magnetic stirring bar and, if air or moisture sensitive, in a flame-dried or oven-dried glassware under nitrogen or argon. Syringes, used to transfer reagents and solvents, were purged with nitrogen or argon prior to use. Reaction

temperatures other than 25 °C were recorded as the bath temperature unless otherwise stated. Prolonged periods of vessel cooling were attained by the use of a cooling bath and immersion cooler. All solvents and reagents were used as commercially supplied, unless otherwise stated. Et_2O and THF were redistilled from sodium-benzophenone and CH_2Cl_2 from CaH_2. Thin layer chromatography (TLC) was performed on pre-coated aluminium backed silica gel 60 plates. The chromatogram was visualized under UV light and/or by staining using potassium permanganate solution, aqueous acidic vanillin or phosphomolybdic acid followed by gentle heating with a heat gun, or using iodine. Flash column chromatography was performed using silica gel, particle size 40–63 µm (eluants are given in parenthesis). The diameter of the columns and the amount of silica gel were calculated according to the recommendations of W. C. Still. [157]

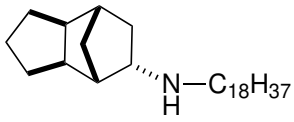
8.2 Preparation of compounds and solutions

8.2.1 *N*-alkylated Tricyclodecanyl-8- and Cholestanyl-6-amines

General Procedure [146, 147]

To a solution of the respective nitrimine derivative (1.0 eq.) in methanol or ether (40 mL per 1.0 g nitrimine) under an inert atmosphere was added the resp. primary amine (1.0 eq.) in one portion. The mixture was magnetically stirred at the specified temperature for 16 h at which time an aliquot was taken for spectroscopic characterization. Then, nickel(II) chloride hexahydrate (4.0 eq.) was added to the crude imine and the green solution was cooled to −30 °C. After stirring for 5 min, sodium borohydride (20 eq.) was added in small portions over a period of 10 min. The apparatus was sealed, equipped with a balloon and the dark-black dispersion magnetically stirred under reflux for 24 h. The crude mixture was then cooled to 25 °C, 2 M aq. NaOH solution (1/10 volume of dispersion) was added and the mixture vigorously shaken several times. The black solid was removed by filtration through Celite and the filtrate was extracted with ether (3×). The combined organic layers were dried (Na_2SO_4), filtered and the solvent removed under reduced pressure. The residue was purified by column chromatography to obtain the pure product.

***N*-octadecyl-8-amino-tricyclodecane (31a)**



From 1-octadecylamine, imine formation at 40 °C.

Column chromatography (SiO_2, pentane/EtOAc/NEt_3 9:1:0.1) yielded the title compound (MW 403.73, 83%) as a white tacky solid.

R_f = 0.08 (SiO_2, pentane/EtOAc/NEt_3 4:1:0.1).

IR (ATR, cm^{-1}) 2913, 2849, 1472, 1352, 1144.

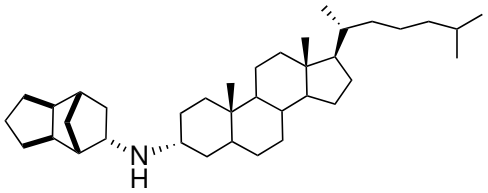
^{1}H NMR (400 MHz, $CDCl_3$)

δ 2.97 (dt, J = 9.3, 3.9 Hz, 1H, N–CH^{tricyc}), 2.61–2.39 (m, 2H, N–$CH_2{}^{alkyl}$), 2.18 (q, J = 8.5 Hz, 1H), 2.09–2.01 (m, 1H), 2.25–0.70 (m, 46H) [included: 1.25 (m, 30H, alkyl-chain), 0.88 (t, J = 6.8 Hz, 3H)], 0.57–0.52 (m, 1H).

^{13}C NMR (100 MHz, $CDCl_3$) δ 58.92, 48.57, 48.44, 43.98, 41.03, 38.36, 37.93, 32.62, 32.21, 32.03, 31.92, 30.46, 29.69, 29.62, 29.36, 27.54, 27.18, 22.69, 14.10.

HRMS (ES+) calc. for $C_{28}H_{54}N$: $(M + H)^+$, 404.4256, found: $(M + H)^+$, 404.4278.

***N*-3α-Cholestanyl-8-amino-tricyclodecane (31b)**



From 3α-amino-5α-cholestane, imine formation at 40 °C.

Column chromatography (SiO_2, pentane/EtOAc/NEt_3 19:1:0.1) yielded the title compound (MW 521.90, 74%) as a white tacky solid.

R_f = 0.35 (SiO_2, pentane/EtOAc/NEt_3 9:1:0.1).

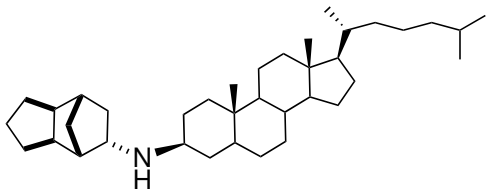
IR (ATR, cm^{-1}) 3356, 2929, 2861, 1444, 1382, 1365.

^{1}H NMR (400 MHz, $CDCl_3$) δ 3.01 (dt, J = 9.4, 4.0 Hz, 1H), 2.83–2.78 (m, 1H), 2.28–0.43 (m, 60H) [incl. methyl groups: 0.89 (d, J = 6.5 Hz, 3H), 0.87 (d, J = 1.9 Hz, 3H), 0.85 (d, J = 1.9 Hz, 3H), 0.77 (s, 3H), 0.64 (s, 3H)].

^{13}C NMR (100 MHz, $CDCl_3$) δ 56.63, 56.45, 56.32, 54.36, 54.32, 50.83, 50.66, 48.58, 44.49, 44.41, 42.63, 41.04, 40.12, 39.89, 39.53, 39.49, 38.57, 38.40, 38.35, 36.28, 36.21, 35.83, 35.55, 34.83, 33.00, 32.71, 32.57, 32.20, 32.08, 28.84, 28.26, 28.01, 27.71, 27.21, 25.42, 24.20, 23.87, 22.82, 22.56, 20.80, 18.68, 12.09, 11.59.

HRMS (ES+) calc. for $C_{37}H_{64}N$: $(M + H)^+$, 522.5039, found: $(M + H)^+$, 522.5047.

***N*-3β-Cholestanyl-8-amino-tricyclodecane (31c)**



From 3β-amino-5α-cholestane, imine formation at 40 °C.

Column chromatography (SiO_2, pentane/EtOAc/NEt_3 9:1:0.1) yielded the title compound (MW 521.90, 56%) as a white tacky solid.

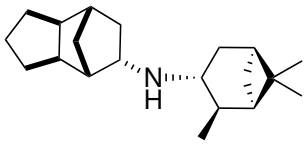
R_f = 0.10 (SiO_2, pentane/EtOAc/NEt_3 9:1:0.1).

Selected spectroscopic features of major diastereoisomer:

IR (ATR, cm^{-1}) 2929, 2862, 1449, 1384.

^{1}H NMR (400 MHz, $CDCl_3$) δ 3.17 (ddd, 1H), 2.45 (m, 1H), 2.13 (m, 1H); 2.03–0.47 (m, 60H) [Me-groups: 0.89 (d, J = 6.5 Hz, 3H), 0.87 (d, J = 1.9 Hz, 3H), 0.85 (d, J = 1.9 Hz, 3H), 0.77 (s, 3H), 0.64 (s, 3H)].

_N_-(-)-isopinocampheyl-8-amino-tricyclodecane (31d)



From (-)-isopinocampheylamine, imine formation at 40 °C.

Column chromatography (SiO_2, pentane/EtOAc/NEt_3 9:1:0.1) yielded the title compound (MW 287.48, 42%) as a white tacky solid.

R_f = 0.20 (SiO_2, pentane/EtOAc/NEt_3 9:1:0.1).

Selected spectroscopic features of major diastereoisomer:

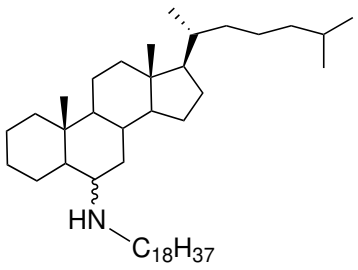
IR (ATR, cm^{-1}) 2925, 2863, 1456, 1383.

^1H NMR (400 MHz, $CDCl_3$)

diastereomer 1: δ 3.14 (ddd, $J = 10.5, 4.4, 4.4$ Hz, 1H), 2.85 (m, 1H).

diastereomer 2: δ 3.06 (ddd, $J = 9.9, 4.2, 4.2$ Hz, 1H), 2.85 (m, 1H).

***N*-octadecyl-6-aminocholestane (43a)**



From 1-octadecylamine, imine formation at 50 °C.

Column chromatography (SiO_2, pentane/EtOAc/NEt_3 19:1:0.1) yielded the title compound (MW 640.16, 87%) as a white tacky solid.

R_f = 0.60 (SiO_2, pentane/EtOAc/NEt_3 9:1:0.1).

IR (ATR, cm^{-1}) 2920, 2850, 1466, 1380, 1366.

^{1}H NMR (400 MHz, $CDCl_3$)

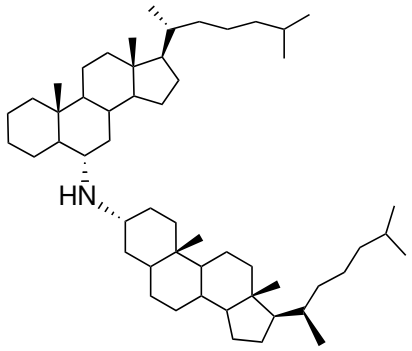
diastereomer 1: δ 2.59 (dt, J = 7.06, 7.06, 14.40 Hz, 2H, NH–CH_2^{alkyl}), 2.56 (m, 1H, NH–CH^{chol}), 2.00–1.94 (m, 1H), 1.90–0.60 (m, 80H) [incl. methyl groups: 0.96 (s, 3H), 0.87 (d, J = 1.9 Hz, 3H), 0.86 (d, J = 1.9 Hz, 3H), 0.68 (s, 3H)].

diastereomer 2: δ 2.56 (m, 1H, NH–CH^{chol}), 2.59 (dt, J = 6.60, 6.60, 11.45 Hz, 2H, NH–CH_2^{alkyl}), 2.00–1.94 (m, 1H), 1.90–0.60 (m, 80H) [incl. methyl groups: 0.96 (s, 3H), 0.87 (d, J = 1.9 Hz, 3H), 0.86 (d, J = 1.9 Hz, 3H), 0.68 (s, 3H)].

^{13}C NMR (100 MHz, $CDCl_3$) δ 59.17, 56.37, 56.33, 55.35, 49.82, 48.89, 42.67, 40.93, 40.14, 39.55, 36.56, 36.41, 36.22, 35.85, 31.94, 30.41, 30.37, 29.72, 29.68, 29.54, 29.38, 28.26, 28.03, 27.41, 26.68, 24.34, 23.86, 22.82, 22.70, 22.57, 22.32, 20.68, 18.70, 16.22, 14.12, 12.19.

HRMS (ES+) calc. for $C_{45}H_{86}N$: $(M+H)^+$, 640.6760, found: $(M+H)^+$, 640.6785.

***N*-3α-Cholestanyl-6-aminocholestane (43b)**



From 3α-amino-5α-cholestane, imine formation at 50 °C.

Column chromatography (SiO_2, pentane/EtOAc/NEt_3 49:1:0.1) yielded the title compound (MW 758.34, 71%) as a white tacky solid.

R_f = 0.95 (SiO_2, pentane/EtOAc/NEt_3 9:1:0.1).

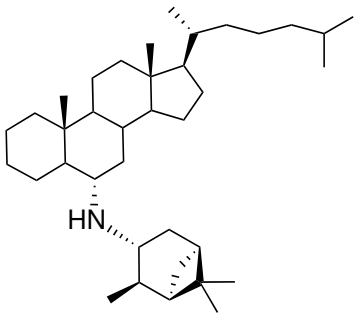
IR (ATR, cm^{-1}) 2925, 2866, 2848, 1466, 1444, 1381, 1366.

^{1}H NMR (400 MHz, $CDCl_3$) δ 2.64 (m, 1H, NH−CH^{3-chol}), 2.55 (m, 1H, NH−CH^{6-chol}), 2.00–0.60 (m, 92H) [incl. methyl groups: 0.99 (s, 3H), 0.91 (d, J = 6.5 Hz, 3H), 0.90 (d, J = 6.5 Hz, 3H), 0.87 (d, J = 1.7 Hz, 3H), 0.86 (d, J = 1.7 Hz, 3H), 0.76 (s, 3H), 0.69 (s, 3H), 0.65 (s, 3H)].

^{13}C NMR (100 MHz, $CDCl_3$) δ 57.25, 56.60, 56.38, 56.34, 56.23, 55.32, 54.69, 51.40, 49.90, 42.66, 42.63, 41.06, 40.16, 40.07, 40.00, 39.53, 37.33, 36.65, 36.21, 35.87, 35.82, 35.57, 32.97, 32.20, 30.41, 28.90, 28.27, 28.02, 27.38, 26.71, 26.21, 24.36, 24.20, 23.85, 22.82, 22.57, 22.34, 20.83, 20.70, 18.70, 16.44, 12.14, 12.10, 11.63.

HRMS (ES+) calc. for $C_{54}H_{96}N$: $(M + H)^+$, 758.7543, found: $(M + H)^+$, 758.7535.

***N*-(-)-isopinocampheyl-6-aminocholestane (43c)**



From (-)-isopinocampheylamine, imine formation at 50 °C.

Column chromatography (SiO_2, pentane/EtOAc/NEt_3 49:1:0.1) yielded the title compound (MW 523.92, 49%) as a white tacky solid.

R_f = 0.90 (SiO_2, pentane/EtOAc/NEt_3 9:1:0.1).

IR (ATR, cm^{-1}) 2924, 2855, 1465, 1382.

^{1}H NMR (400 MHz, $CDCl_3$) δ 2.77–2.67 (m, 2H, NH−CH^{chol} and NH−$CH^{isopino}$), 2.36–2.26 (m, 2H), 2.03–0.63 (m, 60H) [incl. methyl groups: 1.19 (s, 3H), 1.05 (d, J = 7.2 Hz, 3H), 0.97 (s, 3H), 0.95 (s, 3H), 0.91 (d, J = 6.5 Hz, 3H), 0.87 (d, J = 1.7 Hz, 3H), 0.86 (d, J = 1.7 Hz, 3H), 0.68 (s, 3H)].

^{13}C NMR (100 MHz, $CDCl_3$) δ 56.38, 56.04, 55.28, 54.83, 53.06, 49.47, 47.75, 46.44, 42.64, 42.13, 41.05, 40.08, 39.53, 38.65, 37.33, 36.68, 36.21, 35.83, 35.63, 34.86, 30.35, 28.27, 28.11, 28.02, 27.41, 26.70, 24.41, 23.84, 23.31, 22.82, 22.57, 22.30, 20.93, 20.66, 18.71, 16.47, 11.98.

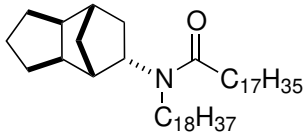
HRMS (ES+) calc. for $C_{37}H_{66}N$: $(M + H)^+$, 524.5195, found: $(M + H)^+$, 524.5197.

8.2.2 Tertiary *N*-8-Tricyclodecanyl- and *N*-6-Cholestanyl-amides

General Procedure

Stearoyl chloride (150 mg, 0.500 mmol, 5.0 eq.) and the respective secondary amine (0.100 mmol, 1.0 eq.) were added to a pressure-resistant vial followed by dry CH_2Cl_2 (2.0 mL) and triethylamine (0.14 mL, 1.00 mmol, 10 eq.). The mixture was stirred at 80 °C for 16 h in the sealed vial. After cooling to room temperature, water (2.0 mL) was added, the organic layer was separated and dried over anhyd. Na_2SO_4. The solvent was removed under vacuum. The residue was purified by column chromatography to obtain the pure product.

***N*-octadecyl-8-tricyclodecanyl-stearoylamide (44a)**



From *N*-octadecyl-8-amino-tricyclodecane (**31a**).

Column chromatography (SiO_2, pentane/EtOAc 49:1) yielded the title compound (MW 670.19, 91%) as a white tacky solid.

R_f = 0.59 (SiO_2, pentane/EtOAc 19:1).

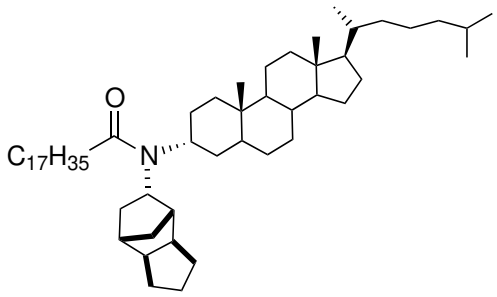
IR (ATR, cm^{-1}) 2921, 2852, 1638, 1465, 1416.

^1H NMR (400 MHz, $CDCl_3$) δ 4.40–2.65 (m, 3H), 2.53–2.17 (m, 3H), 3.00–0.60 (m, 81H).

^{13}C NMR (100 MHz, $CDCl_3$) δ 174.33, 173.94, 66.77, 57.50, 56.35, 48.37, 48.07, 47.15, 46.31, 45.10, 44.75, 44.08, 41.10, 40.13, 34.22, 33.89, 32.38, 32.16, 31.92, 30.94, 30.53, 29.69, 29.66, 29.57, 29.54, 29.36, 29.11, 27.62, 27.06, 26.97, 25.68, 22.69, 14.11.

HRMS (ES+) calc. for $C_{46}H_{88}NO$: $(M + H)^+$, 670.6866, found: $(M + H)^+$, 670.6890.

***N*-3α-Cholestanyl-8-tricyclodecanyl-stearoylamide (44b)**



From *N*-3α-Cholestanyl-8-amino-tricyclodecane (**31b**).

Column chromatography (SiO_2, pentane/EtOAc 49:1) yielded the title compound (MW 788.36, 89%) as a white tacky solid.

R_f = 0.46 (SiO_2, pentane/EtOAc 19:1).

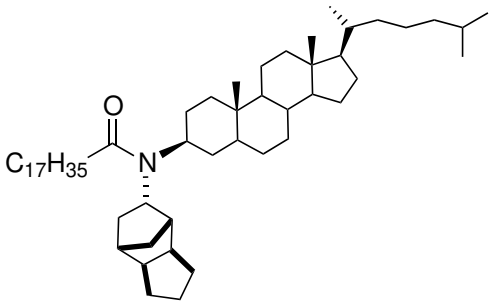
IR (ATR, cm^{-1}) 2921, 2851, 1648, 1466.

^{1}H NMR (400 MHz, $CDCl_3$) δ 4.04–3.91 (m, 1H), 3.27–3.06 (m, 1H), 2.90–0.50 (m, 95H).

^{13}C NMR (100 MHz, $CDCl_3$) δ 173.91, 173.84, 58.67, 58.47, 56.43, 56.36, 56.22, 55.63, 55.48, 51.46, 50.71, 47.92, 47.45, 47.21, 42.73, 41.47, 41.40, 40.75, 40.19, 39.84, 39.51, 39.03, 38.49, 37.47, 36.58, 36.16, 36.05, 35.96, 35.80, 35.39, 33.77, 33.58, 32.53, 32.48, 32.44, 32.28, 32.20, 31.92, 31.72, 31.54, 31.31, 31.19, 29.70, 29.66, 29.53, 29.49, 29.44, 29.36, 29.27, 29.15, 28.58, 28.27, 28.01, 26.93, 25.56, 24.16, 23.82, 22.81, 22.69, 22.56, 21.32, 18.66, 17.40, 16.96, 14.12, 12.14.

HRMS (ES+) calc. for $C_{55}H_{98}N$: $(M + H)^+$, 788.7648, found: $(M + H)^+$, 788.7659.

***N*-3β-Cholestanyl-8-tricyclodecanyl-stearoylamide (44c)**



From *N*-3β-Cholestanyl-8-amino-tricyclodecane (**31c**).

Column chromatography (SiO_2, pentane/EtOAc 49:1) yielded the title compound (MW 788.36, 45%) as a white tacky solid.

R_f = 0.41 (SiO_2, pentane/EtOAc 19:1).

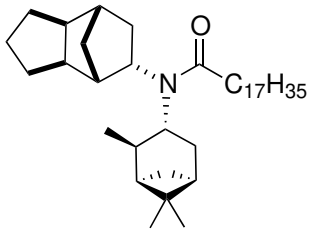
IR (ATR, cm^{-1}) 2922, 2852, 1648, 1466.

^{1}H NMR (400 MHz, $CDCl_3$) δ 4.26–3.00 (m, 1H), 2.99–2.60 (m, 1H), 2.55–0.40 (m, 95H).

^{13}C NMR (100 MHz, $CDCl_3$) δ 174.21, 58.82, 57.71, 56.60, 56.34, 54.16, 48.12, 47.33, 46.87, 42.61, 41.37, 40.15, 40.10, 39.50, 38.90, 38.19, 36.18, 35.93, 35.79, 35.58, 35.50, 32.50, 32.11, 31.93, 30.98, 29.70, 29.66, 29.54, 29.50, 29.37, 28.93, 28.79, 28.27, 28.01, 26.92, 25.60, 24.22, 23.86, 22.82, 22.70, 22.56, 21.21, 18.67, 14.13, 12.69, 12.62, 12.07.

HRMS (ES+) calc. for $C_{55}H_{98}N$: $(M + H)^+$, 788.7648, found: $(M + H)^+$, 788.7663.

N-(-)-isopinocampheyl-8-tricyclodecanyl-stearoylamide (44d)



From *N*-(-)-isopinocampheyl-8-amino-tricyclodecane (**31d**).

Column chromatography (SiO_2, pentane/EtOAc 49:1) yielded the title compound (MW 553.94, 24%) as a white tacky solid.

R_f = 0.50 (SiO_2, pentane/EtOAc 19:1).

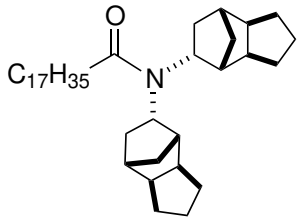
IR (ATR, cm^{-1}) 2923, 2854, 1653, 1465.

^{1}H NMR (400 MHz, $CDCl_3$) δ 4.40–3.86 (m, 1H), 3.74–3.30 (m, 1H), 3.00–0.60 (m, 65H).

^{13}C NMR (100 MHz, $CDCl_3$) δ 174.06, 174.00, 173.75, 47.83, 47.25, 46.13, 44.61, 42.98, 40.75, 39.56, 39.07, 38.49, 36.65, 34.71, 34.57, 33.67, 32.55, 32.00, 31.92, 31.87, 31.72, 31.64, 31.20, 29.70, 29.66, 29.60, 29.55, 29.50, 29.46, 29.36, 29.27, 29.16, 29.12, 27.71, 27.05, 25.06, 22.69, 14.12.

HRMS (ES+) calc. for $C_{38}H_{68}NO$: $(M + H)^+$, 554.5301, found: $(M + H)^+$, 554.5295.

***N*,*N*-di(8-tricyclodecanyl)stearoylamide (44e)**



From 8-tricyclodecanone oxime **28** and 8-tricyclodecanylamine, imine formation at 40 °C. Column chromatography (SiO_2, pentane/EtOAc 49:1) yielded the title compound (MW 551.93, 31%) as a white tacky solid.

R_f = 0.57 (SiO_2, pentane/EtOAc 19:1).

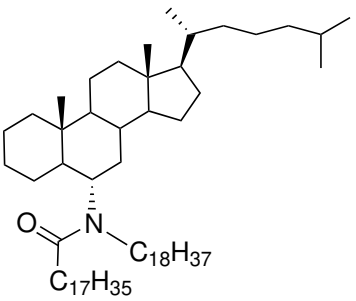
IR (ATR, cm^{-1}) 2920, 2851, 1719, 1655, 1466, 1354, 1261.

^{1}H NMR (400 MHz, $CDCl_3$) δ 3.70–3.30 (m, 2H), 2.60–0.60 (m, 63H).

^{13}C NMR (100 MHz, $CDCl_3$) δ 174.84, 59.76, 48.59, 47.35, 42.08, 40.79, 35.82, 32.57, 32.53, 31.93, 31.81, 29.70, 29.65, 29.59, 29.56, 29.36, 26.93, 25.87, 22.69, 14.12.

HRMS (ES+) calc. for $C_{38}H_{66}NO$: $(M + H)^+$, 552.5144, found: $(M + H)^+$, 552.5150.

***N*-octadecyl-6-cholestanyl-stearoylamide (45a)**



From *N*-octadecyl-6-aminocholestane (**43a**).

Column chromatography (SiO_2, pentane/EtOAc 49:1) yielded the title compound (MW 906.63, 89%) as a white tacky solid.

R_f = 0.70 (SiO_2, pentane/EtOAc 9:1).

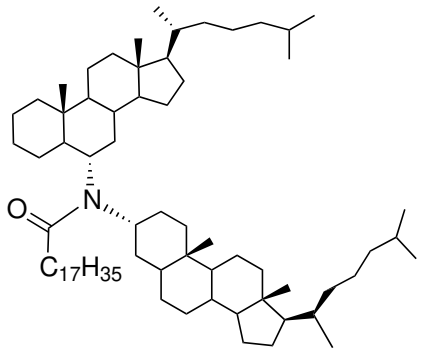
IR (ATR, cm^{-1}) 2920, 2850, 1647, 1466, 1378, 1365.

^{1}H NMR (400 MHz, $CDCl_3$) δ 5.02 and 4.32–3.77 (m, 1H, N–CH^{6-chol}), 3.77–2.90 (m, 2H, N–CH_2^{alkyl}), 2.50–0.50 (m, 116H).

^{13}C NMR (100 MHz, $CDCl_3$) δ 175.34, 56.71, 56.13, 54.01, 50.71, 49.73, 46.31, 42.57, 42.14, 39.80, 39.51, 36.15, 35.80, 34.62, 34.21, 34.03, 32.55, 32.28, 31.93, 29.71, 29.66, 29.58, 29.53, 29.47, 29.37, 29.28, 28.16, 28.01, 27.54, 26.96, 26.41, 24.38, 24.17, 23.80, 22.80, 22.69, 22.55, 21.98, 20.54, 18.66, 16.90, 14.12, 12.21.

MALDI-ToF (LD+) calc. for $C_{63}H_{120}NO$: $(M + H)^+$, 906.9, found: $(M + H)^+$, 907.2.

***N*-3α-Cholestanyl-6-cholestanyl-stearoylamide (45b)**



From *N*-3α-Cholestanyl-6-aminocholestane (**43b**).

Column chromatography (SiO_2, pentane/EtOAc 49:1) yielded the title compound (MW 1024.80, 77%) as a white tacky solid.

R_f = 0.62 (SiO_2, pentane/EtOAc 9:1).

IR (ATR, cm^{-1}) 2923, 2851, 1643, 1466, 1378.

^{1}H NMR (400 MHz, $CDCl_3$) δ 4.42–4.31 (m, 2H), 2.40–0.56 (m, 127H).

^{13}C NMR (100 MHz, $CDCl_3$) δ 173.51, 129.98, 56.78, 56.42, 56.11, 55.12, 51.70, 50.58, 42.62, 42.21, 40.77, 40.16, 39.64, 39.51, 38.67, 38.17, 36.18, 35.79, 35.52, 35.11, 34.28, 33.29, 32.39, 32.20, 32.10, 31.94, 29.73, 29.67, 29.60, 29.55, 29.37, 28.61, 28.26, 28.01, 26.60, 25.60, 24.42, 24.16, 23.89, 23.80, 22.81, 22.70, 22.56, 22.04, 20.89, 20.83, 19.75, 18.70, 18.68, 14.13, 12.28, 12.11, 11.81.

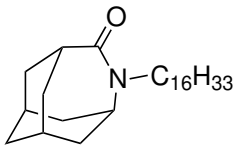
MALDI-ToF (LD+) calc. for $C_{72}H_{130}NO$: $(M + H)^+$, 1025.0, found: $(M + H)^+$, 1024.9.

8.2.3 Synthesis of Lactams

General Procedure [158]

A solution of the respective ketone (0.80 mmol, 1.0 eq.) and 430 mg of 1-azidohexadecane (1.60 mmol, 2.0 eq.) in 2.5 mL of CH_2Cl_2 was cooled to 4 °C in an ice-water bath. 2.2 mL of $TiCl_4$ (2.00 mmol, 2.5 eq.) were added dropwise and the reaction was allowed to warm to 25 °C with immediate gas evolution noted. A precipitate formed within 15 min and the suspension was stirred for a total of 24 h at which time 20 mL of ethyl acetate and partitioned between 200 mL of ethyl acetate and 30 mL of sat. aq. sodium bicarbonate solution. The organic layer was extracted with 30 mL of brine and dried (Na_2SO_4. Evaporation of the solvent was followed by column chromatography to obtain the pure product.

2-Adamantanone derived lactam (49)



From 2-adamantanone **51**.

Column chromatography (SiO_2, pentane/EtOAc 9:1) yielded the title compound (MW 389.66, 96%) as a white tacky solid.

R_f = 0.38 (SiO_2, pentane/EtOAc 4:1).

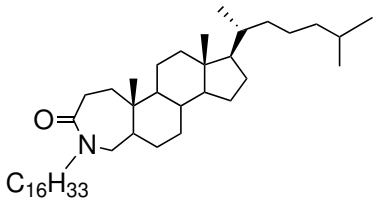
IR (ATR, cm^{-1}) 2914, 2848, 1626, 1487, 1466, 1428, 1210.

^{1}H NMR (400 MHz, $CDCl_3$) δ 3.37 (m, 3H), 2.87-2.84 (m, 1H), 2.06 (br s, 2H), 2.00-1.85 (m, 4H), 1.83-1.75 (m, 4H), 1.69 (br s, 2H), 1.54-1.42 (m, 2H), 1.31 (br s, 26H), 0.87 (br t, J = 6.8 Hz, 3H).

^{13}C NMR (100 MHz, $CDCl_3$) δ 178.60, 52.98, 49.10, 42.42, 35.83, 34.54, 31.91, 31.15, 29.68, 29.64, 29.58, 29.51, 29.34, 28.05, 26.97, 26.34, 22.68, 14.10.

HRMS (ES+) calc. for $C_{26}H_{48}NO$: $(M + H)^+$, 390.3736, found: $(M + H)^+$, 390.3758.

5α-cholestan-3-one derived ϵ-lactams (50)



From 5α-cholestan-3-one **55**.

Column chromatography (SiO_2, pentane/EtOAc 9:1) yielded the title compound (MW 625.62, 80%) as a white tacky solid.

R_f = 0.42 (SiO_2, pentane/EtOAc 4:1).

IR (ATR, cm^{-1}) 2922, 2851, 1631, 1467, 1375.

^{1}H NMR (400 MHz, $CDCl_3$) δ 3.61 (dd, J = 15.4, 8.7 Hz, 1H), 3.32 (m, 2H), 2.60 (t, J = 13.5 Hz, 1H), 2.49 (d, J = 15.4 Hz, 1H), 2.31 (dd, J = 14.4, 7.3 Hz, 1H), 1.97 (br d, J = 12.4 Hz, 1H), 1.91–0.81 (m, 69H), 0.64 (s, 3H).

^{13}C NMR (100 MHz, $CDCl_3$) δ 175.09, 56.40, 56.25, 53.99, 51.43, 48.93, 48.17, 42.34, 39.93, 39.51, 38.07, 36.15, 35.92, 35.79, 35.03, 32.45, 31.93, 31.90, 29.71, 29.67, 29.61, 29.56, 29.47, 29.36, 28.43, 28.23, 28.00, 26.93, 24.16, 23.84, 22.80, 22.69, 22.55, 20.99, 18.63, 14.11, 12.10, 12.02.

HRMS (ES+) calc. for $C_{43}H_{80}NO$: $(M + H)^+$, 626.6240, found: $(M + H)^+$, 626.6227.

8.2.4 Dissolving metal reduction of tertiary amides and *N*-alkylated lactams

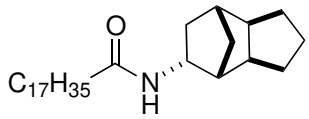
Typical Procedure

A schlenk flask with glass stirring bar was charged with complexant HMHC **1** (340 mg, 1.00 mmol, 10 eq.) and NaK (180 mg, 3.00 mmol, 30 eq., 1:1 atomic ratio, syringed from the center of a stock liquid) in an argon glovebox and connected to an argon Schlenk line. Then, the mixture was cooled to 0 °C in an isopropanol bath (DANGER: Do not use water baths with reaction mixtures involving alkali metals!) and dry THF (7.0 mL) was added under argon counterflow. The mixture immediately formed a deep blue color and was stirred for 10 min at 0 °C to ensure a sufficient alkalide concentration. A solution of amide or lactam substrate (0.10 mmol, 1.0 eq.) in dry THF (2.0 mL) was then added dropwise via a syringe at such a rate as to maintain a blue solution (approx. 3 h) after which the flask was sealed.

After stirring at 25 °C for 20 h, the blue solution was quenched and decolorized by addition of a small amount of water (10 µL), carefully decanted from excess NaK droplets and added to wet ether. A sequence of washing with water, sat. aq. sodium bicarbonate solution, water and brine was applied after confirmation that the crude mixture of relevant products was not affected. The organic layer was separated, dried (Na_2SO_4), and carefully evaporated under reduced pressure. Excess HMHC was partially recovered by extraction of all combined aqueous layers with CH_2Cl_2, separation of the organic layer, drying (Na_2SO_4), and evaporation of the solvent under reduced pressure.

NMR yields were obtained from the crude mixture at this stage. Column chromatography (SiO_2, pentane/EtOAc 49:1 $\rightarrow$ 4:1) yielded the pure secondary amide and any unfunctionalised fragments. No acidic components were identified during the workup and analysis of any acidified aqueous layer.

***N*-8-tricyclodecanyl stearoylamide (54)**



Dissolving metal reduction of *N*-3β-Cholestanyl-8-tricyclodecanyl-stearoylamide **44c** using HMHC(**1**)/NaK/THF system.

Column chromatography (SiO_2, pentane/EtOAc 49:1 → 4:1) yielded the title compound (MW 417.71, 48%) as well as cholestane (MW 388.68, 48%), each as a white tacky solid. Unreacted starting material was recovered (49%).

R_f (**54**) = 0.10 (SiO_2, pentane/EtOAc 9:1).

IR (ATR, cm^{-1}) 3293, 2916, 2849, 1636, 1543, 1467.

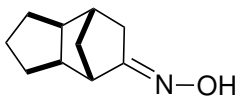
^{1}H NMR (400 MHz, $CDCl_3$) δ 5.37 (m, 1H), 4.15–4.06 (m, 1H), 2.22 (br d, J = 3.9 Hz, 1H), 2.18–1.99 (m, 4H), 1.95 (br d, J = 4.6 Hz, 1H), 1.92–1.55 (m, 7H), 1.43–1.37 (m, 1H), 1.36–1.06 (m, 30H), 1.04–0.91 (m, 2H), 0.88 (t, J = 6.8 Hz, 3H), 0.65–0.54 (ddd, $J = 12.8, 4.5, 3.1$ Hz, 1H).

^{13}C NMR (100 MHz, $CDCl_3$) δ 173.11, 49.96, 48.47, 44.63, 40.97, 39.53, 37.67, 37.02, 32.51, 32.21, 31.99, 31.92, 29.69, 29.65, 29.61, 29.53, 29.35, 27.08, 25.88, 22.68, 14.10.

HRMS (ES+) calc. for $C_{28}H_{52}NO$: $(M + H)^+$, 418.4049, found: $(M + H)^+$, 418.4068.

8.2.5 Preparation of precursors and other compounds

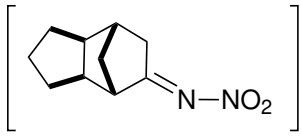
8-Tricyclodecanone oxime 28



A solution of 8-tricyclodecanone **29** (5.00 g, 33 mmol, 1.0 eq) and hydroxylamine hydrochloride (7.00 g, 100 mmol, 3.0 eq.) in pyridine (30 mL) was heated at 75 °C for 2 h. The mixture was poured into cold water (100 mL) and extracted with CH_2Cl_2 (3× 50 mL). The combined organic layers were concentrated to dryness *in vacuo* and the residue recrystallized from hexane to obtain 5.20 g (MW 165.12, 31.5 mmol, 96%) of the title compound (racemic mixture) as a beige solid.

Physical and spectroscopic data were in agreement with those previously reported. [159]

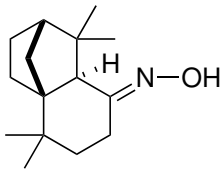
8-Nitrimino-tricyclodecane 30 [145]



To a cold mixture of 8-tricyclodecanone oxime **28** (170 mg, 1.00 mmol, 1.0 eq.) in ether (15 mL) and a solution of sodium nitrite (400 mg, 5.80 mmol, 5.8 eq.) in water (2.0 mL) was added cold 2.0 M H_2SO_4 (4.0 mL, 4.00 mmol, 4.0 eq.) in one portion and the mixture shaken several times. The aqueous layer was withdrawn and discarded. The ethereal layer was allowed to stand at room temperature for 5 h, washed with water (1×10 mL), sat. aq. $NaHCO_3$ solution (2×10 mL), water (1×10 mL), sat. aq. NaCl solution (1×10 mL), dried (Na_2SO_4), and filtered. The resulting ethereal solution contains the unstable title compound (mixture of isomers, >60% yield) which was used *in situ* for the next step. Alternatively, it can be evaporated and re-dissolved in dry methanol for immediate use in the next step.

Selected spectroscopic features of the title compound in the crude mixture:
IR (ATR, cm^{-1}) 2951, 2864, 1650, 1561, 1312.
^{1}H NMR (400 MHz, $CDCl_3$) δ 2.84 (s) / 2.73 (s).
^{13}C NMR (100 MHz, $CDCl_3$) δ 186.72, 186.41.

Isolongifolanone oxime 26



A solution of isolongifolanone **27** (180 mg, 0.800 mmol, 1.0 eq.) and hydroxylamine hydrochloride (170 mg, 2.40 mmol, 3.0 eq.) in pyridine (2.0 mL) was heated at 75 °C for 2 h. The mixture was poured into cold water (5.0 mL) and extracted with CH_2Cl_2 (3× 5.0 mL) to give the crude product which solidified upon standing at 25 °C and was recrystallized from ether/hexane to obtain the title compound (180 mg, MW 235.37, 0.790 mmol, 99%) of the title compound as a white solid.

R_f = 0.10 (SiO_2, pentane/EtOAc 9:1).

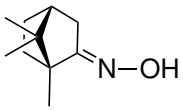
IR (ATR, cm^{-1}) 3244, 2942, 2868, 1687, 1467, 1383, 1366.

^{1}H NMR (400 MHz, $CDCl_3$) δ 8.45 (br s, 1H), 2.78 (dddd, J = 19.4, 9.7, 9.7, 0.8 Hz, 1H), 2.35 (ddd, J = 19.5, 9.2, 2.0 Hz, 1H), 2.02 (m, 1H), 1.83–1.65 (m, 4H), 1.61 (dd, J = 12.0, 4.0 Hz, 1H), 1.37 (ddd, J = 13.8, 9.5, 2.1 Hz, 1H), 1.17 (m, 1H), 1.13 (s, 3H), 1.08–1.01 (m, 1H), 0.92 (s, 3H), 0.90 (s, 3H), 0.83 (s, 3H).

^{13}C NMR (100 MHz, $CDCl_3$) δ 161.07, 55.42, 54.68, 47.95, 45.22, 37.63, 33.30, 31.74, 31.33, 27.57, 26.13, 25.69, 24.54, 23.11, 20.36.

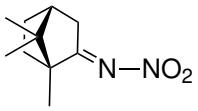
The molecular structure and absolute configuration of the major isomer was determined by X-ray crystallography.

(+)-Camphor oxime (20) [135]



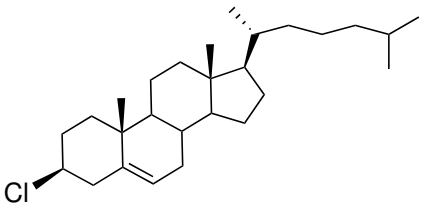
To a solution of (+)-camphor **56** (5.0 g, 32.8 mmol, 1.0 eq.) in absolute ethanol (50 mL) were added pyridine (4.0 mL, 49.4 mmol, 1.5 eq.) and hydroxylamine hydrochloride (5.00 g, 71.9 mmol, 2.2 eq.). The mixture was stirred under reflux for 5 h. After cooling to RT, most of the solvent was removed *in vacuo* and 25 mL of water were added. The precipitate was filtered, washed, and dried *in vacuo* to obtain the title compound (5.0 g, MW 167.25, 29.8 mmol, 91%) as white crystals. Physical and spectroscopic data are in agreement with those previously reported. [135]

(+)-Camphor nitrimine (10) [135]



To a solution of (+)-camphor oxime **20** (600 mg, 3.60 mmol, 1.0 eq.) in glacial acetic acid (17.9 mL) was added a 5% aq. solution of sodium nitrite (8.9 mL, 6.50 mmol, 1.8 eq.). The solution turned yellow immediately after the addition of sodium nitrite and the color faded within 30 min. The reaction mixture was stirred for 3 h after which it was quenched by addition of water (15 mL) and the resulting precipitate was filtered off. The solid was washed with water and dried *in vacuo* to obtain the title compound (440 mg, MW 196.25, 2.23 mmol, 62%) as a very pale yellow crystals. Physical and spectroscopic data are in agreement with those previously reported. [135]

Cholesteryl Chloride (36) [153]



A mixture of cholesterol **35** (3.6 g, 9.30 mmol, 1.0 eq.) and thionyl chloride (10 mL) was allowed to stand at 25 °C for 2 h. The excess reagent was removed under reduced pressure, benzene (10 mL) was added and the solution again concentrated. The dark brown residue was recrystallised from hot acetone to obtain the title compound (3.6 g, MW 405.10, 8.77 mmol, 94%) as yellow crystals.

R_f = 0.70 (SiO_2, pentane).

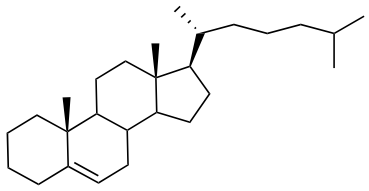
mp 91–94 °C (lit. 93–95.5 °C [153]).

IR (ATR, cm^{-1}) 2933, 2865, 1715, 1670, 1467, 1445, 1434, 1377, 1334.

^{1}H NMR (400 MHz, $CDCl_3$) δ 5.37 (m, 1H), 3.76 (m, 1H), 2.56 (m, 1H), 2.48 (m, 1H), 2.10–1.92 (m, 3H), 1.92–1.78 (m, 3H), 1.61–0.85 (m, 32H) [incl. methyl groups: 1.03 (s, 3H), 0.91 (d, J = 6.5 Hz, 3H), 0.87 (d, J = 1.8 Hz, 3H), 0.86 (d, J = 1.8 Hz, 3H)], 0.68 (s, 3H).

^{13}C NMR (100 MHz, $CDCl_3$) δ 140.81, 122.48, 60.33, 56.70, 56.15, 50.08, 43.41, 42.31, 39.71, 39.52, 39.12, 36.38, 36.19, 35.78, 33.39, 31.83, 31.78, 28.21, 28.01, 24.27, 23.83, 22.82, 22.56, 20.96, 19.25, 18.72, 11.85.

5-Cholestene (37) [153]



To a boiling solution of cholesteryl chloride **36** (3.6 g, 9.00 mmol, 1.0 eq.) in isoamyl alcohol (80 mL) under an argon atmosphere was added sodium (6.3 g, exc.) in small chunks. After all the metal had reacted (approx. 4 h), the solution was cooled to 25 °C and then diluted with water (100 mL). The mixture was extracted with ether (100 mL), the ethereal solution washed successively with water, 1 M aq. HCl solution, water, sat. aq. sodium bicarbonate solution, water and finally brine. After drying over anhyd. Na_2SO_4, the ethereal solution was concentrated under reduced pressure. The residue was recrystallized from methanol to obtain the title compound (3.1 g, MW 370.65, 8.28 mmol, 92%) as colorless fine needles.

R_f = 0.89 (SiO_2, pentane).

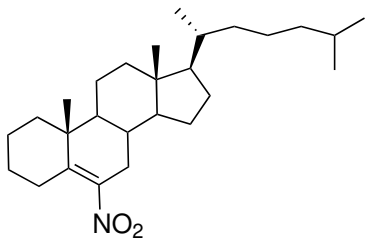
mp 88–90 °C (lit. 89.5–91.2 °C [153]).

IR (ATR, cm^{-1}) 2929, 2885, 1462, 1374, 1364.

^{1}H NMR (400 MHz, $CDCl_3$) δ 5.27 (m, 1H), 2.29–2.19 (m, 1H), 2.03–1.92 (m, 3H), 1.88–1.78 (m, 2H), 1.75–1.70 (m, 1H), 1.62–0.84 (m, 35H) [incl. methyl groups: 1.00 (s, 3H), 0.92 (d, J = 6.6 Hz, 3H), 0.88 (d, J = 1.8 Hz, 3H), 0.86 (d, J = 1.8 Hz, 3H)], 0.68 (s, 3H).

^{13}C NMR (100 MHz, $CDCl_3$) δ 143.73, 118.98, 56.89, 56.19, 50.61, 42.31, 39.89, 39.54, 37.54, 36.22, 35.81, 32.91, 31.90, 31.86, 28.26, 28.08, 28.03, 24.29, 23.85, 22.83, 22.57, 20.78, 19.48, 18.74, 11.88.

6-Nitrocholest-5-ene (38) [152]



Fuming nitric acid (15 mL, freshly prepared and distilled from KNO_3/H_2SO_4) was added dropwise during 10 min to a stirred solution of cholest-5-ene **37** (2.50 g, 6.70 mmol, 1.0 eq.) in dry ether (30 mL) at −5 °C. After 25 min at −5 °C the temperature was slowly raised to 10 °C and stirring continued until brown fumes appeared above the liquid (approx. 1.5 h total). Dilution with water, extraction with ether, and recrystallization from methanol gave the title compound (1.26 g, MW 415.65, 3.00 mmol, 45%) as colorless needles.

R_f = 0.32 (SiO_2, pentane/EtOAc 44:1).

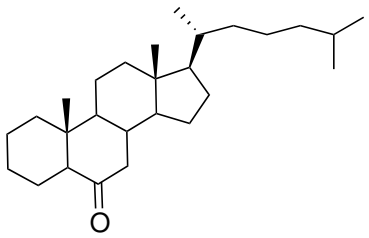
mp 118–121 °C (lit. 120–121.5 °C [152]).

IR (ATR, cm^{-1}) 2932, 2865, 1514, 1460, 1444, 1348.

^{1}H NMR (400 MHz, $CDCl_3$) δ 2.54–2.44 (m, 2H), 2.19–2.00 (m, 3H), 1.99–1.91 (m, 1H), 1.90–1.75 (m, 2H), 1.65–0.96 (m, 25H) [incl. methyl groups: 1.09 (s, 3H), 0.91 (d, J = 6.6 Hz, 3H), 0.87 (d, J = 1.9 Hz, 3H), 0.86 (d, J = 1.9 Hz, 3H)], 0.68 (s, 3H).

^{13}C NMR (100 MHz, $CDCl_3$) δ 144.67, 141.06, 56.19, 56.00, 56.00, 49.48, 42.28, 39.47, 39.42, 39.35, 38.53, 36.12, 35.72, 33.32, 31.49, 28.11, 28.00, 26.61, 25.79, 24.11, 23.82, 22.80, 22.54, 21.60, 21.11, 20.72, 19.63, 18.68, 11.80.

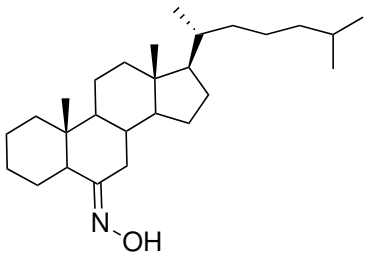
5α-Cholestan-6-one (39) [154]



A solution of 6-nitrocholest-5-ene **38** (1.0 g, 2.40 mmol, 1.0 eq.) in glacial acetic acid (5.0 mL) was diluted with water (2.0 mL). Zinc dust (2.0 g, 31.3 mmol, 13 eq.) was added to the solution in small portions within 5 min (exothermic reaction) and the resulting suspension was heated under reflux for 4 h. The hot solution was then filtered, the filtrate was diluted with water (20 mL) and cooled in an ice-water bath. The white precipitate was collected by filtration and recrystallized from absolute ethanol to obtain the title compound (0.70 g, MW 386.65, 1.80 mmol, 75%) as colorless needles.

Physical and spectroscopic data are in agreement with those previously reported. [160]

5α-Cholestan-6-one oxime (40) [152]



A solution of 5α-cholestan-6-one **39** (1.2 g, 3.10 mmol, 1.0 eq.), hydroxylamine hydrochloride (0.60 g, 8.60 mmol, 2.8 eq.), and sodium acetate hexahydrate (1.2 g) in absolute ethanol (45 mL) was stirred under reflux for 2 h. After addition of water (50 mL) the product was collected by filtration, washed with water, and dried *in vacuo*. The crude material was recrystallized from ethyl acetate to obtain the title compound (1.2 g, MW 401.67, 2.90 mmol, 95%) as beige fine needles.

R_f = 0.46 (SiO_2, pentane/EtOAc 9:1).

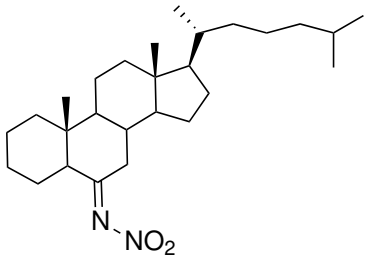
mp 192–197 °C (lit. 204–206 °C [152]).

IR (ATR, cm^{-1}) 3261, 2929, 2863, 1654, 1466, 1443, 1382.

^{1}H NMR (400 MHz, $CDCl_3$) δ 9.57 (br s, 1H), 3.31 (dd, J = 13.6, 4.5 Hz, 1H), 2.04–0.84 (m, 39H) [incl. methyl groups: 0.90 (d, J = 6.5 Hz, 3H), 0.87 (d, J = 1.8 Hz, 3H), 0.85 (d, J = 1.8 Hz, 3H)], 0.74 (s, 3H), 0.65 (s, 3H).

^{13}C NMR (100 MHz, $CDCl_3$) δ 160.81, 56.82, 56.19, 54.74, 51.68, 42.90, 39.79, 39.65, 39.50, 37.92, 36.14, 35.73, 35.70, 29.64, 28.16, 28.00, 26.00, 24.06, 23.81, 22.81, 22.56, 22.11, 21.64, 21.07, 18.66, 12.60, 12.08.

6-Nitrimino-5α-cholestane (34) [145]



To a cold mixture of 5α-Cholestan-6-one oxime **40** (200 mg, 0.500 mmol, 1.0 eq.) in ether (10 mL) and a solution of sodium nitrite (200 mg, 2.90 mmol, 5.8 eq.) in water (1.0 mL) was added cold 2.0 M H_2SO_4 (2.0 mL, 2.00 mmol, 4.0 eq.) in one portion and the mixture was shaken several times. The aqueous layer was withdrawn and discarded. The ethereal layer was allowed to stand at 25 °C for 5 h, washed with water, dried (Na_2SO_4), filtered, concentrated to dryness *in vacuo*, and the residue purified by column chromatography (SiO_2, EtOAc/hexane 1:45). The isolated material was recrystallized from methanol to obtain the title compound (150 mg, MW 430.67, 0.350 mmol, 70%) as colorless crystals.

R_f = 0.5 (SiO_2, pentane/EtOAc 19:1).

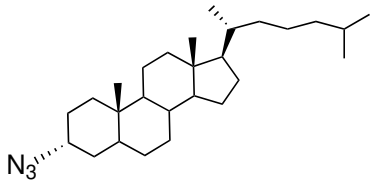
mp 83–87 °C (lit. 84–87 °C [152]).

IR (ATR, cm^{-1}) 2932, 2867, 1626, 1561, 1466, 1382, 1308.

^{1}H NMR (400 MHz, $CDCl_3$) δ 2.42–2.38 (m, 1H), 2.09 (dd, J = 11.9, 3.2 Hz, 1H), 2.04–2.00 (m, 1H), 1.89–0.95 (m, 28H) 0.90 (d, J = 6.5 Hz, 3H), 0.87 (d, J = 1.9 Hz, 3H), 0.85 (d, J = 1.9 Hz, 3H), 0.83 (s, 3H), 0.65 (s, 3H).

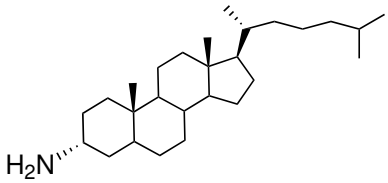
^{13}C NMR (100 MHz, $CDCl_3$) δ 179.51, 56.46, 56.06, 54.55, 52.72, 43.12, 42.28, 39.47, 39.42, 38.35, 38.25, 36.56, 36.08, 35.66, 28.00, 25.38, 23.89, 23.80, 22.80, 22.54, 21.58, 21.36, 21.09, 18.61, 12.66, 12.06.

3α-azido-5α-cholestane 33 [148]



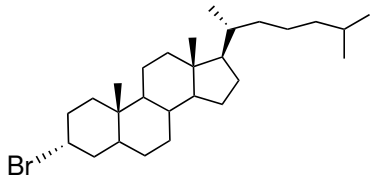
To a magnetically stirred solution of 5α-cholestan-3β-ol (1.9 g, 5.00 mmol, 1.0 eq.), PPH_3 (1.3 g, 5.00 mmol, 1.0 eq.) and diethylazodicarboxylate (0.87 g, 5.00 mmol, 1.0 eq.) in dry THF, a solution of diphenylphosphoryl azide (1.4 g, 5.00 mmol, 1.0 eq.) was added over a period of 15 min and stirring was continued for about 24 h. When the solvent was removed from the reaction mixture under reduced pressure, a thick, oily liquid was obtained which solidified on standing. The title compound was isolated by chromatography through a silica plug using benzene-hexane (50:50) as eluent. The first few fractions (50 mL) were evaporated and yielded the title compound (1.1 g, MW 413.68, 2.71 mmol, 54%) as a white solid. Physical and spectroscopic data are in agreement with those previously reported. [149]

3α-amino-5α-cholestane 32 [149]



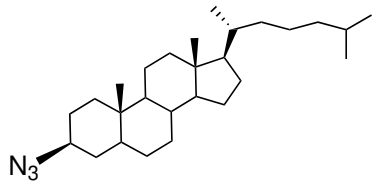
A 1.0 M suspension of $LiAlH_4$ in THF (14 mL, 14.4 mmol, 2.4 eq.) was cooled to 0 °C in an ice–water-salt bath at which temperature 3α-azido-5α-cholestane **33** (2.5 g, 6.00 mmol, 1.0 eq.) was added slowly to the flask. When the initial gas evolution had ceased, the resulting suspension was refluxed for 4 h. After refluxing and cooling to RT, the mixture was diluted with THF to double the volume. The solution was cooled in an ice-water bath and water (⅛ of THF volume), 10 M NaOH (⅕ of THF volume), and water (⅛ of THF volume) were added successively. The solid that formed was filtered off and the filtrate was dried with Na_2SO_4 and concentrated to give the title compound (2.4 g, MW 387.68, 5.82 mmol, 97%) as a white tacky solid. Physical and spectroscopic data are in agreement with those previously reported. [149]

3α-bromo-5α-cholestane 47 [156]



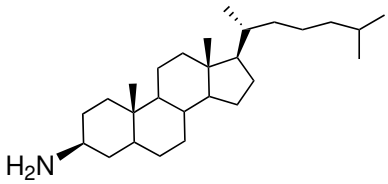
A solution of 5α-cholestan-3β-ol (1.2 g, 3.00 mmol, 1.0 eq.) in anhydrous THF (70 mL) was cooled to 4 °C by an ice-water bath. PPh_3 (1.2 g, 4.50 mmol, 1.5 eq.) was added, the reaction was stirred for 5 min, and a solution of CBr_4 (1.5 g, 4.50 mmol, 1.5 eq.) in anhydrous THF (30 mL) was added dropwise. The reaction was slowly warmed to 25 °C and stirred for 16 h. The solvent was removed *in vacuo*. The resulting residue was resuspended in hexanes (100 mL) and filtered under vacuum to remove insoluble material. The filtrate was concentrated under reduced pressure to give a yellowish solid. Column chromatography (SiO_2, pentane) yielded the title compound (0.60 g (MW 451.57, 1.32 mmol, 44%) as a white solid. Physical and spectroscopic data are in agreement with those previously reported. [156]

3β-azido-5α-cholestane 48 [156]



To a solution of 3α-bromo-5α-cholestane **47** (900 mg, 2.00 mmol, 1.0 eq.) in DMSO (20 mL) was added sodium azide (1.3 g, 20.0 mmol, 20 eq.). The reaction was stirred for 6 h at 80 °C, then cooled to 25 °C and poured into DI water containing ice (50 mL). The product was extracted with diethyl ether (4 × 40 mL), and the organic layers were combined, washed with DI water (100 mL), and dried over anhydrous sodium sulfate. The solvent was removed *in vacuo* to obtain the crude product as lightyellow solid. Column chromatography (SiO_2, pentane) yielded the title compound (630 mg, MW 413.68, 1.52 mmol, 76%) as a white solid. Physical and spectroscopic data are in agreement with those previously reported. [156]

3β-amino-5α-cholestane 57 [149]



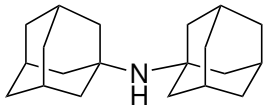
A 1.0 M suspension of $LiAlH_4$ in THF (19 mL, 19.2 mmol, 2.4 eq.) was cooled to 0 °C in an ice–water-salt bath at which temperature 3α-azido-5α-cholestane **33** (3.2 g, 8.00 mmol, 1.0 eq.) was added slowly to the flask. When the initial gas evolution had ceased, the resulting suspension was refluxed for 4 h. After refluxing and cooling to RT, the mixture was diluted with THF to double the volume. The solution was cooled in an ice-water bath and water (⅛ of THF volume), 10 M NaOH (⅕ of THF volume), and water (⅛ of THF volume) were added successively. The solid that formed was filtered off and the filtrate was dried with Na_2SO_4 and concentrated to give the title compound (2.9 g, MW 387.68, 7.44 mmol, 93%) as a white tacky solid. Physical and spectroscopic data are in agreement with those previously reported. [156]

1-azido-hexadecane 58 [161]

$$N_3-C_{16}H_{33}$$

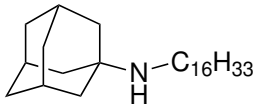
n-Hexadecyl bromide (3.1 mL, 10.0 mmol, 1.0 eq.) and sodium azide (0.78 g, 12.0 mmol, 1.2 eq.) were placed in a 25 mL three-neck round-bottom flask. DMF (80 mL) was added to the reaction flask to make homogeneous solution. The homogeneous solution was kept at 60 °C for 24 h under a nitrogen atmosphere. The products were separated using a mixture of ethyl acetate/water (1:1 %v). The organic phase containing the products was dried with Na_2SO_4 and was filtered. Subsequently, the solvent was evaporated to obtain the title compound (2.5 g, MW 267.45, 9.50 mmol, 95%) as a brown-yellow liquid. Physical and spectroscopic data are in agreement with those previously reported. [161]

1,1-Diadamantylamine 9 [162]



A small stainless steel bomb (inner volume approx. 5 mL), was tightly packed with a ground homogeneous mixture of solid 1-adamantylamine (1.0 g, 6.62 mmol, 2.0 eq.) and 1-adamantyl bromide (0.71 g, 3.31 mmol, 1.0 eq.). After tightly sealing the bomb, it was buried in a sand bath and heated to 220 °C for 48 h. The mass inside the tube turned into a hard beige solid upon cooling to RT. The solid was crushed with a mortar and pestle and dissolved in a mixture of ether (25 mL) and 20% aqueous NaOH (25 mL) by shaking in a separatory funnel. The ether layer was separated and shaken with 10% aq. HCl solution (30 mL) to precipitate di-1-adamantylamine **9** as the hydrochloride salt which was soluble in neither the ether nor aqueous layer. The precipitate was collected by filtration and washed with water. The resulting white solid was shaken with a mixture of ether (20 mL) and 20% aq. NaOH solution (20 mL) to regenerate di-1-adamantylamine **9** in ether. The organic layer was separated and dried over anhyd. Na_2SO_4. Evaporation of the solvent under reduced pressure gave the title compound (0.69 g, MW 285.47, 2.42 mmol, 73%) which was further purified by recrystallization from ether. Physical and spectroscopic data are in agreement with those previously reported. [162]

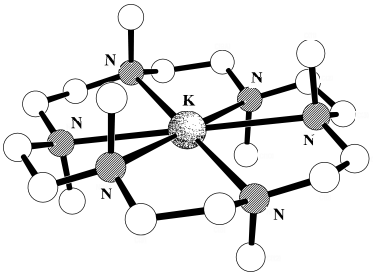
1-Adamantyl-hexadecylamine 8 [163]

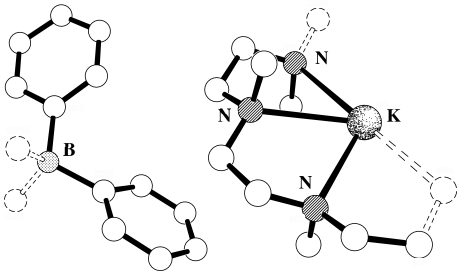


1-Bromohexadecane (1.8 mL, 6.00 mmol, 1.2 eq.) was added to a vigorously stirred solution of 1-adamantylamine (0.76 g, 5.00 mmol, 1.0 eq.) and K_2CO_3 (1.7 g , 12.5 mmol, 2.5 eq.) in DMF (25 mL). The reaction mixture was stirred at 80 °C for 48 h in a flask equipped with a reflux condenser. After evaporation of the solvent, the residue was taken up with water and extracted with CH_2Cl_2. The collected organic layers were concentrated, and the crude was purified by precipitation of the target amine as its HCl-salt from ether and regeneration of the amine by treatment with 4.0 M aq. NaOH solution to obtain the title compound 1.6 g (MW 375.67, 4.25 mmol, 85%) as a white tacky solid. Physical and spectroscopic data are in agreement with those previously reported. [164]

8.3 Crystal data and structures

8.3.1 Crystal data and structure refinement for $HMHC(K)^{+}BPh_4^{-}$





Identification code	AB1603
Formula	$C_{18}H_{42}KN_6$, $C_{24}H_{20}B$
Formula weight	700.88
Temperature	173(2) K
Diffractometer, wavelength	Agilent Xcalibur 3 E, 0.71073 Å
Crystal system, space group	Monoclinic, C2/c
Unit cell dimensions	a = 16.8210(7) Å α = 90° b = 11.1965(4) Å β = 102.896(3)° c = 22.3568(7) Å ς = 90°
Volume, Z	4104.4(3) $Å^3$, 4
Density (calculated)	1.134 Mg/m^3
Absorption coefficient	0.165 mm^{-1}
F(000)	1520
Crystal color / morphology	Colorless blocks
Crystal size	0.35 x 0.28 x 0.23 mm^3
θrange for data collection	2.484 to 28.354°
Index ranges	$-21 \leq h \leq 20$, $-9 \leq k \leq 14$, $-29 \leq l \leq 18$
Reflns collected / unique	6831 / 4097 [R(int) = 0.0238]
Reflns observed [F>4σ(F)]	3151
Absorption correction	Analytical
Max. and min. transmission	0.971 and 0.961
Refinement method	Full-matrix least-squares on F^2
Data / restraints / parameters	4097 / 0 / 231
Goodness-of-fit on F^2	1.031
Final R indices [F>4σ(F)]	$R_1 = 0.0445$, $\omega R_2 = 0.0997$
R indices (all data)	$R_1 = 0.0631$, $\omega R_2 = 0.1099$
Largest diff. peak, hole	0.210, -0.264 $eÅ^{-3}$
Mean and maximum shift/error	0.000 and 0.000

Bond lengths [Å] **Bond angles [°]**

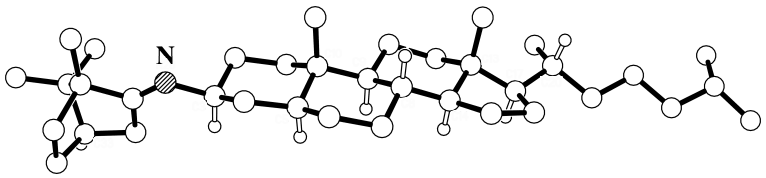
Symmetry transformations used to generate equivalent atoms:
| | #1 -x+½, -y+⅔, -z | | #2 -x+1, y, -z+½ | |

K(1)-N(4)	2.8397(13)	N(4)-K(1)-N(4)#1	180.0
K(1)-N(4)#1	2.8397(13)	N(4)-K(1)-N(7)	61.48(4)
K(1)-N(7)	2.8913(14)	N(4)#1-K(1)-N(7)	118.52(4)
K(1)-N(1)	2.8913(14)	N(4)-K(1)-N(1)	61.80(4)
K(1)-N(7)#1	2.8913(14)	N(4)#1-K(1)-N(1)	118.20(4)
K(1)-N(1)#1	2.8913(14)	N(7)-K(1)-N(1)	119.02(4)
K(1)-C(11)#1	3.1985(19)	N(4)-K(1)-N(7)#1	118.52(4)
K(1)-C(11)	3.1986(19)	N(4)#1-K(1)-N(7)#1	61.48(4)
K(1)-C(12)#1	3.268(2)	N(7)-K(1)-N(7)#1	180.0
K(1)-C(12)	3.268(2)	N(1)-K(1)-N(7)#1	60.98(4)
K(1)-C(10)	3.288(2)	N(4)-K(1)-N(1)#1	118.20(4)
K(1)-C(10)#1	3.288(2)	N(4)#1-K(1)-N(1)#1	61.80(4)
N(1)-C(10)	1.454(2)	N(7)-K(1)-N(1)#1	60.99(4)
N(1)-C(9)#1	1.457(2)	N(1)-K(1)-N(1)#1	180.0
N(1)-C(2)	1.465(2)	N(7)#1-K(1)-N(1)#1	119.01(4)
C(2)-C(3)	1.506(3)	N(4)-K(1)-C(11)#1	152.74(4)
C(3)-N(4)	1.465(2)	N(4)#1-K(1)-C(11)#1	27.26(4)
N(4)-C(5)	1.462(2)	N(7)-K(1)-C(11)#1	109.78(5)
N(4)-C(11)	1.465(2)	N(1)-K(1)-C(11)#1	110.03(4)
C(5)-C(6)	1.512(3)	N(7)#1-K(1)-C(11)#1	70.22(5)
C(6)-N(7)	1.460(2)	N(1)#1-K(1)-C(11)#1	69.96(4)
N(7)-C(12)	1.453(2)	N(4)-K(1)-C(11)	27.26(4)
N(7)-C(8)	1.461(2)	N(4)#1-K(1)-C(11)	152.74(4)
C(8)-C(9)	1.515(3)	N(7)-K(1)-C(11)	70.22(5)
C(9)-N(1)#1	1.457(2)	N(1)-K(1)-C(11)	69.96(4)
B(20)-C(21)	1.640(2)	N(7)#1-K(1)-C(11)	109.78(5)
B(20)-C(21)#2	1.640(2)	N(1)#1-K(1)-C(11)	110.04(4)
B(20)-C(27)#2	1.643(2)	C(11)#1-K(1)-C(11)	180.0
B(20)-C(27)	1.643(2)	N(4)-K(1)-C(12)#1	110.67(5)
C(21)-C(22)	1.396(2)	N(4)#1-K(1)-C(12)#1	69.33(5)
C(21)-C(26)	1.402(2)	N(7)-K(1)-C(12)#1	153.61(4)
C(22)-C(23)	1.387(2)	N(1)-K(1)-C(12)#1	69.53(5)
C(23)-C(24)	1.374(3)	N(7)#1-K(1)-C(12)#1	26.40(4)
C(24)-C(25)	1.383(2)	N(1)#1-K(1)-C(12)#1	110.47(5)
C(25)-C(26)	1.383(2)	C(11)#1-K(1)-C(12)#1	87.85(5)
C(27)-C(28)	1.393(2)	C(11)-K(1)-C(12)#1	92.15(5)
C(27)-C(32)	1.397(2)	N(4)-K(1)-C(12)	69.33(5)
C(28)-C(29)	1.388(2)	N(4)#1-K(1)-C(12)	110.67(5)
C(29)-C(30)	1.380(3)	N(7)-K(1)-C(12)	26.40(4)
C(30)-C(31)	1.372(3)	N(1)-K(1)-C(12)	110.47(5)
C(31)-C(32)	1.387(2)	N(7)#1-K(1)-C(12)	153.60(4)
		N(1)#1-K(1)-C(12)	69.53(5)

C(11)#1-K(1)-C(12)	92.15(5)
C(11)-K(1)-C(12)	87.85(5)
C(12)#1-K(1)-C(12)	180.0
N(4)-K(1)-C(10)	70.04(5)
N(4)#1-K(1)-C(10)	109.96(5)
N(7)-K(1)-C(10)	111.07(5)
N(1)-K(1)-C(10)	26.23(5)
N(7)#1-K(1)-C(10)	68.93(5)
N(1)#1-K(1)-C(10)	153.77(5)
C(11)#1-K(1)-C(10)	92.06(5)
C(11)-K(1)-C(10)	87.94(5)
C(12)#1-K(1)-C(10)	86.91(5)
C(12)-K(1)-C(10)	93.09(5)
N(4)-K(1)-C(10)#1	109.96(5)
N(4)#1-K(1)-C(10)#1	70.04(5)
N(7)-K(1)-C(10)#1	68.93(5)
N(1)-K(1)-C(10)#1	153.77(5)
N(7)#1-K(1)-C(10)#1	111.07(5)
N(1)#1-K(1)-C(10)#1	26.23(5)
C(11)#1-K(1)-C(10)#1	87.94(5)
C(11)-K(1)-C(10)#1	92.06(5)
C(12)#1-K(1)-C(10)#1	93.09(5)
C(12)-K(1)-C(10)#1	86.91(5)
C(10)-K(1)-C(10)#1	180.0
C(10)-N(1)-C(9)#1	111.72(15)
C(10)-N(1)-C(2)	111.36(15)
C(9)#1-N(1)-C(2)	109.62(14)
C(10)-N(1)-K(1)	92.30(11)
C(9)#1-N(1)-K(1)	116.03(11)
C(2)-N(1)-K(1)	114.79(10)
N(1)-C(2)-C(3)	114.17(15)
N(4)-C(3)-C(2)	114.10(14)
C(5)-N(4)-C(3)	108.83(14)
C(5)-N(4)-C(11)	111.04(14)
C(3)-N(4)-C(11)	111.73(14)
C(5)-N(4)-K(1)	117.44(10)
C(3)-N(4)-K(1)	116.37(10)
C(11)-N(4)-K(1)	90.14(9)
N(4)-C(5)-C(6)	114.14(15)
N(7)-C(6)-C(5)	114.24(14)
C(12)-N(7)-C(6)	111.61(15)
C(12)-N(7)-C(8)	111.11(15)
C(6)-N(7)-C(8)	109.67(13)
C(12)-N(7)-K(1)	91.42(11)
C(6)-N(7)-K(1)	115.29(10)
C(8)-N(7)-K(1)	116.53(10)

N(7)-C(8)-C(9)	113.83(14)
N(1)#1-C(9)-C(8)	114.05(15)
N(1)-C(10)-K(1)	61.47(9)
N(4)-C(11)-K(1)	62.60(8)
N(7)-C(12)-K(1)	62.19(10)
C(21)-B(20)-C(21)#2	111.26(18)
C(21)-B(20)-C(27)#2	103.84(7)
C(21)#2-B(20)-C(27)#2	112.78(7)
C(21)-B(20)-C(27)	112.78(7)
C(21)#2-B(20)-C(27)	103.84(7)
C(27)#2-B(20)-C(27)	112.60(18)
C(22)-C(21)-C(26)	114.74(15)
C(22)-C(21)-B(20)	123.33(14)
C(26)-C(21)-B(20)	121.78(13)
C(23)-C(22)-C(21)	122.90(17)
C(24)-C(23)-C(22)	120.42(16)
C(23)-C(24)-C(25)	118.75(16)
C(26)-C(25)-C(24)	120.15(16)
C(25)-C(26)-C(21)	122.99(15)
C(28)-C(27)-C(32)	114.95(15)
C(28)-C(27)-B(20)	122.19(14)
C(32)-C(27)-B(20)	122.56(15)
C(29)-C(28)-C(27)	122.76(17)
C(30)-C(29)-C(28)	120.30(18)
C(31)-C(30)-C(29)	118.81(17)
C(30)-C(31)-C(32)	120.18(17)
C(31)-C(32)-C(27)	123.00(17)

8.3.2 Crystal data and structure refinement for *N*-3β-5α-cholestanyl-bornylimine 11



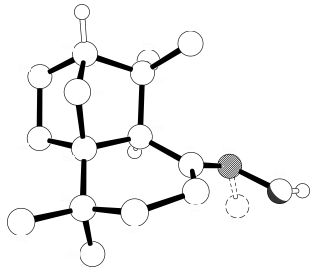
Identification code	AB1705
Formula	$C_{37}H_{63}N$
Formula weight	521.88
Temperature	173(2) K
Diffractometer, wavelength	Agilent Xcalibur PX Ultra A, 1.54184 Å
Crystal system, space group	Monoclinic, $P2_1$
Unit cell dimensions	a = 7.32182(14) Å α = 90°
	b = 9.6895(2) Å β = 93.1990(18)°
	c = 24.0353(5) Å ς = 90°
Volume, Z	1702.51(6) $Å^3$, 2
Density (calculated)	1.018 Mg/m^3
Absorption coefficient	0.416 mm^{-1}
F(000)	584
Crystal color / morphology	Colorless thin plates
Crystal size	0.33 x 0.29 x 0.01 mm^3
θrange for data collection	3.684 to 73.892°
Index ranges	$-6 \leq h \leq 8$, $-7 \leq k \leq 11$, $-29 \leq l \leq 25$
Reflns collected / unique	5705 / 4558 [R(int) = 0.0283]
Reflns observed [F>4σ(F)]	3943
Absorption correction	Analytical
Max. and min. transmission	0.994 and 0.913
Refinement method	Full-matrix least-squares on F^2
Data / restraints / parameters	4558 / 225 / 384
Goodness-of-fit on F^2	1.054
Final R indices [F>4σ(F)]	$R_1 = 0.0421$, $\omega R_2 = 0.1022$
R indices (all data)	$R_1 = 0.0510$, $\omega R_2 = 0.1095$
Absolute structure parameter	-0.4(8)
Largest diff. peak, hole	0.160, -0.176 $eÅ^{-3}$
Mean and maximum shift/error	0.000 and 0.001

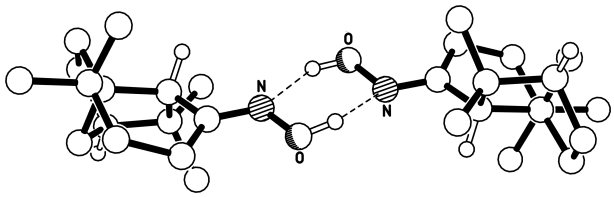
Bond lengths [Å]		Bond angles [°]	
C(1)-C(2)	1.533(3)	C(2)-C(1)-C(10)	112.56(18)
C(1)-C(10)	1.545(3)	C(3)-C(2)-C(1)	112.52(19)
C(2)-C(3)	1.528(3)	N(28)-C(3)-C(4)	109.4(2)
C(3)-N(28)	1.467(3)	N(28)-C(3)-C(2)	107.65(19)
C(3)-C(4)	1.525(3)	C(4)-C(3)-C(2)	110.38(19)
C(4)-C(5)	1.532(3)	C(3)-C(4)-C(5)	112.48(19)
C(5)-C(6)	1.526(3)	C(6)-C(5)-C(4)	112.05(18)
C(5)-C(10)	1.557(3)	C(6)-C(5)-C(10)	111.83(18)
C(6)-C(7)	1.527(3)	C(4)-C(5)-C(10)	112.83(18)
C(7)-C(8)	1.538(3)	C(5)-C(6)-C(7)	112.09(19)
C(8)-C(14)	1.522(3)	C(6)-C(7)-C(8)	112.25(18)
C(8)-C(9)	1.546(3)	C(14)-C(8)-C(7)	111.15(18)
C(9)-C(11)	1.537(3)	C(14)-C(8)-C(9)	108.78(17)
C(9)-C(10)	1.553(3)	C(7)-C(8)-C(9)	110.73(18)
C(10)-C(19)	1.535(3)	C(11)-C(9)-C(8)	110.42(17)
C(11)-C(12)	1.538(3)	C(11)-C(9)-C(10)	113.80(17)
C(12)-C(13)	1.540(3)	C(8)-C(9)-C(10)	112.60(17)
C(13)-C(18)	1.531(3)	C(19)-C(10)-C(1)	108.81(18)
C(13)-C(14)	1.544(3)	C(19)-C(10)-C(9)	110.80(18)
C(13)-C(17)	1.555(3)	C(1)-C(10)-C(9)	110.57(17)
C(14)-C(15)	1.524(3)	C(19)-C(10)-C(5)	112.37(18)
C(15)-C(16)	1.548(3)	C(1)-C(10)-C(5)	106.60(18)
C(16)-C(17)	1.557(3)	C(9)-C(10)-C(5)	107.62(17)
C(17)-C(20)	1.541(3)	C(9)-C(11)-C(12)	112.97(17)
C(20)-C(21)	1.526(4)	C(11)-C(12)-C(13)	111.63(18)
C(20)-C(22)	1.536(4)	C(18)-C(13)-C(12)	110.47(19)
C(22)-C(23)	1.525(4)	C(18)-C(13)-C(14)	112.65(19)
C(23)-C(24")	1.518(15)	C(12)-C(13)-C(14)	106.78(17)
C(23)-C(24)	1.518(8)	C(18)-C(13)-C(17)	110.64(19)
C(23)-C(24')	1.538(13)	C(12)-C(13)-C(17)	116.17(19)
C(24)-C(25)	1.526(8)	C(14)-C(13)-C(17)	99.70(17)
C(25)-C(26)	1.507(10)	C(8)-C(14)-C(15)	119.35(19)
C(25)-C(27)	1.510(11)	C(8)-C(14)-C(13)	115.72(17)
C(24')-C(25')	1.498(14)	C(15)-C(14)-C(13)	103.75(18)
C(25')-C(26')	1.522(15)	C(14)-C(15)-C(16)	103.56(19)
C(25')-C(27')	1.530(14)	C(15)-C(16)-C(17)	106.79(19)
C(24")-C(25")	1.534(16)	C(20)-C(17)-C(13)	119.81(19)
C(25")-C(26")	1.520(16)	C(20)-C(17)-C(16)	112.52(19)
C(25")-C(27")	1.528(17)	C(13)-C(17)-C(16)	103.15(18)
N(28)-C(29)	1.257(4)	C(21)-C(20)-C(22)	110.6(2)
C(29)-C(30)	1.522(4)	C(21)-C(20)-C(17)	113.0(2)
C(29)-C(34)	1.533(4)	C(22)-C(20)-C(17)	110.1(2)
C(30)-C(36)	1.507(5)	C(23)-C(22)-C(20)	115.4(2)
C(30)-C(31)	1.548(5)	C(24")-C(23)-C(22)	112.7(9)

C(30)-C(35)	1.559(5)
C(31)-C(32)	1.538(7)
C(32)-C(33)	1.539(6)
C(33)-C(35)	1.543(5)
C(33)-C(34)	1.545(4)
C(35)-C(37)	1.532(5)
C(35)-C(38)	1.538(4)

C(24)-C(23)-C(22)	113.1(4)
C(22)-C(23)-C(24')	111.0(7)
C(23)-C(24)-C(25)	114.9(7)
C(26)-C(25)-C(27)	116.3(9)
C(26)-C(25)-C(24)	110.8(9)
C(27)-C(25)-C(24)	114.3(7)
C(25')-C(24')-C(23)	118.0(12)
C(24')-C(25')-C(26')	114.7(13)
C(24')-C(25')-C(27')	114.0(13)
C(26')-C(25')-C(27')	111.3(13)
C(23)-C(24")-C(25")	113.2(15)
C(26")-C(25")-C(27")	113.0(16)
C(26")-C(25")-C(24")	111.3(16)
C(27")-C(25")-C(24")	111.8(16)
C(29)-N(28)-C(3)	119.0(2)
N(28)-C(29)-C(30)	123.4(3)
N(28)-C(29)-C(34)	130.2(3)
C(30)-C(29)-C(34)	106.5(3)
C(36)-C(30)-C(29)	114.6(3)
C(36)-C(30)-C(31)	115.1(3)
C(29)-C(30)-C(31)	104.5(3)
C(36)-C(30)-C(35)	118.4(3)
C(29)-C(30)-C(35)	99.9(2)
C(31)-C(30)-C(35)	102.1(3)
C(32)-C(31)-C(30)	104.2(3)
C(31)-C(32)-C(33)	103.3(3)
C(32)-C(33)-C(35)	102.8(3)
C(32)-C(33)-C(34)	106.1(3)
C(35)-C(33)-C(34)	102.3(3)
C(29)-C(34)-C(33)	101.5(3)
C(37)-C(35)-C(38)	107.6(3)
C(37)-C(35)-C(33)	114.2(3)
C(38)-C(35)-C(33)	113.1(4)
C(37)-C(35)-C(30)	113.5(3)
C(38)-C(35)-C(30)	114.2(3)
C(33)-C(35)-C(30)	94.1(3)

8.3.3 Crystal data and structure refinement for *rac*-isolongifolanone oxime 26





Identification code	AB1706
Formula	$C_{15}H_{25}NO$
Formula weight	235.36
Temperature	173(2) K
Diffractometer, wavelength	Agilent Xcalibur PX Ultra A, 1.54184 Å
Crystal system, space group	Monoclinic, Cc
Unit cell dimensions	a = 23.2611(5) Å α = 90°
	b = 13.3529(2) Å β = 101.7441(19)°
	c = 17.7891(4) Å ς = 90°
Volume, Z	5409.66(18) $Å^3$, 16
Density (calculated)	1.156 Mg/m^3
Absorption coefficient	0.545 mm^{-1}
F(000)	2080
Crystal color / morphology	Colorless tabular needles
Crystal size	0.35 x 0.15 x 0.06 mm^3
θrange for data collection	3.837 to 73.895°
Index ranges	$-28 \leq h \leq 27$, $-16 \leq k \leq 15$, $-18 \leq l \leq 22$
Reflns collected / unique	23463 / 7647 [R(int) = 0.0338]
Reflns observed [F>4σ(F)]	6959
Absorption correction	Analytical
Max. and min. transmission	0.971 and 0.870
Refinement method	Full-matrix least-squares on F^2
Data / restraints / parameters	7647 / 30 / 638
Goodness-of-fit on F^2	1.048
Final R indices [F>4σ(F)]	$R_1 = 0.0676$, $\omega R_2 = 0.1664$
R indices (all data)	$R_1 = 0.0727$, $\omega R_2 = 0.1763$
Absolute structure parameter	0.2(4)
Largest diff. peak, hole	0.559, -0.221 $eÅ^{-3}$
Mean and maximum shift/error	0.000 and 0.000

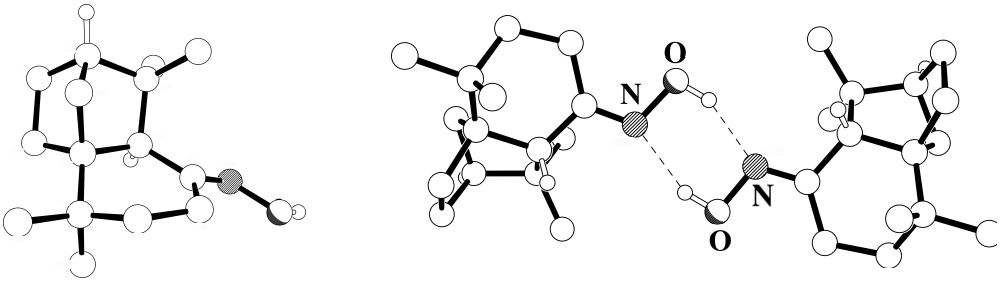
Bond lengths [Å]		Bond angles [°]	
C(1A)-N(12A)	1.283(5)	N(12A)-C(1A)-C(2A)	120.2(3)
C(1A)-C(2A)	1.494(6)	N(12A)-C(1A)-C(10A)	117.0(3)
C(1A)-C(10A)	1.508(4)	C(2A)-C(1A)-C(10A)	122.5(3)
C(2A)-C(3A)	1.521(7)	C(1A)-C(2A)-C(3A)	116.9(4)
C(3A)-C(4A)	1.515(7)	C(4A)-C(3A)-C(2A)	113.3(4)
C(4A)-C(15A)	1.527(6)	C(3A)-C(4A)-C(15A)	107.5(4)
C(4A)-C(14A)	1.530(6)	C(3A)-C(4A)-C(14A)	110.4(4)
C(4A)-C(5A)	1.541(6)	C(15A)-C(4A)-C(14A)	107.9(4)
C(5A)-C(6A)	1.550(5)	C(3A)-C(4A)-C(5A)	108.7(3)
C(5A)-C(11A)	1.551(5)	C(15A)-C(4A)-C(5A)	112.2(3)
C(5A)-C(10A)	1.567(5)	C(14A)-C(4A)-C(5A)	110.2(4)
C(6A)-C(7A)	1.561(6)	C(4A)-C(5A)-C(6A)	116.0(3)
C(7A)-C(8A)	1.542(5)	C(4A)-C(5A)-C(11A)	117.6(3)
C(8A)-C(11A)	1.530(6)	C(6A)-C(5A)-C(11A)	99.9(3)
C(8A)-C(9A)	1.559(5)	C(4A)-C(5A)-C(10A)	114.5(3)
C(9A)-C(16A)	1.518(6)	C(6A)-C(5A)-C(10A)	105.2(3)
C(9A)-C(17A)	1.541(5)	C(11A)-C(5A)-C(10A)	101.5(3)
C(9A)-C(10A)	1.583(5)	C(5A)-C(6A)-C(7A)	104.6(3)
N(12A)-O(13A)	1.416(4)	C(8A)-C(7A)-C(6A)	102.3(3)
N(12A)-O(13E)	1.48(2)	C(11A)-C(8A)-C(7A)	101.5(4)
C(1B)-N(12B)	1.280(5)	C(11A)-C(8A)-C(9A)	102.0(3)
C(1B)-C(10B)	1.508(4)	C(7A)-C(8A)-C(9A)	111.0(3)
C(1B)-C(2B)	1.510(5)	C(16A)-C(9A)-C(17A)	107.7(4)
C(2B)-C(3B)	1.524(5)	C(16A)-C(9A)-C(8A)	114.5(3)
C(3B)-C(4B)	1.547(5)	C(17A)-C(9A)-C(8A)	107.6(3)
C(4B)-C(5B)	1.536(5)	C(16A)-C(9A)-C(10A)	111.6(3)
C(4B)-C(15B)	1.537(5)	C(17A)-C(9A)-C(10A)	114.2(3)
C(4B)-C(14B)	1.538(5)	C(8A)-C(9A)-C(10A)	101.2(3)
C(5B)-C(11B)	1.551(5)	C(1A)-C(10A)-C(5A)	114.8(3)
C(5B)-C(6B)	1.553(5)	C(1A)-C(10A)-C(9A)	116.7(3)
C(5B)-C(10B)	1.554(4)	C(5A)-C(10A)-C(9A)	104.4(3)
C(6B)-C(7B)	1.556(6)	C(8A)-C(11A)-C(5A)	95.5(3)
C(7B)-C(8B)	1.542(5)	C(1A)-N(12A)-O(13A)	113.1(3)
C(8B)-C(11B)	1.540(6)	C(1A)-N(12A)-O(13E)	118(3)
C(8B)-C(9B)	1.556(5)	N(12B)-C(1B)-C(10B)	115.4(3)
C(9B)-C(16B)	1.525(5)	N(12B)-C(1B)-C(2B)	125.0(3)
C(9B)-C(17B)	1.530(5)	C(10B)-C(1B)-C(2B)	119.6(3)
C(9B)-C(10B)	1.587(5)	C(1B)-C(2B)-C(3B)	115.8(3)
N(12B)-O(13B)	1.434(4)	C(2B)-C(3B)-C(4B)	116.2(3)
N(12B)-O(13F)	1.49(2)	C(5B)-C(4B)-C(15B)	113.0(3)
C(1C)-N(12C)	1.282(5)	C(5B)-C(4B)-C(14B)	110.8(3)
C(1C)-C(2C)	1.503(5)	C(15B)-C(4B)-C(14B)	108.3(3)
C(1C)-C(10C)	1.503(4)	C(5B)-C(4B)-C(3B)	108.9(3)
C(2C)-C(3C)	1.532(5)	C(15B)-C(4B)-C(3B)	106.9(3)

C(3C)-C(4C)	1.545(5)
C(4C)-C(5C)	1.524(5)
C(4C)-C(15C)	1.537(5)
C(4C)-C(14C)	1.540(5)
C(5C)-C(11C)	1.547(4)
C(5C)-C(6C)	1.552(5)
C(5C)-C(10C)	1.569(4)
C(6C)-C(7C)	1.540(6)
C(7C)-C(8C)	1.530(6)
C(8C)-C(11C)	1.537(6)
C(8C)-C(9C)	1.561(5)
C(9C)-C(16C)	1.523(6)
C(9C)-C(17C)	1.539(6)
C(9C)-C(10C)	1.572(5)
N(12C)-O(13C)	1.423(4)
N(12C)-O(13G)	1.45(2)
C(1D)-N(12D)	1.273(5)
C(1D)-C(2D)	1.490(5)
C(1D)-C(10D)	1.508(4)
C(2D)-C(3D)	1.538(5)
C(3D)-C(4D)	1.543(5)
C(4D)-C(14D)	1.528(5)
C(4D)-C(5D)	1.532(5)
C(4D)-C(15D)	1.536(5)
C(5D)-C(11D)	1.542(5)
C(5D)-C(6D)	1.545(5)
C(5D)-C(10D)	1.563(4)
C(6D)-C(7D)	1.558(5)
C(7D)-C(8D)	1.521(6)
C(8D)-C(11D)	1.541(5)
C(8D)-C(9D)	1.546(5)
C(9D)-C(16D)	1.520(6)
C(9D)-C(17D)	1.544(6)
C(9D)-C(10D)	1.574(5)
N(12D)-O(13H)	1.43(2)
N(12D)-O(13D)	1.432(4)

C(14B)-C(4B)-C(3B)	108.7(3)
C(4B)-C(5B)-C(11B)	117.8(3)
C(4B)-C(5B)-C(6B)	116.0(3)
C(11B)-C(5B)-C(6B)	99.7(3)
C(4B)-C(5B)-C(10B)	113.6(3)
C(11B)-C(5B)-C(10B)	102.2(3)
C(6B)-C(5B)-C(10B)	105.5(3)
C(5B)-C(6B)-C(7B)	104.4(3)
C(8B)-C(7B)-C(6B)	102.6(3)
C(11B)-C(8B)-C(7B)	100.9(3)
C(11B)-C(8B)-C(9B)	102.2(3)
C(7B)-C(8B)-C(9B)	111.1(3)
C(16B)-C(9B)-C(17B)	107.3(3)
C(16B)-C(9B)-C(8B)	114.7(3)
C(17B)-C(9B)-C(8B)	109.1(3)
C(16B)-C(9B)-C(10B)	111.0(3)
C(17B)-C(9B)-C(10B)	113.8(3)
C(8B)-C(9B)-C(10B)	101.1(3)
C(1B)-C(10B)-C(5B)	113.5(3)
C(1B)-C(10B)-C(9B)	116.0(3)
C(5B)-C(10B)-C(9B)	104.5(3)
C(8B)-C(11B)-C(5B)	95.1(3)
C(1B)-N(12B)-O(13B)	112.5(3)
C(1B)-N(12B)-O(13F)	131(3)
N(12C)-C(1C)-C(2C)	123.5(3)
N(12C)-C(1C)-C(10C)	114.5(3)
C(2C)-C(1C)-C(10C)	122.0(3)
C(1C)-C(2C)-C(3C)	115.8(3)
C(2C)-C(3C)-C(4C)	115.4(3)
C(5C)-C(4C)-C(15C)	112.2(3)
C(5C)-C(4C)-C(14C)	111.0(3)
C(15C)-C(4C)-C(14C)	108.2(3)
C(5C)-C(4C)-C(3C)	109.3(3)
C(15C)-C(4C)-C(3C)	107.0(3)
C(14C)-C(4C)-C(3C)	109.0(3)
C(4C)-C(5C)-C(11C)	117.6(3)
C(4C)-C(5C)-C(6C)	116.8(3)
C(11C)-C(5C)-C(6C)	100.6(3)
C(4C)-C(5C)-C(10C)	113.3(3)
C(11C)-C(5C)-C(10C)	101.3(3)
C(6C)-C(5C)-C(10C)	105.1(3)
C(7C)-C(6C)-C(5C)	103.7(3)
C(8C)-C(7C)-C(6C)	103.8(3)
C(7C)-C(8C)-C(11C)	100.9(3)
C(7C)-C(8C)-C(9C)	111.2(3)
C(11C)-C(8C)-C(9C)	101.9(3)

C(16C)-C(9C)-C(17C)	107.8(4)
C(16C)-C(9C)-C(8C)	113.9(3)
C(17C)-C(9C)-C(8C)	109.2(3)
C(16C)-C(9C)-C(10C)	111.8(3)
C(17C)-C(9C)-C(10C)	113.3(3)
C(8C)-C(9C)-C(10C)	100.8(3)
C(1C)-C(10C)-C(5C)	113.6(3)
C(1C)-C(10C)-C(9C)	116.7(3)
C(5C)-C(10C)-C(9C)	104.8(3)
C(8C)-C(11C)-C(5C)	94.9(3)
C(1C)-N(12C)-O(13C)	113.3(3)
C(1C)-N(12C)-O(13G)	127(3)
N(12D)-C(1D)-C(2D)	124.5(3)
N(12D)-C(1D)-C(10D)	114.2(3)
C(2D)-C(1D)-C(10D)	121.3(3)
C(1D)-C(2D)-C(3D)	115.6(3)
C(2D)-C(3D)-C(4D)	116.0(3)
C(14D)-C(4D)-C(5D)	110.3(3)
C(14D)-C(4D)-C(15D)	108.3(3)
C(5D)-C(4D)-C(15D)	112.7(3)
C(14D)-C(4D)-C(3D)	109.7(3)
C(5D)-C(4D)-C(3D)	108.5(3)
C(15D)-C(4D)-C(3D)	107.3(3)
C(4D)-C(5D)-C(11D)	117.5(3)
C(4D)-C(5D)-C(6D)	116.7(3)
C(11D)-C(5D)-C(6D)	100.7(3)
C(4D)-C(5D)-C(10D)	113.2(3)
C(11D)-C(5D)-C(10D)	101.7(3)
C(6D)-C(5D)-C(10D)	105.1(3)
C(5D)-C(6D)-C(7D)	103.5(3)
C(8D)-C(7D)-C(6D)	103.4(3)
C(7D)-C(8D)-C(11D)	100.8(3)
C(7D)-C(8D)-C(9D)	111.0(3)
C(11D)-C(8D)-C(9D)	102.2(3)
C(16D)-C(9D)-C(17D)	107.6(4)
C(16D)-C(9D)-C(8D)	114.2(3)
C(17D)-C(9D)-C(8D)	109.3(3)
C(16D)-C(9D)-C(10D)	111.2(3)
C(17D)-C(9D)-C(10D)	113.1(3)
C(8D)-C(9D)-C(10D)	101.5(3)
C(1D)-C(10D)-C(5D)	113.7(3)
C(1D)-C(10D)-C(9D)	116.7(3)
C(5D)-C(10D)-C(9D)	104.3(3)
C(8D)-C(11D)-C(5D)	95.0(3)
C(1D)-N(12D)-O(13H)	119(2)
C(1D)-N(12D)-O(13D)	113.0(3)

8.3.4 Crystal data and structure refinement for *R*-isolongifolanone oxime 26



Identification code	AB1707
Formula	$C_{15}H_{25}NO$
Formula weight	235.36
Temperature	173(2) K
Diffractometer, wavelength	Agilent Xcalibur PX Ultra A, 1.54184 Å
Crystal system, space group	Orthorhombic, $P2_12_12_1$
Unit cell dimensions	a = 9.6956(2) Å $\alpha = 90°$ b = 11.7474(2) Å $\beta = 90°$ c = 23.9324(6) Å $\varsigma = 90°$
Volume, Z	2725.85(11) $Å^3$, 8
Density (calculated)	1.156 Mg/m^3
Absorption coefficient	1.147 mm^{-1}
F(000)	1040
Crystal color / morphology	Colorless blocks
Crystal size	0.31 x 0.29 x 0.12 mm^3
θrange for data collection	3.694 to 73.594°
Index ranges	$-11 \leq h \leq 8$, $-13 \leq k \leq 14$, $-28 \leq l \leq 28$
Reflns collected / unique	8009 / 5199 [R(int) = 0.0292]
Reflns observed [F>4σ(F)]	4511
Absorption correction	Analytical
Max. and min. transmission	0.948 and 0.883
Refinement method	Full-matrix least-squares on F^2
Data / restraints / parameters	7647 / 30 / 638
Goodness-of-fit on F^2	1.023
Final R indices [F>4σ(F)]	$R_1 = 0.0434$, $\omega R_2 = 0.1063$
R indices (all data)	$R_1 = 0.0518$, $\omega R_2 = 0.1141$
Absolute structure parameter	-0.02(19)
Largest diff. peak, hole	0.296, -0.152 $eÅ^{-3}$
Mean and maximum shift/error	0.000 and 0.000

Bond lengths [Å]

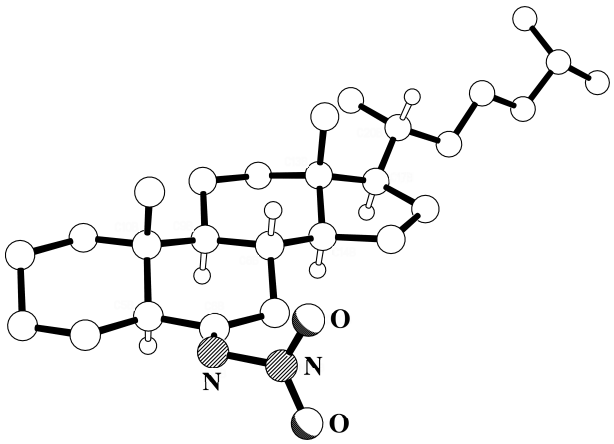
C(1A)-N(12A)	1.278(3)
C(1A)-C(2A)	1.508(3)
C(1A)-C(10A)	1.512(3)
C(2A)-C(3A)	1.521(4)
C(3A)-C(4A)	1.542(4)
C(4A)-C(5A)	1.530(3)
C(4A)-C(15A)	1.531(3)
C(4A)-C(14A)	1.533(4)
C(5A)-C(6A)	1.546(3)
C(5A)-C(11A)	1.548(3)
C(5A)-C(10A)	1.568(3)
C(6A)-C(7A)	1.561(4)
C(7A)-C(8A)	1.535(4)
C(8A)-C(11A)	1.521(4)
C(8A)-C(9A)	1.567(4)
C(9A)-C(16A)	1.529(4)
C(9A)-C(17A)	1.532(4)
C(9A)-C(10A)	1.579(3)
N(12A)-O(13A)	1.419(3)
C(1B)-N(12B)	1.274(3)
C(1B)-C(2B)	1.504(3)
C(1B)-C(10B)	1.517(3)
C(2B)-C(3B)	1.524(4)
C(3B)-C(4B)	1.541(4)
C(4B)-C(14B)	1.532(4)
C(4B)-C(15B)	1.533(3)
C(4B)-C(5B)	1.533(3)
C(5B)-C(6B)	1.543(3)
C(5B)-C(11B)	1.548(3)
C(5B)-C(10B)	1.566(3)
C(6B)-C(7B)	1.559(4)
C(7B)-C(8B)	1.542(4)
C(8B)-C(11B)	1.524(4)
C(8B)-C(9B)	1.556(3)
C(9B)-C(16B)	1.536(4)
C(9B)-C(17B)	1.538(4)
C(9B)-C(10B)	1.580(3)
N(12B)-O(13B)	1.418(3)

Bond angles [°]

N(12A)-C(1A)-C(2A)	122.2(2)
N(12A)-C(1A)-C(10A)	115.1(2)
C(2A)-C(1A)-C(10A)	122.5(2)
C(1A)-C(2A)-C(3A)	115.7(2)
C(2A)-C(3A)-C(4A)	115.3(2)
C(5A)-C(4A)-C(15A)	111.7(2)
C(5A)-C(4A)-C(14A)	110.5(2)
C(15A)-C(4A)-C(14A)	108.6(2)
C(5A)-C(4A)-C(3A)	108.5(2)
C(15A)-C(4A)-C(3A)	107.1(2)
C(14A)-C(4A)-C(3A)	110.4(2)
C(4A)-C(5A)-C(6A)	116.6(2)
C(4A)-C(5A)-C(11A)	117.4(2)
C(6A)-C(5A)-C(11A)	99.9(2)
C(4A)-C(5A)-C(10A)	113.61(19)
C(6A)-C(5A)-C(10A)	105.09(19)
C(11A)-C(5A)-C(10A)	102.14(19)
C(5A)-C(6A)-C(7A)	103.2(2)
C(8A)-C(7A)-C(6A)	103.5(2)
C(11A)-C(8A)-C(7A)	101.1(2)
C(11A)-C(8A)-C(9A)	101.6(2)
C(7A)-C(8A)-C(9A)	111.5(2)
C(16A)-C(9A)-C(17A)	107.7(2)
C(16A)-C(9A)-C(8A)	113.7(2)
C(17A)-C(9A)-C(8A)	109.9(2)
C(16A)-C(9A)-C(10A)	111.2(2)
C(17A)-C(9A)-C(10A)	114.0(2)
C(8A)-C(9A)-C(10A)	100.42(19)
C(1A)-C(10A)-C(5A)	114.69(19)
C(1A)-C(10A)-C(9A)	115.7(2)
C(5A)-C(10A)-C(9A)	104.65(18)
C(8A)-C(11A)-C(5A)	95.5(2)
C(1A)-N(12A)-O(13A)	112.65(19)
N(12B)-C(1B)-C(2B)	122.4(2)
N(12B)-C(1B)-C(10B)	114.7(2)
C(2B)-C(1B)-C(10B)	122.8(2)
C(1B)-C(2B)-C(3B)	115.4(2)
C(2B)-C(3B)-C(4B)	114.9(2)
C(14B)-C(4B)-C(15B)	108.9(2)
C(14B)-C(4B)-C(5B)	111.0(2)
C(15B)-C(4B)-C(5B)	111.2(2)
C(14B)-C(4B)-C(3B)	110.0(2)
C(15B)-C(4B)-C(3B)	107.4(2)
C(5B)-C(4B)-C(3B)	108.4(2)

C(4B)-C(5B)-C(6B)	116.4(2)
C(4B)-C(5B)-C(11B)	117.3(2)
C(6B)-C(5B)-C(11B)	99.7(2)
C(4B)-C(5B)-C(10B)	113.91(19)
C(6B)-C(5B)-C(10B)	104.92(19)
C(11B)-C(5B)-C(10B)	102.61(18)
C(5B)-C(6B)-C(7B)	103.0(2)
C(8B)-C(7B)-C(6B)	103.70(19)
C(11B)-C(8B)-C(7B)	100.9(2)
C(11B)-C(8B)-C(9B)	101.58(19)
C(7B)-C(8B)-C(9B)	111.4(2)
C(16B)-C(9B)-C(17B)	107.3(2)
C(16B)-C(9B)-C(8B)	113.2(2)
C(17B)-C(9B)-C(8B)	110.2(2)
C(16B)-C(9B)-C(10B)	112.5(2)
C(17B)-C(9B)-C(10B)	113.5(2)
C(8B)-C(9B)-C(10B)	100.30(19)
C(1B)-C(10B)-C(5B)	115.37(19)
C(1B)-C(10B)-C(9B)	115.2(2)
C(5B)-C(10B)-C(9B)	104.52(18)
C(8B)-C(11B)-C(5B)	95.35(19)
C(1B)-N(12B)-O(13B)	113.5(2)

8.3.5 Crystal data and structure refinement for 6-nitrimino-5α-cholestane 34



Identification code	AB1713
Formula	$C_{27}H_{46}N_2O_2$
Formula weight	430.66
Temperature	173(2) K
Diffractometer, wavelength	Agilent Xcalibur PX Ultra A, 1.54184 Å
Crystal system, space group	Monoclinic, $P2_1$
Unit cell dimensions	a = 10.8571(2) Å α = 90°
	b = 14.2420(3) Å β = 94.1766(17)°
	c = 16.5989(3) Å ς = 90°
Volume, Z	2559.83(8) $Å^3$, 4
Density (calculated)	1.117 Mg/m^3
Absorption coefficient	0.533 mm^{-1}
F(000)	952
Crystal color / morphology	Colorless blocks
Crystal size	0.45 x 0.30 x 0.19 mm^3
θrange for data collection	4.095 to 73.864°
Index ranges	$-13 \leq h \leq 8$, $-17 \leq k \leq 11$, $-20 \leq l \leq 19$
Reflns collected / unique	8654 / 6794 [R(int) = 0.0263]
Reflns observed [F>4σ(F)]	5705
Absorption correction	Analytical
Max. and min. transmission	0.930 and 0.865
Refinement method	Full-matrix least-squares on F^2
Data / restraints / parameters	6794 / 1 / 570
Goodness-of-fit on F^2	1.033
Final R indices [F>4σ(F)]	$R_1 = 0.0414$, $\omega R_2 = 0.0995$
R indices (all data)	$R_1 = 0.0529$, $\omega R_2 = 0.1092$
Absolute structure parameter	-0.1(2)
Largest diff. peak, hole	0.178, -0.181 $eÅ^{-3}$
Mean and maximum shift/error	0.000 and 0.000

Bond lengths [Å]		Bond angles [°]	
C(1A)-C(2A)	1.537(4)	C(2A)-C(1A)-C(10A)	113.1(3)
C(1A)-C(10A)	1.542(4)	C(3A)-C(2A)-C(1A)	111.8(3)
C(2A)-C(3A)	1.526(6)	C(4A)-C(3A)-C(2A)	111.3(3)
C(3A)-C(4A)	1.517(5)	C(3A)-C(4A)-C(5A)	109.9(3)
C(4A)-C(5A)	1.533(4)	C(6A)-C(5A)-C(4A)	114.2(3)
C(5A)-C(6A)	1.499(5)	C(6A)-C(5A)-C(10A)	110.3(2)
C(5A)-C(10A)	1.561(4)	C(4A)-C(5A)-C(10A)	113.6(3)
C(6A)-N(28A)	1.281(4)	N(28A)-C(6A)-C(5A)	117.5(3)
C(6A)-C(7A)	1.503(4)	N(28A)-C(6A)-C(7A)	126.7(3)
C(7A)-C(8A)	1.547(4)	C(5A)-C(6A)-C(7A)	115.8(3)
C(8A)-C(14A)	1.532(4)	C(6A)-C(7A)-C(8A)	111.5(3)
C(8A)-C(9A)	1.541(4)	C(14A)-C(8A)-C(9A)	109.1(2)
C(9A)-C(11A)	1.541(4)	C(14A)-C(8A)-C(7A)	110.9(2)
C(9A)-C(10A)	1.555(4)	C(9A)-C(8A)-C(7A)	111.0(2)
C(10A)-C(19A)	1.538(4)	C(8A)-C(9A)-C(11A)	110.8(2)
C(11A)-C(12A)	1.546(4)	C(8A)-C(9A)-C(10A)	112.3(2)
C(12A)-C(13A)	1.534(4)	C(11A)-C(9A)-C(10A)	113.8(2)
C(13A)-C(18A)	1.535(4)	C(19A)-C(10A)-C(1A)	110.2(3)
C(13A)-C(14A)	1.547(4)	C(19A)-C(10A)-C(9A)	111.6(2)
C(13A)-C(17A)	1.564(3)	C(1A)-C(10A)-C(9A)	109.6(2)
C(14A)-C(15A)	1.523(4)	C(19A)-C(10A)-C(5A)	110.0(2)
C(15A)-C(16A)	1.550(4)	C(1A)-C(10A)-C(5A)	107.5(2)
C(16A)-C(17A)	1.564(4)	C(9A)-C(10A)-C(5A)	107.9(2)
C(17A)-C(20A)	1.536(4)	C(9A)-C(11A)-C(12A)	113.5(2)
C(20A)-C(21A)	1.528(5)	C(13A)-C(12A)-C(11A)	111.3(2)
C(20A)-C(22A)	1.545(4)	C(12A)-C(13A)-C(18A)	111.0(2)
C(22A)-C(23A)	1.524(4)	C(12A)-C(13A)-C(14A)	107.3(2)
C(23A)-C(24A)	1.521(4)	C(18A)-C(13A)-C(14A)	111.8(2)
C(24A)-C(25A)	1.537(4)	C(12A)-C(13A)-C(17A)	116.7(2)
C(25A)-C(27A)	1.509(5)	C(18A)-C(13A)-C(17A)	109.2(2)
C(25A)-C(26A)	1.530(5)	C(14A)-C(13A)-C(17A)	100.5(2)
N(28A)-N(29A)	1.421(4)	C(15A)-C(14A)-C(8A)	118.8(2)
N(29A)-O(30A)	1.210(4)	C(15A)-C(14A)-C(13A)	104.7(2)
N(29A)-O(31A)	1.221(4)	C(8A)-C(14A)-C(13A)	113.1(2)
C(1B)-C(2B)	1.533(4)	C(14A)-C(15A)-C(16A)	103.4(3)
C(1B)-C(10B)	1.542(4)	C(15A)-C(16A)-C(17A)	107.2(2)
C(2B)-C(3B)	1.527(5)	C(20A)-C(17A)-C(13A)	118.2(2)
C(3B)-C(4B)	1.528(5)	C(20A)-C(17A)-C(16A)	112.2(2)
C(4B)-C(5B)	1.528(4)	C(13A)-C(17A)-C(16A)	103.8(2)
C(5B)-C(6B)	1.508(5)	C(21A)-C(20A)-C(17A)	112.9(2)
C(5B)-C(10B)	1.563(4)	C(21A)-C(20A)-C(22A)	108.8(2)
C(6B)-N(28B)	1.274(4)	C(17A)-C(20A)-C(22A)	111.6(2)
C(6B)-C(7B)	1.509(4)	C(23A)-C(22A)-C(20A)	113.9(2)
C(7B)-C(8B)	1.549(4)	C(24A)-C(23A)-C(22A)	113.0(2)

C(8B)-C(14B)	1.520(4)
C(8B)-C(9B)	1.536(4)
C(9B)-C(11B)	1.538(4)
C(9B)-C(10B)	1.561(4)
C(10B)-C(19B)	1.533(4)
C(11B)-C(12B)	1.537(4)
C(12B)-C(13B)	1.528(4)
C(13B)-C(18B)	1.540(4)
C(13B)-C(14B)	1.547(4)
C(13B)-C(17B)	1.556(4)
C(14B)-C(15B)	1.522(4)
C(15B)-C(16B)	1.551(4)
C(16B)-C(17B)	1.566(4)
C(17B)-C(20B)	1.530(4)
C(20B)-C(21B)	1.529(5)
C(20B)-C(22B)	1.541(4)
C(22B)-C(23B)	1.524(4)
C(23B)-C(24B)	1.518(5)
C(24B)-C(25B)	1.526(5)
C(25B)-C(27B)	1.476(8)
C(25B)-C(26B)	1.520(6)
N(28B)-N(29B)	1.425(4)
N(29B)-O(30B)	1.214(3)
N(29B)-O(31B)	1.220(3)

C(23A)-C(24A)-C(25A)	115.3(3)
C(27A)-C(25A)-C(26A)	110.9(3)
C(27A)-C(25A)-C(24A)	112.8(3)
C(26A)-C(25A)-C(24A)	109.7(3)
C(6A)-N(28A)-N(29A)	114.5(3)
O(30A)-N(29A)-O(31A)	125.3(3)
O(30A)-N(29A)-N(28A)	117.4(3)
O(31A)-N(29A)-N(28A)	117.0(3)
C(2B)-C(1B)-C(10B)	113.6(3)
C(3B)-C(2B)-C(1B)	111.6(3)
C(2B)-C(3B)-C(4B)	110.8(3)
C(3B)-C(4B)-C(5B)	110.4(3)
C(6B)-C(5B)-C(4B)	113.6(3)
C(6B)-C(5B)-C(10B)	110.0(2)
C(4B)-C(5B)-C(10B)	113.3(2)
N(28B)-C(6B)-C(5B)	116.9(3)
N(28B)-C(6B)-C(7B)	126.7(3)
C(5B)-C(6B)-C(7B)	116.4(3)
C(6B)-C(7B)-C(8B)	111.9(2)
C(14B)-C(8B)-C(9B)	111.2(2)
C(14B)-C(8B)-C(7B)	111.3(2)
C(9B)-C(8B)-C(7B)	110.1(2)
C(8B)-C(9B)-C(11B)	112.1(2)
C(8B)-C(9B)-C(10B)	111.0(2)
C(11B)-C(9B)-C(10B)	113.5(2)
C(19B)-C(10B)-C(1B)	109.6(2)
C(19B)-C(10B)-C(9B)	111.3(2)
C(1B)-C(10B)-C(9B)	110.9(2)
C(19B)-C(10B)-C(5B)	110.2(2)
C(1B)-C(10B)-C(5B)	107.9(2)
C(9B)-C(10B)-C(5B)	106.8(2)
C(12B)-C(11B)-C(9B)	113.1(2)
C(13B)-C(12B)-C(11B)	111.8(2)
C(12B)-C(13B)-C(18B)	110.5(2)
C(12B)-C(13B)-C(14B)	106.8(2)
C(18B)-C(13B)-C(14B)	112.0(2)
C(12B)-C(13B)-C(17B)	117.5(2)
C(18B)-C(13B)-C(17B)	109.4(2)
C(14B)-C(13B)-C(17B)	100.2(2)
C(8B)-C(14B)-C(15B)	118.3(2)
C(8B)-C(14B)-C(13B)	113.8(2)
C(15B)-C(14B)-C(13B)	104.0(2)
C(14B)-C(15B)-C(16B)	103.9(2)
C(15B)-C(16B)-C(17B)	106.7(2)
C(20B)-C(17B)-C(13B)	119.1(2)
C(20B)-C(17B)-C(16B)	112.4(2)

C(13B)-C(17B)-C(16B)	103.1(2)
C(21B)-C(20B)-C(17B)	112.6(3)
C(21B)-C(20B)-C(22B)	109.6(3)
C(17B)-C(20B)-C(22B)	111.0(2)
C(23B)-C(22B)-C(20B)	113.9(3)
C(24B)-C(23B)-C(22B)	113.9(3)
C(23B)-C(24B)-C(25B)	115.4(3)
C(27B)-C(25B)-C(26B)	109.4(5)
C(27B)-C(25B)-C(24B)	112.0(4)
C(26B)-C(25B)-C(24B)	111.4(4)
C(6B)-N(28B)-N(29B)	114.2(2)
O(30B)-N(29B)-O(31B)	125.1(3)
O(30B)-N(29B)-N(28B)	117.5(2)
O(31B)-N(29B)-N(28B)	117.2(3)

8.4 Supporting information

All ^{1}H NMR, ^{13}C NMR and MS spectra are available from the author.

References

[1] Edwards P.P. The electronic properties of metal solutions in liquid ammonia and related solvents. *Advances in Inorganic Chemistry and Radiochemistry*, 25, 135–185, 1982. doi:10.1016/S0898-8838(08)60140-3.

[2] Weyl W. Ueber metallammonium-verbindungen. *Annalen der Physik*, 121, 601–612, 1864. doi:10.1002/andp.18641970407.

[3] Thompson J.C. *Electrons in liquid ammonia*. Monographs on the Physics and Chemistry of Materials. Clarendon Press, 1976. ISBN 9780198513438.

[4] Kraus C.A. Solutions of metals in non-metallic solvents; i. general properties of solutions of metals in liquid ammonia. *Journal of the American Chemical Society*, 29(11), 1557–1571, 1907. doi:10.1021/ja01965a003.

[5] Down J.L., Lewis J., Moore B., Wilkinson G. The solubility of alkali metals in ethers. *Journal of the Chemical Society (Resumed)*, 209, 3767, 1959. doi:10.1039/jr9590003767.

[6] Pedersen C.J. Cyclic polyethers and their complexes with metal salts. *Journal of the American Chemical Society*, 89(26), 7017–7036, 1967. doi:10.1021/ja01002a035.

[7] Dye J.L., DeBacker M.G., Nicely V.A. Solubilization of alkali metals in tetrahydrofuran and diethyl ether by use of a cyclic polyether. *Journal of the American Chemical Society*, 92(17), 5226–5228, 1970. doi:10.1021/ja00720a043.

[8] Kaempf B., Raynal S., Collet A., Schu. Die aufl o sung von alkalimetallen in aromatischen kohlenwasserstoffen durch kryptatbildung. *Angewandte Chemie*, 86(18), 670–671, 1974. doi:10.1002/ange.19740861806.

[9] Blades H., Hodgins J.W. Absorption spectra of metals in solution. *Canadian Journal of Chemistry*, 22(2), 411–425, 1955. doi:10.1139/v55-049.

[10] Douthit R.C., Dye J.L. Absorption spectra of sodium and potassium in liquid ammonia. *Journal of the American Chemical Society*, 82(17), 4472–4478, 1960. doi:10.1021/ja01502a009.

[11] Burow D.F., Lagowski J.J. *Solvated Electron - Spectroscopy of Dilute Metal-Deuteroammonia Solutions*. 1965. doi:10.1021/ba-1965-0050.ch010.

[12] Lindner J., Unterreiner A.N., Vöhringer P. Femtosecond relaxation dynamics of solvated electrons in liquid ammonia. *ChemPhysChem*, 7(2), 363–369, 2006. doi:10.1002/cphc.200500467.

[13] Harris R.L., Lagowski J.J. Metal-ammonia solutions. 12. effect of 18-crown-6 on spectra of potassium-ammonia solutions. *The Journal of Physical Chemistry*, 84(10), 1091–1096, 1980. doi:10.1021/j100447a004.

[14] Jortner J. Energy levels of bound electrons in liquid ammonia. *The Journal of Chemical Physics*, 30(3), 839–846, 1959. doi:10.1063/1.1730055.

[15] Copeland D.A., Kestner N.R., Jortner J. Excess electrons in polar solvents. *The Journal of Chemical Physics*, 53(3), 1189–1216, 1970. doi:10.1063/1.1674119.

[16] Zurek E., Edwards P.P., Hoffmann R. A molecular perspective on lithium-ammonia solutions. *Angewandte Chemie (International ed. in English)*, 48(44), 8198–232, 2009. doi:10.1002/anie.200900373.

[17] Varriale L., Tonge N.M., Bhalla N., Ellis A.M. Communications: The electronic spectrum of li(nh3)4. *The Journal of Chemical Physics*, 132(16), 3, 2010. doi:10.1063/1.3396023.

[18] Dye J.L., Redko M.Y., Huang R.H., Jackson J.E. Role of cation complexants in the synthesis of alkalides and electrides. *Adv. Inorg. Chem.*, 59, 205–231, 2006. doi:10.1016/S0898-8838(06)59006-3.

[19] Dye J.L. Compounds of alkali metal anions. *Angewandte Chemie International Edition in English*, 18(8), 587–598, 1979. doi:10.1002/anie.197905871.

[20] Greene R.N. 18-crown-6: a strong complexing agent for alkali metal cations. *Tetrahedron Letters*, 18, 1793–1796, 1972. doi:10.1016/S0040-4039(01)85270-9.

[21] Dye J.L. Electrides: ionic salts with electrons as the anions. *Science (New York, N.Y.)*, 247(4943), 663–8, 1990. doi:10.1126/science.247.4943.663.

[22] Dye J.L. *Progress in Inorganic Chemistry*, volume 32 of *Progress in Inorganic Chemistry*. John Wiley & Sons Inc., 1984. ISBN 9780470166338. doi:10.1002/9780470166338.

[23] Dye J.L. Electrons as anions. *Science (New York, N.Y.)*, 301(5633), 607–8, 2003. doi:10.1126/science.1088103.

[24] Dye J.L. Electrides: early examples of quantum confinement. *Acc Chem Res*, 42(10), 1564–72, 2009. doi:10.1021/ar9000857.

[25] Dye J.L. The alkali metals: 200 years of surprises. *Philos Trans A Math Phys Eng Sci*, 373(2037), 2015. doi:10.1098/rsta.2014.0174.

[26] Issa D., Dye J.L. Synthesis of cesium 18-crown-6: the first single-crystal electride? *Journal of the American Chemical Society*, 104(13), 3781–3782, 1982. doi:10.1021/ja00377a066.

[27] Hansell C. Electrides explained. *Nature Chemistry*, 7(5), 369–369, 2015. doi:10.1038/nchem.2254.

[28] Jedlinski Z., Stolarzewicz A., Grobelny Z., Szwarc M. Solvated electrons, and not potassium (k-) anions, the initial products of dissolution of potassium by solutions of crown ethers. *The Journal of Physical Chemistry*, 88(25), 6094–6095, 1984. doi:10.1021/j150669a006.

[29] Barrett A.G.M., Godfrey C.R.A., Hollinshead D.M., Prokopiou P.A., Barton D.H.R., et al. Dissolving metal reduction of esters to alkanes. a method for the deoxygenation of alcohols. *Journal of the Chemical Society, Perkin Transactions 1*, pages 1501–1509, 1981. doi:10.1039/p19810001501.

[30] Kuchenmeister M.E., Dye J.L. Synthesis and structures of two thermally stable sodides with the macrocyclic complexant hexamethyl hexacyclen. *Journal of the American Chemical Society*, 111, 935–938, 1989. doi:10.1021/ja00185a024.

[31] Kuchenmeister M.E. *"Synthesis and characterization of new alkalides and electrides via the tertiary amine complexing agents: Steps toward thermal stability"*. Doctoral thesis. Michigan State University, Michigan, 1989.

[32] Ellaboudy A.S., Bender C.J., Kim J., Shin D.h., Kuchenmeister M.E., et al. Multinuclear endor study of trapped electrons in the polycrystalline sodide cs+(hmhcy)na-. *Journal of the American Chemical Society*, 113(7), 2347–2352, 1991.

[33] Redko M.Y., Vlassa M., Jackson J.E., Misiolek A.W., Huang R.H., et al. Inverse sodium hydride - a crystalline salt that contains h+ and na-. *J. Am. Chem. Soc.*, 124(21), 5928–5929, 2002. doi:10.1021/ja025655+.

[34] Redko M.Y., Jackson J.E., Huang R.H., Dye J.L. Design and synthesis of a thermally stable organic electride. *J Am Chem Soc*, 127(35), 12,416–22, 2005. doi:10.1021/ja053216f.

[35] Vlassa M., Huang R., Jackson J.E., Dye J.L. Synthesis and characterization of 4,7-dimethyl-1,4,7,10,15,18-hexaazabicyclo[8.5.5]octane. crystal structures of the cryptate and of the first small azacage complexes with six-coordinate lithium geometry. *Tetrahedron*, 58(29), 5849–5854, 2002. doi:10.1016/s0040-4020(02)00562-8.

[36] Matalon S., Golden S., Ottolenghi M. Nature of the visible absorption bands in metal-amine solutions. *The Journal of Physical Chemistry*, 73(9), 3098–3101, 1969. doi:10.1021/j100843a052.

[37] Lok M.T., Tehan F.J., Dye J.L. Spectra of na-, k-, and e-solv in amines and ethers. *The Journal of Physical Chemistry*, 76, 2975–2981, 1972.

[38] Barthel E.R., Martini I.B., Schwartz B.J. Direct observation of charge-transfer-to-solvent (ctts) reactions: Ultrafast dynamics of the photoexcited alkali metal anion sodide (na-). *The Journal of Chemical Physics*, 112(21), 9433–9444, 2000. doi:10.1063/1.481563.

[39] Barthel E.R., Martini I.B., Schwartz B.J. How does the solvent control electron transfer? experimental and theoretical studies of the simplest charge transfer reaction. *The Journal of Physical Chemistry B*, 105(49), 12,230–12,241, 2001. doi:10.1021/jp011150e.

[40] Martini I.B., Barthel E.R., Schwartz B.J. Manipulating the production and recombination of electrons during electron transfer: femtosecond control of the charge-transfer-to-solvent (ctts) dynamics of the sodium anion. *Journal of the American Chemical Society*, 124(25), 7622–7634, 2002. doi:10.1021/ja025942d.

[41] Cavanagh M.C., Larsen R.E., Schwartz B.J. Watching na atoms solvate into (na+,e-) contact pairs: untangling the ultrafast charge-transfer-to-solvent dynamics of na- in tetrahydrofuran (thf). *J Phys Chem A*, 111(24), 5144–57, 2007. doi:10.1021/jp071132i.

[42] Bragg A.E., Cavanagh M.C., Schwartz B.J. Linear response breakdown in solvation dynamics induced by atomic electron-transfer reactions. *Science*, 321(5897), 1817–22, 2008. doi:10.1126/science.1161511.

[43] Edwards P.P. Magnetic resonance studies of alkali metals in nonaqueous solvents. *The Journal of Physical Chemistry*, 88(17), 3772–3780, 1984. doi:10.1021/j150661a019.

[44] Ceraso J.M., Dye J.L. 23na nmr spectrum of the sodium anion. *The Journal of Chemical Physics*, 61(4), 1585, 1974. doi:10.1063/1.1682119.

[45] Edwards P.P., Ellaboudy A.S., Holton D.M. Nmr spectrum of the potassium anion k-. *Nature*, 317(6034), 242–244, 1985. doi:10.1038/317242a0.

[46] Ellaboudy A.S., Holton D.M., Pyper N.C., Edwards P.P., Wood B., et al. Gas like nature of the sodium anion in solution. *Nature*, 321(6071), 684–685, 1986. doi:10.1038/321684a0.

[47] Holton D.M., Ellaboudy A., Pyper N.C., Edwards P.P. Nuclear spin-lattice relaxation in the sodium anion, na-. *The Journal of Chemical Physics*, 84(3), 1089, 1986. doi:10.1063/1.450551.

[48] Pyper N.C., Edwards P.P. Nuclear shielding in the alkali metal anions. *Journal of the American Chemical Society*, 108(1), 78–81, 1986. doi:10.1021/ja00261a013.

[49] Tinkham M.L., Dye J.L. First observation by potassium-39 nmr of k- in solution and in crystalline potassides. *Journal of the American Chemical Society*, 107(21), 6129–6130, 1985. doi:10.1021/ja00307a063.

[50] Edwards P.P., Ellaboudy A.S., Holton D.M., Pyper N.C. The chemical dynamics of na-in liquid 12-crown-4 solutions deduced from23na nuclear spin relaxation rates. *Molecular Physics*, 69(2), 209–227, 1990. doi:10.1080/00268979000100151.

[51] Dye J.L., Andrews C.W., Ceraso J.M. Nuclear magnetic resonance studies of alkali metal anions. *The Journal of Physical Chemistry*, 79(26), 3076–3079, 1975. doi:10.1021/j100593a058.

[52] Dye J.L., Andrews C.W., Mathews S.E. Strategies for the preparation of compounds of alkali metal anions. *The Journal of Physical Chemistry*, 79(26), 3065–3070, 1975. doi:10.1021/j100593a056.

[53] Sokól M., Grobelny J., Jedliński Z.J. 39k nmr spectroscopy of potassium solutions in tetrahydrofuran containing 18-crown-6. relaxation study. *Magnetic Resonance in Chemistry*, 28(11), 934–938, 1990. doi:10.1002/mrc.1260281106.

[54] Sokól M., Grobelny J., Grobelny Z., Jedliński Z.J. A 39k nmr study of potassium solution in tetrahydrofuran containing cryptand[2.2.2]. *Spectrochimica Acta Part A: Molecular Spectroscopy*, 47(11), 1547–1550, 1991. doi:10.1016/0584-8539(91)80249-i.

[55] Sokól M., Grobelny J., Grobelny Z., Stolarzewicz A. Relaxation study of potassium anions and cations in tetrahydrofuran containing 15-crown-5 by potassium-39 nmr. *The Journal of Physical Chemistry*, 97(3), 763–766, 1993. doi:10.1021/j100105a038.

[56] Sokól M., Grobelny Z., Stolarzewicz A. Different behavior of k- and na- interacting with k+ complexed by dicyclohexano-24-crown-8 in tetrahydrofuran. *The Journal of Physical Chemistry*, 99(33), 12,670–12,676, 1995. doi:10.1021/j100033a046.

[57] Zurek E. Alkali metals in ethylenediamine: a computational study of the optical absorption spectra and nmr parameters of m(en)3(δ+)·m(δ-) ion pairs. *Journal of the American Chemical Society*, 133(13), 4829–39, 2011. doi:10.1021/ja1085244.

[58] Dewald R.R., Dye J.L. Solubilities and conductances of alkali metals in ethylenediamine. *The Journal of Physical Chemistry*, 68(1), 128–134, 1964. doi:10.1021/j100783a021.

[59] Huang R.H., Ward D.L., Dye J.L. Alkali-metal-anion dimers and chains in alkalide structures. *Journal of the American Chemical Society*, 111(15), 5707–5708, 1989. doi:10.1021/ja00197a031.

[60] Wasse J.C., Howard C.A., Thompson H., Skipper N.T., Delaplane R.G., et al. The structure of calcium-ammonia solutions by neutron diffraction. *J Chem Phys*, 121(2), 996–1004, 2004. doi:10.1063/1.1755663.

[61] Wasse J.C., Hayama S., Skipper N.T., Benmore C.J., Soper A.K. The structure of saturated lithium– and potassium–ammonia solutions as studied by using neutron diffraction. *The Journal of Chemical Physics*, 112(16), 7147–7151, 2000. doi:10.1063/1.481280.

[62] Wasse J.C., Hayama S., Masmanidis S., Stebbings S.L., Skipper N.T. The structure of lithium–ammonia and sodium–ammonia solutions by neutron diffraction. *The Journal of Chemical Physics*, 118(16), 7486–7494, 2003. doi:10.1063/1.1563594.

[63] Wasse J.C., Hayama S., Skipper N.T., Fischer H.E. Structure of a metallic solution of lithium in ammonia. *Physical Review B*, 61(18), 11,993–11,997, 2000. doi:10.1103/PhysRevB.61.11993.

[64] Hayama S., Wasse J.C., Skipper N.T., Soper A.K. Structure of solutions of lithium in methylamine across the metal-nonmetal transition. *The Journal of Physical Chemistry B*, 106(1), 11–14, 2002. doi:10.1021/jp0155361.

[65] Thompson H., Wasse J.C., Skipper N.T., Hayama S., Bowron D.T., et al. Structural studies of ammonia and metallic lithium-ammonia solutions. *J Am Chem Soc*, 125(9), 2572–81, 2003. doi:10.1021/ja021227s.

[66] Seel A.G., Swan H., Bowron D.T., Wasse J.C., Weller T., et al. Electron solvation and the unique liquid structure of a mixed-amine expanded metal: The saturated li-nh3 -menh2 system. *Angew Chem Int Ed Engl*, 56(6), 1561–1565, 2017. doi:10.1002/anie.201609192.

[67] Dye J.L. Electrides and alkalides - comparison with metal solutions. *Le Journal de Physique IV*, 01(C5), C5–259–C5–282, 1991. doi:10.1051/jp4:1991531.

[68] Rosenthal M.D., Maxfield B.W. Electrical transport properties and preparation of the metal-ammonia compound lithium tetraammine. *Journal of Solid State Chemistry*, 7(2), 109–123, 1973. doi:10.1016/0022-4596(73)90143-6.

[69] Cate R.C., Thompson J.C. Low-temperature electronic properties of li(nh3)4. *Journal of Physics and Chemistry of Solids*, 32(2), 443–447, 1971. doi:10.1016/0022-3697(71)90028-x.

[70] Morgan J.A., Schroeder R.L., Thompson J.C. Phase changes and electrical conductivity of concentrated lithium—ammonia solutions and the solid eutectic. *The Journal of Chemical Physics*, 43(12), 4494–4499, 1965. doi:10.1063/1.1696722.

[71] Lemaster E.W., Thompson J.C. Hall effect, magnetoresistance, and thermoelectric power in lithium tetraammine. *Journal of Solid State Chemistry*, 4(1), 163–171, 1972. doi:10.1016/0022-4596(72)90144-2.

[72] Stacy A.M., Johnson D.C., Sienko M.J. Low temperature magnetic susceptibility of the expanded metal compounds li(nh3)4, li(nd3)4, and li(ch3nh2)4. *The Journal of Chemical Physics*, 76(8), 4248–4254, 1982. doi:10.1063/1.443502.

[73] Glaunsinger W.S., Zolotov S., Sienko M.J. Magnetic susceptibility of tetraamminelithium(zero) in the range 1.5–194°k. *The Journal of Chemical Physics*, 56(10), 4756–4768, 1972. doi:10.1063/1.1676949.

[74] White T.R., Hsu S.P., Mobley M.J., Glaunsinger W.S. Magnetic properties of metal-ammonia compounds. *The Journal of Physical Chemistry*, 88(17), 3890–3895, 1984. doi:10.1021/j150661a039.

[75] Mott N.F. On the transition to metallic conduction in semiconductors. *Canadian Journal of Physics*, 34(12A), 1356–1368, 1956. doi:10.1139/p56-151.

[76] Edwards P.P., Sienko M.J. The transition to the metallic state. *Accounts of Chemical Research*, 15(3), 87–93, 2002. doi:10.1021/ar00075a004.

[77] Wagner M.J., Dye J.L. Alkalides, electrides, and expanded metals. *Annual Review of Materials Science*, 23(1), 223–253, 1993. doi:10.1146/annurev.ms.23.080193.001255.

[78] DeBacker M.G., Mkadmi E.B., Sauvage F.X., Lelieur J.P., Wagner M.J., et al. The lithium-sodium-methylamine system: does a low-melting sodide become a liquid metal? *Journal of the American Chemical Society*, 118(8), 1997–2003, 1996. doi:10.1021/ja952634p.

[79] Pyper N.C., Edwards P.P. Metallization of alkali anions in condensed phases. *Journal of the American Chemical Society*, 122(21), 5092–5099, 2000. doi:10.1021/ja993644j.

[80] Herzfeld K.F. On atomic properties which make an element a metal. *Physical Review*, 29(5), 701–705, 1927. doi:10.1103/PhysRev.29.701.

[81] Lehn J.M. Cryptate inclusion complexes, effects on solute-solute and solute-solvent interactions and on ionic reactivity. *Pure and Applied Chemistry*, 52(10), 2303–2319, 1980. doi:10.1351/pac198052102303.

[82] Grobelny J., Sokól M., Jedliński Z.J. Complexation of potassium cations by tetraglyme and 18-crown-6 as evidenced by 39k nmr spectroscopy. *Magnetic Resonance in Chemistry*, 29(7), 679–680, 1991. doi:10.1002/mrc.1260290708.

[83] Bloembergen N., Purcell E.M., Pound R.V. Relaxation effects in nuclear magnetic resonance absorption. *Physical Review*, 73(7), 679–712, 1948. doi:10.1103/PhysRev.73.679.

[84] Millet O., Loria J.P., Kroenke C.D., Pons M., Palmer A.G. The static magnetic field dependence of chemical exchange linebroadening defines the nmr chemical shift time scale. *Journal of the American Chemical Society*, 122(12), 2867–2877, 2000. doi:10.1021/ja993511y.

[85] Grobelny Z., Stolarzewicz A., Sokol M., Grobelny J., Janeczek H. Enhanced stability of potassium solutions in tetrahydrofuran containing 15-crown-5. *The Journal of Physical Chemistry*, 96(12), 5193–5196, 1992. doi:10.1021/j100191a082.

[86] Stein G., Treinin A. Electron-transfer spectra of anions in solution. part 1.—absorption spectra and ionic radii. *Transactions of the Faraday Society*, 55, 1086–1090, 1959. doi:10.1039/TF9595501086.

[87] Riedel R., Barrett A.G.M. *Alkali metal solutions using liquid aza crown ether analogue - characterisation and synthetic application.* Master thesis, 2014.

[88] Fuoss R.M. Solution of the conductance equation. *Journal of the American Chemical Society*, 57(3), 488–489, 1935. doi:10.1021/ja01306a502.

[89] Fuoss R.M., Kraus C.A. Properties of electrolytic solutions. iv. the conductance minimum and the formation of triple ions due to the action of coulomb forces. *Journal of the American Chemical Society*, 55(6), 2387–2399, 1933. doi:10.1021/ja01333a026.

[90] Shedlovsky T. The computation of ionization constants and limiting conductance values from conductivity measurements. *Journal of the Franklin Institute*, 225(6), 739–743, 1938. doi:10.1016/S0016-0032(38)90931-7.

[91] Li W., Kagan G., Hopson R., Williard P.G. Measurement of solution viscosity via diffusion-ordered nmr spectroscopy (dosy). *Journal of Chemical Education*, 88(9), 1331–1335, 2011. doi:10.1021/ed100941t.

[92] Metz D.J., Glines A. Density, viscosity, and dielectric constant of tetrahydrofuran between -78 and 30.degree. *The Journal of Physical Chemistry*, 71(4), 1158–1158, 1967. doi:10.1021/j100863a067.

[93] Williams D.B., Lawton M. Drying of organic solvents: quantitative evaluation of the efficiency of several desiccants. *The Journal of Organic Chemistry*, 75(24), 8351–8354, 2010. doi:10.1021/jo101589h.

[94] Sakhanov A., Prscheborovsky J. The conductivity and dissociation of silver nitrate in solvents with dielectric constant below 13. *Jour. Russ. Chem. Soc.*, 47, 849–858, 1915.

[95] Sakhanov A.N. Investigations upon abnormal electrolytic dissociation. *The Journal of Physical Chemistry*, 21(3), 169–189, 1916. doi:10.1021/j150174a001.

[96] Sakhanov A., Rabinowitch A.I. The conductivity and dissociation of silver nitrate in solvents with dielectric constant between 13-80. *Jour. Russ. Chem. Soc.*, 47, 859–870, 1915.

[97] Barthel J., Gerber R., Gores H.J. The temperature dependence of the properties of electrolyte solutions. vi. triple ion formation in solvents of low permittivity exemplified by libf4 solutions in dimethoxyethane. *Berichte der Bunsengesellschaft für physikalische Chemie*, 88(7), 616–622, 1984. doi:10.1002/bbpc.19840880709.

[98] Chen Z., Hojo M. Relationship between triple ion formation constants and the salt concentration of the minimum in the conductometric curves in low-permittivity

solvents. *The Journal of Physical Chemistry B*, 101(50), 10,896–10,902, 1997. doi: 10.1021/jp971398x.

[99] Weingärtner H. Corresponding states for electrolyte solutions. *Pure and Applied Chemistry*, 73(11), 1733–1748, 2001. doi:10.1351/pac200173111733.

[100] Bhattacharjee A., Roy M.N. Ion association and solvation behavior of tetraalkylammonium iodides in binary mixtures of dichloromethane + n,n-dimethylformamide probed by a conductometric study. *Phys Chem Chem Phys*, 12(43), 14,534–42, 2010. doi:10.1039/c0cp00532k.

[101] Ekka D., Roy M.N. Conductance, a contrivance to explore ion association and solvation behavior of an ionic liquid (tetrabutylphosphonium tetrafluoroborate) in acetonitrile, tetrahydrofuran, 1,3-dioxolane, and their binaries. *The Journal of Physical Chemistry B*, 116(38), 11,687–11,694, 2012. doi:10.1021/jp302465s.

[102] Cade E.A., Petenuci J. r., Hoffmann M.M. Aggregation behavior of several ionic liquids in molecular solvents of low polarity–indication of a bimodal distribution. *Chemphyschem*, 17(4), 520–9, 2016. doi:10.1002/cphc.201500990.

[103] Roy M.N., Ray T., Chandra Roy M., Datta B. Study of ion-pair and triple-ion origination of an ionic liquid ([bmmim][bf4]) predominant in solvent systems. *RSC Adv.*, 4(107), 62,244–62,254, 2014. doi:10.1039/c4ra09506e.

[104] Datta B., Roy M.N. Essential foundation of triple-ion and ion-pair formation of tetraheptylammonium iodide (hept4ni) salt in organic solvents investigated by physicochemical approach. *Physics and Chemistry of Liquids*, 53(5), 574–586, 2014. doi: 10.1080/00319104.2013.864565.

[105] Levin Y., Fisher M.E. Criticality in the hard-sphere ionic fluid. *Physica A: Statistical Mechanics and its Applications*, 225(2), 164–220, 1996. doi:10.1016/0378-4371(95)00336-3.

[106] Weingärtner H., Weiss V.C., Schröer W. Ion association and electrical conductance minimum in debye–hückel-based theories of the hard sphere ionic fluid. *The Journal of Chemical Physics*, 113(2), 762–770, 2000. doi:10.1063/1.481822.

[107] Lee B.S., Lin S.T. The origin of ion-pairing and redissociation of ionic liquid. *J Phys Chem B*, 121(23), 5818–5823, 2017. doi:10.1021/acs.jpcb.7b01189.

[108] Plechkova N.V., Rogers R.D., Seddon K.R. *Ionic Liquids: From Knowledge to Application - Chapter Chemical Speciation in Ionic Liquids and their Mixtures with Polar Solvents Using Dielectric Spectroscopy.* ACS Symposium Series. 2010. ISBN 0-8412-6997-1 0-8412-2491-9. doi:10.1021/bk-2009-1030.

[109] Gestblom B., Songstad J., Mattinen J., Bernáth G., Eberson L. Solvent properties of dichloromethane. vi. dielectric properties of electrolytes in dichloromethane. *Acta Chemica Scandinavica*, 41b, 396–409, 1987. doi:10.3891/acta.chem.scand.41b-0396.

[110] Kumar A., Singh G. Measurement of dielectric constant and loss factor of the dielectric material at microwave frequencies. *Progress In Electromagnetics Research*, 69, 47–54, 2007. doi:10.2528/pier06111204.

[111] Barthel J., Buchner R., Eberspächer P.N., Münsterer M., Stauber J., et al. Dielectric relaxation spectroscopy of electrolyte solutions. recent developments and prospects. *Journal of Molecular Liquids*, 78(1-2), 83–109, 1998. doi:10.1016/s0167-7322(98)00085-3.

[112] Marcus Y., Hefter G. Ion pairing. *Chem Rev*, 106(11), 4585–621, 2006. doi:10.1021/cr040087x.

[113] Barthel J., Kleebauer M., Buchner R. Dielectric relaxation of electrolyte solutions in acetonitrile. *Journal of Solution Chemistry*, 24(1), 1–17, 1995. doi:10.1007/bf00973045.

[114] Farber H., Petrucci S. Electrical conductance, ultrasonic relaxation, and microwave dielectric relaxation of sodium perchlorate in tetrahydrofuran. *The Journal of Physical Chemistry*, 80(3), 327–335, 1976. doi:10.1021/j100544a025.

[115] Haynes W.M., Lide D.R., Bruno T.J. *CRC Handbook of Chemistry and Physics, 97th Edition.* 97th edition edition, 2016. ISBN 1498754287.

[116] Engineering W. Dielectric loss factor measurement over rf frequencies between 0.1 - 40.0 ghz for common organic chemicals. *online*, last accessed Sep 2018.

[117] Badiali J.P., Cachet H., Cyrot A., Lestrade J.C. Dielectric properties of electrolyte solutions. lithium perchlorate solutions in tetrahydrofuran + benzene mixtures. *Journal of the Chemical Society, Faraday Transactions 2*, 69, 1973. doi:10.1039/f29736901339.

[118] Hayes R., Warr G.G., Atkin R. At the interface: solvation and designing ionic liquids. *Phys Chem Chem Phys*, 12(8), 1709–23, 2010. doi:10.1039/b920393a.

[119] Hayes R., Imberti S., Warr G.G., Atkin R. Pronounced sponge-like nanostructure in propylammonium nitrate. *Phys Chem Chem Phys*, 13(30), 13,544–51, 2011. doi: 10.1039/c1cp21080g.

[120] Liu L., Hao J. Study of ionic liquid microemulsions: Ethylammonium nitrate/tritonx-100/cyclohexane. *Tenside Surfactants Detergents*, 54(3), 214–219, 2017. doi:10.3139/113.110500.

[121] Zech O., Harrar A., Kunz W. *Nonaqueous Microemulsions Containing Ionic Liquids – Properties and Applications*, volume 11 of *Ionic Liquids*. IntechOpen, Rijeka.

[122] Kashyap H.K., Santos C.S., Annapureddy H.V.R., Murthy N.S., Margulis C.J., et al. Temperature-dependent structure of ionic liquids: X-ray scattering and simulations. *Faraday Discuss.*, 154, 133–143, 2012. doi:10.1039/c1fd00059d.

[123] Bowron D.T., Soper A.K., Jones K., Ansell S., Birch S., et al. Nimrod: The near and intermediate range order diffractometer of the isis second target station. *Review of Scientific Instruments*, 81(3), 033,905 1–10, 2010. doi:10.1063/1.3331655.

[124] Sivia D. *Elementary Scattering Theory: For X-ray and Neutron Users*. OUP Oxford, 2011. ISBN 9780199228676.

[125] Squires G.L. *Introduction to the Theory of Thermal Neutron Scattering*. Cambridge University Press, 2012. ISBN 1107644062.

[126] Dyke J., Levason W., Light M.E., Pugh D., Reid G., et al. Aza-macrocyclic complexes of the group 1 cations - synthesis, structures and density functional theory study. *Dalton Trans*, 44(31), 13,853–66, 2015. doi:10.1039/c5dt01865j.

[127] Benkeser R.A., Watanabe H., Mels S.J., Sabol M.A. New electrochemical method for the selective reduction of aliphatic amides to aldehydes or alcohols. *The Journal of Organic Chemistry*, 35(4), 1210–1211, 1970. doi:10.1021/jo00829a089.

[128] Bedenbaugh A.O., Payton A.L., Bedenbaugh J.H. Lithium-methylamine studies. 3. reduction of carboxamides. *The Journal of Organic Chemistry*, 44(25), 4703–4705, 1979. doi:10.1021/jo00393a051.

[129] *Comprehensive Organic Name Reactions and Reagents - 109. Bouveault–Blanc Reduction.* John Wiley and Sons, Inc., 2010. ISBN 978-0-471-70450-8. doi: 10.1002/9780470638859.conrr109.

[130] Bouveault L., Blanc G. Préparation des alcools primaires au moyen des acides correspondants. *Comptes rendus hebdomadaires des séances de l'Académie des sciences*, 136, 1676–1678, 1903.

[131] Bouveault L., Blanc G. Préparation des alcools primaires au moyen des acides correspondants. *Comptes rendus hebdomadaires des séances de l'Académie des sciences*, 137, 60–62, 1903.

[132] Mathre D.J., Guida W.C. Dissolving metal reductions with sodium potassium alloy in the presence of 18-crown-6. *Tetrahedron Letters*, 21(50), 4773–4776, 1980. doi: 10.1016/0040-4039(80)80136-5.

[133] Pez G.P., Mador I.L., Galle J.E., Crissey R.K., Forbes C.E. Selective alkali metal and hydrogen reduction of benzene to cyclohexene. *Journal of the American Chemical Society*, 107(13), 4098–4100, 1985. doi:10.1021/ja00299a068.

[134] Ohsawa T., Oishi T. Dissolving metal reduction k metal-crown ether-toluene system for reductive defluorination. *Journal of Inclusion Phenomena*, 2(1-2), 185–194, 1984. doi:10.1007/BF00663255.

[135] Page P.C.B., Murrell V.L., Limousin C., Laffan D.D.P., Bethell D., et al. The first stable enantiomerically pure chiral n-h oxaziridines: synthesis and reactivity. *The Journal of Organic Chemistry*, 65(13), 4204–4207, 2000. doi:10.1021/jo000176j.

[136] Garst M.E., Dolby L.J., Esfandiari S., Fedoruk N.A., Chamberlain N.C., et al. Reductions with lithium in low molecular weight amines and ethylenediamine. *The Journal of Organic Chemistry*, 65(21), 7098–7104, 2000. doi:10.1021/jo0008136.

[137] Lemoucheux L., Seitz T., Rouden J., Lasne M.C. Preparation of tertiary amides from carbamoyl chlorides and organocuprates. *Org Lett*, 6(21), 3703–6, 2004. doi: 10.1021/ol0487130.

[138] Li J.J. *Science of Synthesis 27, Category 4: Compounds with Two Carbon Heteroatom Bonds, Product Class 20: N-Nitroimines and N-Nitrosoimines.* Thieme

Verlagsgruppe, Stuttgart, New York, Delhi, Rio, 2005. ISBN 9783131841117. doi: 10.1055/b-003-125723.

[139] Kyung J.H., Clapp L.B. Pathway control of products in the reaction of nitrosyl chloride on oximes. *The Journal of Organic Chemistry*, 41(11), 2024–2027, 1976. doi:10.1021/jo00873a030.

[140] Adamopoulos S., Boulton A.J., Tadayoni R., Webb G.A. On the formation and nitrogen nuclear magnetic resonance spectra of some nitrimines ('pernitroso–ketones'), and the mechanism of oxime cleavage by nitrous acid. *J. Chem. Soc., Perkin Trans. 1*, (0), 2073–2077, 1987. doi:10.1039/p19870002073.

[141] Witt O.N. Ferdinand tiemann. ein lebensbild. *Berichte der deutschen chemischen Gesellschaft*, 34(3), 4403–4455, 1901. doi:10.1002/cber.190103403176.

[142] Tiemann F. Ueber campher. *Berichte der deutschen chemischen Gesellschaft*, 28(1), 1079–1093, 1895. doi:10.1002/cber.189502801232.

[143] Rothman E.S., Day A.R. Hydantoins from alicyclic ketones and aldehydes. *Journal of the American Chemical Society*, 76(1), 111–113, 1954. doi:10.1021/ja01630a030.

[144] Barton D.H.R., Sammes P.G., Silva M. Photochemical transformations—xx. *Tetrahedron*, 22, 57–67, 1966. doi:10.1016/s0040-4020(01)99095-7.

[145] Ahmad M.S., Raza S.K. Thermolytic transformation of steroidal nitroimines. *Indian J. Chem. B*, 23, 774–775, 1984.

[146] Sokolova A.S., Yarovaya O.C., Korchagina D.V., Zarubaev V.V., Tretiak T.S., et al. Camphor-based symmetric diimines as inhibitors of influenza virus reproduction. *Bioorg Med Chem*, 22(7), 2141–8, 2014. doi:10.1016/j.bmc.2014.02.038.

[147] Osby J.O., Ganem B. Rapid and efficient reduction of aliphatic nitro compounds to amines. *Tetrahedron Letters*, 26(52), 6413–6416, 1985. doi:10.1016/s0040-4039(00)99014-2.

[148] Lal B., Pramanik B.N., Manhas M.S., Bose A.K. Diphenylphosphoryl azide a novel reagent for the stereospecific synthesis of azides from alcohols. *Tetrahedron Letters*, 18(23), 1977–1980, 1977. doi:10.1016/s0040-4039(01)83657-1.

[149] Sugandhi E.W., Slebodnick C., Falkinham J. O. r., Gandour R.D. Synthesis and antimicrobial evaluation of water-soluble, dendritic derivatives of epimeric 5alpha-cholestan-3-amines and 5alpha-cholestan-3-yl aminoethanoates. *Steroids*, 72(8), 615–26, 2007. doi:10.1016/j.steroids.2007.04.001.

[150] de Armas P., Francisco C.G., Hernández R., Salazar J.A., Suárez E. Steroidal n-nitroamines. part 4. intramolecular functionalization of n-nitroamine radicals: synthesis of 1,4-nitroimine compounds. *Journal of the Chemical Society, Perkin Transactions 1*, 0(12), 3255–3265, 1988. doi:10.1039/P19880003255.

[151] Shamsuzzaman, Mashrai A., Ahmad A., al. e. Synthesis, evaluation and docking studies on steroidal pyrazolones as anticancer and antimicrobial agents. *Medicinal Chemistry Research*, 23(1), 348–362, 2014. doi:10.1007/s00044-013-0636-y.

[152] Bull J.R., Jones E.R.H., Meakins G.D. 470. nitro-steroids. part ii. a new route to nitro-steroids. *Journal of the Chemical Society (Resumed)*, pages 2601–2614, 1965. doi:10.1039/jr9650002601.

[153] Dauben W.G., Takemura K.H. A study of the mechanism of conversion of acetate to cholesterol via squalene1. *Journal of the American Chemical Society*, 75(24), 6302–6304, 1953. doi:10.1021/ja01120a504.

[154] Dodson R.M., Riegel B. The stereochemistry of the i-steroids and their transformation products. *The Journal of Organic Chemistry*, 13(3), 424–437, 1948. doi:10.1021/jo01161a018.

[155] Pinkus J.L., Cohen T. Bis(5.alpha.-cholestan-3.alpha.-yl)amine, a diaxial bis-steroidal amine. *Journal of Organic Chemistry*, 33(9), 3538–3541, 1968. doi:10.1021/jo01273a039.

[156] Boonyarattanakalin S., Martin S.E., Sun Q., Peterson B.R. A synthetic mimic of human fc receptors: defined chemical modification of cell surfaces enables efficient endocytic uptake of human immunoglobulin-g. *J Am Chem Soc*, 128(35), 11,463–70, 2006. doi:10.1021/ja062377w.

[157] Still W.C., Kahn M., Mitra A. Rapid chromatographic technique for preparative separations with moderate resolution. *The Journal of Organic Chemistry*, 43(14), 2923–2925, 1978. doi:10.1021/jo00408a041.

[158] Desai P., Schildknegt K., Agrios K.A., Mossman C., Milligan G.L., et al. Reactions of alkyl azides and ketones as mediated by lewis acids: schmidt and mannich reactions using azide precursors. *Journal of the American Chemical Society*, 122(30), 7226–7232, 2000. doi:10.1021/ja000490v.

[159] Bondavalli F., Lanteri S., Longobardi M., Schenone P. Synthesis and pharmacological activity of derivatives of exo-trimethylenenorbornane. i. *Farmaco, Edizione Scientifica*, 34(11), 945–951, 1979.

[160] Takatsuto S., Ikekawa N. Synthesis of 5.alpha.-cholestan-6-one derivatives with some substituents at the c-1, c-2, or c-3 position. *Chemical & Pharmaceutical Bulletin*, 35(3), 986–995, 1987. doi:10.1248/cpb.35.986.

[161] Baek S.Y., Kim Y.W., Yoo S.H., Chung K., Kim N.K., et al. Synthesis and rust preventing properties of dodecyl succinate derivatives containing triazole groups. *Industrial & Engineering Chemistry Research*, 51(28), 9669–9678, 2012. doi:10.1021/ie300316f.

[162] Sarker H., Greer M.L., Blackstock S.C. Synthesis, structure, and conformational dynamics of bridgehead-substituted nitrosamines. di-1-adamantylnitrosamine and di-1-norbornylnitrosamine. *The Journal of Organic Chemistry*, 61(9), 3177–3182, 1996. doi:10.1021/jo951842x.

[163] Simoni E., Daniele S., Bottegoni G., Pizzirani D., Trincavelli M.L., et al. Combining galantamine and memantine in multitargeted, new chemical entities potentially useful in alzheimer's disease. *J Med Chem*, 55(22), 9708–21, 2012. doi:10.1021/jm3009458.

[164] Mukhopadhyay P., Zavalij P.Y., Isaacs L. High fidelity kinetic self-sorting in multicomponent systems based on guests with multiple binding epitopes. *J Am Chem Soc*, 128(43), 14,093–102, 2006. doi:10.1021/ja063390j.